To the Graduate Council:

I am submitting herewith a dissertation written by Ming-Ya Tang entitled "Dynamic SAXS Studies of the Crazing and Fracture of Polystyrene." I have examined the final copy of this dissertation for form and content and recommend that it be accepted in partial fulfillment of the requirements for the degree of Doctor of Philosophy, with a major in Polymer Engineering.

John F. Fellers

John F. Fellers, Major Professor

We have read this dissertation
and recommend its acceptance:

L. E. Nielsen

Jan-Chyong Lin

Lynda J. Magid

Accepted for the Council:

Lew Minkel

The Graduate School

4

DYNAMIC SAXS STUDIES OF THE CRAZING AND FRACTURE OF POLYSTYRENE

A Dissertation

Presented for the

Doctor of Philosophy

Degree

The University of Tennessee, Knoxville

Ming-Ya Tang

March 1984

DEDICATION

This dissertation is dedicated to my parents, Mr. and Mrs. Chih-Chu Tang (湯 之 楚), whose love, support, and encouragement made this work possible.

ACKNOWLEDGEMENTS

The author wishes to thank her advisor, Dr. J. F. Fellers, for giving her the chance to work under him and for his help during the course of this work.

Great appreciation goes to Dr. J. S. Lin for his extremely helpful consultations concerning the operatation of the National Center for Small Angle Scattering Research facilities, data treatment, and enlightening discussion.

The author appreciates the financial support given her by the Chemical, Metallurgical and Polymer Engineering Department. The National Science Foundation provided finance assistance through grant DMR-80-26051. Appreciation is extended to Dow Chemical Company for supplying some of the polystyrene samples used in this research.

The author is indebted to P. A. Westbrook for materials on surface scattering phenomenon.

Lastly, the author thanks the entire faculty and staff of the Department of Chemical, Metallurgical and Polymer Engineering.

ABSTRACT

Small-angle x-ray scattering (SAXS) studies of bulk polystyrene (PS) under uniaxial tension have been made at room temperature to investigate the stress induced changes in microstructure. The SAXS facilities in the National Center for Small Angle Scattering Research at Oak Ridge National Laboratory were used. The effects of molecular weight, molecular weight distribution, and molecular orientation on the fracture mechanism have been investigated. The formation of crazes is indicated by an abrupt increase in the scattering power. The excess scattering power induced by stress can be resolved into the surface scattering and the volume scattering components. Surface scattering, which is caused by specular reflection from the planar microcrack interfaces, shows as an intense streak on the intersection of the incident plane and the detector plane and contributes most of the excess scattering power. By converting the observed scattering intensity into absolute units, the surface scattering invariant relating to the interfacial area of microcracks and the volume fraction of microvoids are determined. From the surface scattering component, the average length of the steps caused by the microcrack jumping from one craze-matrix interface to the other is determined and is found to increase with the degree of molecular orientation. When the tensile force is not parallel nor perpendicular to the molecular orientation direction, the interfaces of the crazes are no longer perpendicular to the tensile direction. This suggests the strain-based criteria for crazing is more suitable than the stress-based criteria.

TABLE OF CONTENTS

CHAPTER		PAGE
1.	INTRODUCTION	1
2.	HISTORICAL BACKGROUND	3
2.1	Microstructure in Glassy Polymers	3
2.1.1	Random Coil Model	3
2.1.2	Folded Chain Fringed Micellar Grain Model	5
2.1.3	Meander Model	6
2.2	Molecular Orientation in Glassy Polymers	7
2.2.1	Orientation Behavior	7
2.2.2	Stress Optical Law	8
2.2.3	Structure Changes in Oriented Polystyrene	10
2.3	Fracture Process in Glassy Polymers	12
2.3.1	Features of Fracture Surface	12
2.3.2	Model of Fracture Process	16
2.4	Microstructure of Craze in Glassy Polymers	17
2.4.1	Craze Investigation by Optical Measurement	18
2.4.2	Craze Investigation by Electron Diffraction	19
2.4.3	Craze Investigation by Electron Microscopy	19
2.4.4	Craze Investigation by Wide-Angle X-Ray Scattering	23
2.4.5	Craze Investigation by Small-Angle X-Ray Scattering	23
2.4.6	Effect of Molecular Weight on Craze Microstructure	31
2.4.7	Effect of Molecular Orientation on Craze Microstructure	32
3.	SMALL-ANGLE X-RAY SCATTERING THEORY	36
3.1	Introduction	36
3.2	Basic Theory	39
3.2.1	Basic Assumptions	40
3.2.2	Scattering Amplitude	41
3.2.3	Scattering Intensity	45
3.2.4	Real Space and Reciprocal Space	46
3.2.5	Correlation Function and Invariant	47
3.2.6	Ewald's Sphere and Intensity Profile	52

CHAPTER PAGE

3. (continued)

3.3 Relations Between Theory and Experiment 55
3.3.1 Definition of Coordinates in the Detector Plane 55
3.3.2 The Collimation Error 56
3.3.3 The Precision of Measurement 57
3.3.4 Termination Effect 57

3.4 Structure Analysis of a Macroscopically Isotropic System 58
3.4.1 General Cases 59
3.4.2 Two-Phase System in General 60
3.4.2.1 Scattering Power 60
3.4.2.2 Porod's Law 61
3.4.2.3 Chord Length 62
3.4.2.4 Specific Inner Surface 63
3.4.3 Dilute Particle Dispersions 64
3.4.3.1 General Description 64
3.4.3.2 Guinier's Law 65

3.5 Structure Analysis of an Anisotropic System 67
3.5.1 Two-Phase System in General 68
3.5.1.1 Scattering Power 68
3.5.1.2 Porod's Law 68
3.5.1.3 Guinier's Law 69
3.5.2 Types of Anisotropic System 69
3.5.2.1 Cylindrically Symmetrical System . . 69
3.5.2.2 Other Types of Symmetry 72

4. EXPERIMENTAL 73

4.1 Sample Preparation 73
4.1.1 Materials 73
4.1.2 Preparation of Unoriented Sample 75
4.1.3 Preparation of Oriented Sample 77

4.2 SAXS Apparatus 80
4.2.1 X-Ray Generator 82
4.2.2 Monochromator 82
4.2.3 Collimator 84
4.2.4 Specimen Chamber and Dynamic Device 84
4.2.5 Detector 86
4.2.6 Computer 86

CHAPTER PAGE

4. (continued)

4.3 Analysis of Data and Computer Programs 87
4.3.1 Introduction: Software for the ORNL 10-m SAXS Instrument 87
4.3.2 Data Acquisition and Instrument Control . . . 87
4.3.3 Data Base File Management 88
4.3.4 Data Plotting and Analysis Programs 89
4.3.5 Analysis of Data 90
4.3.5.1 Background and Dark Current Correction 90
4.3.5.2 Detector Sensitivity 93
4.3.5.3 Transmission Coefficient 93
4.3.5.4 Analysis for Isotropic Systems . . . 96
4.3.5.5 Analysis for Crazed Systems 97

5. ABSOLUTE INTENSITY MEASUREMENT OF SAXS AT ORNL AND THE ORIGIN OF SAXS FROM UNDEFORMED POLYSTYRENE 98

5.1 Introduction 98

5.2 Definition of Absolute Intensity 99

5.3 Lupolen as Calibration Standard 102

5.4 Experimental 102

5.5 Data Analysis 105

5.6 Calibration Procedure 107
5.6.1 Calibration for Long Geometry 107
5.6.2 Calibration for Short Geometry 112
5.6.3 Superposition of Long and Short Geometry Data 116

5.7 Origin of SAXS from Undeformed Polystyrene 117

5.8 Conclusion 126

6. SURFACE SCATTERING PHENOMENON AND THE SAXS STUDIES OF POLYSTYRENE CRAZE 127

6.1 Introduction 127

6.2 Theory 131
6.2.1 Refractive Index of X-Rays 131

CHAPTER PAGE

6. (continued)

6.2.2 Electromagnetic Optics of Isotropic Media . . 133
6.2.2.1 The Laws of Reflection and Refraction 133
6.2.2.2 Fresnel Formulae 135
6.2.2.3 The Reflectance and Transmittance . . 136
6.2.2.4 Total Reflection 136
6.2.2.5 Penetration of a Totally Reflected Electromagnetic Wave into the Film Between Two Media 140
6.2.3 Scattering of Electromagnetic Waves by a Rough Surface 142
6.2.3.1 A Rough Surface 145
6.2.3.2 Surface Scattering Factor 147
6.2.3.3 Comparison Between Surface Scattering and Volume Scattering 150
6.2.3.4 Surface Scattering Intensity 150
6.2.3.5 Relations Between Theory and Experiment 153
6.2.3.6 Roughness Analysis of a Two-Dimensional Isotropic Surface . . 156

6.3 Numerical Results 159

6.4 Experimental Results 165
6.4.1 Laminated Polystyrene Sample 165
6.4.2 Polystyrene Craze 168

6.5 Summary and Conclusions 178

7. SAXS OF CRAZES IN UNORIENTED POLYSTYRENE 180

7.1 General Description 180

7.2 Characterization of the Origin of SAXS from Crazed Polystyrene 186

7.3 Data Analysis 187
7.3.1 Surface Scattering Analysis 188
7.3.2 Volume Scattering Analysis 195

7.4 Results and Discussion 201
7.4.1 Effect of Stress 201
7.4.2 Effect of Molecular Weight 205
7.4.3 Effect of Molecular Weight Distribution . . . 212

7.5 Summary and Conclusions 214

CHAPTER PAGE

8. SAXS OF CRAZES IN ORIENTED POLYSTYRENE 217

8.1 Introduction 217

8.2 Experimental 219

8.3 Results and Discussion 220
8.3.1 Varying Extension Ratio 222
8.3.2 Varying Molecular Weight 237
8.3.3 Varying Stretching Temperature 241
8.3.4 Varying Test Angle 245

8.4 Conclusions 254

9. RECOMMENDATIONS 261

LIST OF REFERENCES 263

APPENDICES 276

APPENDIX A - Program SAXS.FOR 277

APPENDIX B - Program TOTAL.FOR 311

APPENDIX C - Program GAMMA.FOR 319

VITA 323

LIST OF TABLES

TABLE		PAGE
2-1	Comparison of the features of electron microscopy and small-angle x-ray scattering as investigative tools for crazes studies	25
4-1	Polymer characterization	74
5-1	Geometry of the ORNL SAXS camera used in the Lupolen calibration measurement	104
6-1	Material constants used to calculate the critical angle of total reflection for three typical material systems	139
6-2	Comparison of volume scattering and surface scattering	151
8-1	Sample characterizations for the study of orientation effects on crazing	221

LIST OF FIGURES

FIGURE		PAGE
2-1	Model representations of the various interpretations of the nature of the amorphous state: (A) random coils [1]; (B) folded chain fringed micellar grains [2]; (C) meander model [3]	4
2-2	Features of the fracture surface of polystyrene (49)	13
2-3	Characteristic regions of the fracture surface of polystyrene: (A) optical micrograph showing a plane view; (B) schematic drawings of the three distinct regions of the fracture surface [48]	15
2-4	Transmission electron micrographs of crazes in (A) a pre-crazed polystyrene specimen [66]; (B) a microtomed thin section of polystyrene [48]; (C) a "thick" thin film of polystyrene [48]	21
2-5	Schematic drawing for the model of a craze as proposed by Beahan et al. (68)	24
3-1	Scattering from two scattering centers	43
3-2	Ewald's sphere of diffraction and the two-dimensional detector plane	53
3-3	Cylindrical and cartesian coordinates (A) in real space and (B) in reciprocal space	71
4-1	Schematic diagram of the environmental oven and associated control system (145)	79
4-2	Schematic drawing of the ORNL 10-meter small-angle x-ray scattering camera (147)	81
4-3	Schematic drawing of the deformation device on the ORNL 10-meter SAXS camera (148)	83
4-4	Typical background scattering contour plot	91
4-5	Spatial distribution of the iron-55 radiation on the two-dimensional detector plane	94
5-1	Transmitted intensity versus number of nickel foils	109

FIGURE PAGE

5-2 Two-dimensional contour plot of the scattering intensity of Lupolen measured with long geometry 110

5-3 Radial averaged small-angle x-ray scattering intensity of Lupolen 23/7 versus s measured with long geometry 111

5-4 Two-dimensional contour plot of the scattering intensity of Lupolen measured with short geometry 114

5-5 Radial averaged small-angle x-ray scattering intensity of Lupolen 23/7 versus s measured with short geometry 115

5-6 Superposition of absolute intensity data for Lupolen 23/7 measured with long geometry and short geometry 118

5-7 Dependence of the absolute scattering intensity for PS108 on s 120

5-8 Porod plot of PS108: I(s) versus $1/s^4$ 122

5-9 Molecular weight dependence of the thermal frozen-in electron density fluctuation for polystyrene at room temperature 123

5-10 Molecular weight distribution dependence of the thermal frozen-in electron density fluctuation for polystyrene at room temperature 124

6-1 Reflection and refraction of an electromagnetic wave . . . 134

6-2 The reflectance curve calculated by Fresnel formulae for smooth surfaces of three representative material systems 138

6-3 Penetration of the totally reflected electromagnetic wave into the film between two media 141

6-4 Reflectance of a polystyrene matrix film between void media as a function of glancing angle ϵ at various thickness d 143

6-5 Transition from specular reflection to diffuse surface scattering from surfaces of various degree of roughness (171) 144

6-6 Schematic representation of a rough surface separating two media of refractive indices n_1 and n_2 146

FIGURE PAGE

6-7 Sample axes with respect to laboratory reference axes . . 154

6-8 Profiles of surfaces with (A) large correlation distance and (B) small correlation distance (171) 158

6-9 Three-dimensional plot for the calculated optical factor of PS-void interface upon parallel incidence of x-rays . . 160

6-10 Calculated angular distribution of optical factor on the plane of incidence versus scattering angle 2θ for three kinds of interfaces 161

6-11 Three-dimensional plot for the calculated surface scattering intensity distribution on the detector plane by assuming an isotropic Gaussian correlation function for the PS-void interface. (A) τ = 10 μm; (B) τ = 0.1 μm 163

6-12 Comparison among the three calculated surface scattering intensity distribution on the plane of incidence for three kinds of interfaces with different Gaussian correlation lengths 164

6-13 Calculated angular distribution of the surface scattering intensity on the plane of incidence for a PS-void interface at various tilting angles α 166

6-14 Effect of varying the interfacial electron contrast on the SAXS patterns from laminated PS film samples: (A) PS-air; (B) PS-epoxy 167

6-15 Observed surface scattering intensity and calculated surface scattering factor on the plane of incidence versus scattering angle 2θ for PS-air and PS-epoxy interfaces 169

6-16 Surface roughness correlation function $G(r_p)$ of PS-air and PS-epoxy interfaces versus length r_p 170

6-17 Comparison of SAXS patterns from: (A) typical polystyrene crazes; (B) laminated polystyrene film sample 171

6-18 Effect of tilting on the SAXS patterns of crazes in initially unoriented polystyrene: (A) incident x-ray is normal to the tensile axis; (B) sample is tilted eight degrees toward the tensile axis; (C) contour pattern obtained by subtracting (B) from (A) 173

FIGURE PAGE

6-19 Surface scattering intensity and surface scattering factor on the plane of incidence versus scattering angle 2θ for polystyrene crazes 175

6-20 Comparison of the surface roughness correlation functions of polystyrene craze and PS-air interfaces 176

6-21 Transmission electron micrographs of (A) a fractured craze [66] and (B) an air craze in the process of fracturing [208] 177

7-1 Variation of craze SAXS pattern in initially unoriented polystyrene with loading state. PSBI: $\overline{Mn}$ = 160,000; DP = 1.14 181

7-2 Logarithmic intensity distribution along different azimuthal slices for a typical craze SAXS pattern in unoriented polystyrene. PSBI; σ = 3500 psi 184

7-3 Intensity distribution along the meridional direction and the equatorial direction as a function of loading state. PSBI: $\overline{Mn}$ = 160,000; DP = 1.14 185

7-4 Typical variations of surface scattering intensity distribution along the meridional direction with stress levels 189

7-5 Surface scattering factor versus surface scattering reciprocal space vector $\vec{s}_p$ at various stress levels . . . 191

7-6 Variations of surface roughness correlation function $G(r_p)$ with stress levels 192

7-7 (A) Surface scattering invariant, (B) volume scattering invariant, and (C) microvoid fraction as a function of the stress level. PSBI: $\overline{Mn}$ = 160,000; DP = 1.14 193

7-8 (A) Correlation distance τ of surface roughness distribution and (B) chord length $\bar{l}$ of microvoids as a function of stress. PSBI: $\overline{Mn}$ = 160,000, DP = 1.14 . . . 196

7-9 Typical correlation function of electron density fluctuation of polystyrene crazes. PSBI; σ = 4000 psi . 200

7-10 Proposed model for crazing and fracture 204

FIGURE PAGE

7-11 (A) Stress-strain behavior and (B) the variation of normalized intensity with stress for monodisperse polystyrene of different molecular weights 206

7-12 Comparison of (A) the surface scattering intensity and (B) the surface roughness correlation function at fracture for monodisperse polystyrene of different molecular weights 207

7-13 Surface scattering invariant versus stress level for monodisperse polystyrene of different molecular weights . 208

7-14 Comparison of (A) surface scattering invariant Ks at fracture and (B) correlation distance τ of surface roughness distribution at fracture for monodisperse polystyrene of different molecular weights 210

7-15 (A) Volume scattering invariant and (B) microvoid fraction versus stress level for monodisperse polystyrene of different molecular weights 211

7-16 Comparison of the chord length $\bar{\ell}$ of microvoids at fracture for monodisperse polystyrene of different molecular weights 213

7-17 (A) Surface scattering invariant Ks, (B) volume scattering invariant Kv, and (C) microvoid fraction as a function of the stress level for two polystyrenes with different molecular weight distributions 215

8-1 Stress-strain curves for uniaxially oriented polystyrene with various extension ratios prepared at the same stretching temperature Ts and cross-head speed $\dot{\gamma}$. PSBI: $\overline{Mn}$ = 160,000; DP = 1.14; Ts = 115°C; $\dot{\gamma}$ = 500%/min 223

8-2 Comparison of the SAXS patterns at different deformation stages for the specimens studied in Figure 8-1. (A) No stress; (B) craze initiation; (C) fracture; and (D) relaxed for 10^7 seconds after fracture 225

8-3 Comparison of the meridional and equatorial scattering intensity distributions at the fracture point for the specimens studied in Figure 8-1 230

8-4 Comparison of the meridional and equatorial scattering intensity distribution for each specimen studied in Figure 8-1 at the fracture point 232

FIGURE PAGE

8-5 Variation of the meridional and equatorial scattering intensity at 2θ = 1.5 mrad and 2θ = 5 mrad with stress for the specimens studied in Figure 8-1 234

8-6 (A) Stress-strain curves and (B) stress-normalized intensity curves for uniaxially oriented polystyrenes of various molecular weight prepared using the same conditions. Ts = 115°C; $\dot{\gamma}$ = 500%/min; L/L_o = 3.0 . . . 238

8-7 Comparison of the SAXS patterns at different deformation stages for the specimens studied in Figure 8-6 239

8-8 Comparison of the meridional and equatorial scattering intensity distributions for each specimen studied in Figure 8-6 at the fracture point 240

8-9 Variation of the meridional and equatorial scattering intensity at 2θ = 1.5 mrad and 2θ = 5 mrad with stress for the specimens studied in Figure 8-6 242

8-10 Comparison of the SAXS patterns at different deformation stages for the PS103 series. $\overline{Mn}$ = 118,000; $\dot{\gamma}$ = 500%/min; L/L_o = 3.0 243

8-11 Variation of the meridional and equatorial scattering intensity at 2θ = 1.5 mrad and 2θ = 5 mrad with stress for the PS103 series 244

8-12 Comparison of the SAXS patterns at different deformation stages for the PS109 series. $\overline{Mn}$ = 186,000; $\dot{\gamma}$ = 500%/min; L/L_o =3.0 246

8-13 Variation of the meridional and equatorial scattering intensity at 2θ = 1.5 mrad and 2θ = 5 mrad with stress for the PS109 series 247

8-14 (A) Stress-strain curves and (B) stress-normalized intensity curves for tensile tests on specimens cut at different angles from uniaxially oriented polystyrene sheet 248

8-15 Comparison of the SAXS patterns taken prior to fracture for various ψ_m 249

8-16 Definition of craze directions in (A) reciprocal space and (B) real space 250

FIGURE PAGE

8-17 Variation of craze directions defined by (A) angle ψ_s and (B) angle ψ_v with test angle ψ_m 252

8-18 Variation of the scattering intensity along (A) $\vec{n}_s$ and (B) $\vec{n}_v$ at 2θ = 1.5 mrad with stress 255

8-19 Variation of the scattering intensity along (A) $\vec{n}_s$ and (B) $\vec{n}_v$ at 2θ = 5 mrad with stress 256

8-20 Comparison of the SAXS patterns of the fractured specimens relaxed for 10^7 seconds for various ψ_m 257

8-21 Relaxations of the specimens with (A) $\psi_m = 30^o$ and (B) $\psi_m = 45^o$ at various stages after fracture 258

LIST OF SYMBOLS

Symbol	Definition	Units
$\mathring{A}$	Angstrom unit	10^{-10} meter
a	area of a detector element	cm^2
$\vec{b}$	radius vector in three-dimensional reciprocal (Fourier) space	$\mathring{A}^{-1}$
b	magnitude of radius vector $\vec{b}$; $b = \lvert\vec{b}\rvert = 2\sin\theta/\lambda$	$\mathring{A}^{-1}$
b_1, b_2, b_3	orthogonal components of $\vec{b}$	$\mathring{A}^{-1}$
C	stress-optical constant	
c_1, c_2, c_3	principal axes of the strain ellipsoid	
c	velocity of light in vacuum = 2.99733E10 cm/sec	cm/sec
dv_R	an element of volume in the real space	$\mathring{A}^3$
dv_s	an element of volume in the reciprocal space	$\mathring{A}^{-3}$
DP	polydispersity = $\overline{Mw}/\overline{Mn}$	
$dP/d\Omega$	surface scattering intensity	$\mathring{A}^4/\mathring{A}^4$-cm thickness
E	electric field strength of a propagating electromagnetic wave at the observation point	
Eo	maximum strength of the electric field	
Ee	amplitude scattered by one electron	
e	charge of an electron = 4.8029E-10 esu	esu
$\vec{e}_1, \vec{e}_2, \vec{e}_3$	orthogonal unit vectors in the real space	
eu	electron unit, absolute unit for the x-ray scattering intensity	electron**2
$F(\vec{s})$	absolute scattering amplitude function of a structure = E/Ee	

Symbol	Definition	Units
$F^*(\vec{s})$	complex conjugate of $F(\vec{s})$	
f	scattering factor of the scattering center at position $\vec{R}$	
f_θ^2	polarization factor = $(1 + \cos^2 2\theta)/2$	
$\mathcal{F}$	symbol for three-dimensional Fourier transformation	$\mathring{A}^3$
$\mathcal{F}^{-1}$	symbol for three-dimensional inverse Fourier transformation	$\mathring{A}^{-3}$
$\mathcal{F}_1$	symbol for one-dimensional Fourier transformation	$\mathring{A}$
$\mathcal{F}_2$	symbol for two-dimensional Fourier transformation	$\mathring{A}^2$
$G(\vec{r}_p)$	correlation function of surface roughness distribution function	
$g(\vec{s}_p)$	surface scattering factor = $\left\|\xi(\vec{s}_p)\right\|^2$	$\mathring{A}^4$/cm thickness
$I(\vec{s})$	absolute intensity function in the reciprocal space = $\left\|F(\vec{s})\right\|^2$	eu/$\mathring{A}^3$
$Ie(\vec{s})$	observed intensity for one electron = $\left\|Ee(\vec{s})\right\|^2$	
i	$+\sqrt{-1}$	
i_1	angle of incidence in medium 1	
i_2	angle of refraction in medium 2	
i_1'	angle of reflection in medium 1	
i_c	critical incident angle for total reflection to occur	
i_e	Thomson factor = e^4/m^2c^4 = 7.94030E-26 cm^2	cm^2
Jo	zero order Bessel function	
Ks	surface scattering invariant	$\mathring{A}^4/\mathring{A}^2$-cm thickness
K or Kv	volume scattering invariant	eu/$\mathring{A}^6$

Symbol	Definition	Units
Kp	Porod's constant	eu/A^{o7}
$\vec{k}$	wave vector parallel to the scattered wave	A^{o-1}
$\vec{ko}$	wave vector parallel to the incident wave	A^{o-1}
$\vec{k}_p$	component of the scattered wave vector parallel to the interface plane between two media	A^{o-1}
$\vec{ko}_p$	component of the incident wave vector parallel to the interface plane between two media	A^{o-1}
$\vec{kr}$	wave vector parallel to the reflected wave	A^{o-1}
$\vec{kt}$	wave vector parallel to the transmitted wave	A^{o-1}
k	wave number of the scattered wave $= \lvert\vec{k}\rvert = 2\pi/\lambda$	A^{o-1}
ko	wave number of the incident wave $= \lvert\vec{ko}\rvert = 2\pi/\lambda$	A^{o-1}
k_B	Boltzmann's constant = 1.38062E-16 erg/^oK	erg/^oK
L	distance from the emitting electron to the point of observation	cm
L/L_o	extension ratio	
$\bar{\ell}$	correlation length of electron density fluctuation	A^o
ℓ_c	average chord length	A^o
$\overline{Me}$	entanglement molecular weight	gm/gm-mole
$\overline{Mn}$	number averaged molecular weight	gm/gm-mole
$\overline{Mw}$	weight averaged molecular weight	gm/gm-mole
m	mass of a rest electron = 9.108E-28 gm	gm
$\vec{n}$	normal upon the interface between two media	
$\vec{n}_s$	normal upon the craze plane	

Symbol	Definition	Units
$\vec{n_v}$	transverse axis of the microvoids in the crazes	
n	absolute refractive index	
n_1	absolte refractive index of medium 1	
n_2	absolte refractive index of medium 2	
n_{12}	relative refractive index of medium 2 respective to medium 2 = n_2/n_1	
Δn	birefringence	
Po	intensity of the primary beam	counts/sec
P_{obs}	observed scattering intensity	counts/sec
$Q(\vec{r})$	self-convolution of the electron density function = $\tilde{\rho}^2(\vec{R})$	eu/A^6
$\vec{R}$, $\vec{R'}$	position vector in the real space	A
$\vec{R_p}$, $\vec{R_p'}$	projection of the position vector R on the interface plane between two media	A
R	magnitude of the position vector $\vec{R}$; $R = \lvert\vec{R}\rvert$	A
R_p	magnitude of the vector $\vec{R_p}$; $R_p = \lvert\vec{R_p}\rvert$	A
Rg	electronic radius of gyration	A
$\vec{r}$	shift vector in the real space = $\vec{R'} - \vec{R}$	A
$\vec{r_p}$	projection of the shift vector $\vec{r}$ on the interface plane between two media = $\vec{R_p'} - \vec{R_p}$	A
r_1, r_2, r_3	orthogonal components of $\vec{r}$	A
r_{12}	Fresnel reflection coefficient	
r_{12}^*	Complex congugate of r_{12}	
S	total interfacial area under irradiation	A^2

Symbol	Definition	Units
$\vec{s}$	scattering vector in the three-dimensional reciprocal space = $\vec{k} - \vec{ko}$	$\mathring{A}^{-1}$
$\vec{s}_p$	projection of the scattering vector $\vec{s}$ on the interface plane between two media = $\vec{k}_p - \vec{ko}_p$	$\mathring{A}^{-1}$
s	magnitude of the scattering vector $\vec{s}$; $s = \lvert\vec{s}\rvert = 4\pi \sin\theta / \lambda$	$\mathring{A}^{-1}$
s_1, s_2, s_3	orthogonal components of $\vec{s}$	$\mathring{A}^{-1}$
T	temperature	^oK or ^oC
Tg	glass transition temperature	^oC
Ts	hot-stretching temperature	^oC
t	thickness of the scattering sample	cm
t_{12}	Fresnel transmission coefficient	
$\vec{u_1}, \vec{u_2}, \vec{u_3}$	orthogonal unit vectors in the reciprocal space	
V	volume of the sample of a scatterer	$\mathring{A}^3$
V_2	volume occupied by the disperse phase	$\mathring{A}^3$
x_i	volume fraction of phase i	
α	tilt angle	mrad or degree
α_1, α_2	principal polarizabilities	
$\dot{\gamma}$	cross-head speed of Instron	min^{-1}
$\gamma(\vec{r})$	correlation function of electron density fluctuation	
$\delta(\vec{R}_p)$	roughness function specifying the shape of the interface between two media	$\mathring{A}^2$ $\mathring{A}^2$
$\overline{\delta^2}$	mean square of the surface roughness distribution	$\mathring{A}^4$ $\mathring{A}^4$
ϵ	glancing angle	mrad or degree

Symbol	Definition	Units
$\eta(\vec{R})$	local electron density deviation	electron/$\mathring{A}^3$
$\overline{\eta^2}$	mean square electron density fluctuation	electron^2/$\mathring{A}^6$
$\xi(\vec{s_p})$	surface scattering amplitude = $\mathcal{F}_2[\delta(\vec{R_p})]$	$\mathring{A}^2$
K	isothermal compressibility	(dyne/cm^2)$^{-1}$
λ	wavelength	$\mathring{A}$
μm	micron unit	10^{-6} meter
μ	azimuthal angle measured from the meridional direction of the two-dimensional scattering pattern	degree
μ_ℓ	linear absorption coefficient of the sample	cm^{-1}
ν	frequency of a electromagnetic wave	sec^{-1}
ψ_m	angle between the tensile direction and the molecular orientation direction	degree
ψ_s	angle between the tensile direction and the normal to the craze plane	degree
ψ_v	angle between the tensile direction and the transverse direction of the microvoids in crazes	degree
$\bar{\rho}$	mean electron density averaged over the scattering volume	electron/$\mathring{A}^3$
$\rho(\vec{R})$	electron density distribution function of the structure	electron/$\mathring{A}^3$
ρ_i	electron density of phase i	electron/$\mathring{A}^3$
σ_1, σ_2	principal stresses	psi
θ	Bragg angle	mrad or degree
2θ	scattering angle (angle between the incident and scattered waves)	mrad or degree
τ	correlation distance of the surface roughness distribution	μm

Symbol	Definition	Units
ω	angular frequency of a electromagnetic wave $= 2\pi\nu$	sec^{-1}
$\underset{\sim}{2}$	symbol for self-convolution operation	

CHAPTER 1

INTRODUCTION

An understanding of the macroscopic response of an amorphous polymer to deformation is dependent upon the elucidation of the influence of physical structure over a broad dimensional range and the effects of processing history on its micromechanics. The goal of this dissertation is to study the stress induced microstructure variations of amorphous polystyrene having various molecular weights.

Craze formation is an important mode of plastic deformation in glassy amorphous polymers. The most salient characteristics of crazes in glassy polymers are mainly drawn from the results of investigation using optical microscopy, scanning electron microscopy, or transmission electron microscopy. On a macroscopic scale, crazing is visible to the naked eye as a clouding or blushing of the originally transparent material which causes the scattering and reflection of light. On a microscopic scale, crazes are sharply bounded regions between the uncrazed polymer matrix, typically separated by less than 1 μm, linked by craze matter consisting of oriented, fibrillar polymer interspersed with voids ca. 100 - 500 Å in size. Crack nucleation occurs within the craze. In the early stages of growth the crack propagates along or through the craze. This is followed by bifurcation and branching of the crack and finally total fracture.

There are inherent difficulties associated with electron microscopy. These difficulties include electron beam damage,

modification of craze structure due to unloading, aging, microtomy, or impregnation, and possible differences in the physical and mechanical properties of thin films and bulk specimens. In contrast, small-angle x-ray scattering (SAXS) avoids these difficulties.

Since there is a large electron density difference between void and polymer, crazes cause SAXS. Although SAXS has been used by other workers to study the craze microstructure in polymers, the interpretation of what has been observed has been confused until the recent attention given to the total reflection phenomenon. The work presented here is divided into two parts. The first part consists mainly of a theoretical analysis for the specular reflection phenomenon arising in SAXS studies of two-phase systems with smooth, parallel interfacial surfaces. The second part of this work is to characterize the structure of crazes from the SAXS data and to provide further understanding of the effects of molecular weight, molecular weight distribution, and molecular orientation on the fracture processes of polystyrene.

CHAPTER 2

HISTORICAL BACKGROUND

2.1 Microstructure in Unoriented Glassy Polymers

The basic structural elements of high polymer solids are the chain molecules. The variety of their structure and flexibility permits different modes of organization and mechanical interaction. In recent years the understanding of the non-ordered or amorphous state of solid polymers has been the subject of lively discussions and careful studies. An up-to-date reference for the general discussion of amorphous polymers is in Faraday Discussions of No. 68, 1979 entitled "Organization of Macromolecules in the Condensed Phase." Figure 2-1 shows model representations of the various interpretations of the nature of the amorphous state:

(A) interpenetrating random coils (1)

(B) folded chain fringed micellar grains (2)

(C) meander model (3).

2.1.1 Random Coil Model

Until about 1960 the general view prevailed that the chain molecules in isotropic, amorphous polymers have a random conformation and that the random coil or spaghetti model gives an adequate description of the "structure" of these polymers (1). This model predicts that the conformation statistics of the molecule in the bulk is the same as when dissolved in a theta solvent. This implies the absence of long-range order and, for sufficiently long macromolecules,

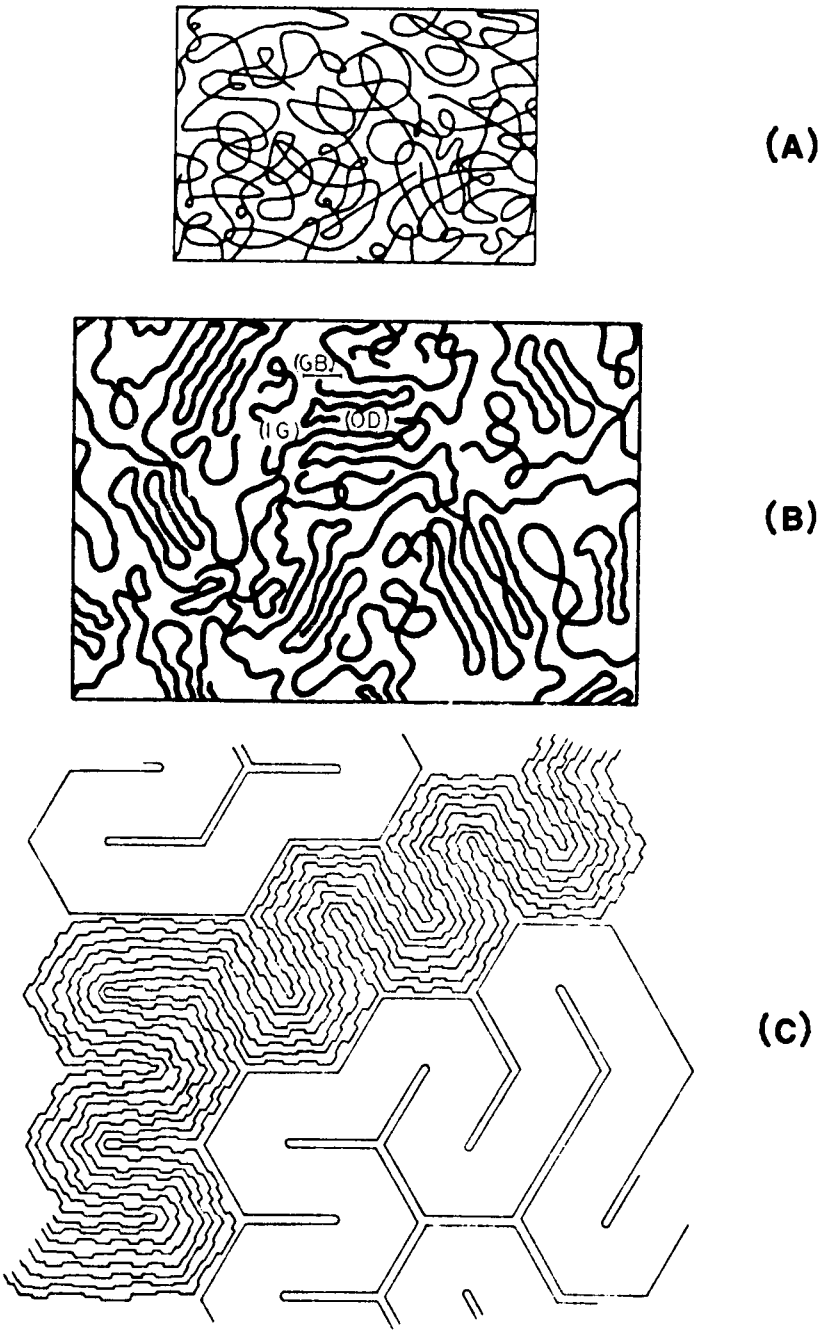


Figure 2-1. Model representations of the various interpretations of the nature of the amorphous state: (A) random coils [1]; (B) folded chain fringed micellar grains [2]; and (C) meander model [3].

extensive interpenetrations and entanglements. Flory (4, 5) summarized his extended observations on polymers in solution, stress temperature coefficients in the rubbery state, temperature coefficient of the intrinsic viscosity and root-mean-square end-to-end distance of chain molecules, and concluded that these measurements are consistent with the random coil structure of chains in bulk. Recent results obtained from small-angle x-ray scattering (SAXS) (e.g., 6, 7) and small-angle neutron scattering (e.g., 8, 9, 10) provide support for this model. Among these scattering studies, Benoit's (9) can be taken as representative. The radii of gyration of eight molecular weight polystyrene polymers were found to be the same, with experimental error, as those of the polymers in a theta solvent.

2.1.2 Folded Chain Fringed Micellar Grain Model

In the years following 1960 the concept of a close range order of the chain molecules within amorphous polymers has gained a growing support. A sizeable number of investigations, based primarily on electron microscope observations, have cast doubts upon the utility of the random coil model for representing the structure of these polymers. The results of the investigations are well summarized in ref.(2), (11), and (12). The essential and initially surprising feature of these results has been the observation of heterogeneities, typically on a scale of 30 to 100 Å, in a number of polymers including polycarbonate (PC), poly(ethylene terephthalate) (PET), natural rubber, isotactic and atactic polystyrene (PS), poly(vinyl chloride) (PVC), and poly(methyl methacrylate) (PMMA).

Yeh (2) proposed a two-phase folded chain fringed micellar grain model for the amorphous state in general, whether glassy or molten. The model contains two major elements as depicted in Figure 2-1 (B). One element, which he called the grain (30 to 100 Å), consists of an ordered domain of parallel chain segments brought about primarily by intramolecular folding of parts of a long chain molecule. The grains are generally connected to one another as in a string of beads, especially for those molecules that are longer than can be obtained within a single grain. Surrounding the grain is the second phase (10 to 50 Å) consisting primarily of molecular chain segments in a truly disordered state, which may include low molecular weight molecules, chain ends, or segments of molecules going from one grain to another.

However, an extensive body of evidence from SAXS and high resolution electron microscopy (13) strongly disproved this two-phase model. The SAXS from PC, PMMA, PET, PVC and PS was inconsistent, both in the form and magnitude of the scattered intensity, with the presence of nodules as representative of the bulk structure. The electron microscope results provided no evidence for heterogeneities on a scale and volume fraction of the reported nodules. Only the pepper and salt features characteristic of microscope operation near the resolution limit were seen.

2.1.3 Meander Model

The meander model developed by Pechhold (3) is also a two-phase model in which bundles of chain molecules fold to give an isotropic and dense-packed polymer material, as described in Figure 2-1 (C). By

starting with a nondefective (all trans- conformation) bundle of molecules (e.g. ideal crystal), and introducing more and more molecular defects (e.g. gauche- conformation) into the system, Pechhold was able to calculate the mean diameter of a bundle, which came to be about 50 Å (14). This model also allows the quantitative discussion of the melt transition as well as of the thermal properties of the melt (15). Although recent neutron scattering experiments (e.g., 8, 9, 10) strongly disprove the existence of a distinct meander arrangement of chains, Pechhold's considerations have greatly fertilized the efforts to study the structure of amorphous state.

2.2 Molecular Orientation in Glassy Polymers

2.2.1 Orientation Behavior

Molecular orientation in amorphous polymer samples submitted to uni- or biaxial extension in the rubbery state may be frozen-in by somewhat rapid cooling to temperatures below the glass transition temperature (Tg). Generally the degree of orientation in polymers is related to their processing conditions. For example, in injection molding the main variables were found to be barrel temperature, mold temperature, and injection pressure (16). It was suggested by several authors (e.g., 17, 18, 19) that the most appropriate temperature range for producing orientation in glassy polymers is located just above the glass transition region. This particular temperature range in which all polymers behave as viscoelastic rubbers, may be broad, depending on the nature of the polymer and on the rate of deformation. The

latter has to be high enough compared to the reciprocal characteristic relaxation time of the polymer network in order to avoid disorientation during stretching and subsequent cooling to temperatures below Tg.

In general, molecular mobility in the glassy state is insufficient for disorientation to occur within a measurable span of time, even in the absence of external stress, notwithstanding the inherent tendency of the molecular chains to revert to the unoriented, most probable, random state. The frozen-in elastic potential energy will, however, be dissipated as soon as the sample is heated to temperatures in or above the glass transition range, as a result of enhanced molecular mobility.

2.2.2 Stress Optical Law

The optical birefringence method is widely used to characterize the orientation state in polymers. The relationship of birefringence to stress in amorphous polymers was first studied by Kuhn and Grun (20) and Treloar (21). Kuhn and Grun (20) obtained a relationship between applied stress and birefringence in uniaxially drawn rubbers using Brewster's law and a Gaussian stress-strain relationship. However, this was limited to the case of simple extension in which the optical properties correspond to those of a uniaxial crystal whose optic axis coincides with the direction of extension. Treloar (21) generalized this analysis to the pure homogeneous case where the refractive index ellipsoid will have three unequal axes n_1, n_2, n_3 corresponding to the principal axes c_1, c_2, c_3 of the strain

ellipsoid, respectively. The form of stress optical law is (21)

$$n_1 - n_2 = C(\sigma_1 - \sigma_2) \qquad \text{Eq.(2-1)}$$

where

$$C = 2\pi(n_o^2 + 2)^2(\alpha_1 - \alpha_2)/45k_BTn_o$$

n_o = mean refractive index

1, 2, 3 = subscripts stand for principal axes

σ_1, σ_2 = principal stresses

α_1, α_2 = principal polarizabilities

k_B = Boltzmann constant

T = absolute temperature

This linear relationship between birefringence and principal stress difference in dry and solvent swollen rubbers was experimentally verfied by Treloar (21) for uni- and bi-axial extensions.

For glassy polymers, it has been assumed that the maximum shrinkage stress is identical with the frozen-in internal entropic stress, resulting from the deformation of the rubberlike molecular network and that the value of the maximum shrinkage stress should be directly related, therefore, to the orientation birefringence (18). Rudd and Andrews (22) found a unique, nonlinear relationship independent of thermomechanical history in the case of uniaxially oriented polystyrene filaments. The results reported by Jones (23) can be represented by a linear relationship for uniaxially oriented polystyrene sheets of variable thermomechanical history and the stress-optical coefficient (SOC) calculated from this relationship, -5200 Brewsters, is in good agreement with other literature data. The

stress (force applied during quench) -birefringence data obtained by Matsumoto and Bogue (24), Oda, White, and Clark (19), and Carey, Wust, and Bogue (17) on polystyrene, when plotted together, shows a general relationship, independent of how the sample is oriented or when the birefringence is measured (17). In general, a unique linear relationship does not exist (18). The calculated SOC is not constant but decreases (in absolute value) with increasing internal stress in accordance with the results reported in ref.(17) and (22). The fact that the network deformation as well as the development of molecular orientation in glassy polymers is not in accordance with the simplest molecular theory for the deformation of a rubber network has been confirmed by neutron diffraction studies of polystyrene (25, 26).

2.2.3 Structure Changes in Oriented Polystyrene

Generally speaking, the random coil model serves as the simplest and a suitable model to describe the long-range arrangements of molecular chains in the amorphous state. While the two-phase domain models appear apparently incongruous, there is, however, a considerable body of evidence for short-range order associated with local chain alignments.

Wide-angle x-ray scattering (WAXS) is connected with measures of local order coming from both interchain and intrachain distances. The typical WAXS from unoriented polystyrene is a uniform, isotropic two-ring pattern. The high intensity outside ring ($2\theta = 20^{\circ}$, CuKα) also appears in x-ray pattern of styrene monomers but the inner ring ($2\theta = 9^{\circ}$) does not (27). It was suggested that intramolecular

scattering contributes to the outside ring and both intra- and intermolecular scattering contribute to the inner ring (28). Brady and Yeh (29) examined the relationship between x-ray anisotropy, birefringence, and free shrinkage in a cold drawn polystyrene. They showed that the x-ray anisotropy decreased to zero on annealing below glass transition temperature, while the shrinkage was relatively small and the birefringence decreased from -0.027 to -0.011. Quantitative WAXS results from oriented polystyrene (30, 31, 32) showed that the inner ring tends to show equatorial alignment, whereas the outside ring orients along the meridian. This is shown more clearly by the "oscillation curves" of May (31) who compared his results with the radial distribution function for polystyrene calculated by Wecker et al. (28). Tanabe and Kanetsuna (32) suggested that the change of inner ring represents the orientation of phenyl groups in a plane perpendicular to the fiber axis and the change of outside ring represents the piling-up of phenyl groups along the direction of the fiber axis. The former change causes a monotonic increase in birefringence with increasing draw ratio. The latter change indicates the interchain phenyl groups tend to pack at spacings of 5 - 6 $\mathring{A}$ in a plane perpendicular to the fiber axis, and chain segments tend to pack parallel to the fiber axis. Infrared measurements of the dichroic ratio of atactic polystyrene absorption bands indicate the orientation process produces the alignment of chains as well as an increase in the amount of trans conformational segments (33). A value of $35^{\circ} \pm 3^{\circ}$ is obtained for the angle between the normal to the plane of the phenyl group and the chain axis (33).

2.3 The Fracture of Glassy Polymers

In glassy polymers the application of stress produces a small and nearly instantaneous deformation. It is characterized by a large Young's modulus (10E10 - 10E11 dynes/cm^2). The range of elastic deformation is very small, a few percent. Many research groups have reported that the onset of nonlinearity in the tensile stress-strain curve is accompanied by the initiation of crazes in the brittle fracture region (34, 35, 36) or by the initiation of shear bands in the ductile failure region (37, 38). Crazing and shear banding are the two deformation modes which develop inhomogeneously when glassy polymers undergo appreciable plastic deformation before fracture occurs.

The models that have been developed for the fracture process in terms of the formation and initial growth of a crack within a previously formed craze have arisen mainly from experimental work on the fracture of polystyrene (39 - 50). The main approach has been the use of optical and scanning electron microscope observations of the fracture surfaces, optical examination of the growth of cracks within crazes, and transmission electron microscope observations of the micromorphology of crazes formed in thin films and to correlate these with observations on fracture surfaces.

2.3.1 Features of Fracture Surface

The main features of the fracture surface of amorphous, glassy polymers can be summarized conveniently by reference to Figure 2-2. Figure 2-2 (A) shows a composite optical micrograph of the fracture

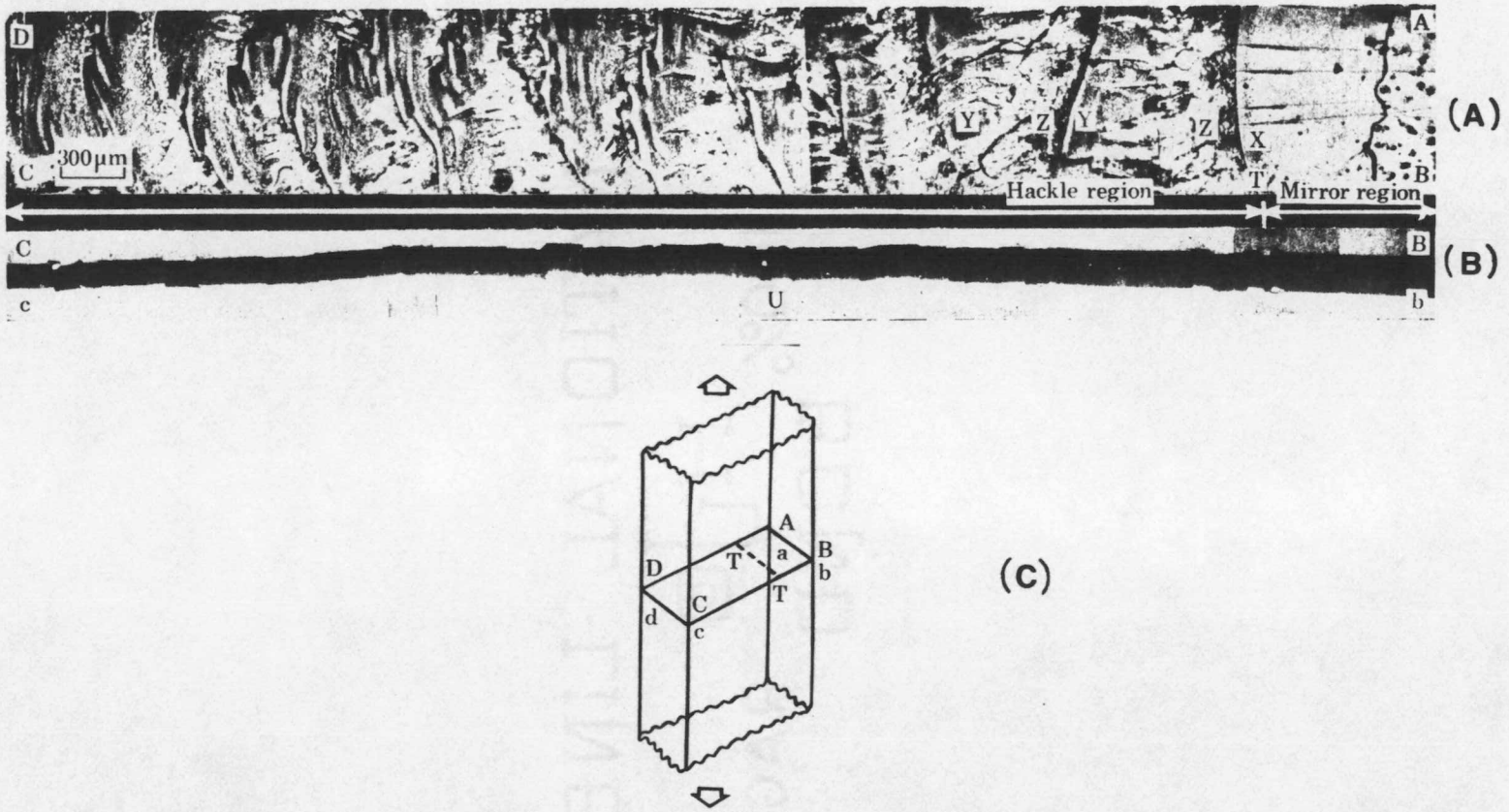


Figure 2-2. Features of the fracture surface of polystyrene (49).

surface and the corresponding side view of the two halves of the fractured specimen revealing the stepped arrangement of the fracture path is shown in Figure 2-2 (B). The relative orientation of these two views is illustrated in Figure 2-2 (C). The fracture surface can be divided into several characteristic regions as illustrated schematically in Figure 2-3 (A). The fracture starts at the smooth mirror region associated with the slow propagation of the crack within the craze in which brittle fracture is nucleated (39, 40, 43, 47, 49). The rough region, usually called "hackle," is associated with the fast propagation of the crack through bundles of crazes which form ahead of the advancing crack (39, 40, 43, 47, 49). This particular mode of fracture is quite common in amorphous thermoplastics when they are strained at low temperatures or high rates. The lined region, usually called "mackerel," is associated with the propagation of the crack along the interface between the craze, in which the crack nucleated, and the bulk material. The mackerel pattern is caused by the crack jumping from one craze-matrix interface to the other (43). The exact details of the fracture surface morphology vary with the molecular weight of polymer (42, 51), the testing temperature (41, 47, 50, 51), and the strain rate (44, 46, 50). At sufficiently high temperatures (near Tg) and high strain rates the progation of the crack changes to viscous rupture instead of viscous flow (46, 50). At low strain rates the fracture surface is formed mainly by viscous flow and is fairly smooth. One typical example for the fracture surface formed by viscous flow is in ref.(44) in which polystyrene specimens were broken

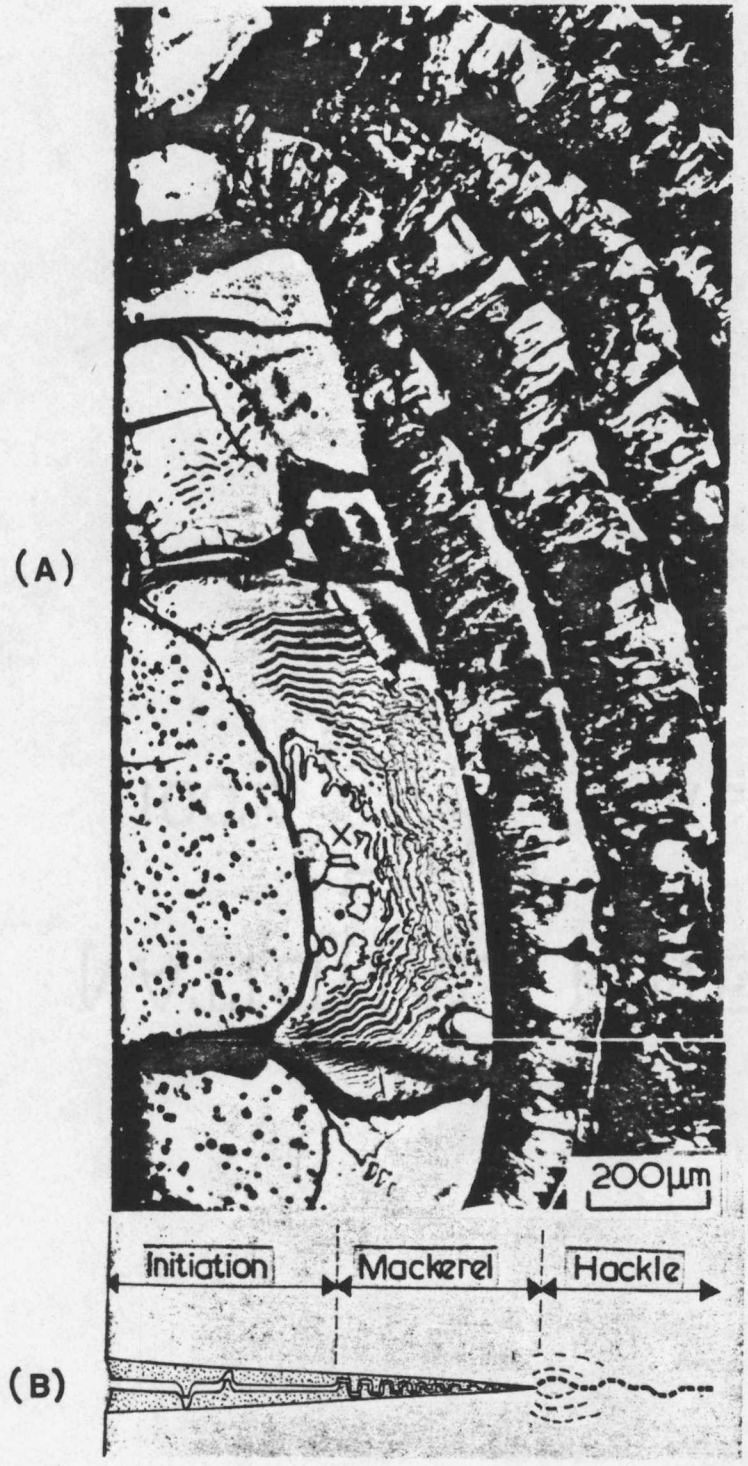


Figure 2-3. Characteristic regions of the fracture surface of polystyrene: (A) optical micrograph showing a plane view; (B) schematic drawings of the three distinct regions of the fracture surface (48).

in tension at strain rates below 1.3E-6 sec^{-1} at room temperature. When polystyrene was broken in fast bending at 90°C, the fracture surfaces were formed by alternative viscous rupture and viscous flow of the craze layer (50). Where the fracture is extremely fast, it may occur in a practically brittle manner, preceded only by a very thin or practically imperceptible layer of craze.

2.3.2 Model of Fracture Process

The examination of fracture surfaces of bulk specimens of glassy polymers (mostly polystyrene) has resulted in the formulation of the model for the fracture process summarized in Figure 2-3 (B). The stages involved are described as follows (40, 43, 44, 45, 49, 50):

(1) Localized regions of plastic flow occur by the formation of fine crazes at points where intermolecular strength is weaker than average.

(2) Small voids develop within the crazes during the growth of the crazes. Fracture is initiated near the center of the craze, where voids grow and coalesce to form a planar cavity within the craze.

(3) At a critical stage the planar void propagates as a crack by tearing of the craze material on a path parallel to, and in the center of the plane of the craze. The tearing crack interacts with cavities formed in other parts of the craze and produces smooth mirror fracture surface features. What happens at this stage resembles the parting of a layer of oil (craze) between two glass plates (uncrazed polymer matrix) when these are pried apart at low velocities by a process similar to viscoelastic flow.

(4) The crack propagates catastrophically on an irregular path and produces a lined fracture surface during acceleration and rough fracture surface at fast propagation. What happens is similar to a viscous rupture process.

2.4 Microstructure of Crazes in Glassy Polymers

The study of the fracture surfaces of glassy polymers has revealed a direct connection between the fracture process and the formation of craze. What has been shown is that two processes may be involved in the propagation of a crack in a preformed craze: (1) cavitation of the craze and final separation by tearing of the material in the craze layer; (2) splitting of the material along the interface between the craze and the uncrazed material (40, 43, 44, 45, 49). Additionally the craze microstructure might be expected to reflect the physical aspects of polymer structure which give rise to this unique phenomenon. The microstructure of crazes is of interest for these reasons.

Polymer crazes in their appearance are similar to the very fine cracks known for a long time to occur on the surfaces of inorganic materials such as ceramics. Crazing is visible to the naked eye as a clouding or blushing of the originally transparent material which causes the scattering and reflection of light. The first indication that crazes were something other than simple featureless cracks was obtained in studies by Sauer et al. (52, 53) of crazing in polystyrene. Since then, crazing is probably the most studied mode of deformation in polymers. Three comprehensive reviews (38, 54, 55) on this subject have been given.

The tools of use in characterizing craze microstructure have been optical measurement, electron diffraction, scanning electron microscopy (SEM), transmission electron microscopy (TEM), wide-angle x-ray scattering (WAXS), and small-angle x-ray scattering (SAXS). The experimental observations by each tool are discussed as follows.

2.4.1 Craze Investigation by Optical Measurement

The craze is visible by virtue of the different optical properties of the filling from those of the bulk. The fact that crazes can reflect light strongly means simply that they have lower refractive indices than the surrounding bulk polymer and that they have smooth (compare to wavelength of light) parallel boundaries. By measuring the critical angle for total reflection of light at the craze-bulk polymer interface (56, 57, 58) or by interferometric studies (59) the refractive index of crazes can be determined. The void content of crazes, determined from the craze refractive indices, are 40 - 60% in unbroken, unstressed crazes in glassy polymers (57, 58) and 69 - 75% in crazes on the fracture surface of polystyrene (59). The latter is considerably higher than the former.

Electron microscope observations (see 2.4.3) have shown that the material between voids is fibrils of molecular bundles. By optical birefringence measurement Brown (60) showed that crazes in polystyrene films are highly birefringent, consisting of the sum of a positive form term and a negative orientation term. By assuming a model of parallel rods, the orientational birefringence of the fibrils is calculated as high as -0.020. This is fairly large for polystyrene.

2.4.2 Craze Investigation by Electron Diffraction

By using the technique of selected area electron diffraction in the transmission electron microscope, Brown (61) was able to obtain electron diffraction patterns from crazes only. These patterns show that craze fibrils are highly oriented but in other ways not different from bulk polystyrene. The comparison with diffraction patterns from oriented films reemphasized the highly oriented nature of the craze fibrils. Using the same technique Brown (62) detected the refraction effects caused by the planar parallel interfaces of crazes.

2.4.3 Craze Investigation by Electron Microscopy

Many valuable studies of craze microstructure have been carried out with electron microscopy (e.g., 43 - 45, 49, 51, 63 - 70). The techniques fall into two main categories: first, those associated with the examination of fracture surfaces of bulk specimens using scanning electron microscopy and also replication combined with conventional transmission electron microscoppy, and secondly, those associated with the transmission electron microscopy of thin polymer films or sections which provide information about the microstructure of the specimen and of the changes in internal structure which occur during the fracture process. Any changes in microstructure which occur during the fracture process are likely to be reflected in the fracture surface morphology. The first approach provides evidence for the craze controlled fracture process. The second approach provides details of the morphogy of crazes.

The transmission electron microscopy of craze microstructure usually employs one of the following techniques:

(1) Investigation of thin sections of precrazed bulk specimens prepared by ultramicrotomy (63, 66 - 68).

(2) Investigation on crazes formed in thin sections of bulk specimens prepared by ultramicrotomy and then strained in a microstraining device (66, 69).

(3) Investigation on crazes formed in solvent-cast thin polymer films with thickness in the range of several hundred Ångstroms to several microns (68, 69).

The transmission electron micrographs of crazes obtained by each method are compared in Figure 2-4 (A), (B), and (C), respectively. The microstructure of crazes in a thin section of precrazed bulk specimen is similar to that formed by straining a microtomed thin section of uncrazed bulk specimen (66, 68). The microstructure of crazes formed in thin films and in the bulk specimen are similar but with the exception that much finer fibril (less than 100 Å in diameter) structures are observed in thin films at large deformations (68). Generally speaking, crazes are sharply bounded regions with planar interfaces between the uncrazed matrix and the craze. The width of craze is usually less than 1 μm. Like cracks, crazes in isotropic materials form in a plane normal to the major principal stress axis (the tensile axis) and only propagate if the stress at their tip exceeds a certain value. The crazes are different from simple featureless cracks as they are filled with "craze matter." The

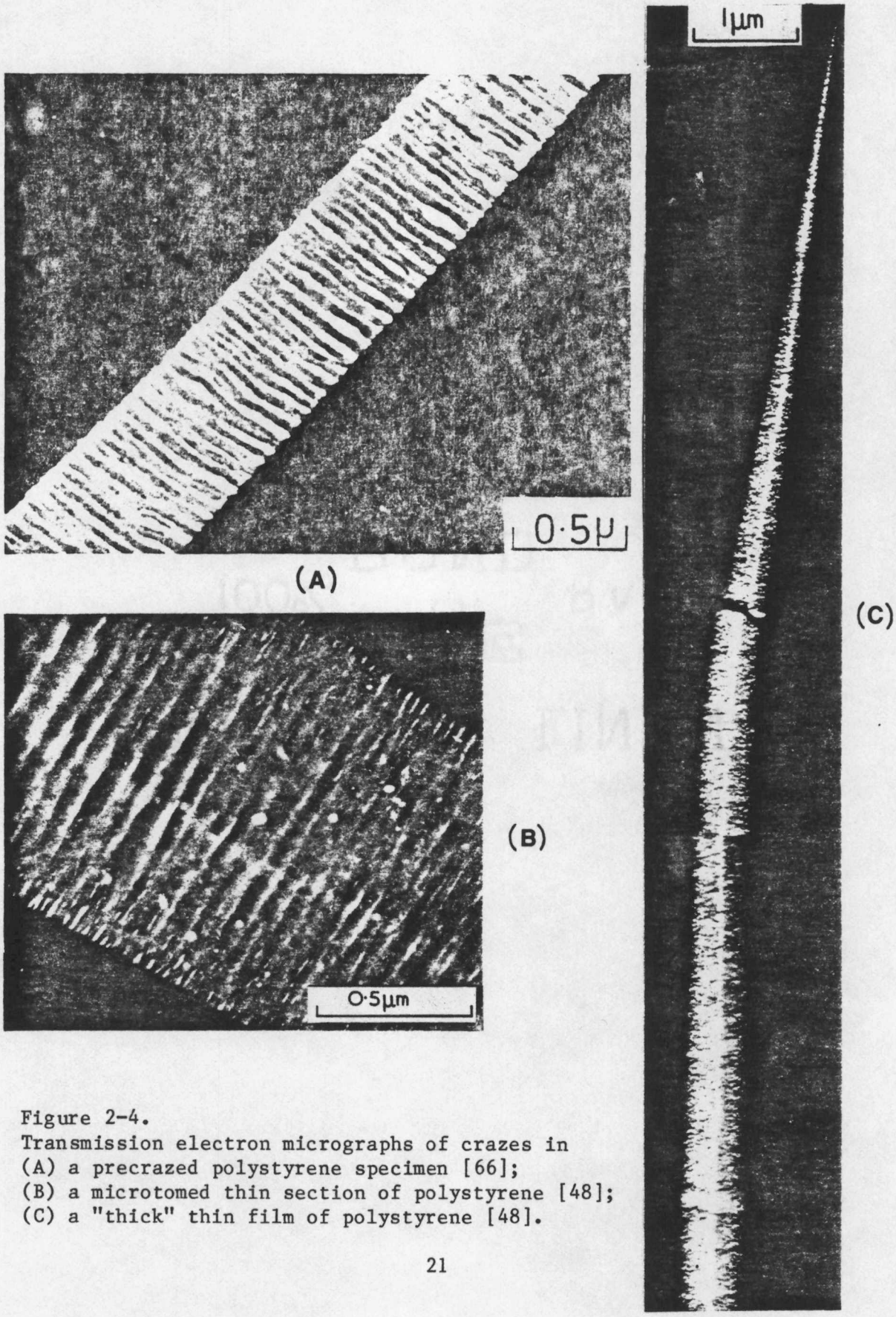


Figure 2-4.
Transmission electron micrographs of crazes in
(A) a precrazed polystyrene specimen [66];
(B) a microtomed thin section of polystyrene [48];
(C) a "thick" thin film of polystyrene [48].

craze matter consists of highly oriented fibrils of about 200 to 500 Å in diameter interspersed with voids of the same order of dimension as the fibrils and has an average density of 40 to 60% of the matrix density. There are numerous cross fibrils which are about 60 to 100 Å in diameter which link the main fibril structure together and tend to orient normally to major fibrils which are oriented primarily along the direction of the major principal stress axis. Also present are bands of large voids at the center (midrib) of the craze and at the craze-matrix interfaces.

Beahan, Bevis, and Hull found that there is a change in the microstructure of the craze along its length, with coarser, thicker fibrils being found in the tapered section near craze tip (66, 68, 70). They observed that a narrow craze has a coarse microstructure consisting of fibrils with diameters in the range 250 - 400 Å, the wider craze has a mixed microstructure, and further widening of the craze results in a further refinement of the fibril structure but there is still a residual zone of coarse fibrils at the interface and along the mid-plane. They suggested that the fine fibrils arise as a result of the thickening of the crazes. They also observed an increase in width of the crazes and constant craze density with increasing total deformation. At low strain rates, the craze grows in thickness by the drawing of further matrix material and to some extent by an increase in the orientation of the fibrils. The fine microstructure occurs at narrower craze widths with increasing strain rate. The increases in the orientation and elongation of the fibrils

lead eventually to their break down. The model of crazing proposed by Beahan et al. (68) is shown schematically in Figure 2-5.

2.4.4 Craze Investigation by Wide-Angle X-Ray Scattering

Wide-angle x-ray investigation of crazed polystyrene and uncrazed polystyrene have been described in the early publications about crazes (52, 53). Changes in the x-ray pattern of crazed polystyrene are similar to those of oriented polystyrene. Since the size of the incident x-ray beams after collimation was wider than the size of a single craze (several microns wide), a considerable amount of the scattering was from uncrazed polymer matrix. Therefore, comparisons could not be made with homogeneously oriented polystyrene to get the information about the degree of orientation of craze fibrils.

2.4.5 Craze Investigation by Small-Angle X-Ray Scattering

Until now, EM and SAXS have been the two major tools used mostly to investigate the microstructure of crazes. The specific features of both techniques are compared in Table 2-1. From this table we can see there are inherent difficulties associated with electron microscopy. These difficulties include modification of craze structure due to sample preparation, possible differences in the physical and mechanical properties of thin films and bulk specimen, and electron beam damage during measurement. The results obtained with EM are direct and some times very detailed. It follows that EM should be used as a complementary technique as often as possible. The EM results should serve as a guide to the interpretation of SAXS, in

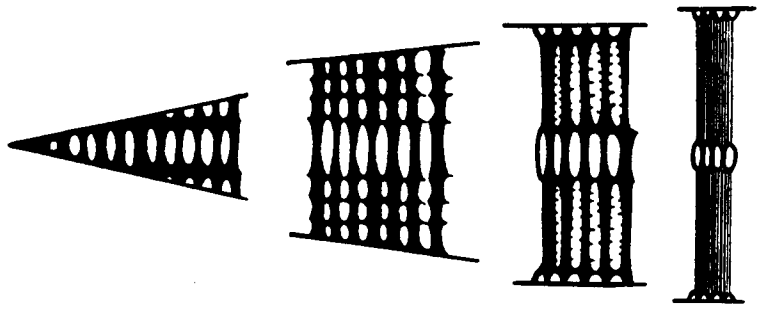


Figure 2-5. Schematic drawing for the model of a craze as proposed by Beahan et al. (68).

Table 2-1

Comparison of the features of electron microscopy and small-angle x-ray scattering as investigative tools for craze studies

	SAXS	EM
Sample Preparation	simple and non-destructive	usually are destructive TEM: dispersion or slicing or replication or solution casting; staining. SEM: shadowing
Measurement	usually are non-destructive	suffers radiation damage from the electron beam
Results	-quantitative -statistically averaged over the sample	semi-quantitative selective
	-image lost due to loss of phase coherency	image directly observed, some times very detailed
	-reproducible	

particular when a model approach must be applied. When there is no additional information about the system, SAXS does not lead to a "unique" structure corresponding to the scattering pattern. A detailed discussion for the SAXS theory is given in Chapter 3.

Zhurkov, Kuksenko, and Slutsker (71) studied crazes (they called "submicrocrack") generated in crystalline and amorphous polymers by tensile stress using a slit-collimated x-ray beam. They did not report any difference in the scattering behavior of crazes formed in crystalline and amorphous polymers. Applying Guinier analysis (72), they concluded these microcracks measure some hundredths of a micron and have the shape of flat discs and are oriented with their planes perpendicular to the loading axis.

LeGrand, Kambour, and Haaf (73) studied crazes in unstressed polystyrene using point-collimated radiation. When the x-ray beam was directed along the plane of the crazes they observed an anisotropic pattern with the major axis of the scattering ellipse lying normal to the craze plane. From the fibril structure as investigated by EM, one would expect a streak perpendicular to the fibril axis and parallel to the craze surfaces. They attempted to explain the anomalous anisotropy as due to the highly oriented polystyrene molecules in the fibrils. By applying Guinier analysis (72) to calculate the radius of gyration and Porod analysis (74) to calculate the range of inhomogeneity, they determined the size of the scattering element to be 90 to 115 $\mathring{A}$.

Steger and Nielsen (75) studied microvoid formation during deformation of rubber modified high-impact polystyrene (HIPS) with a slit-collimated Kratky camera. They used the Porod analysis (74) to obtain the homogeneity length both parallel and normal to the craze plane and concluded that craze voids form as spheres and are elongated by the applied tensile stress up to the yield point. Beyond yield the elongation ratio is always about five, and increasing strain produces greater numbers of voids with the average size decreasing. If the stress on the specimen is relieved, the voids relax back toward a spherical shape and about half of them close.

Wendorff (76 - 78) studied the microvoids formed in semi-crystalline polyoxymethylene under stress by using a slit-collimated Kratky camera. He determined the shape, size distribution and concentration of microvoids by calculating the correlation length at different angle between the draw direction and scattering direction and the invariant. He concluded the average shape of the microvoids approximated to a rotational ellipsoid with the small axis of the ellipsoid - the axis of rotation - coincided with the draw direction. The major discovery is that the mechanism of microvoid formation depends on the mode of deformation - homogeneous or inhomogeneous deformation via neck formation, continuous or cyclic deformation - and on the structure of the polymers - amorphous or partially crystalline material. For cyclic deformation, the number of the defects depended solely on the stress amplitude whereas their size increased with an increasing number of cycles (76). In the case of

continuous homogeneous deformation, the average size of the defects was independent of the strain whereas the concentration of the defects increased exponentially with increasing strain (77).

Biskup et al. (79) investigated the crazing of rubber modified polystyrene (ABS and HIPS) during a tensile deformation by using a slit-collimated Kratky camera. They found the crazing rate of HIPS was much higher than that of ABS and after unloading HIPS showed a considerable recovery in contrast to ABS. Using Guinier's analysis (72), the radius of gyration for the voids were determined to be about 750 - 970 $\mathring{A}$ for ABS and 700 - 790 $\mathring{A}$ for HIPS.

Parades and Fischer (80) made a SAXS study of crazes in both polycarbonate and poly(methyl methacrylate) produced by straining these polymers at high temperatures, unloading and then quenching the samples to room temperature. They used a slit-collimated Kratky camera to measure the scattering both parallel and normal to craze plane. For scattering parallel to the craze plane they observed a clear maximum which they ascribed to interfibrillar interference. Using a model of a liquid-like order of fibril axes in the craze, they derived a mean fibril spacing from this maximum. By assuming a fibril volume fraction, they could estimate a mean fibril diameter. They also observed that the scattered intensity normal to the craze was considerably larger at small angles than that parallel to the craze.

Brown and Kramer (81) made SAXS studies on crazes formed in air in polystyrene and polycarbonate as well as on crazes formed in methanol in polystyrene by using both pinhole- and slit- collimated

cameras. The SAXS pattern from all their craze samples consists of a cross through the origin, one very intense streak normal to the craze plane and a second, less intense, streak parallel to the craze plane. By tilting about one of the axis (direction in the craze plane and the plane of the sheet), they observed a sharp decrease in the scattering intensity normal to the craze plane and no change in the scattering intensity parallel to the craze plane. They concluded then at least a portion of the intense streak normal to the craze plane is due to the external reflection of x-rays from the craze surfaces.

Westbrook (82) has recently performed dynamic studies on craze formation and relaxation in polystyrene as a function of molecular weight and strain rate using a pinhole-collimation [Oak Ridge National Laboratory (ORNL) SAXS] camera. He observed definite structural differences between low and high molecular weight polystyrene. He found there is a sharp decrease in scattering intensity immediately after the sample breaks (unload) and related this phenomenon to the elastic relaxation of voids. The amount of reduced intensity (the ratio of intensity after sample breaks to that at breaking point) increases with decreasing molecular weight. He also confirmed that the intensity streak normal to the craze plane comes from total reflection at craze interfaces by simulating the scattering pattern with a flat surface laminated polystyrene sample.

More recently Martinson et al. (83, 84) have used high intensity x-rays at the Stanford Synchrotron Radiation Laboratory to study crazes in glassy polymers as a function of time during relaxation at

constant strain. With a measurement period of 30 seconds, they observed the scattering intensity parallel to the strain direction increases with time much faster than that perpendicular to the strain direction does. They tried to explain it by proposing that the application of stress starts a rapid creation of approximately uniform spherical voids which migrate and coalesce to form crazes and relieve the stress. This differs from other models (75, 81) in which void and craze formation coincides in place and time.

From the above discussion we can see there is much controversy in the literature of SAXS studies of crazes because of the following reasons:

1) differences in the collimation geometry of SAXS cameras,
2) measurement was performed when the sample is under stress (or strain) or free from stress,
3) differences in data interpretation.

First of all, the use of a slit-collimated camera to investigate a highly anisotropic scattering system, and whether the methodology employed for the analysis of data collected by slit-collimated camera from isotropic system can be applied to anisotropic system is not certain yet. In the second place, it is evident that the voids relax after the stress on the specimen is relieved (75 - 79, 82). Thirdly, the detailed origin of small-angle x-ray scattering in crazed polymers is still in doubt. For the component of scattering intensity parallel to the tensile axis, some workers interpreted it as diffraction (71 - 80, 83, 84) and others as reflection (81, 82). For the component of

scattering perpendicular to the tensile axis, some investigators attributed it to be void scattering (71 - 79, 82 - 84) and others attributed it to be fibrillar interference (80, 81). These controversial points make the SAXS studies of crazes much more complex than other scattering systems. From the information obtained from tilting experiments (81, 82) and laminated sample (82) it is confirmed that the total reflection of x-rays from flat craze interfaces does contribute to the observed scattering intensity. In order to get more useful information about crazes via SAXS studies, it is necessary to characterize the nature of the origin which causes total reflection of x-rays and then we can deduce meaningful information from both the total reflection phenomenon and the true scattering phenomenon.

2.4.6 Effect of Molecular Weight on Craze Microstructure

Rudd (85) and Kambour (86) reported that both craze strength and time to failure decrease with decreasing molecular weight, and they explained their results in terms of decreased number of tie molecules. Bray and Hopfenberg (87) found that low molecular weight (116,000) polystyrene crazed more rapidly than the high molecular weight (537,000) polystyrene mercury-cast films. Brady and Yeh (69) showed by TEM studies that fibrils formed within the craze were always on the order of a few hundred Angstroms in diameter regardless of molecular weight. However, a dense fibrillar structure was observed for high molecular weight, and for molecular weight less than 20,000 few fibrils are formed and rapidly breakdown to form cracks. Similar results were obtained by Fellers and Kee (88). These authors suggest

that the craze initiation stress is independent of molecular weight when $\overline{Mn} > 2\overline{Me}$ ($\overline{Me}$ is entanglement molecular weight) where as craze development and breakdown are clearly molecular weight dependent. When $\overline{Mn} < 2\overline{Me}$ crazes do not form, presumably because a network of physical entanglements has not developed. They also observed that the gross structure of the craze is sensitive to the molecular weight, with crazes in high molecular weight samples being very fine, numerous, long, and straight as compared to the ones in lower molecular weight samples, which are coarser in texture and somewhat shorter in length. This phenomenon seems to be related to the homogeneity of the stress field which is better the more numerous and the stronger the fibrils. Wellinghoff and Baer (51) reported that void expansion and fiber formation did not take place in polystyrene with $\overline{Mn}$ = 10,000, whereas significant void growth and fiber formation was first observed with $\overline{Mn}$ = 37,500. They also showed that when 1% of $\overline{Mn}$ = 670,000 polystyrene was introduced into $\overline{Mn}$ = 10,000 polystyrene, a craze was formed with many fibrils stretched between the matrix surfaces.

2.4.7 Effect of Polymer Orientation on Craze Microstructure

Molecular orientation parallel to the tensile axis has long been recognized as a factor or a means to increase resistance to craze initiation (also growth and breakdown). Previous investigations show that a transverse orientation of the chains with respect to the direction of principal stress enhances craze initiation (89, 90). Because there are fewer chain segments pointing in the direction of

principal stress, critical local strains are obtained at smaller stresses. On the other hand the craze initiation stress increases with the degree of alignment of the chains in the stress direction (increasing degree of orientation, small angle ψ_m between the orientation and tensile stress). In the case of good alignment, craze initiation stresses will be higher than the stress for shear yielding so that no crazing is observed. By WAXS studies, Tanabe and Kanetsuna (32) suggested that polystyrene chain segments tend to pack parallel to the orientation direction. It is reasonable to explain that the improved packing efficiency along the orientation direction suppresses the formation of crazes and the growth of crack. The TEM studies of Farrar and Kramer (91) showed that the crazes produced by straining parallel to the molecular orientation direction have a higher frbrillar volume fraction (V_f = 0.45) than crazes in unoriented polystyrene (V_f = 0.25) and the crazes produced by straining perpendicular to the molecular orientation direction have a much lower fibrillar fraction (V_f = 0.05) than both. The studies of polystyrene crazing by Haward, Murphy, and White (89) showed that crazing stress was a linear function of strain birefringence in a series of injection-molded specimens in which birefringence was varied by varying the molding temperature at fixed injection rate (i.e. by varying melt shear stress). However, it is not yet clear that birefringence alone can serve as crazing resistance independent of molecular weight, stretching temperature and rate.

In anisotropic materials craze orientation is more complex, being a function of the degree of anisotropy and the relative directions of orientation and applied load. Harris and Ward (92) observed two types of crazes formed in oriented sheets of poly(ethylene terephthalate) of nominal draw ratio 2:1. These crazes were termed tensile and shear crazes. Tensile crazes were found for $\psi_m = 90^\circ$, $\psi_m = 75^\circ$, and in a few specimens for $\psi_m = 60^\circ$. No tensile crazes were seen for $\psi_m < 60^\circ$. In addition to the tensile crazes, shear crazes were found to form along directions close to the direction of the deformation bands.

Beardmore and Rabinowitz (93) did tensile tests on poly(methyl methacrylate) and polycarbonate. Specimens were cut at various angles to the direction of orientation and then deformed uniaxially at 77°K (the low temperature favors the crazing process relative to shear direction). Only when $\psi_m = 0^\circ$ or $\psi_m = 90^\circ$ were the craze planes normal to the stress direction. For poly(methyl methacrylate) the deviation from the orthogonal relationship between the craze plane and the stress direction reached a maximum when the angle between the orientation and stress directions was about 40°. The maximum deviation from orthogonality increased linearly with the degree of orientation of the sheet as measured by its birefringence (20° deviation for a birefringence of 0.00045). A qualitatively similar effect was seen with polycarbonate given a 140% stretch at 155°C (room temperature birefringence = 0.033).

Conversely, Hull and Hoare (90) observed that for polystyrene molecular orientation had only a small effect on the orientation of

craze plane. They also found that at 20°C yielding in tension occurs in samples drawn to $L/L_o = 2.6$ or more and at a $\psi_m(L/L_o)$ smaller than 20° to 30°. These different behaviors indicate molecular structure plays an important role in the deformation mechanism of polymers.

CHAPTER 3

SMALL-ANGLE X-RAY SCATTERING THEORY

3.1 Introduction

It was in the course of a systematic attempt to see if any radiation could be produced which would traverse matter opaque to ordinary light that Roentgen discovered x-rays (94). This radiation was named by Roentgen "x-rays," indicating their unknown nature. Since then, these rays have attracted great interest and experimenters over the world have studied their characteristics.

In 1912 Max von Laue proposed at a seminar at the University of Munich the idea that a crystal might act toward x-rays in much the same manner as a grating acts toward light, since in both cases the regular distances are several times the wavelength. He accordingly asked Friedrich and Knipping to try the experiment of passing a narrow beam of x-rays through a crystal of zinc blende. The idea that crystals diffract x-rays was successfully proved (95). Since then, it was recognized that interferences of x-ray electromagnetic waves scattered from materials offer a more or less direct and quantitative picture of the atomic arrangement in crystals.

In 1929 Raman and Krishnamurti (96) found that carbon black gives rise to a diffuse continuous scattering at small angles, which they explained in terms of electrons with large intermediate distances. At that time it was not recognized that all ordinary crystals produce small angle scattering too, since it was mostly unobservable.

The old theory (97 - 99) related the forward scattering of electromagnetic waves to the existence of density fluctuations of the material. By about the late 1930's, Guinier (100), Kratky (101), and Hosemann (102) respectively developed a quantitative treatment and have shown how this scattering could be used. Guinier's main idea had been that the intensity function is practically due to the particle scattering, although initially the exact meaning of the particle remained undecided. On the other hand, Kratky is of the opinion that in the case of densely packed systems such continuous small-angle scattering is caused by the interference effect among the particles, which is basically the same as the conventional theories of liquids and gas interferences. Hosemann tried to interrelate the theory of x-ray diffraction by crystals, conventional interference theory, and Guinier's particle scattering theory. By about the early 1940's, discontinuous small-angle scattering from certain natural fibers, notably collagen and keratin was detected by Bear (103) and Kratky and Sekora (104). This revealed the existence of macrolattices and macrocells with absolutely new kinds of distortions.

The first book on small angle x-ray scattering (SAXS) written by Guinier and Fournet (72) was published in 1955. It has now become a standard, and contains an extensive bibliography by Yudowitch. The theories in this book can be used to interpret the SAS pattern only if two conditions are fulfilled. (1) Multiple scattering is negligible; (2) double Bragg reflections (DBR) are negligible. When multiple scattering is prominent, it is still possible to draw from the

experimental data the values of parameters characterizing the structure of the sample, but the formulas are quite different from the classical ones. A complete survey of the DBR phenomenon in a distorted crystal was given in the Small Angle Scattering meeting, held in Kansas City, Missouri, USA, 1958 (105).

The main general development made in the period after "Guinier and Fournet" can be found in the papers from the International Conferences on SAS (106 - 110). Among the papers of the Fourth Conference are four extensive reviews, which cover the entire field of SAS applications. A second bibliography was compiled by Renouprez (111) in 1970. The second book on SAXS written by van Hutten (112) was published in 1981. It deals with the basic SAXS theory and general treatment of structure characterization. The main application is on the study of polyethylene shish-kebab fibers and lamellar structures, accompanied by some other systems. More recently an excellent book on SAXS edited by Glatter and Kratky (113) was released. This book provides detailed fundamental theoretical and experimental aspects as well as methods for data evaluation and applications to some specific areas. There are also excellent review papers (e.g. 114 - 118) and sections in some books (119 - 121) concerning SAXS.

In this chapter, the definitions of some terms which are important in x-ray diffraction theories will be introduced. These terms include: scattering amplitude and absolute scattering amplitude, scattering intensity and absolute scattering intensity,

scattering vector, and reciprocal space and real space. Then the discussion will be degenerated to the special case of SAXS and the important concepts of correlation function (122), scattering invariant (74), and intensity distribution profile (112, 119) will be introduced. It turns out the treatment of SAXS data may be very difficult since it involves three-dimensional Fourier transformation. However, from the early days of SAXS some principal parameters and characterization functions for some particular cases were developed. Among those that are the most often used treatment for SAXS data of polymer crazes will be briefly reviewed.

3.2 Basic Theory

The study of the structure of a substance is based on the diffraction phenomena caused by its interaction with electromagnetic radiation. X-rays of wavelength about 1 $\mathring{A}$ (1E-8 cm) are usually used for this purpose. A beam of x-rays falling on an assembly of atoms will interact with the electrons and will thereby be scattered. According to common usage, small-angle scattering means the coherently scattered intensity whose domain extends up to scattering angles 2θ of only a few degrees, whereas the domain of large (or wide) angle scattering by crystals, liquids and gases begins from about $2\theta = 5^{o}$ (depending on the wavelength of the x-ray, the size of the lattice cell, etc.).

3.2.1 Basic Assumptions

The basic theory of small-angle x-ray scattering (SAXS) starts from a considerable number of assumptions. As such it is a simplification of the general theory concerned with the scattering of electromagnetic radiation. The following conventions form the basis of the theory presented in this chapter.

(1) Since the vibration frequency is so high in x-rays, only the interaction with the individual electrons needs to be considered: each electron acts as a secondary radiation source.

(2) The incident radiation used is monochromatic and unpolarized.

(3) The wavelength of both the incident and scattered x-rays are identical (elastic or unmodified scattering).

(4) The Fraunhofer approximation holds, which means that the incident beam may be regarded as a bundle of parallel rays and, similarly, that parallel scattering waves are thought to merge in a point of registration at infinite distance (74, 119).

(5) The nature of the incident electromagnetic field is the same passing through the material system, apart from an attenuation by absorption.

(6) Only single scattering is considered: scattered x-rays interfere with other scattered x-rays, but do not undergo any further interactions with other scattering centers. As an upper limit for single scattering a value of 0.1 for the ratio of the total scattered power to the transmitted primary power can be taken (123).

(7) Incoherent or Compton scattering, which results from the mobility of the electrons, is very weak at small angles and is negligible (113, 124).

(8) At small angles, the intensity resulting from surface imperfections (125) and surface reflections (see Chapter 6) are neglected.

3.2.2 Scattering Amplitude

In wave theory, the electric field strength E of a propagating electromagnetic wave at position $\vec{R}$ and time t is expressed by a complex exponential notation named complex amplitude

$$E(t, \vec{R}) = Eo \cdot \exp[i(\varepsilon + \omega t - \vec{k} \cdot \vec{R})] \qquad \text{Eq.(3-1)}$$

where

$\vec{R}$ = position vector from the origin to an arbitrary point in space

Eo = the maximum strength of the electric field

$i = \sqrt{-1}$

ε = phase shift

ω = angular frequency of the wave = $2\pi\nu$

ν = frequency of the wave

$\vec{k}$ = wave vector = $2\pi\vec{a}/\lambda$

k = wave number = $|\vec{k}| = 2\pi/\lambda$

λ = wavelength

$\vec{a}$ = unit length vector along an arbitrary direction in space

An essential property of electromagnetic waves is that if two or more wave systems cross in a certain region of space, the electric and

magnetic field strengths in this region are found simply by adding as vectors the fields from the individual wave systems. Both interference and scattering phenomena can be explained in terms of superposition of waves. Figure 3-1 shows an analytical construction for the interference and scattering from two scattering centers. The directions of the incident wave and the observed scattered wave are represented by the wave vectors $\vec{ko}$ and $\vec{k}$, respectively, and form an angle 2θ to each other. The origin ($\vec{R} = 0$) is located at one center, the position of the other being $\vec{R}$. The initial plane wave falls on these centers, each of which becomes a source of a secondary spherical wave. The initial wave, in general, arrives with different phases at the two centers, so that the scattered waves will have a corresponding phase difference. Constructive interference (addition of waves) occurs in directions for which the phases are the same; destructive, in those for which they are opposite. The intensity distribution has a strict relation to the structure of the system.

If λ is very large relative to the distance R between the centers, the two scattered waves will have nearly the same phases in all directions, in which case the scattered intensity would be independent of angle; interference occurs only if the separation is comparable with the wavelength, and does not occur if $\lambda >> R$. SAXS, therefore, can be used to study the structure on the level of 10 to 1000 Å.

Consider now the scattering by a center at position $\vec{R}$. The path difference for the wave that scatters in direction $\vec{k}$ relative to the

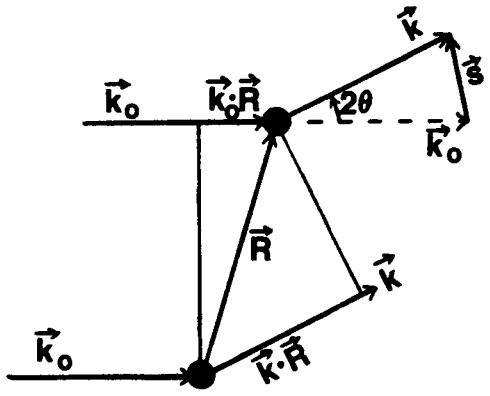


Figure 3-1. Scattering from two scattering centers.

wave scattered at $\vec{R} = 0$ in the same direction is

$$\vec{k}\cdot\vec{R} - \vec{ko}\cdot\vec{R} = (\vec{k} - \vec{ko})\cdot\vec{R}. \qquad \text{Eq.(3-2)}$$

So the amplitude of the wave scattered by the center at $\vec{R}$ is

$$E = Ee\cdot f\cdot\exp[-i\cdot(\vec{k} - \vec{ko})\cdot\vec{R}]$$

$$= Ee\cdot f\cdot\exp[-i\cdot(\vec{s}\cdot\vec{R})] \qquad \text{Eq.(3-3)}$$

where Ee is the amplitude scattered by one electron for the same conditions (see 3.2.3) and f is the scattering factor of the center at $\vec{R}$. Vector $\vec{s}$ is the scattering vector defined as

$$\vec{s} = \vec{k} - \vec{ko} \qquad \text{Eq.(3-4)}$$

with magnitude $s = |\vec{s}| = 4\pi\sin\theta/\lambda$. It is also convenient to use the vector

$$\vec{b} = \vec{s}/2\pi = (\vec{k} - \vec{ko})/2\pi. \qquad \text{Eq.(3-5)}$$

The absolute scattering amplitude is defined as

$$F = E/Ee \qquad \text{Eq.(3-6)}$$

so that F is independent of the experimental arrangements as well as of the wavelength of the incident beam. Therefore, for a system containing N scattering centers, N being large, the amplitudes of the waves scattered from all the centers add up:

$$F(\vec{s}) = \sum_{n=1}^{N} F_n$$

$$= \sum_{n=1}^{N} f_n\cdot\exp[-i\cdot(\vec{s}\cdot\vec{R})]. \qquad \text{Eq.(3-7)}$$

Eq.(3-7) is of universal application in the sense that it extends the concept of f_n for a single center to any physical scattering unit (electron, atom, molecule, particle, colloidal substance, and so on) (119, 126).

3.2.3 Scattering Intensity

Another basic property of electromagnetic waves is that they transfer energy (from a source to a detector) without transferring the medium in which the waves occur. The power density (i.e. power per unit area across the wave transmitted in the direction of propagation) is propoetional to the square of the scattering amplitude or to the product of the amplitude and its complex conjugate. Since there are no detectors which can respond fast enough to demonstrate x-ray frequencies directly, then any detector of electromagnetic radiation in the x-ray range responds only to the average power over many cycles of the waves. This time-averaged power is what we ordinarily know as the x-ray intensity.

The absolute value of the scattering amplitude, and hence the intensity, must be deduced from the scattering characteristics for one electron. Classical electromagnetic theory (119, 126) gives the coherent scattering intensity of a free electron under unpolarized incident x-rays as

$$Ie(\vec{s}) = Ee(\vec{s})\cdot Ee^{*}(\vec{s}) = \left|Ee(\vec{s})\right|^{2}$$

$$= Po\cdot\frac{1}{L^{2}}\cdot\left(\frac{e^{2}}{mc^{2}}\right)^{2}\cdot f_{\theta}^{2} \qquad \text{Eq.(3-8)}$$

where Po is the intensity of the incident beam, L is the distance from the emitting electron to the point of observation, e = 4.8029E-10 esu is the charge of an electron, m = 9.108E-28 gm is the mass of a rest electron, and c = 2.99793E10 cm/sec is the velocity of light. $f_{\theta}^{2} = (1 + \cos^{2}2\theta)/2$ is the polarization factor which is almost equal to one for SAXS. The value of $i_{e} = e^{4}/m^{2}c^{4} = 7.94030E\text{-}26\ cm^{2}$ was first

calculated by Thomson (127) and is called the Thomson factor. It is a measure of the effective cross-section for the scattering of electromagnetic waves by an electron provided that, besides the excited vibration of the electron, no other absorption effects occur.

The general form for the observed scattering intensity of any object is then given by

$$P_{obs} = P_o \cdot \frac{1}{L^2} \cdot i_e \cdot f_\theta^2 \cdot I(\vec{s}) \qquad \text{Eq.(3-9)}$$

where

$$I(\vec{s}) = F(\vec{s}) \cdot F^*(\vec{s}) = |F(\vec{s})|^2. \qquad \text{Eq.(3-10)}$$

Eq.(3-9) points out the first step to be taken in a structure analysis. For this, the observed scattering intensity P_{obs} is separated into the absolute intensity $I(\vec{s})$ and other experimental factors. $I(\vec{s})$ is expressed in "electron units"; this term is defined as the ratio of observed intensity from the sample (assuming perfect collimation conditions) to that from a single classical electron under identical conditions and at the same angle (128). It is assumed everywhere in what follows that

$$I(\vec{s}) \text{ [=] eu = electron**2.} \qquad \text{Eq.(3-11)}$$

3.2.4 Real Space and Reciprocal Space

Since x-rays are scattered by electrons, the set of discrete points in position $\vec{R}_n$ can be replaced by an object with a continuous distribution of electron density $\rho(\vec{R})$. Then Eq.(3-7) can be replaced by an integral for the continuous function $\rho(\vec{R})$:

$$F(\vec{s}) = \int_o^\infty \rho(\vec{R}) \cdot \exp[-i \cdot (\vec{s} \cdot \vec{R})] dv_R. \qquad \text{Eq.(3-12)}$$

The integration is carried out over the entire volume of the system with a volume element dv_R. All types of scattering from objects of different shapes and distributions of scattering material can be discussed by referring to Eq.(3-12).

The integral in Eq.(3-12) is a three-dimensional Fourier integral. The amplitude F depends on the vectors $\vec{s}$. The vector $\vec{s}$ defines a space which is reciprocal to the physical space (or called real space) defined by the vectors $\vec{R}$. The space defined by $\vec{s}$ is, therefore, called the Fourier space or the reciprocal space and $F(\vec{s})$ is defined as the Fourier transform of $\rho(\vec{R})$. If we know $\rho(\vec{R})$, we can calculate $F(\vec{s})$. On the other hand, if we know $F(\vec{s})$ we can also calculate $\rho(\vec{R})$ by an inverse transformation. $\rho(\vec{R})$ is, therefore, called the inverse Fourier transform of $F(\vec{s})$. Thus,

$$F(\vec{s}) = \int_0^\infty \rho(\vec{R}) \cdot \exp[-i \cdot (\vec{s} \cdot \vec{R})] dv_R = \mathcal{F}[\rho(\vec{R})] \qquad \text{Eq.(3-13a)}$$

$$\rho(\vec{R}) = \int_0^\infty F(\vec{s}) \cdot \exp[i \cdot (\vec{s} \cdot \vec{R})] dv_s = \mathcal{F}^{-1}[F(\vec{s})] \qquad \text{Eq.(3-13b)}$$

in which $\mathcal{F}$ and $\mathcal{F}^{-1}$ denote the operations of three-dimensional Fourier transformation and inverse Fourier transformation, respectively.

3.2.5 Correlation Function and Invariant

In Eq.(3-12) the electron density distribution in the scattering system is described by a continuous function $\rho(\vec{R})$. This does not yet, however, describe the structure of the material system completely; this distribution does not tell us whether the peaks and valleys of the electron density distribution are crowded close together or whether they are far apart. A second function, the correlation function, describes this aspect of the structure.

From Eqs.(3-10) and (3-12), the intensity can be expressed as

$$I(\vec{s}) = \left|\int_0^\infty \rho(\vec{R})\cdot\exp[-i\cdot(\vec{s}\cdot\vec{R})]dv_R\right|^2$$

$$= \int_0^\infty\int_0^\infty \rho(\vec{R})\cdot\rho(\vec{R'})\cdot\exp[-i\cdot\vec{s}\cdot(\vec{R'}-\vec{R})]dv_R dv_{R'},$$

$$= \int_0^\infty\int_0^\infty \rho(\vec{R})\cdot\rho(\vec{R}+\vec{r})\cdot\exp[-i\cdot(\vec{s}\cdot\vec{r})]dv_R dv_r \qquad \text{Eq.(3-14)}$$

with

$$\vec{r} = \vec{R'} - \vec{R} = \text{constant}.$$

This equation can be rewritten as

$$I(\vec{s}) = \int_0^\infty Q(\vec{r})\cdot\exp[-i\cdot(\vec{s}\cdot\vec{r})]dv_r \qquad \text{Eq.(3-15)}$$

in which $Q(\vec{r})$ is the self-convolution or convolution of square of the electron density function

$$Q(\vec{r}) = \int_0^\infty \rho(\vec{R})\cdot\rho(\vec{R}+\vec{r})\cdot dv_R = \overset{2}{\rho}(\vec{R}). \qquad \text{Eq.(3-16)}$$

The symbol $\overset{2}{\sim}$ denotes the self-convolution operation. $Q(\vec{r})$ is called the Q-function by Hosemann (119) or interatomic distance function in crystallography in which the integration is confined to the unit cell (126). If $\rho(\vec{R})$ is the electron density of an infinitely large crystal, it is known as the Patterson function (129). The integral in Eq.(3-15) is a three-dimensional Fourier integral. Thus, the intensity function $I(\vec{s})$ and the Q-function are reciprocal Fourier transforms:

$$I(\vec{s}) = \int_0^\infty Q(\vec{r})\cdot\exp[-i\cdot(\vec{s}\cdot\vec{r})]dv_r = \mathcal{F}[Q(\vec{r})], \qquad \text{Eq.(3-17a)}$$

$$Q(\vec{r}) = \int_0^\infty I(\vec{s})\cdot\exp[+i\cdot(\vec{s}\cdot\vec{r})]dv_s = \mathcal{F}^{-1}[I(\vec{s})]. \qquad \text{Eq.(3-17b)}$$

$Q(\vec{r})$ is a function that takes into account the electron densities at two points at a relative position and averages their product over the volume of the system.

The Fourier transform of the intensity function (3-17b) at $\vec{r} = 0$, namely Q(0) is

$$\int_0^\infty I(\vec{s})dv_s = Q(0). \qquad \text{Eq.(3-18)}$$

This is the value of $Q(\vec{r})$ at the origin; on the other hand from Eq.(3-16), the definition of this function is

$$Q(0) = \int_0^\infty \rho(\vec{R})\cdot\rho(\vec{R})dv_R. \qquad \text{Eq.(3-19)}$$

The strongest peak in $Q(\vec{r})$ lies at the origin; it gives the distances of the scattering units to themselves. From Eq.(3-19) we see that the value of the peak at the vertex at $\vec{r} = 0$ is defined by the square of the electron density.

The integral in Eq.(3-16) is taken over the scattering volume with electron density distribution $\rho(\vec{R})$. If there exists no long range order in the system, i.e., there is no correlation between two points separated widely enough, then at large $\vec{r}$ the respective electron densities should become independent, and might be replaced by the mean value $\bar{\rho}$ (113). Eq.(3-16) must so tend towards a constant value $V\bar{\rho}^2$, while the initial value Q(0) is $V\overline{\rho^2}$. So the structure is represented by the finite region where $\rho(\vec{R})$ deviates from the final value, since the latter obviously contains no information. This is in accordance with the fact that a constant value throughout the total volume (always assumed to be very large) acts like a blank object and cannot make any contribution to the scattering pattern (except for extremely small angles not accessible to experiments). It is convenient, therefore, to drop this "background" from the beginning.

With this in mind, Debye and Bueche (122) redefine the electron density at any point in the sample by means of the relation

$$\rho(\vec{R}) = \bar{\rho} + \eta(\vec{R}) \qquad \text{Eq.(3-20)}$$

where $\eta(\vec{R})$ designates the local density deviations. Eq.(3-14) can now be written as

$$I(\vec{s}) = \int_o^\infty \int_o^\infty [\bar{\rho} + \eta(\vec{R})] \cdot [\bar{\rho} + \eta(\vec{R} + \vec{r}) \cdot \exp[-i \cdot (\vec{s} \cdot \vec{r})] dv_R dv_r \qquad \text{Eq.(3-21)}$$

This intensity expression can be divided into four terms corresponding respectively to terms in $\bar{\rho}^2$, $\bar{\rho} \cdot \eta(\vec{R})$, $\bar{\rho} \cdot \eta(\vec{R} + \vec{r})$, and $\eta(\vec{R}) \cdot \eta(\vec{R} + \vec{r})$ (72). If $\eta \ll \bar{\rho}$, the first three terms are negligible as compared with the fourth term. Eq.(3-21) can be simplified as

$$I(\vec{s}) = \int_o^\infty \int_o^\infty \eta(\vec{R}) \cdot \eta(\vec{R} + \vec{r}) \cdot \exp[-i \cdot (\vec{s} \cdot \vec{r})] dv_R dv_r . \qquad \text{Eq.(3-22)}$$

In this equation, the integral, $\eta(\vec{R}) \cdot \eta(\vec{R} + \vec{r}) dv_R$, depends uniquely on $\vec{r}$. It is a self-convolution of the function $\eta(\vec{R})$. The correlation function is then defined as (122)

$$\gamma(\vec{r}) = \frac{\int_o^\infty \eta(\vec{R}) \cdot \eta(\vec{R} + \vec{r}) dv_R}{\int_o^\infty \eta(\vec{R}) \cdot \eta(\vec{R}) dv_R} = \frac{\int_o^\infty \eta(\vec{R}) \cdot \eta(\vec{R} + \vec{r}) dv_R}{\overline{\eta^2} V} . \qquad \text{Eq.(3-23)}$$

If no assumptions whatever are made about the nature of the inhomogeneities that gives rise to small-angle scattering from a specimen, the only parameter that can be determined is $\overline{\eta^2}$ - the mean square electron density fluctuation, which may be called the scattering power of the system (72, 120).

Because the correlation function has been normalized by dividing by $\overline{\eta^2}V$, it is determined only by the spatial extent of the fluctuations, and is independent of the irradiated volume V and the scattering power $\overline{\eta^2}$. In this case, $\gamma(0) = 1$ and $\gamma \rightarrow 0$ for large r. From Eqs.(3-22) and (3-23) the expression for the intensity is then

$$I(\vec{s}) = \overline{\eta^2}V \cdot \int_o^\infty \gamma(\vec{r}) \cdot \exp[-i \cdot (\vec{s} \cdot \vec{r})] dv_r = \overline{\eta^2}V \cdot \mathcal{F}[\gamma(\vec{r})]. \qquad \text{Eq.(3-24)}$$

Inversely,

$$\gamma(\vec{r}) = \frac{1}{\overline{\eta^2}V} \cdot \int_o^\infty I(\vec{s}) \cdot \exp[+i \cdot (\vec{s} \cdot \vec{r})] dv_s = \frac{1}{\overline{\eta^2}V} \cdot \mathcal{F}^{-1}[I(\vec{s})]. \qquad \text{Eq.(3-25)}$$

Obviously Eq.(3-24) takes a particularly simple form for $\vec{s} = 0$,

$$I(0) = \overline{\eta^2}V \cdot \int_o^\infty \gamma(\vec{r}) dv_r. \qquad \text{Eq.(3-26)}$$

The meaning of this equation requires some consideration. At $\vec{s} = 0$, all secondary waves are in phase, so that we might expect I(0) to be equal to the square of the total number of electrons in the irradiated volume V (113). This cannot be observed, however. Eq.(3-26) may be interpreted in the sense that each electron of the volume V acts in coherence only with a surrounding region, as defined by $\gamma(\vec{r})$. So I(0) should be regarded as an extrapolated value, rather than as a measurable quantity.

Eq.(3-25) shows the integral of the intensity over the reciprocal space is directly related to the mean square fluctuation of electron density, irrespective of special features of the structure. If, for example, parts of the system were shifted or deformed, the scattering

pattern might be altered considerably, but the integral in Eq.(3-25) must remain invariant. By virtue of this property, Porod (74) gave an important definition called the invariant

$$K = \frac{1}{(2\pi)^3} \cdot \int_o^\infty I(\vec{s}) dv_s = \int_o^\infty I(\vec{b}) dv_b = \overline{\eta^2} V. \qquad \text{Eq.(3-27)}$$

The determination of K in absolute units allows a calculation of the scattering power $\overline{\eta^2}$ (mean square electron density fluctuation). However, the normalization with K allows the calculation of correlation function $\gamma(\vec{r})$ from intensities in arbitrary units.

3.2.6 Ewald's Sphere and Intensity Profile

Eq.(3-4) shows that for a particular direction of the incident beam, the end points of the vectors $\vec{s}$ lie on the surface of a sphere of radius $2\pi/\lambda$. The condition of interference can be fulfilled if, and only if, $\vec{s}$ is anywhere on this surface. This sphere is called Ewald's sphere of reflection (130). As shown in Figure 3-2, the sphere of reflection is drawn with P as its center and $2\pi/\lambda$ as its radius. O is the origin of the reciprocal space. The vectors joining P with any point B on the surface of the sphere give the directions of the scattered ray. From Eq.(3-10) it follows that for every scattering vector $\vec{s}$ there is an intensity $I(\vec{s})$ associated with it. The intensities, therefore, are found on the surface formed by intersecting the Ewald's sphere with the intensity figure $I(\vec{s})$. For small-angle scattering where $s < 0.1\ \text{Å}^{-1}$ the sphere may usually be approximated by its tangent plane T at O. Then, the SAXS pattern is determined by a plane section of the intensity figure.

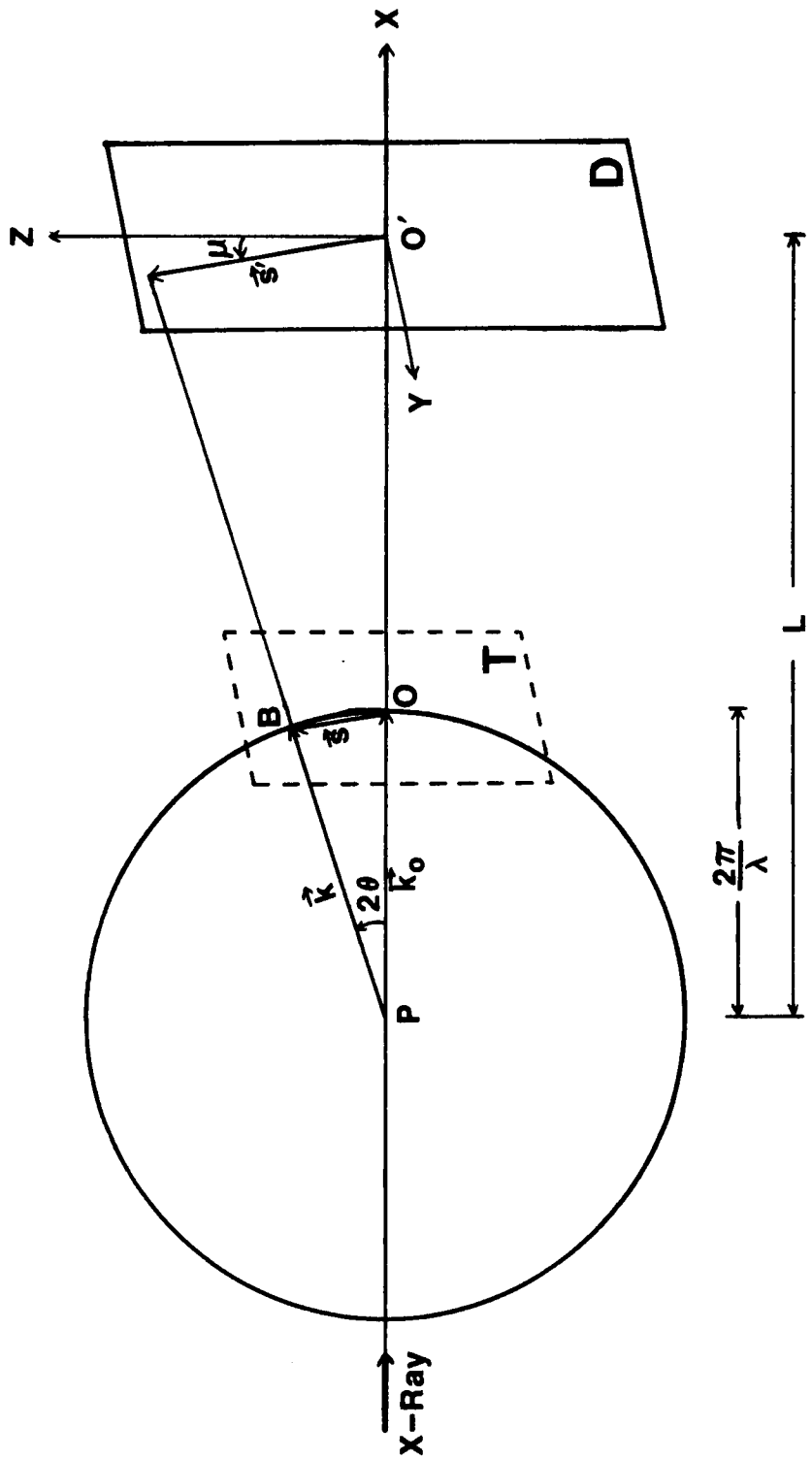


Figure 3-2. Ewald's sphere of diffraction and the two-dimensional detector plane.

Consider now the two-dimensional scattering pattern. A coordinate system is defined as shown in Figure 3-2, with $\vec{u}_1$, $\vec{u}_2$, $\vec{u}_3$ as the orthogonal unit length vectors in reciprocal space, where $\vec{u}_2$ is in the direction of $\vec{ko}$. Then $\vec{s}$ can be represented as (s_1, s_2, s_3):

$$\vec{s} = s_1 \cdot \vec{u}_1 + s_2 \cdot \vec{u}_2 + s_3 \cdot \vec{u}_3 . \qquad \text{Eq.(3-28)}$$

Similarly, unit length vectors $\vec{e}_i$ parallel to $\vec{u}_i$ can be chosen in real space as a base for the vectors R and r. The plane T defined by $\vec{u}_1$ and $\vec{u}_3$ is the tangent plane to the Ewald's sphere mentioned above. The intensity in this plane is given by (112, 119)

$$\begin{aligned} I(s_1,0,s_3) &= \overline{\eta^2} V \cdot \int_o^\infty\int_o^\infty\int_o^\infty \gamma(r_1,r_2,r_3) \cdot \exp[-i \cdot (s_1 \cdot r_1 + s_3 \cdot r_3)] dr_1 dr_2 dr_3 \\ &= \overline{\eta^2} V \cdot \int_o^\infty\int_o^\infty \gamma_p(r_1,r_3) \cdot \exp[-i \cdot (s_1 \cdot r_1 + s_3 \cdot r_3)] dr_1 dr_3 \\ &= \overline{\eta^2} V \cdot \mathcal{F}_2[\gamma_{pp}(r_1,r_3)] \qquad \text{Eq.(3-29a)} \end{aligned}$$

where $\mathcal{F}_2$ is the symbol for two-dimensional Fourier transform and

$$\gamma_p(r_1,r_3) = \int_o^\infty \gamma(r_1,r_2,r_3) dr_2 . \qquad \text{Eq.(3-29b)}$$

Thus the distribution of the intensity function $I(\vec{s})$ on the plane $s_2 = 0$ is nothing but a two-dimensional Fourier transform of the two-dimensional function $\gamma_p(r_1, r_3)$ in the physical space, i.e., the projection of the correlation function $\gamma(\vec{r})$ on the plane $r_2 = 0$. Similarly,

$$\gamma(r_1, 0, r_3) = \frac{1}{\overline{\eta^2} V} \cdot \mathcal{F}_2^{-1}[I_p(s_1, s_3)] \qquad \text{Eq.(3-30a)}$$

where

$$I_p(s_1, s_3) = \int_o^\infty I(s_1, s_2, s_3) ds_2 \qquad \text{Eq.(3-30b)}$$

and

$$I(0, 0, s_3) = \overline{\eta^2} V \cdot \mathcal{F}_1[\gamma_{pp}(r_3)] \qquad \text{Eq.(3-31a)}$$

$$\gamma_{pp}(r_3) = \int_o^\infty \gamma(r_1, r_2, r_3) dr_1 dr_2 \qquad \text{Eq.(3-31b)}$$

$$\gamma(0,\ 0,\ s_3) = \frac{1}{\eta^2 V} \cdot \mathcal{F}_1^{-1}[I_{pp}(s_3)] \qquad \text{Eq.(3-32a)}$$

$$I_{pp}(s_3) = \int_o^\infty I(s_1,\ s_2,\ s_3)ds_1ds_2 \qquad \text{Eq.(3-32b)}$$

The meaning of Eq.(3-31a) is that for any line through the origin of reciprocal space, the course of the intensity along that line is related to the projection of the structure onto that line. Ultimately this means the intensity $I(\vec{s})$ at any point is determined solely by the total number of electrons in planes perpendicular to $\vec{s}$ (112, 119). It is independent of the distribution of matter within these planes. Eqs.(3-29) to (3-32) are just the application of the integral properties of the Fourier transform.

The considerations above are important for analyzing the information obtained for a given type of sample and method of measurement. They are particularly useful for anisotropic scatterers.

3.3 Relations Between Theory and Experiment

3.3.1 Definition of Coordinates in the Detector Plane

The collection of photon counts is carried out behind the sample, at a distance L, which is large enough to obtain a reasonable extension of the pattern. Because of the small angles involved, the detector plane D may be defined as a plane parallel to the tangent plane T to the Ewald's sphere at the origin of the reciprocal space and perpendicular to the incident x-ray beam (see Figure 3-3). Each point in the plane D has a distance L to the sample and can be defined by its coordinates (x, z) with y-axis being in the direction of $\vec{ko}$. The origin O' of the detector plane is where the point-like primary

beam incident at plane D. For a point on plane D, its position vector $\vec{s}'$ relative the origin O′ can be denoted as

$$\vec{s}' = x \cdot \vec{u_1}' + z \cdot \vec{u_3}' \qquad \text{Eq.(3-33a)}$$

with magnitude

$$\vec{s}' = |\vec{s}'| = (x^2 + z^2)^{1/2} = L \cdot \tan(2\theta) \approx L \cdot 2\theta \approx L \cdot 2\sin\theta \qquad \text{Eq.(3-33b)}$$

where $\vec{u_1}'$ and $\vec{u_3}'$ are unit length vectors parallel to x-axis and z-axis, respectively. Moreover, since plane D is parallel to plane T, $\vec{s}' // \vec{s}$ and hence:

$$s = \left(\frac{2\pi}{\lambda}\right)\left(\frac{s'}{L}\right). \qquad \text{Eq.(3-34)}$$

Eq.(3-34) enables the calculations of coordinates in reciprocal space for the registered scattering pattern. Further, the azimuthal angle μ of the scattering pattern will be defined as the angle between $\vec{u_3}'$ (i.e. the meridional direction) and $\vec{s}'$ and it can be determined by

$$\tan(\mu) = x/z = s_1/s_3. \qquad \text{Eq.(3-35)}$$

3.3.2 The Collimation Error

In all scattering experiments one has to use a slit or pinhole in order to limit the beam of x-rays. Ideally the opening should be point-like. But for various reasons it is not possible to make the opening as fine as desirable and, consequently, experimental results involve collimation errors. The actually observed SAXS pattern $I'(\vec{s}')$ is given by the convolution of the ideal pattern $I(\vec{s}')$ produced by a point-like beam and the intensity distribution $Po(\vec{s}')$ of the primary beam registered on the detector plane (112, 119):

$$I'(\vec{s}') = \int_{\Sigma} Po(\vec{w}) I(\vec{s}' - \vec{w}) d\Sigma = \widehat{PoI}. \qquad \text{Eq.(3-36)}$$

where $\vec{w}$ is an auxiliary vector to be varied throughout the entire detector plane, $d\Sigma$ is an element of surface in the $\vec{w}$ space, and Eq.(3-36) is a two-dimensional convolution integral.

3.3.3 The Precision of Measurement

Every measurement represents some integration process, since the detector cannot count the value of the function $g(\vec{s}')$ at a point but only over a certain resolution element of the detector, which has a finite size $\Delta\Sigma$, however small. Thus the observed function is not the original function $g(\vec{s}')$ we intend to measure but a new function $g'(\vec{s}')$ which is given by the convolution product of the original function and the normalized precision function $g_p(\vec{s}')$ of the resolution element $\Delta\Sigma$ (119)

$$g'(\vec{s}') = \int_{\Sigma} g(\vec{w}) \cdot g_p(\vec{s}' - \vec{w}) d\Sigma = \widehat{g g_p}. \qquad \text{Eq.(3-37)}$$

In Eq.(3-37) it is assumed that the center of the resolution element lies at $\vec{s}'$ and that the precision function $g_p(\vec{s}')$ has finite values only within the element $\Delta\Sigma$ and vanishes outside it.

3.3.4 Termination Effect

In section 3.2 the integration in all cases are carried from zero to infinity. Therefore in principle, the SAXS measurement should be extended to both the smallest and largest possible values of s in order to obtain information about the finer details of the structure.

In the large angle region, a separation between SAXS and WAXS must be made first. This is an arbitrary procedure but is directly

connected with the model in which the electron density profile on the atomic level is smeared out. Because of this, the measurement need not be carried further than to the value of s for which the intensity level reaches a background level or to the onset of wide-angle scattering. By choosing a suitable expression one can actually perform the separation in the transition zone (see 3.4.2.2).

In the low angle region, the scattering curves may be extrapolated to the zero angle by curve fitting technique, e.g., a plot of ln(I) versus s^2, or s^2I versus s, or a power expansion in s.

3.4 Structure Analysis of a Macroscopically Isotropic System

The primary object of SAXS analysis is to deduce the structure from the observed scattering pattern. From the early days of SAXS the properties of the scattering pattern were studied in order to extract in a simple way some quantities to characterize the system. The results for some particular cases will be discussed.

A system may on the average have spherical symmetry as a result of the statistics of the random array of molecules, particles, or of ordered regions. It makes no difference here whether this is a property of the structure itself or a consequence of some change in time (rotation of particles or the like). Then the intensity distribution in reciprocal space has spherical symmetry and is described by a single parameter s (the distance in reciprocal space from the origin). The x-ray pattern in this case is bound to contain only sharp or diffuse rings and has circular symmetry.

3.4.1 General Cases

The spherically symmetrical $I(\vec{s})$ is transformed to $\gamma(\vec{r})$ by the Fourier intergral, Eq.(3-24). $\gamma(\vec{r})$ is also spherically symmetrical (i.e., depends only on r, the length of the vector $\vec{r}$), by virtue of the reciprocity, though this will not be true for $\eta(\vec{R})$ in real space. Likewise, the phase factor $\exp[-i\cdot(\vec{s}\cdot\vec{r})]$ can be replaced by its average, taken over all directions of $\vec{r}$. This is expressed by the fundamental formula of Debye (131):

$$\langle\exp[-i\cdot(\vec{s}\cdot\vec{r})]\rangle = \frac{\sin(s\cdot r)}{s\cdot r} \qquad \text{Eq.(3-38)}$$

by means of which Eq.(3-24) is reduced to the form

$$I(s) = \overline{\eta^2}V\cdot\int_0^{\infty}4\pi r^2\cdot\gamma(r)\cdot\frac{\sin(s\cdot r)}{s\cdot r}dr. \qquad \text{Eq.(3-39)}$$

The formala for the correlation function can be shown in the same way to be

$$\gamma(r) = \frac{1}{(2\pi)^3\cdot\overline{\eta^2}V}\cdot\int_0^{\infty}4\pi s^2\cdot I(s)\,\frac{\sin(s\cdot r)}{s\cdot r}ds. \qquad \text{Eq.(3-40)}$$

Eq.(3-39) is the most general formula for the scattering of isotropic systems. In this equation, the vector $\vec{r}$ loses all indications of its spatial position in the spherically symmetrical functions; the vectors for the various pairs of scattering units are superimposed by spherical rotation, and so we can establish only the distances between scattering units, not the spatial orientation of the distances. Obviously Eq.(3-39) and Eq.(3-40) take a particularly simple form for $s = 0$ and $r = 0$,

$$I(0) = \overline{\eta^2}V \cdot \int_0^\infty 4\pi r^2 \cdot \gamma(r)dr \qquad \text{Eq.(3-41)}$$

$$\gamma(0) = \frac{1}{(2\pi)^3 \cdot \overline{\eta^2}V} \cdot \int_0^\infty 4\pi s^2 \cdot I(s)ds = 1. \qquad \text{Eq.(3-42)}$$

And the invariant for an isotropic system becomes (74)

$$K = \frac{1}{(2\pi)^3} \cdot \int_0^\infty 4\pi s^2 \cdot I(s)ds = \overline{\eta^2}V. \qquad \text{Eq.(3-43)}$$

3.4.2 Two-Phase Systems in General

The category two-phase systems includes a great variety of substances, e.g. porous materials, micro phase-separated systems, semi-crystalline polymers, and colloidal dispersions. The electron densities in the two phases are supposed to be uniform and separated by a sharp boundary. The general parameters used to characterize the system will be discussed.

3.4.2.1 Scattering Power

The mean square electron density fluctuation $\overline{\eta^2}$, which is also called the scattering power of the system (72, 120), of a two-phase system can be expressed as:

$$\overline{\eta^2} = x_1 \cdot x_2 \cdot (\rho_1 - \rho_2)^2 = (\Delta\rho)^2 \cdot x_1 \cdot x_2 \qquad \text{Eq.(3-44)}$$

where ρ_1 is the electron density of phase 1, the "solvent," for solid systems normally called "matrix" if a majority phase can be defined, and x_1 is its volume fraction. The "solute," i.e. the disperse phase, has the electron density ρ_2 and occupies a volume fraction $x_2 = 1 - x_1$ of the total volume V. The validity of this expression does not depend on the degree of dispersion (dilution) within the system

but only on $\Delta\rho$. Eq.(3-44) is in agreement with Babinet's principle (74, 132, 133), which states that the scattering pattern does not change when the densities of the phases are interchanged (without an alteration in the geometry of the structure).

3.4.2.2 Porod's Law

For a two-phase system, Porod (74) enunciated the asymptotic behavior of the scattering curve at large angles (denoted by $s \rightarrow \infty$). This can be understood by expanding $\gamma(r)$ into a power series

$$\gamma(r) = 1 - a_1 r + a_2 r^2 + a_3 r^3 + \ldots. \qquad \text{Eq.(3-45)}$$

The intensity can then be derived from Eq.(3-39). The terms with a_1, a_2 etc. are found to give oscillatory contributions with an average value of zero (72, 74):

$$I(s) = \frac{4\pi K}{s^4}\left(-2!a_1 + \frac{4!a_3}{s^2} - \frac{6!a_5}{s^4} + \ldots.\right) \qquad \text{Eq.(3-46)}$$

Sharp phase boundaries cause $\gamma(r)$ to be linear for small values of r, which implies:

$$\lim_{s\rightarrow\infty} I(s) = (2\pi)^4 \cdot Kp/s^4. \qquad \text{Eq.(3-47)}$$

This inverse fourth power law, derived independently by Porod (74) and Debye et al. (134), is best known as the Porod's law. It is valid for single particles, dense packed systems, and for non-particulate structures (with a slight modification of the factor only), provided that there exists a well defined internal surface.

3.4.2.3 Chord Length

The Porod constant Kp can be used to find an important characterization parameter, the average chord length $\bar{\ell}$ (135). It is simply related to the derivative of $\gamma(r)$ at the origin:

$$\bar{\ell} = -\frac{1}{\gamma'(0)} = \frac{K}{2\pi^3 Kp}. \qquad \text{Eq.(3-48)}$$

$\bar{\ell}$ is a measure of the size of the inhomogeneities. Although it is necessary to use the absolute intensity in evaluting the invariant, the scattering power, and the Porod's constant, it is not necessary for the evaluation of the correlation and its derivative and the chord length. The meaning of $\bar{\ell}$ can be understood as follows. If one draw a straight line in an arbitrary direction from a point in matter, this line will be divided into segments which are alternatively occupied by phase 1 and phase 2. Their number-average lengths are given by $\bar{\ell}_1$ and $\bar{\ell}_2$ for the respective phases. The following relations can be established:

$$\frac{1}{\bar{\ell}} = \frac{1}{\bar{\ell}_1} + \frac{1}{\bar{\ell}_2} \qquad \text{Eq.(3-49)}$$

$$\bar{\ell} = x_1 \cdot \bar{\ell}_1 = x_2 \cdot \bar{\ell}_2. \qquad \text{Eq.(3-50)}$$

Debye et al. (134) have shown for a "random" two-phase system of irregular structure:

$$\gamma(r) = \exp(-\frac{r}{\bar{\ell}}). \qquad \text{Eq.(3-51)}$$

The intensity arising from this correlation function is:

$$I(s) = \overline{\eta^2} V \frac{8\pi\overline{\ell}^3}{[1 + (s\cdot\overline{\ell})^2]^2}. \qquad \text{Eq.(3-52)}$$

In this case the plot of $[I(s)]^{-1/2}$ vs. s^2, the so-called the Debye plot, is a straight line from which $\overline{\ell}$ can be calculated. Note that in this special case

$$\overline{\ell}_c = 2\overline{\ell} = 2\cdot\int_0^\infty \gamma(r)dr \qquad \text{Eq.(3-53)}$$

where $\overline{\ell}_c$ is the integral width of the correlation function. Eq.(3-48) and Eq.(3-52) has used to calculate the size of inhomogeneities (voids) in polymer crazes (73, 75 - 78).

3.4.2.4 Specific Inner Surface

When it can be verified experimentally that the intensity in the tail of a scattering curve follows the theoretical inverse fourth power law, an important structural parameter can be obtained therefrom, namely, the specific inner surface in units of (m^2/m^3), which is defined as the ratio of the area of the phase interface S to the volume occupied by the disperse phase V_2. It was shown that (74, 135):

$$\frac{S}{V_2} = \frac{4x_1x_2}{\overline{\ell}}, \qquad \text{Eq.(3-54)}$$

or

$$\frac{S}{V_2} = \frac{8\pi^3 Kp}{K}. \qquad \text{Eq.(3-55)}$$

Note that again absolute intensities are not required for the determination of the specific surface.

3.4.3 Dilute Particle Dispersions

3.4.3.1 General Description

Among the various inhomogeneous systems that can scatter x-rays at small angles, dilute particulate systems are most amenable to definitive theoretical interpretation. The application of the well-developed theory of particulate scattering to polymer problems is restricted principally to polymer solutions composed of large, discrete macromolecules dispersed in suitable solvents to an essentially monomolecular state, or to solid polymers such as synthetic and natural fibers for which the primary particles are not well defined.

Consider a dilute solution of N identical particles of constant electron density ρ_2, dispersed in a medium (solvent) of constant electron density ρ_1. The scattering amplitude for a single particle is given by Eq.(3-13a):

$$F_n(\vec{s}) = (\rho_1 - \rho_2)\cdot\int_o^\infty \exp[-i\cdot(\vec{s}\cdot\vec{R})]dv_R. \qquad \text{Eq.(3-56)}$$

By assuming a center of symmetry of the particle, the phase factor, $\exp[-i\cdot(\vec{s}\cdot\vec{R})]$, can then be replaced by $\cos(\vec{s}\cdot\vec{R})$:

$$F_n(\vec{s}) = (\Delta\rho)\cdot\int_o^\infty \cos(\vec{s}\cdot\vec{R})dv_R. \qquad \text{Eq.(3-57)}$$

The scattering amplitude from such a system is given by Eq.(3-7):

$$F(\vec{s}) = \sum_{n=1}^{N} F_n,$$

which is the sum of all the N particles.

In general, $F(\vec{s})$ is dependent on the orientation of the particle and for non-centrosymmetric particles it is even a complex function. In an isotropic system all the possible orientations are realized and the resulting intensity distribution has spherical symmetry. If the particles are separated from each other widely enough, it is plausible to assume they will make independent contributions to the diffracted intensity. The scattering intensity of the dilute system can be written as:

$$I(s) = N \cdot \overline{F_n^2(s)}. \qquad \text{Eq.(3-58)}$$

The averages are taken over all orientations of a particle.

3.4.3.2 Guinier's Law

By expanding the term $\cos(\vec{s} \cdot \vec{R})$ in Eq.(3-57) into a power series for the small angle region,

$$\cos(\vec{s} \cdot \vec{R}) = 1 - (\vec{s} \cdot \vec{R})^2/2 + \ldots ,$$

Guinier (100, 136, 137) showed that for a dilute, monodisperse system in which the particles assume all orientations with equal probability the scattering intensity can be described by a power series as follows:

$$I(s) = N \cdot (\Delta\rho)^2 \cdot v^2 \left(1 - \frac{s^2}{3} Rg^2 + \ldots\right) \qquad \text{Eq.(3-59)}$$

where Rg is the so-called (electronic) radius of gyration of the particle, which is the root mean square of the distances of all the electrons from the electronic center of gravity of the particle (72),

$$Rg^2 = \frac{\sum_k f_k r_k^2}{\sum_k f_k} \qquad \text{Eq.(3-60)}$$

where f_k is the scattering factor of the k-th electron ($f_k = 1$), which is a distance r_k from the electronic center of gravity. To a good approximation, particle scattering at very small angles can be described by:

$$I(s) = I(0) \cdot \exp[-\frac{1}{3} s^2 Rg^2], \qquad \text{Eq.(3-61)}$$

which is the familiar law of Guinier. A so-called Guinier plot is based on the following representation:

$$\ln[I(s)] = \ln[I(0)] - \frac{1}{3} s^2 Rg^2. \qquad \text{Eq.(3-62)}$$

According to this, a plot of $\ln[I(s)]$ vs. s^2 yields a straight line with a slope $-Rg^2/3$. In practice, a Guinier plot may be curved due to anisotropic particle shape or polydispersity (72, 137). From the derivation of Eq.(3-59) it follows that the limiting slope, i.e. the derivative of this Guinier plot for $s \rightarrow 0$, always produces the true radius of gyration. This holds good, however, only in the absence of interparticle interference effects. For a polydisperse system a Z-average radius of gyration is found,

$$\overline{Rg^2} = \frac{\sum_k Rg_k^8}{\sum_k Rg_k^6} \qquad \text{Eq.(3-63)}$$

which is mainly determined by the large particles. This is because the limiting intensity I(0) is proportional to the square of the particle volume [Eq.(3-59), Eq.(3-60)]. On the whole, the Guinier approximation holds surprisingly well in the majority of cases except for very anisotropic particles.

Guinier's law has been widely applied to calculate the size of biomolecules in solutions (e.g., 115 - 118). the radius of gyration of random coils in solid polymer solutions [e.g., SAXS study of iodinated polystyrene in polystyrene (6) and brominated polystyrene in polystyrene (7), and SANS study of duterated polystyrene in polystyrene (8, 9, 10)] and many other kinds of systems. In some parallel studies, the particle size as obtained by SAXS and that determined by electron microscopy showed consistent results.

3.5 Structure Analysis of an Anisotropic System

The SAXS pattern of an isotropic system is independent of its orientation and provides all the available information at once. To gain insight into the specific problems associated with anisotropic systems, the intensity distribution in reciprocal space must be considered. What was said in section 3.2.6 about the intensity distribution along any line through the origin of reciprocal space (i.e. the center of the SAXS pattern) invariably holds: this intensity profile is determined by the projection of the whole structure onto that line. The projected correlation function that can be calculated from it will be detailed only for particular orientations of the line, notably when it is perpendicular to extensive phase boundary-planes. The following paragraphs consider the applicability of the general scattering laws, originally derived for isotropic systems, to anisotropic systems and their classification.

3.5.1 Two-Phase Anisotropic System in General

3.5.1.1 Scattering Power

For a two-phase system with uniform electron density separated by a sharp boundary, Eq.(3-44) is still true:

$$\overline{\eta^2} = x_1 \cdot x_2 \cdot (\rho_1 - \rho_2)^2. \qquad \text{Eq.(3-44)}$$

3.5.1.2 Porod's Law

Porod's law was originally derived for systems of spherical symmetry. Ruland (138) has shown that Porod's law is also valid for anisotropic small-angle scattering from lamellar two-phase systems but Porod's constant Kp contains a directional dependence. Kp is directionally dependent not only due to the orientation distribution of the lamellar stacks but also due to possible correlations between the orientation and the structure of the stacks (electron density, composition, thickness, etc.).

Wu (139) has shown theoretically the application of Porod's law to systems with a preferred orientation. He showed that for an ellipsoid with principal axes $\lambda_1 R$, $\lambda_2 R$, and $\lambda_3 R$ and with the incident beam parallel to one of the principal axes (say $\lambda_2 R$),

$$\lim_{s \to \infty} I(s, \mu) = (2\pi)^4 \cdot \frac{Kp(\mu)}{s^4} \qquad \text{Eq.(3-64)}$$

where

$$Kp(\mu) = \frac{A(\Delta\rho)^2 \cdot 8\pi^2 \cdot R^2}{[(\lambda_1 \sin\mu)^2 + (\lambda_3 \cos\mu)^2]^2},$$

A is a scattering constant, μ the azimuthal angle of the observed

two-dimensional scattering pattern with $\mu = 0^{o}$ being the meridian direction and $\mu = 90^{o}$ the equatorial direction, and λ_1, λ_2, and λ_3 are the aspect ratio of the principal axes.

3.5.1.3 Guinier's Law

The intensity scattered by an individual inhomogeneity of arbitrary shape can be shown to be

$$I(\vec{s}) = I(0)\cdot\exp[-s^2 R_t^2(\vec{s})] \qquad \text{Eq.(3-65)}$$

where $R_t(\vec{s})$ is the inertial distance of the particle with respect to a plane through its center perpendicular to $\vec{s}$. This can be regarded as the fundamental Guinier equation (72, 137). Guinier's law has been widely applied to calculate the size of microvoids in polymer crazes (71, 73, 79, 83).

3.5.2 Types of Anisotropic System

3.5.2.1 Cylindrically Symmetrical System

In this case the system is supposed to be isotropic in planes perpendicular to one specific direction (axial direction). This results in cylindrical symmetry of the intensity figure around a unique axis parallel to the axial direction. All the information is contained in the scattering pattern in a plane including the unique axis, which can be found by placing the unique axis perpendicular to the incident x-ray beam. The scattering pattern arising from the beam parallel to the axial direction is circularly symmetrical and can only provide information about the radial structure.

A cylindrical function can be constructed by using cylindrical coordinates. The real space vector $\vec{r}$ will be given by its coordinate z in the axial direction, the radial distance p from the origin, and an azimuthal angle ϕ (see Figure 3-3). The reciprocal space vertor $\vec{s}$ is defined by the corresponding coordinates (P, Φ, Z). As mentioned in section 3.2.5 the convolution $Q(\vec{r})$ of the electron density distribution function $\rho(\vec{R})$ is the inverse Fourier transform of the intensity function $I(\vec{s})$. Calculation of the inverse transform of the intensity using I(P, Φ, Z) for $I(\vec{s})$ gives

$$Q(\vec{r}) = Q(p, z)$$

$$= \frac{1}{(2\pi)^3} \cdot \int_0^{\infty}\int_{-\infty}^{\infty} P \cdot I(P,Z) \cdot \exp(-i \cdot Z \cdot z) \cdot \left[\int_0^{2\pi} \exp[-i \cdot P \cdot p \cdot \cos(\Phi - \phi)]\, d\phi\right] dP \cdot dZ.$$

Eq.(3-66)

The integral in ϕ becomes the zero order Bessel function Jo(P·p). Since I(P,Z) = I(P,-Z) due to the combination of centrosymmetry with axial symmetry, the complex form exp(-i·Z·z) can be replaced by cos(Z·z). Hence,

$$Q(p,z) = \frac{1}{(2\pi)^3} \cdot \int_0^{\infty}\int_{-\infty}^{\infty} I(P,Z) \cdot Jo(P \cdot p) \cdot \cos(Z \cdot z) \cdot 2\pi P \cdot dP \cdot dZ.$$

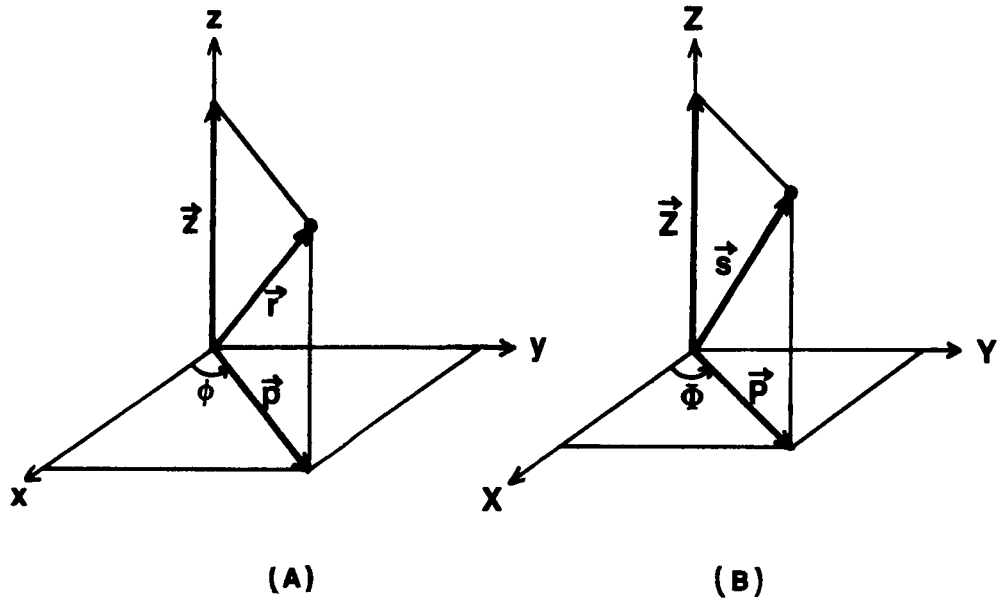
Eq.(3-67)

This is the cylindrical Patterson function in crystallography and was derived by Wrinch (140) and by Vineyard (141).

In a similar way, the intensity function and the two-dimensional correlation function are related to each other by

$$I(P,Z) = \overline{\eta^2} V \cdot \int_0^{\infty}\int_{-\infty}^{\infty} \gamma(p,z) \cdot Jo(P \cdot p) \cdot \cos(Z \cdot z) \cdot 2\pi p \cdot dp \cdot dz,$$

Eq.(3-68)



(A) (B)

Figure 3-3. Cylindrical and cartesian coordinates (A) in real space and (B) in reciprocal space.

$$\gamma(p,z) = \frac{1}{(2\pi)^3 \overline{\eta^2}_V} \cdot \int_0^\infty \int_{-\infty}^\infty I(P,Z) \cdot Jo(P \cdot p) \cdot \cos(Z \cdot z) \cdot 2\pi P \cdot dP \cdot dZ. \qquad \text{Eq.(3-69)}$$

At s = 0 and r = 0;

$$I(0) = \overline{\eta^2}_V \cdot \int_0^\infty \int_{-\infty}^\infty \gamma(p,z) \cdot 2\pi p \cdot dp \cdot dz \qquad \text{Eq.(3-70)}$$

$$\gamma(0) = \frac{1}{(2\pi)^3 \cdot \overline{\eta^2}_V} \cdot \int_0^\infty \int_{-\infty}^\infty I(P,Z) \cdot 2\pi P \cdot dP \cdot dZ = 1. \qquad \text{Eq.(3-71)}$$

And the invariant expression becomes

$$K = \frac{1}{(2\pi)^3} \cdot \int_0^\infty \int_{-\infty}^\infty 2\pi P \cdot I(P,Z) dP \cdot dZ = \overline{\eta^2}_V. \qquad \text{Eq.(3-72)}$$

3.5.2.2 Other Types of Symmetry

If the symmetry is lower than axial, the intensity figure is invariably centrosymmetric. However, there is no unique axis of the sample that allows the determination of $I(\vec{s})$ at once. In principle then, $I(\vec{s})$ cannot be determined from a finite number of "irradiations." Usually things are somewhat simplified by the presence of symmetry planes. In many cases, patterns obtained with the beam along the main directions will yield the most relevant information. Some examples are:

(a) biaxial texture in which the intensity figure is symmetrical with respect to two mirror planes;

(b) uniplanar-axial texture in which only one mirror plane exists. With the x-rays parallel to the mirror plane, axially symmetrical patterns are obtained. In the mirror plane the intensity is only centrosymmetric.

CHAPTER 4

EXPERIMENTAL

This chapter deals with the experimental work, from the sample preparation to the measurements and the reduction of data.

4.1 Sample Preparation

4.1.1 Materials

Since the study is confined to the crazing phenomenon of glassy polymers, the main requirement for the amorphous polymers to be studied is their crazing ability below their glass transition temperature. The availability in desired molecular weight and distribution must also be considered. Atactic polystyrene can fulfill these requirements. Table 4-1 displays all the polystyrenes used with their number-averaged molecular weight $\overline{Mn}$, weight-averaged molecular weight $\overline{Mw}$, and polydispersities $\overline{Mw}/\overline{Mn}$. Except PSBI (a bimodal polystyrene) all of them were supplied in the form of pellets by Dow Chemical. The material parameters studied include molecular weight, molecular weight distribution, and the molecular orientation.

To design a specimen suitable for the dynamic SAXS experiment, the variables to be considered are the thickness (the path through which x-rays travel), width, and length of the tensile bar. The optimum thickness of the specimen is given to a good approximation by (142)

$$t_m = 1/\mu_\ell$$

Table 4-1

Polymer characterization

Polymer	$\overline{Mn}$	$\overline{Mw}$	$\overline{Mw}/\overline{Mn}$
PS103*	118,000	125,000	1.05
Ps109*		193,000	
PS108*	247,000	267,000	1.08
PSBI**	159,704	182,500	1.14
PS685D***	159,958	305,935	1.91

* monodispersed polystyrene obtained from Dow Chemical Company through Lu Ho Tung

** 50/50 bimodal blend of PS103 and PS108

*** commercial polystyrene obtained from Dow Chemical Company; characterized by GPC.

μ_ℓ being the linear absorption coefficient of the specimen for the x-ray wavelength employed. When CuK radiation is employed, μ_ℓ = 4.45 cm^{-1} for polystyrene from which t_m = 0.22 cm. The chosen thickness for the unoriented polystyrene sample is 0.16 cm. Next, the sample should be wide enough to cover the incident x-ray beam, but narrow enough not to exceed the available loading limit to break the sample. The beam width is 0.1 cm, the maximum available tensile force by the existing hydraulic system is 120 lbf, and the breaking strength is 6000 to 8000 psi for unoriented polystyrene. Thus the width of the specimen must not exceed 0.8 cm. The gauge length is the distance (2.0 cm to 4.5 cm) between the sample holders mounted on the pullrods.

4.1.2 Preparation of Unoriented Sample

The tensile bars are made by cutting from molded polystyrene platelets. The platelets are compression molded in a picture frame mold whose thickness equals the desired sample thickness. The tensile bars of unoriented polystyrene were prepared by the following procedures:

1. The polystyrene pellets were vacuum dried at room temperature for 24 hours to remove the moisture in the material.

2. The hot press was heated to 180 ^{o}C.

3. Weigh about 25 grams of vacuum dried pellets and place inside the picture frame mold of dimension 12.7 cm x 12.7 cm x 0.16 cm, which was sandwiched between two molding plates with polished surfaces.

4. The polystyrene sandwich was placed on the hot press and preheat at 180°C for ten minutes in order to melt the pellets.

5. Increase the force on the hot press to 1500 psi over a period of ten minutes, such that the molten pellets form a uniform platelet.

6. Release the force on the hot press, and turn off the heat source. The platelet was left in the mold, which was still sandwiched between the two parts of hot press, and wait for 10 hours to let the platelet cool down to room temperature, such that there was no residual stress.

7. Remove the platelet from the mold frame.

8. Cut the platelet into tensile bars of desired dimension: width = 0.78 cm and length = 5.5 cm by using a low speed water cooled diamond saw. The cut edges of the tensile bars were polished by stroking in the tensile direction with 600 grit sandpaper.

The density of the specimens ranged between 1.047 to 1.049 g/cm**3 as measured by the density gradient column method. The birefringence of the specimens was measured as zero, indicating there was no residual stress in them.

The preparation of PSBI samples was slightly more complicated than the above.

1. Weight equal weights of PS103 and PS108 pellets and add into an empty clean flask. Add toluene of reagent grade to the flask to make a 5wt.% polymer solution. Shake the solution for 24 hours to insure complete mixing of the two molecular weight polystyrenes at the molecular level. Transfer the polymer solution into a separatory funnel with a capillary end.

2. Fill a 1000 ml beaker with about 500 ml of methanol, which was then stirred with a magnetic stirrer. Force the polymer solution to exit from the separatory funnel as a thin stream into the methanol bath. This stream formed a fibril of polymer as the solvents were flushed out and wound around the whirlpool. This was essentially a wet-spinning procedure. Each 500 ml of methanol can coagulate 50 ml of polymer solution.

3. Remove the batch of coagulated polymer from the methanol bath and wash with fresh methanol several times. When the fibrils were broken into small chunks, place in fresh methanol again, and allow to soak for 24 hours.

4. The collected coagulated polymers were vacuum dried at room temperature for 10 hours, followed by at 40°C for 10 hours, and then at 60°C for 24 hours such that there was no residual solvent. Step-heating was necessary since fast removal of solvent would lead more porous polymers which would result visible holes in the sheets molded in the next step.

5. The resulting dried polymer was then molded into sheets of 0.0254 cm (0.001 in) thickness at 180°C. Lastly, these sheets were stacked together and molded into a platelet of thickness 0.16 cm as described above.

4.1.3 Preparation of Oriented Sample

The SAXS studies of the deformation behavior of oriented polystyrene are divided into two parts: (i) tensile direction is parallel to the initial molecular orientation direction, and (ii)

tensile direction forms different angles to the initial molecular orientation direction.

For the first part, the oriented samples were prepared by uniaxially stretching using an Instron tensile tester equipped with an environmental oven. This oven, a modification of that developed by Matsui (143) and Matsumoto (144), consists of an air oven containing radiant heaters and having also an external blower system which introduces varying mixtures of room air and heated air (see Figure 4-1). Further, Wust (145) developed a control system which automatically introduces a linear cooling rate (or heating rate) by adjusting the relative amounts of room air and heated air. Rates up to 4.5^{o}C/sec were attainable. A small background level of radiant heat was used to smooth out axial temperature variations. The temperature was monitored with a bare thermocouple in the air stream very near the sample. The stripes of unoriented polystyrene prepared in Section 4.1.2 were clamped between the grips in the Instron tensile tester. After the oven is heated to the desired stretch temperature and then waiting for ten more minutes to reach the equilibrium state, the samples are stretched to the desired draw ratio at constant cross-head speed. The drawn sample were quenched rapidly (within 30 seconds) by opening doors of the oven and subjecting them to room air.

For the second part of the experimental work, sheets of 4.8 cm by 4.8 cm dimension were cut from the isotropic platelet prepared by compression molding. The sheets were placed in a T. M. Long Biaxial Tester (T. M. Long Co., Inc., Somerville, New Jersey, USA) and

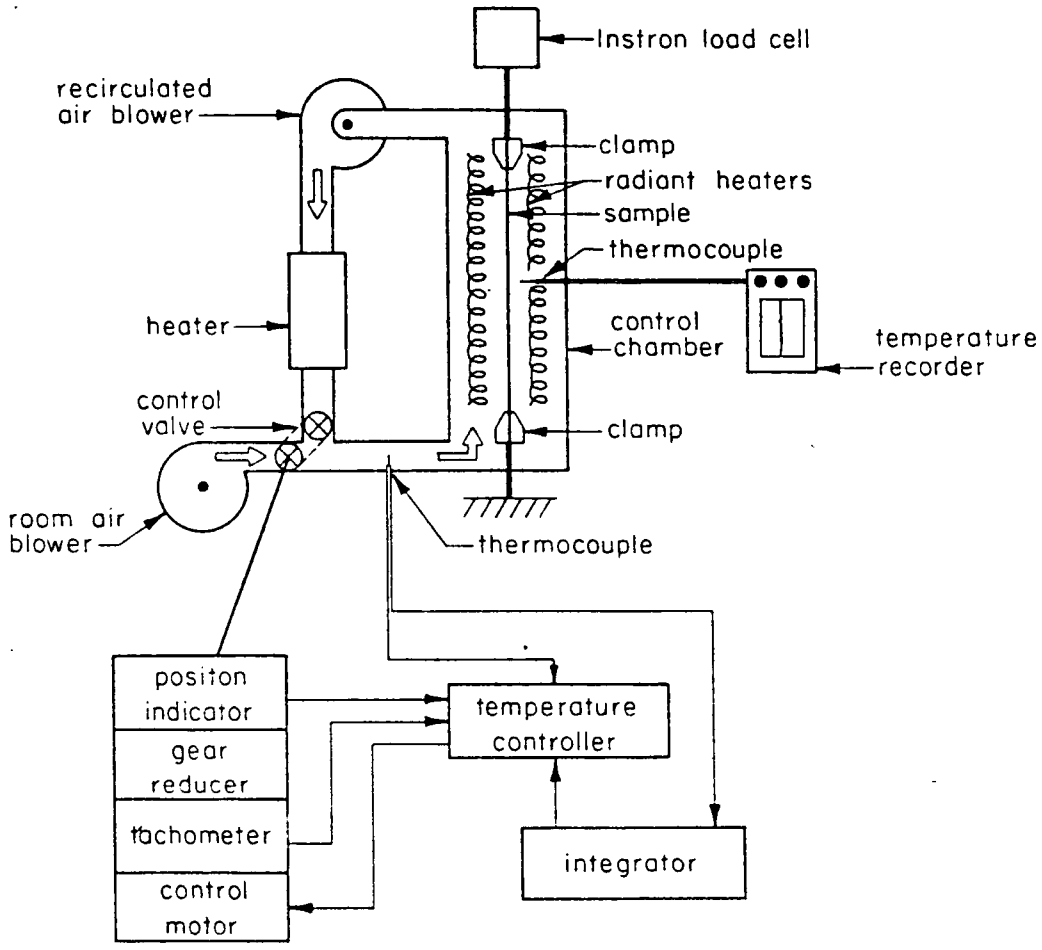


Figure 4-1. Schematic diagram of the environmental oven and associated control system (145).

uniaxially stretched at free transverse direction to the desired draw ratio. Stripes were cut from the drawn sheets at 15 degree angle increment to the machine stretching direction.

The orientation states in the samples were characterized by optical birefringence measurements at room temperature. The in plane (Δn_{12}) and out of plane (Δn_{23}) birefringence were measured in an instrument of the type devised by Stein (146). It consists of a light source, polarizer, spatially positioning sample holder, analyzer and a Babinet compensator mounted on an optical bench. The sample holder involves mounting the sample on a goniometer that may be rotated from 0° to 45°. $\Delta n_{12} = n_1 - n_2$ is measured at 0° with light perpendicular to the sample. Δn_{13} is obtained from tilting the sample and calculated by means of Stein's formula (146). The results showed that $\Delta n_{23} = \Delta n_{13} - \Delta n_{12}$ were usually slightly negative.

4.2 SAXS Apparatus

All of the SAXS measurements were performed at Oak Ridge National Laboratory (ORNL) using the National Center for Small Angle Scattering Research (NCSASR) 10-meter x-ray facilities (147). Figure 4-2 depicts the schematic drawing of the ORNL 10-meter SAXS camera. The design of the NCSASR SAXS instrument (147) is unusual in the use of the two-dimensional position-sensitive detector (2DPSD) and a high-speed interface between the detector and a minicomputer to record the two-dimensional data array. This unique feature makes the NCSASR SAXS camera especially useful for studies of anisotropic systems. In addition to that, a hydraulic deformation device and a double layer

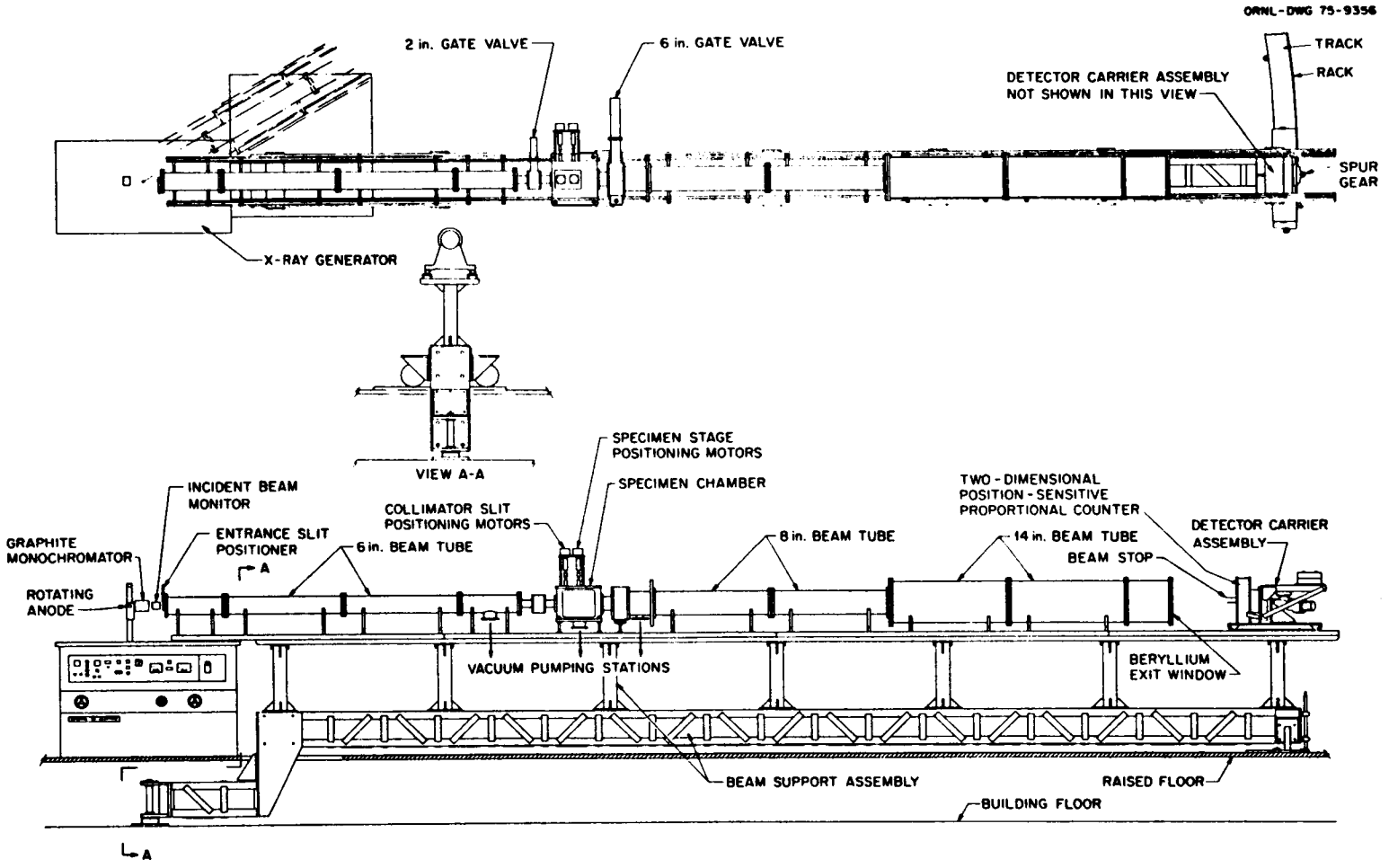


Figure 4-2. Schematic drawing of the ORNL 10-meter small-angle x-ray scattering camera (147).

enviromental chamber are equipped for the dynamic SAXS studies of material deformation and relaxation (148). Figure 4-3 is the schematic drawing of the deformation device which is interchangeable with the static sample chamber used in conventional SAXS. A brief description of this instrument is given below, more complete details are given in the original paper (147).

4.2.1 X-Ray Generator

The x-ray generator, manufactured by Rigaku-Denki, mainly consists of the power supply, rotating anode, and tungsten filament. With the x-ray source operating at 40 kV and 40 mA and a source to sample distance of 162 cm, the measured power through the collimation system can reach a typical value of 2.5×10^6 photons per second per square millimeter opening of the collimator with a newly changed filament, polished copper anode, and good alignment.

4.2.2 Monochromator

Monochromatization is very essential to obtain high-quality SAXS results. At ORNL, this is done by reflecting the characteristic K x-rays emitted by the copper anode off a small, flat piece of pyrolytic graphite crystal to select the α-component of K x-rays. The monochromator is mounted on a stage which can be translated and rotated into the beam emerging at a $\sim 6^{\circ}$ take off angle from the x-ray generator, and can be tilted about a horizontal axis to make the diffracted beam horizontal. The exit angle of x-ray from the generator with respect to the collimation apparatus is adjusted to optimize the flux.

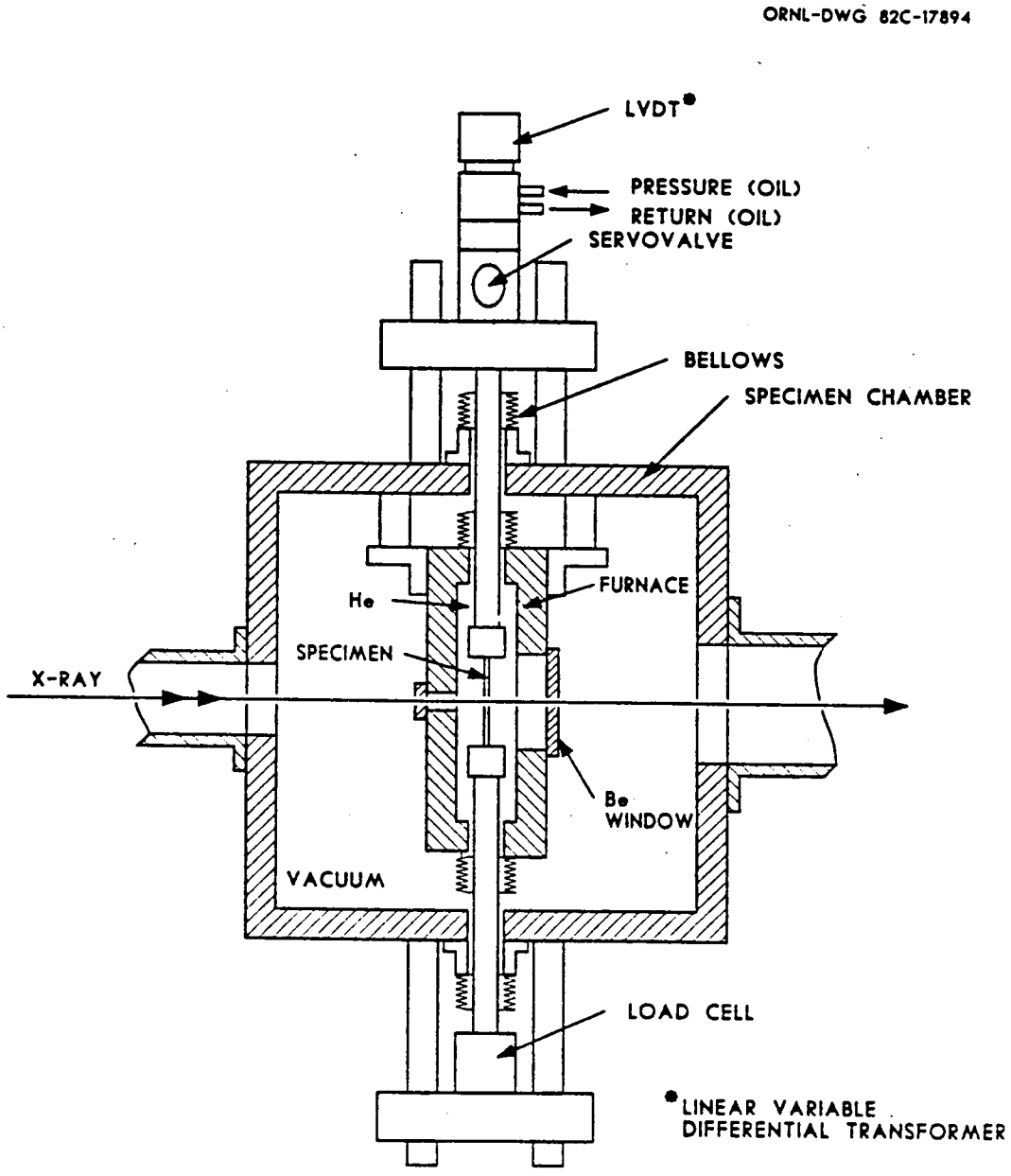


Figure 4-3. Schematic drawing of the deformation device on the ORNL 10-meter SAXS camera (148).

4.2.3 Collimator

The collimation system consists of two pinholes separated by 154 cm. The first is a 1-mm-diam hole in a lead sheet mounted on an x-y positioning stage in the front of the beam line. The second consists of a set of four specially polished tungsten edges mounted to make a 1-mm square hole. These edges have surfaces parallel to the incident beam cut to make an inclined angle of 88° with the plane perpendicular to the incident beam. This hole is mounted on an x-y positioning stage located inside the specimen chamber. The flight path between the holes consists of sections of 0.5- or 1.0-m lengths of 15-cm-diam aluminun pipes bolted to unistrut rails.

4.2.4 Specimen Chamber and Dynamic Device

The specimen chamber for dynamic SAXS measurements consists of a 30 x 30 x 35 cm vacuum chamber containing an externally operated x-y positioning devices for the second pinhole and a dynamic deformation device (148). The positioners are driven by a pair of stepping motors which may be controlled manually or via the computer. A piece of glassy carbon (recently it was replaced with a carbon black-polyethylene composite) is installed on a sliding mechanism mounted on the second pinhole stage. By use of a stepping motor equipped with an eccentric cam, the glassy carbon can be reproducibly moved into the incident beam or out of the beam. The intense glassy carbon scattering is measured periodically as a second check on the incident beam intensity, and the attenuation of intensity by placing the sample in the beam is measured to determine the transmission coefficient of the specimen.

The sample is mounted and gripped between the two clamps (jaws) of the moving arms of the dynamic deformation device (Figure 4-3). The load cell is attached to the lower arm which is fixed at the bottom. The force exerted on the sample during deformation is monitored by the load cell. The upper arm is connected to a servovalve which is activated by a hydraulic system (Terra Tek Inc.). A linear variable differential transformer (LVDT) is mounted on the upper driving arm in order to observe the displacement. The deformation device can be operated either via CAMAC dataway (Computer Automated Measurement And Control) through a programmable function generator for system control (force or displacement) and fast data acquisition or via manual control. Since the deformation behavior of glassy polymers is an irreversible process, a step increase in load is achieved by manual operation.

The deformation device is also equipped with an environmental chamber which consists of two compartments. The outer compartment is made of aluminum which is designed with identical dimensions with that of the existing one and is usually operated under vacuum. The inner compartment is made of brass with two beryllium windows for the x-ray path. Since all of the deformation experiments were performed at room temperature, the environmental chamber is not installed in this investigation.

The flight path from the specimen chamber to the detector consists of 0.5- and 1.0-m lengths of 20- and 35-cm-diam vacuum pipes. Scattered radiation travelled through this beam line and a 30-cm-diam 5-mm-thick beryllium window in the end. The incident beam stop is

attached with wax on the center of the exterior of the beryllium window. To decrease the time necessary to evacuate the system after changing specimens, the specimen chamber is isolated from the collimation and scattering beam lines by electropneumatic gate valves. Each of the three sections is separately pumped to a vacuum of $< 10\ \mu m$ Hg.

4.2.5 Detector

The detector is a two-dimensional position-sensitive proportional counter developed by Borkowski and Kopp (149). Physically, it is cased in a round aluminum disk of 40 cm in diameter and 10 cm deep, with an active area of 20 x 20 cm having 64 x 64 resolution elements. It is mounted on a small dolly which can travel the length of the unistrut rails under manual control. The detector is positioned just touching the beryllium window on the flight path. The data array, which is represented as 64 x 64 matrix, is recorded in the memory of the minicomputer by a high-speed interface which uses a microprocessor to map the digitized x-y position of the incident photon into an allocated minicomputer memory address. A maximum of 2^{16} events can be recorded per channel before overflow occurs, because the minicomputer is a 16-bit computer and data are stored in the digital form.

4.2.6 Computer

A Modular Computer Systems ModComp II/220 CP computing system is employed as the on-line computer system for the collection, manipulation, and display of the data recorded by the 2DPSD. A

Tektronix Model 4014-1 Graphics Terminal with a 48-cm display screen is employed as the graphics display system.

4.3 Analysis of Data and Computer Programs

4.3.1 Introduction: Software for the ORNL 10-m SAXS Instrument

In the following sections the processing of experimental data is surveyed. The description is centered around the FORTRAN computer programs which have been developed as a complement of software for the ORNL 10-meter SAXS instrument. This special software can be divided into four categories: (1) operating system, (2) data acquisition control program, (3) data base file management system, (4) data plotting and analysis programs. Some additional programs that were used specifically for the system under study will be mentioned in Section 4.3.5.

4.3.2 Data Acquisition and Instrument Control

Three high-priority foreground tasks called OVF, MOT, and SAX are responsible for all aspects of data acquisition and instrument control. The task OVF performs two functions. First, it loads the absolute starting address of a 200-word overflow buffer array into a dedicated memory location. Second, it examines the critical overflow address buffer (i.e. the 190th word of the array) regularly in every 10 ms, independently of the activity of all other programs simultaneously in execution. Without such control, at high data flow rates the custom hardware instruction could overwrite all of the core, including the operating system, with overflow address.

The task MOT controls the movements of two pairs of stepping motors which drive the x-y positioning devices for the second pinhole and the x-y positioning devices for the sample stage (in static sample chamber only), respectively.

The task SAX is an interactive program which communicates with the user in simple English. Its various directives provide complete control of the camera functions among which are (a) enter header record that contains the necessary identification or information regarding any particular measurement; (b) start and stop data acquisition; (c) zero data array; (d) save data (header record and the 64 x 64 data array recorded by the 2DPSD); (e) move motors; (f) enable and disable various interrupts; and (g) print experiment status reports. All the commands in the data acquisition may be entered from a user's console or read from a disc file written in advance.

4.3.3 Data Base File Management

Because of the limited storage available for the data base on the ModComp disc, a FORTRAN direct access data base management system has been developed. It includes three programs, namely, MANAGER, FETCH, and SAVE in which the contents of the data base can be displayed and the remaining space can be estimated; independent experiments with variable data array sizes can be transferred from the on-line data base disc through the memory core of the computer onto a separate data base disc for permanent storage and vice versa; the data array can be stored on an on-line storage disc, fetched from the storage disc back

to the memory core of the computer for further analysis, deleted, and otherwise manipulated. Additional software, programs PDP and I27, have been written to allow an individual experiment to be transmitted to the on-line data base in the central time-sharing PDP-10 computer. The experimental data can then be transferred to the user's own magnetic tapes for permanent storage and further analysis.

4.3.4 Data Plotting and Analysis Programs

A FORTRAN interface package has been developed which allows all plotting on the Tektronix graphics terminal to be coded with standard CALCOMP subroutines. Further, some powerful plotting packages have been developed. CR4CON is a two-dimensional isointensity contour plotting program. INTRIGUE is a general-purpose plotting package designed to make linear, logarithmic, and semi-logarithmic plots. Hard copies of the plots seen on the Tektronix screen can be obtained from the on-line hardcopier or by transmitting them to the central computer for better quality ink hard copies.

The SAXS data recorded by the 2DPSD can be reduced and analyzed via the proper execution of the following background FORTRAN programs which are developed for the users.

FILE enables the user to fetch data from the disc storage to the data analysis array of the computer to analyze previously saved runs, to save the processed data back to the disc storage, or to copy the contents of the data acquisition array into the analysis array to examine data currently being taken.

BKC enables the user to correct the raw data for empty beam backgrounds, dark current, and for possible sensitivity variation of the detector.

CONTOUR enables the user to perform two-dimensional contour plots, find the beam center, set the range for radial average, and compute the linear averaging intensity along a slice of variable width at arbitrary azimuthal angles.

RADIAL enables the user to perform the circular averaging routine for producing intensity versus scattering angle data for isotropic scatterers.

4.3.5 Analysis of Data

4.3.5.1 Background and Dark Current Correction

The instrument backgrounds and the dark current in the detection system are determined in separate runs. The instrument backgrounds are determined by recording the scattering data with no sample in the beam at the same operating power for an extensive time period (usually no less than 1000 seconds at operating power of 40 kV, 40 mA). A typical background scattering contour plot is shown in Figure 4-4. This pattern was taken at 40 kV, 40 mA with sample to detector distance of 5 meters and a measuring time of 1000 seconds. In some cases (for example, running a liquid sample), the background intensity must be taken with a control sample (e.g., the liquid sample cell) in the beam.

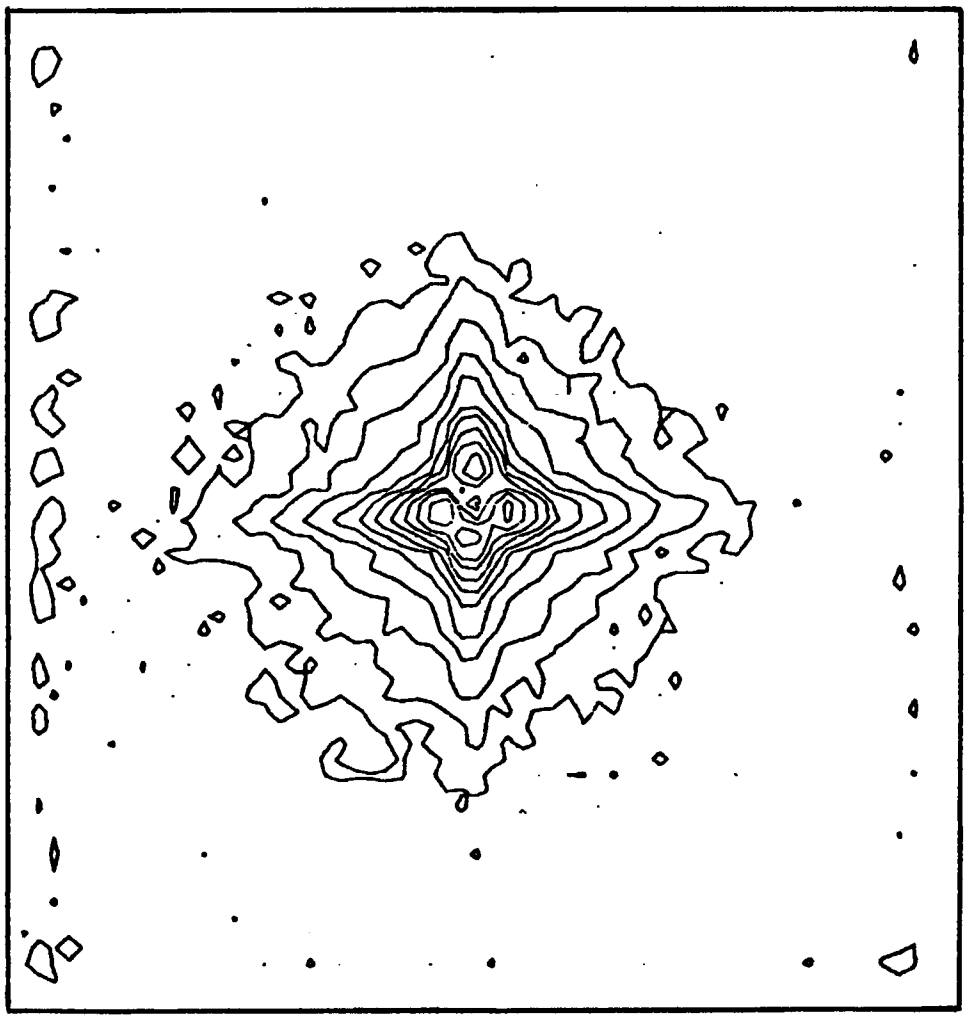


Figure 4-4. Typical background scattering contour plot.

The dark current consists of the radiation events that originate in cosmic radiation and electronic noise. The dark current is determined by recording the counts with the two specimen chamber gate valves shut at the same operating power for an extensive time period (usually no less than 1000 seconds). The dark current intensity is low, usually an integral count rate of 21 to 24 counts per second over the 4096 channel elements were recorded. The fluctuation of this value depends on the neighboring environment of the SAXS laboratory.

The instrument backgrounds and the dark current must be subtracted from the raw data of the specimen run. This can be done by executing program BKC. BKC calculates:

$$P_{NET,i} = [P_{RAW,i} - P_{DC,i} \times \frac{SMON}{CMON}] - \frac{TS}{TBAC} \times \frac{SMON}{BMON} \times [P_{BAC,i} - P_{DC,i} \times \frac{BMON}{CMON}]$$

where

P_i: number of photons registered at element i of 2DPSD during the run

P_{NET}: background corrected counts of scattering from specimen

P_{RAW}: raw counts of specimen run

P_{DC}: counts of dark current run

P_{BAC}: counts of empty beam run

SMON: beam monitor counts during specimen run

CMON: beam monitor counts during dark current run

BMON: beam monitor counts during an empty beam run

TS: transmission coefficient of the specimen

TBAC: transmission coefficient of background which is one for an empty beam

The detector has 64 x 64 virtual resolution elements, and the above corrections are performed element by element.

4.3.5.2 Detector Sensitivity

The sensitivity of the detector is determined by placing a radioactive iron-55 (Fe-55) isotope in the specimen position and recording the intensity with the x-ray source to specimen chamber gate valve shut. The measuring time normally is no less than 20,000 seconds so that over four million counts are registered for better statistics. The iron-55 isotope produces an integral count of 190 counts per second. The spatial distribution of this radiation (see Figure 4-5) is a measure of the non-uniformity in sensitivity of the detector, as well as the shadowing effect of the aluminum grid, which supports the exit beryllium window, and the beam stop. All scattering patterns should be corrected for this non-uniformity by dividing by the normalized sensitivity pattern. With the proper command BKC, BKC calculates:

$$P_i = P_{NET,i}/S_i,$$

where

$$S_i = P_{SEN,i}/S_{AVE},$$

with $P_{SEN,i}$ being the counts of iron-55 run at channel i and S_{AVE} the average intensity of the iron-55 run per channel.

4.3.5.3 Transmission Coefficient

The transmission coefficient is defined as the ratio of the intensity transmitted through the specimen to the incident x-ray power:

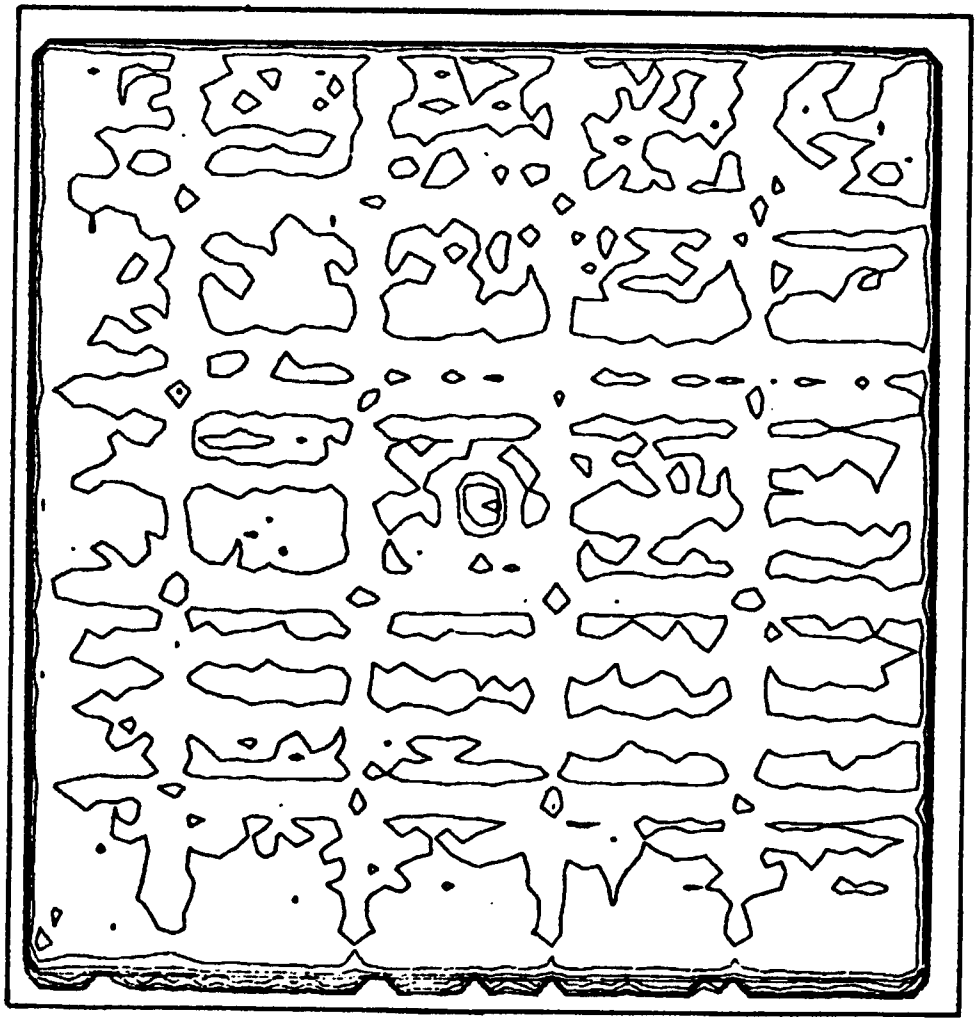


Figure 4-5. Spatial distribution of the iron-55 radiation on the two-dimensional detector plane.

$$TS = P_{trans}/P_o = \exp[-\mu_\ell t],$$

where t is the thickness of the specimen and μ_ℓ the linear absorption coefficient of the specimen which depends on its chemical composition and mass density.

At ORNL SAXS laboratory when this investigation was carried out in the beginning, the transmission coefficient was measured by the following procedures:

1. Set the x-ray generator voltage and current to 15 kV and 6 mA respectively.

2. Measure the glassy carbon intensity over a period of 100 seconds with no sample in the beam (ICARBON).

3. Measure the intensity over the same period with the sample mounted in the beam (ICSAM).

4. Measure the dark current over the same period (IDC).

5. Remove the glassy carbon and measure the intensity scattered by the sample alone (ISAM).

If ISAM < 0.1 x ICARBON, this means we have a weakly scattering system, the transmission coefficient is calculated by:

TS = [ICSAM - IDC]/[ICARBON - IDC].

Otherwise, the transmission coefficient is calculated by:

TS = [ICSAM - 0.37 x ISAM]/ICARBON

where 0.37 is the transmission coefficient of the glassy carbon used.

During the time period when the experimental work was performed at ORNL SAXS laboratory, two modifications for the transmission coefficient measurements have been done. First, the glassy carbon is

replaced by a piece of carbon black-polyethylene composite. The intensity of the composite is low enough that all of the intensity measurements can be performed at the same operating power for specimen run and the experimental error caused by setting the operating power slightly different between each run can thus be avoided. Second, it was found that placing the sample after the glassy carbon (i.e. normal sample position) during transmission coefficient measurements could overestimate the value for strongly scattering systems such as Lupolen. Therefore, mounting the sample before the first pinhole during the measurements was suggested and this has proved to be satisfactory.

4.3.5.4 Analysis for Isotropic Systems

The typical procedure for data analysis at ORNL SAXS laboratory is accomplished in the following steps.

1. If the data sets are stored on an off-line data base disc, program MANAGER is excecuted to onload the data sets to on-line disc storage.

2. Program FILE is executed to fetch data from the disc storage to the data analysis array of the computer.

3. Program BKC is executed to correct the data for empty beam background, dark current, and detector sensitivity.

4. Program CONTOUR is executed to plot the two-dimensional contour pattern, set the beam center, and fix the limits for radial average.

5. Program RADIAL is executed to calculate the radial average intensity.

6. The radial average intensity data are transmitted to author's magnetic tape through the central PDP-10 computer at ORNL.

The data are then transferred to the on-line disc storage of the central DEC-10 computer at UTCC (University of Tennessee Computer Center) for further analysis which is based on the FORTRAN program FFSAXS3 developed by Vonk (150). Three subroutines were used, namely, SMOOTH, BACKGR, and INVARI. The functions of each subroutine are described below.

1. Subroutine SMOOTH smooths and interpolates the scattering intensity data.

2. Subroutine BACKGR computes on the basis of a two-phase approximation for the system. The scattering curve is fitted to Porod's law $(2\pi)^4 Kp/s^4 + K_L$. The fit is made by least-squares method. The background K_L is eliminated from the scattering intensity for further analysis.

3. Subroutine INVARI calculates the values of $(1/2\pi)^3 \cdot \int_0^\infty 4\pi s^2 I(s) ds$. This program uses a Gaussian approximation to extrapolate the scattering intensity to s = 0.

4.3.5.5 Analysis for Crazed Systems

For the analysis of crazed systems, all of the 64 x 64 data array after correction of empty beam background, dark current, and detector sensitivity are transmitted to authour's magnetic tape for further analysis. The principle of analysis is based on the discussion presented in Chapters 6 to 8. The programs named SAXS, TOTAL, and GAMMA are listed in Appendices A to C.

CHAPTER 5

ABSOLUTE INTENSITY MEASUREMENT OF SAXS AT ORNL AND THE ORIGIN OF SAXS FROM UNDEFORMED POLYSTYRENE

The Lupolen platelet designated as 23/7 was used as a calibration standard to determine the absolute scattered intensity from various materials under investigation. This chapter deals mainly with work done at ORNL using the NCSASR 10-meter x-ray facilities (136). Calibration expressions are derived for different geometries of the camera system. The applications of absolute intensity measurement such as the calculations of the invariant, thermal frozen-in density fluctuations and concentration of inhomogeneities are briefly discussed for amorphous polystyrene. It is concluded that the origin of small-angle x-ray scattering in polystyrene can be attributed mostly to the foreign particles present in the polymer and the thermal frozen-in electron density fluctuation is only slightly molecular weight dependent.

5.1 Introduction

The study of the structure of a substance can be based on the diffraction phenomena caused by the interaction of electrons in materials with electromagnetic radiation. X-rays of wavelength about 1 $\mathring{A}$ are usually used for this purpose. A beam of x-rays falling on an assembly of atoms will interact with the shell electrons of atoms and will thereby be scattered. Small-angle x-ray scattering (SAXS) techniques have been commonly used for the study of structural

inhomogeneities on the level of ten to several thousand Angstroms. The importance of absolute intensity measurements has been recognized in the past, and a wide variety of techniques and applications have been reported (128, 151 - 152).

The purpose here is to get normalization expressions for the absolute intensity measurement in the NCSASR 10-meter SAXS camera. This will be done by using Lupolen 23/7 as a calibration standard. Next, several example applications will be illustrated.

5.2 Definition of Absolute Intensity

The term absolute intensity in SAXS has been defined in several ways:

(1) the ratio of the scattered intensity to the incident beam intensity (e.g. 151, 153);

(2) the ratio of scattered intensity from the sample to that from a single classical electron under identical conditions and at the same angle, called the "electron units" (e.g. 154);

(3) the ratio of the number of x-ray photons (or neutrons) scattered into a unit solid angle (Ω) per second per scattering entity to the incident beam, called the differential scattering cross section with units of cm**2/scatterer and denoted by $d\Sigma/d\Omega$ (e.g. 128, 155).

All definitions require the determination of the power of the incident beam. Generally the methods for determining the power of the primary beam can be classified into two groups: (A) direct attenuation of the incident beam using absorbing filters (156) or

mechanical devices (157), and (B) indirect measurement of the scattering power from a calibration standard including gas (158), liquid (159) and solid (153, 160 -163) samples. Before discussing the calibration procedure and applications we should like to define what we consider the essential relationships to be employed in the calibration procedure for the scattering of a sample of arbitrary structure.

Classical electromagnetic theory (119, 124) gives the coherent scattering intensity of a free electron under unpolarized incident x-rays as

$$I_{el}(\vec{s}) = \frac{Po}{L^2}\left(\frac{e}{mc^2}\right)^2 f_\theta^{\,2} \qquad \text{Eq.(5-1)}$$

where $\vec{s}$ is the reciprocal space scattering vector ($|\vec{s}| = 4\pi\sin\theta/\lambda$), 2θ is the scattering angle, λ is the wavelength of incident x-rays, Po is the power of the incident x-ray beam, L is the distance from the emitting electrons to the point of observation, e = 4.8029E-10 esu is the charge of an electron, m = 9.108E-28 gm is the mass of a rest electron, and c = 2.99793E10 cm/sec is the velocity of light. $f_\theta^{\,2} = (1 + \cos^2 2\theta)/2$ is the polarization factor which is almost equal to one for SAXS. The value of $i_e = (e^2/mc^2)^2 = 7.94030E\text{-}26\ cm^2$ was first calculated by Thomson (127) and is called the Thomson factor. It is a measure of the effective cross section for the scattering of electromagnetic waves by an electron provided that, besides the excited vibration of the electron, no other absorption effects occur.

Now, if we have a collection of electrons whose density distribution is given by $\rho(\vec{R})$ and if they are excited by the same primary wave as in Eq.(5-1), then the observed coherently scattered intensity, P_{obs}, is given by (124)

$$P_{obs}(\vec{s}) = (Po/L^2)\cdot i_e \cdot f_\theta^2 F(\vec{s})F^*(\vec{s}) \qquad \text{Eq.(5-2)}$$

where

$$F(\vec{s}) = \int_o^\infty \rho(\vec{R})\exp[-i\cdot(\vec{s}\cdot\vec{R})]dv_R$$

$F^*(\vec{s})$ = conjugate of $F(\vec{s})$

$\vec{R}$ = a position vector in real space.

Eq.(5-2) points out the first step to be taken in a structural analysis. Besides the factors i_e and f_θ^2, which are independent of the density distribution of the scattering matter, and another factor Po/L^2, which depends on the experimental arrangements, the coherently scattered intensity contains the important factor FF* which alone depends on the electron density distribution function $\rho(\vec{R})$. This important factor is called the absolute intensity function I_{eu}

$$I_{eu}(\vec{s}) = F(\vec{s})\cdot F^*(\vec{s}) = P_{obs}(\vec{s})/I_{el}(\vec{s}). \qquad \text{Eq.(5-3)}$$

I_{eu} is expressed in electron units. From this definition, the differential x-ray scattering cross section and the absolute intensity in electron units are related by (128)

$$\frac{d\Sigma(\vec{s})}{d\Omega} = \frac{d\Sigma_{el}}{d\Omega}\cdot f_\theta^2 I_{eu}(\vec{s}) \qquad \text{Eq.(5-4)}$$

where

$$\frac{d\Sigma_{el}}{d\Omega} = i_e.$$

It is assumed everywhere in what follows that P stands for observed intensity in arbitrary units and I in absolute units

$$I(\vec{s}) \; [=] \; \text{eu} = \text{electron}^2$$

and the subscript eu will be dropped hereafter.

From these definitions, it can be seen that the definition used by Kratky (153) is not independent of the experimental conditions and thus does not easily allow interlaboratory comparison of data from the same kind of material.

5.3 Lupolen As A Calibration Standard

The application of the Lupolen (polyethylene) platelet as a standard sample for the absolute SAXS intensity measurement was first introduced by Kratky and his coworkers (153, 160 - 161). The power of the primary beam is determined first with a direct method and then the scattering intensity of Lupolen platelet is measured corresponding to this incident beam. More specifically the scattering intensity of Lupolen at an angle of $2\theta = 35.3'$, corresponding to a Bragg's value of 150 $\mathring{A}$ is chosen for further comparison (153). This angle is selected because of the linearity of the scattering curve in this region. With the help of this calibrated sample, the absolute intensity of the incident beam or the intensity scattered by any object under investigation can then be obtained by a simple comparison method.

5.4 Experimental

The experiments were performed at the Oak Ridge National Laboratory using the 10-meter x-ray small-angle scattering camera

(147). This instrument consists of a rotating anode x-ray source, pinhole collimation, a two-dimensional position-sensitive proportional counter (149), and a mini-computer system for data acquisition and analysis. The camera geometry used is given in Table 5-1. The system was constructed in such a way that the change in the angular range can be achieved by lengthening or shortening the aluminum beampath between the sample chamber and the detector. All measurements were carried out at room temperature.

The Lupolen was designated as 23/7 and provided by Anton Paar Co., Graz, Austria. The platelet has been pretreated thermally in order to achieve homogenization and has been proven to be thermally, chemically and physically stable and unaffected by long exposures to x-rays (153). It has a uniform thickness of 2.73 mm.

The transmission coefficient of the sample is obtained by the transmission measurement,

$$TS = \exp[-\mu_{\ell} t] = P_{trans}/Po.$$

where μ_{ℓ} is the linear absorption coefficient, t the thickness of the sample, P_{trans} the transmitted intensity and Po the incident x-ray power.

The empty camera background scattering and the electronic noise in the detector system were determined in separate runs. The sensitivity of the detector was determind by placing a radioactive iron-55 isotope at the sample position in the sample chamber and counting the uniformly distributed intensity.

Table 5-1

Geometries of the ORNL SAXS camera
used in the Lupolen calibration measurement

	Long Geometry	Short Geometry
Wavelength	1.5417 $\mathring{A}$	1.5417 $\mathring{A}$
X-Ray Source	CuKα	CuKα
First Collimator Size	1 mm in diameter	1 mm in diameter
Second Collimator Size	1 mm x 1 mm	1 mm x 1mm
Collimator-Collimatior Distance	1540 mm	1540 mm
Sample-Source Distance	1620 mm	1620 mm
Sample-Detector Distance	5048 mm	1120 mm
Detector Element (Channels)	64 x 64	64 x 64
Channel Conversion	0.324 channel/mm	0.324 channel/mm
Beam Stop Size	8 mm x 8 mm	10 mm x 5 mm
s Range	0.0022 - 0.1 $\mathring{A}^{-1}$	0.04 - 0.5 $\mathring{A}^{-1}$

5.5 Data Analysis

From Eq.(5-2) and Eq.(5-3) it follows that for every scattering vector $\vec{s}$ there is an intensity $I(\vec{s})$ associated with it. The intensities can be found on the surface formed by intersecting the Ewald's sphere (130) with the intensity I(s), as shown in Figure 3-2. For small-angle scattering where $|\vec{s}| < 0.1\ \mathring{A}^{-1}$ the sphere may usually be approximated by its tangent plane at the origin of the reciprocal space. Then, the SAXS pattern is determind by a plane section of the intensity figure.

Consider now the two-dimensional scattering pattern in an orthogonal coordinate system. $\vec{u}_1$, $\vec{u}_2$, $\vec{u}_3$ are the orthogonal unit vectors in reciprocal space, where $\vec{u}_2$ is in the direction of incident x-ray beam. Then $\vec{s}$ can be represented as (s_1, s_2, s_3):

$$\vec{s} = s_1 \cdot \vec{u}_1 + s_2 \cdot \vec{u}_2 + s_3 \cdot \vec{u}_3 . \qquad \text{Eq.(5-5)}$$

We also have to consider the absorption effect of the sample. Assuming a sample with a linear x-ray absorption coefficient μ_ℓ in the form of a platelet of thickness t, the scattering intensity, P_{obs}, detected by a two-dimensional detector plane is given by

$$P_{obs}(s_1, 0, s_3) = Po(\frac{a}{L^2}) \cdot t \cdot \exp[-\mu_\ell t] \cdot i_e \cdot I(s_1, 0, s_3) \qquad \text{Eq.(5-6)}$$

where a is the area of a detector resolution element and Po is the flux of the primary beam on the detector plane as measured under the same conditions of the experiment.

For an isotropic system displaying a scattering pattern with rotational symmetry, Eq.(5-6) can be reduced into

$$P_{obs}(s) = Po(\frac{a}{L^2})\cdot t\cdot\exp[-\mu_{\ell}t]\cdot i_e\cdot I(s) \qquad \text{Eq.(5-7)}$$

with $s = |\vec{s}|$. An important parameter used to characterize the system without the need of making any further assumptions is the integral intensity, usually called the "invariant" (74):

$$K = (1/2\pi)^3\cdot\int_o^\infty 4\pi s^2 I(s)\cdot ds$$
$$= \int_o^\infty 4\pi b^2 I(b)\cdot db \qquad \text{Eq.(5-8)}$$

where $b = s/2\pi = 2\sin\theta/\lambda$. For a two phase system,

$$K = (\rho_1 - \rho_2)^2 x_1\cdot x_2 \qquad \text{Eq.(5-9)}$$

in which x_1 and x_2 are the volume fractions of the phases with electron densities ρ_1 and ρ_2, respectively. Both phases are supposed to be internally homogeneous.

The raw scattering data obtained experimentally can be reduced and analyzed via the NCSASR SAXS Programs. The raw scattering data were first corrected for instrumental background and dark current counts according to the relation:

$$P_{NET} = [P_{RAW} - P_{DC} * \frac{SMON}{CMON}] - \frac{TS}{TBAC} * \frac{SMON}{BMON}[P_{BAC} - P_{DC} * \frac{BMON}{CMON}]$$

Eq.(5-10)

where P_{NET} is the background corrected intensity, P_{RAW} is the raw scattering intensity from specimen, P_{DC} is the dark current counts, SMON is the beam monitor counts during the scattering run of the sample, CMON is the beam monitor counts during the dark current run, TS is the transmission coefficient of the sample, TBAC is the transmission coefficient of the background run, BMON is the beam

monitor counts while measuring background scattering, and P_{BAC} is the background scattering intensity. The background corrected data were then corrected for the uniformity of the detection efficiency of each detector channel element. Then the sensitivity corrected data were plotted as a two-dimensional contour plot and the center of the scattering pattern was set. For an isotropic scattering system, the scattering data can be radially averaged using a program called RAD. The radially averaged data, P_{RAD}, were normalized to 1000 beam monitor counts and were divided by its transmission coefficient. In order to convert P_{RAD} into correct units used in Eq.(5-7), we have to do the following normalization,

$$P_{obs}(s) = P_{RAD}(s)*(SMON/1000)*TS/(\text{counting time in seconds})$$

$$[=] \text{ counts/second/channel}^2.$$

Then the absolute scattering intensity can be obtained by

$$I(s) = \frac{P_{obs}(s)}{Po \cdot t \cdot \exp[-\mu_\ell t] \cdot i_e \cdot a/L^2}$$

$$[=] \text{ eu/Ang**3} = 10E24 \text{ eu/cm**3} \qquad \text{Eq.(5-11)}$$

5.6 Calibration Procedure

5.6.1 Calibration for Long Geometry

The power in the incident beam, i.e., the number of x-ray photons per unit cross-sectional area, was directly determined by the multiple nickel foil technique (156), according to the absorption equation,

$$P_{trans} = Po \cdot \exp[-\mu_\ell t].$$

With removal of the beam stop, the tramsmitted intensity can be measured by placing a set of nickel foils with uniform thickness of 0.001 inch in the beam path to attenuate the intensity of the primary beam. The measured intensity was corrected for the dark current P_{DC} and the dead time τ of the detector and its associated counting electronics according to

$$P_{trans} = \frac{P_{obs} - P_{DC}}{1 - (P_{obs} - P_{DC})*\tau}$$

where τ = 7E-6 sec. Then P_{trans} was plotted against the thickness of the nickel foils, as shown in Figure 5-1. The power of the incident beam, determined from the intercept, was 2.505E+6 counts/(sec*mm^2). This value depends on the size of the collimator openings.

The two-dimensional contour plot of the scattering data of Lupolen 23/7 measured with long geometry is shown in Figure 5-2. The radially averaged scattering data of Lupolen 23/7 measured with the long geometry are plotted on Figure 5-3 in units of cps/channel^2. Two curves are shown, curve 1 corresponds to the measurement performed immediately after the direct determination of Po and curve 2 is one of the data taken during later experiments. From Eq.(5-7), the absolute scattering intensity of Lupolen $I_c(s = 0.042\ \mathring{A}^{-1})$, corresponding to an angle of 2θ = 35.3′ (Bragg's value of 150 $\mathring{A}$), is given by

$$I_c(s = 0.042\ \mathring{A}^{-1}) = \frac{P_c(s = 0.042\ \mathring{A}^{-1})}{Po \cdot t \cdot \exp[-\mu_\ell t] \cdot i_e \cdot a/L^2}$$

or

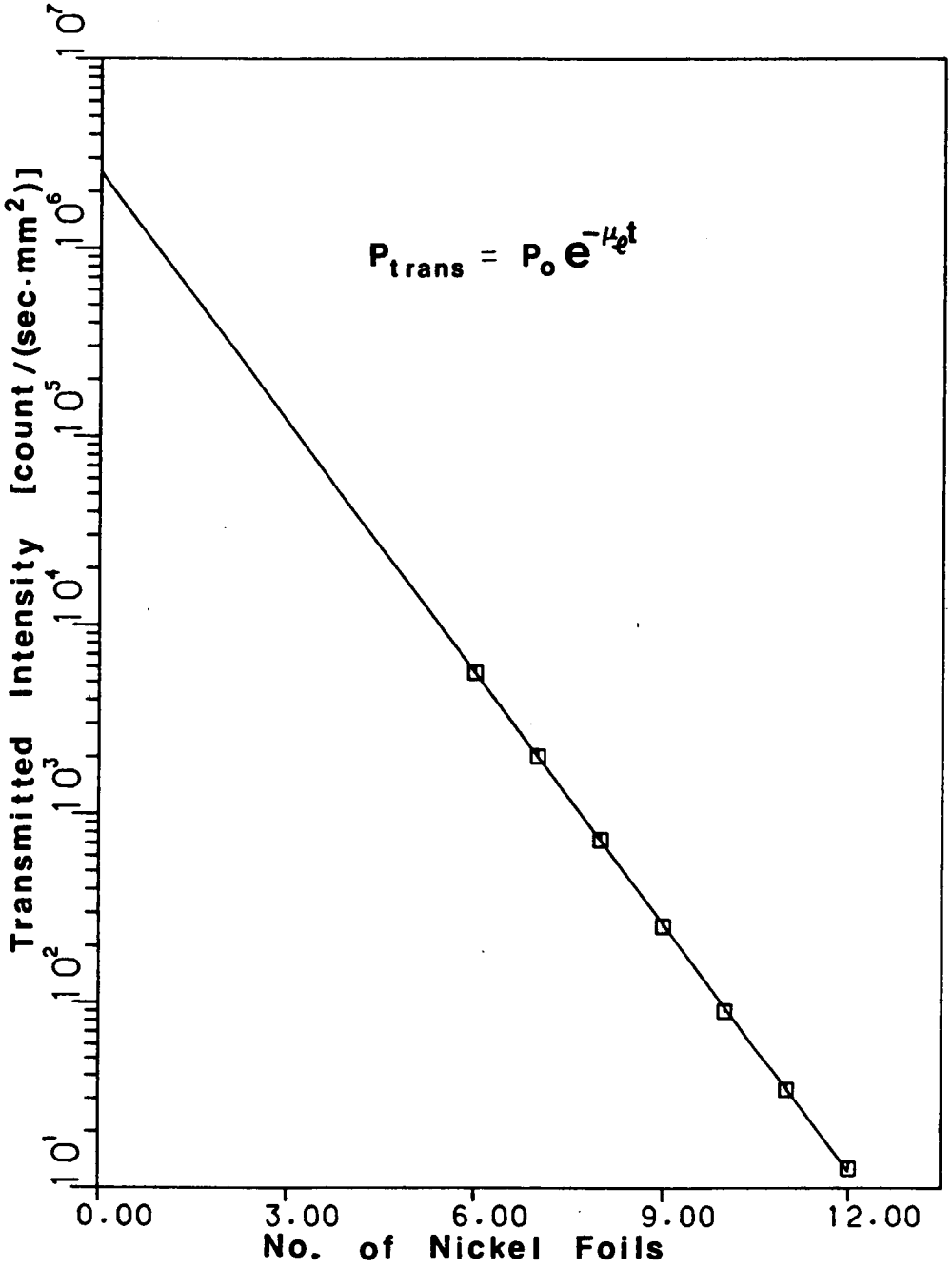


Figure 5-1. Transmitted intensity versus number of nickel foils. Measuring condition: long geometry, 40 mA, 40 kV, and room temperature. The thickness of nickel foil is 0.001 inch.

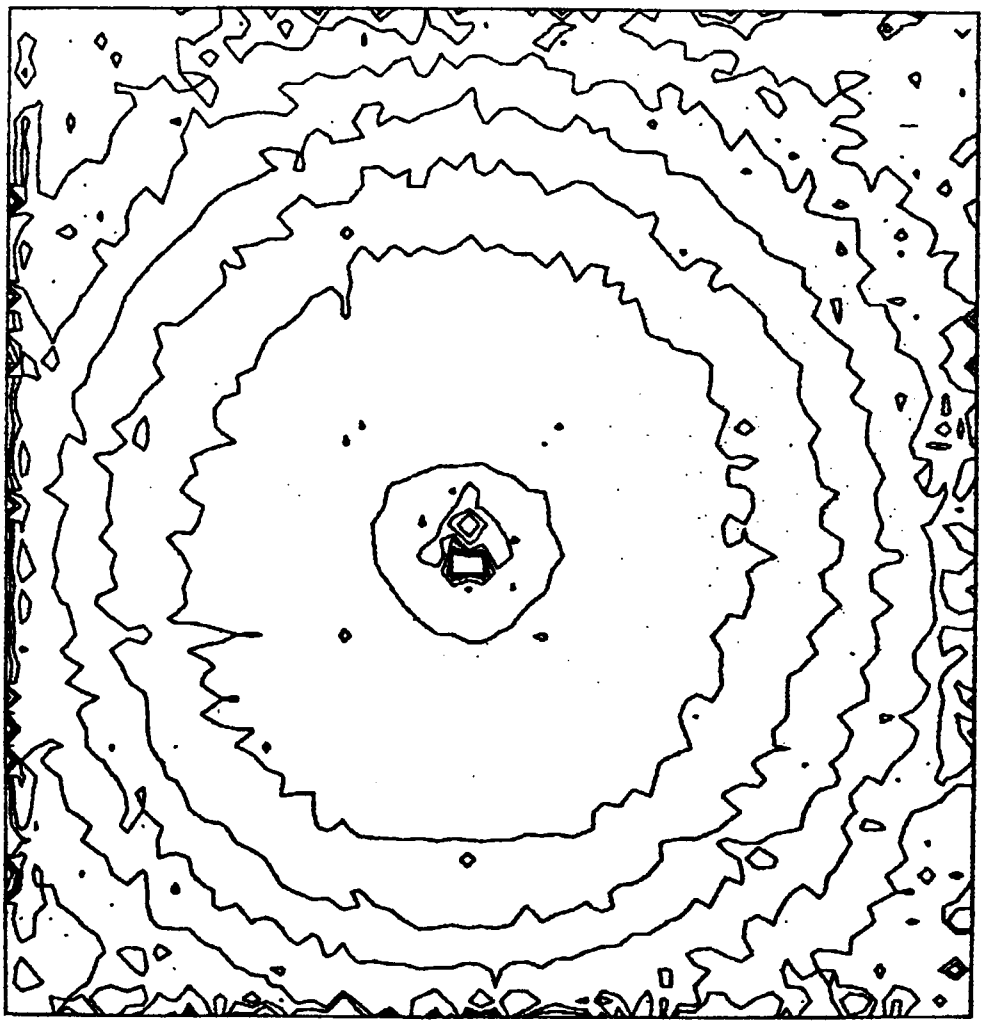


Figure 5-2. Two-dimensional contour plot of the scattering intensity of Lupolen measured with long geometry.

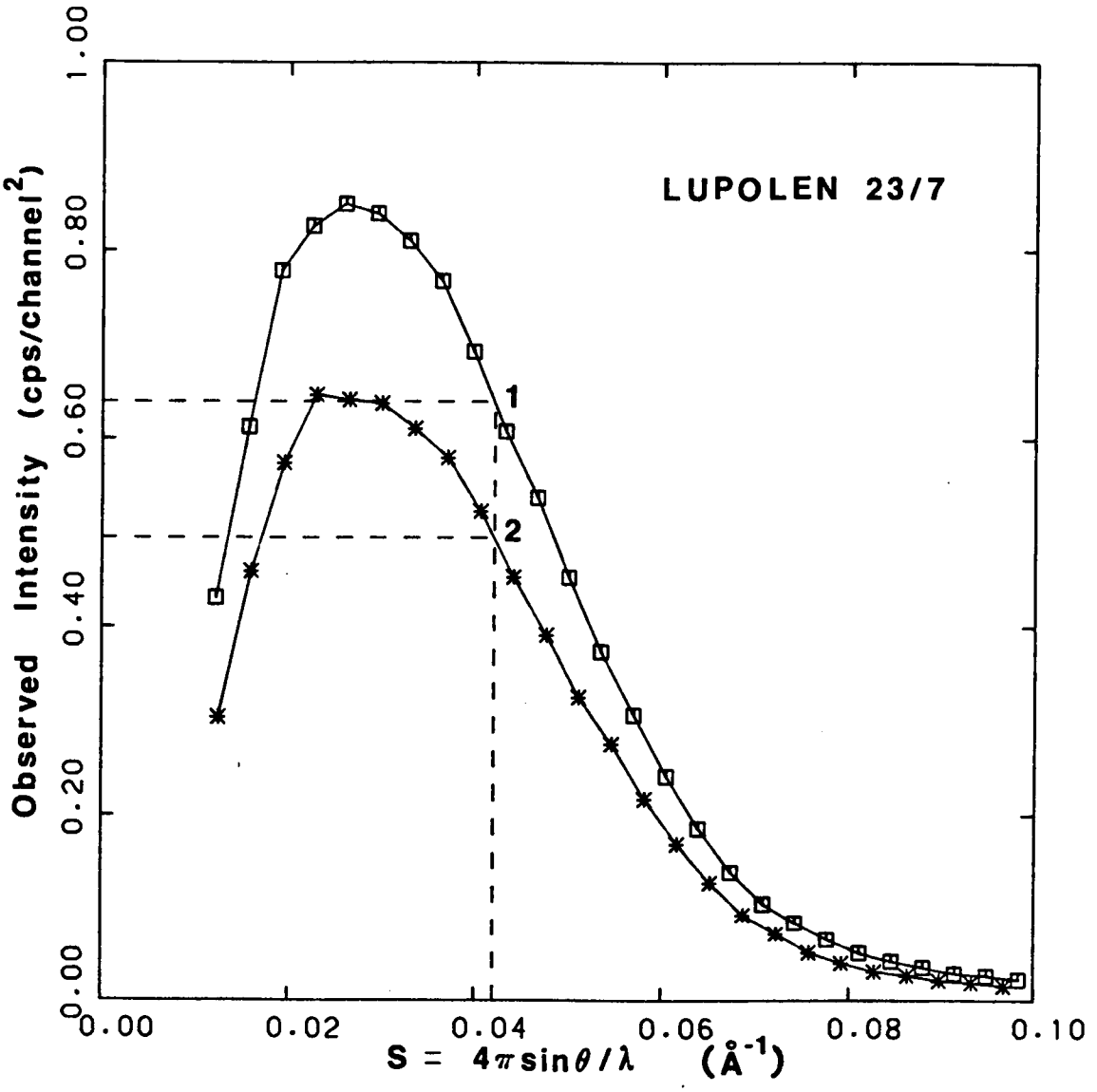


Figure 5-3. Radial averaged small-angle x-ray scattering intensity of Lupolen 23/7 versus s measured with long geometry.

$$Po = \frac{P_c(s = 0.042\ \mathring{A}^{-1})}{I_c(s = 0.042\ \mathring{A}^{-1}) \cdot t \cdot \exp[-\mu_\ell t] \cdot i_e \cdot a/L^2}$$

where the subscript c stands for calibration sample. Because of the proven material stability of Lupolen, the intensity scattered by the calibration sample does not change after repeated exposure to x-rays, i. e., $I_c(s = 0.042\ \mathring{A}^{-1})$ is a constant. Therefore,

$$Po = K_{c,L} P_c(s = 0.042\ \mathring{A}^{-1}) \qquad \text{Eq.(5-12)}$$

where $K_{c,L}$ is the calibration constant for long geometry,

$$K_{c,L} = 1/[I_c(s = 0.042\ \mathring{A}^{-1}) \cdot t \cdot \exp(-\mu_\ell t) \cdot i_e \cdot (a/L^2)].$$

From curve 1 on Figure 5-3, $P_c(s = 0.042\ \mathring{A}^{-1}) = 0.640$ cps/channel^2. Thus,

$$K_{c,L} = \frac{Po}{P_c(s = 0.042\ \mathring{A}^{-1})} = \frac{2.505E6 \text{ counts}/(\text{sec}*\text{mm}^2)}{0.640 \text{ cps/channel}^2}$$

$$= 3.912E6 \text{ sec}*\text{channel}^2/(\text{sec}*\text{mm}^2).$$

The incident beam intensity for the experimental condition of curve 2 on Figure 5-3 can then be determined as

$$Po' = K_{c,L} P_c'(s = 0.042\ \mathring{A}^{-1})$$

$$= 3.912E6 \text{ sec}*\text{channel}^2/(\text{sec}*\text{mm}^2) \times 0.495 \text{ cps/channel}^2$$

$$= 1.935E6 \text{ counts}/(\text{sec}*\text{mm}^2).$$

5.6.2 Calibration for Short Geometry

The calibration method described above is good for long geometry only since the scattering intensity obtained from Lupolen at an s value of $0.042\ \mathring{A}^{-1}$ is not within the acceptable accuracy with the short geometry. Instead, the magnitude of thermal density fluctuations of Lupolen is used for the purpose of calibration.

In polymeric materials there are several factors which give rise to a somewhat constant scattering background at larger angles and lead to deviations from Porod's law. These deviations appear to be due to disorder, thermal motion, or the onset of wide-angle scattering. Wiegand and Ruland (164) have shown this background intensity may be developed as a power series in even powers of the scattering power of the scattering vector $\vec{s}$. An empirical method which is an approximation to the series has been proposed by Vonk (165).

Vonk's method involves the use of the first or second term in the expansion such that the background intensity is given by

$$I_{back}(s) = Fl + v \cdot s^{**}n, \qquad \text{Eq.(5-13)}$$

where v is a constant and n is an even integer between 0 and 10 of which the one ensuring the best fit of the curve to the experimental points is adopted. Fl is the intensity value extrapolated to zero angle. This value reflects the magnitude of thermal density fluctuations and may be related to the isothermal compressibility. So the total scattering intensity at relatively large angles is

$$I_{back}(s) = Kp/s^{**}4 + Fl + v \cdot s^{**}n, \qquad \text{Eq.(5-14)}$$

where Kp is the Porod constant (135).

Figure 5-4 is the two-dimensional contour plot for the scattering data of Lupolen measured with the short geometry. Figure 5-5 plots the radially averaged small-angle scattering data of Lupolen 23/7 obtained with the short geometry having units of cps/channel^2. It can be seen from Figure 5-5 that the range of data points measured with short geometry is not sufficient for the calculation of the invariant, and then use its magnitude for the purpose of calibration.

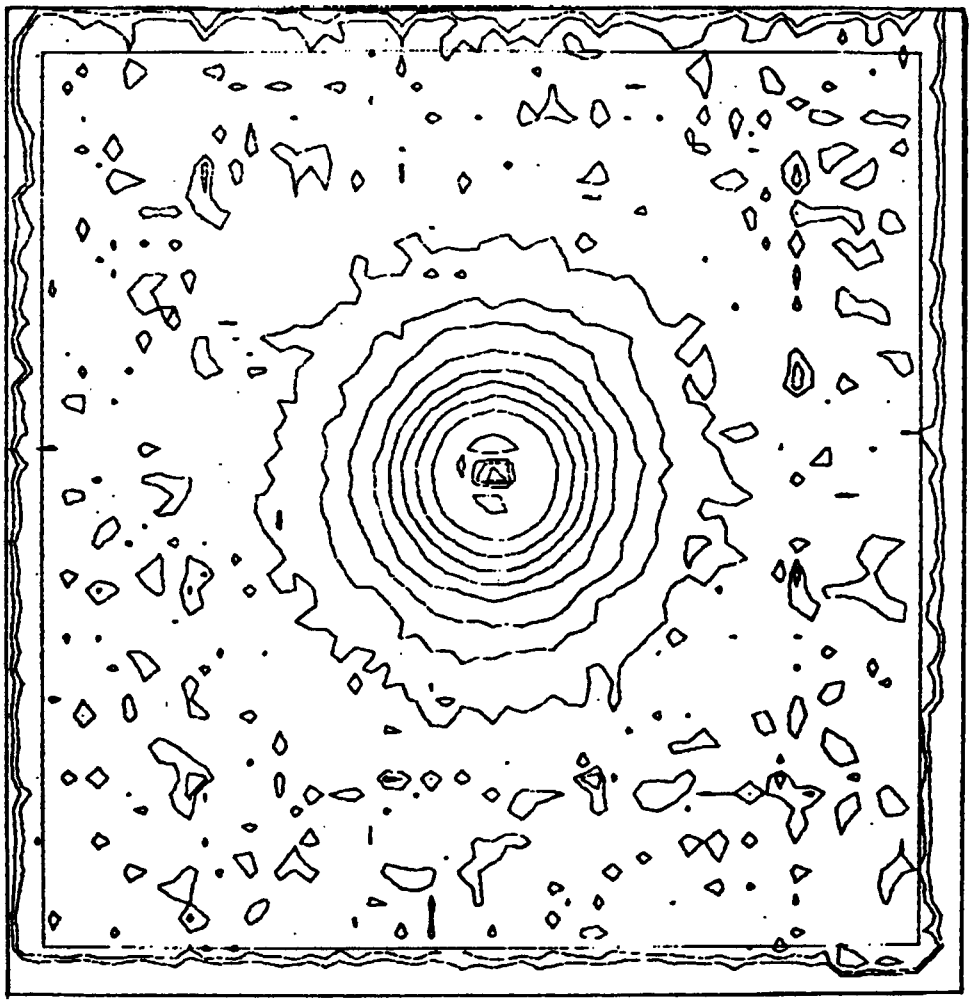


Figure 5-4. Two-dimensional contour plot of the scattering intensity of Lupolen measured with short geometry.

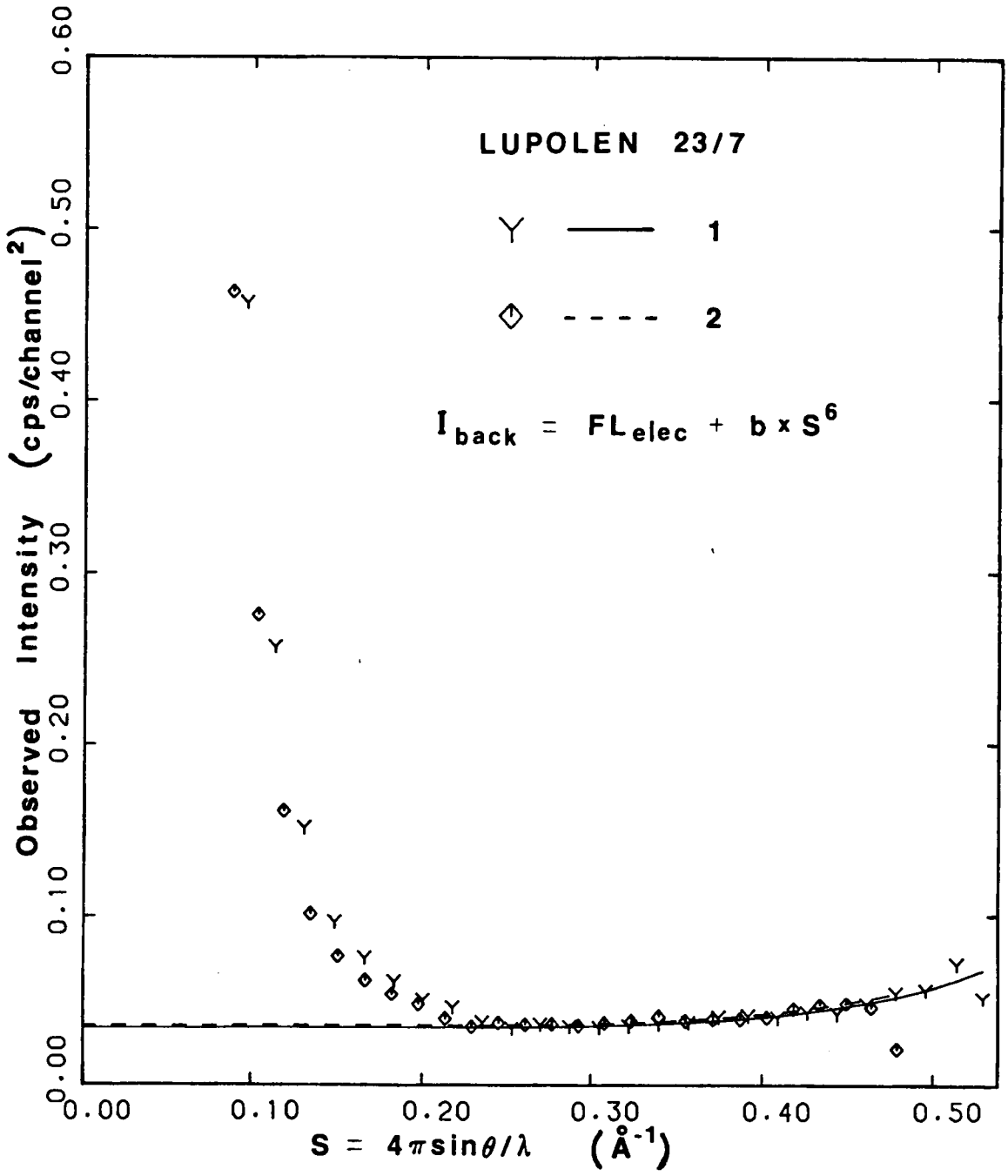


Figure 5-5. Radial averaged small-angle x-ray scattering intensity of Lupolen 23/7 versus s measured with short geometry.

Two sets of data are shown in Figure 5-5, a dashed line of the type of Eq.(5-14) with n = 6 is fitted to the experimental points of each data set at relatively large angles, where the contribution of the first term was felt to be negligible. The Po of curve 1 on Figure 5-5, which is determined by multiple foil technique, is 2.108E6 counts/(sec*mm^2). From Eq.(5-7),

$$Fl_c = \frac{Fl_{c,obs}}{Po \cdot t \cdot \exp[-\mu_\ell t] \cdot i_e \cdot a/L^2}$$

or

$$Po = K_{c,S} Fl_{c,obs} \qquad \text{Eq.(5-15)}$$

where $K_{c,S}$ is a calibration constant for short geometry,

$$K_{c,S} = 1/[Fl_c \cdot t \cdot \exp(-\mu_\ell t) \cdot i_e \cdot (a/L^2)].$$

$Fl_{c,obs}$ of curve 1 on Figure 5-4 is determined as 0.0338 cps/channel^2. Thus,

$$K_{c,S} = \frac{Po}{Fl_{c,obs}} = \frac{2.108E6 \text{ counts/(sec*mm}^2\text{)}}{0.0338 \text{ cps/channel}^2}$$

$$= 6.450E7 \text{ sec*channel}^2/(\text{sec*mm}^2).$$

Therefore the incident beam intensity for the experimental condition of curve 2 on Figure 5-4 can be determined as

$$Po' = K_{c,S} Fl_{c,obs}'$$

$$= 6.450E7 \text{ sec*channel}^2/(\text{sec*mm}^2) \times 0.0354 \text{ cps/channel}^2$$

$$= 2.283E6 \text{ counts/(sec*mm}^2).$$

5.6.3 Superposition of Long and Short Geometry Data

The intensity data of Lupolen measured with long geometry and short geometry in units of counts/sec/element are converted into

electron units and then superposed. From Eq.(5-7),

$$I_c(s) = \frac{P_c(s)}{Po \cdot t \cdot \exp[-\mu_e t] \cdot i_e \cdot a/L^2}$$

The constants used are :

	Long Geometry	Short Geometry
TS	0.396	0.396
t (mm)	2.73	2.73
L (mm)	5048.0	1120.0
Po (counts/sec*mm^2)	2.505E6	2.108E6

The data are plotted on Figure 5-6 in electron units. The superposition is quite good.

The calculated electron density fluctuation of Lupolen is 0.246 eu/$\mathring{A}^3$, this corresponds to a crystallinity of about 80% by comparing to literature data for polyethylene (166). The crystallinity of our Lupolen is determined as 40% by WAXS technique. Since the value of the frozen-in electron density fluctuation for polystyrene determined by Rathje and Ruland (166) was also much higher than that determined by Renninger and Uhlmann (167) and by our group (see 5.7), the inconsistency in the value of crystallinity of Lupolen as determined by WAXS and SAXS may be caused by the discrepancies in the instruments used in labarotories.

5.7 Origin of SAXS from Undeformed Polystyrene

The molecular weight dependence of the SAXS form atactic polystyrene is discussed in this section. This material was chosen

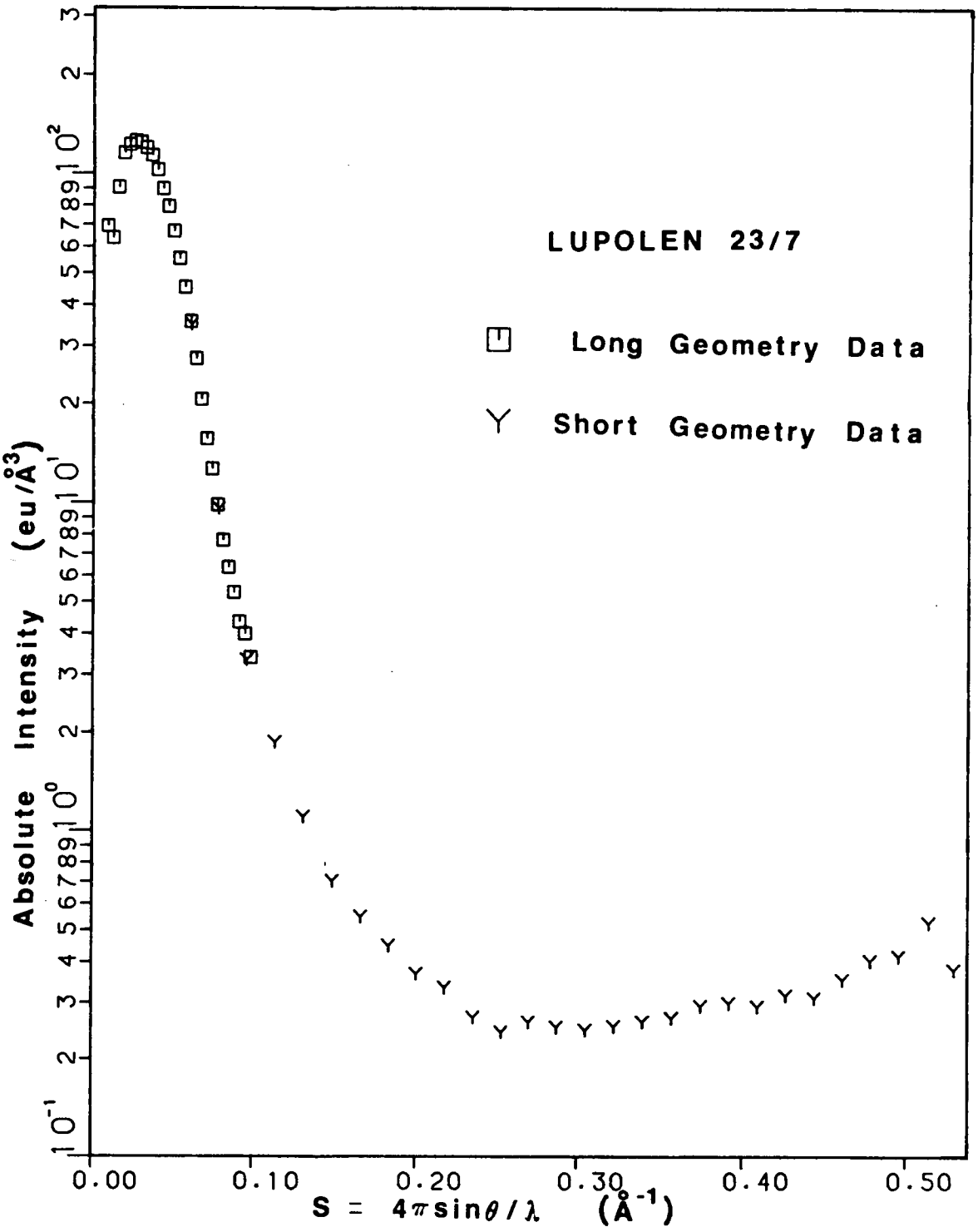


Figure 5-6. Superposition of absolute intensity data for Lupolen 23/7 measured with long geometry and short geometry.

because our primary goal is to study the PS crazing phenomenology and partly because we can easily find literature data in absolute units to compare with our data. The samples are monodispersed and polydispersed polystyrene supplied in the form of pellets by Dow Chemical. The specimens were prepared by compression molding into platelets of thickness 1.6 mm at $180^{o}C$ and then cooled to room temperature. The density of the specimens ranged between 1.047 to 1.049 g/cm^3 as measured by the density gradient column method. The birefringence of the specimens were measured as zero, indicating there is no residual stress in the sample. From Eq.(5-7), the absolute intensity is given by

$$I_s(s) = \frac{P_s(s)}{Po \cdot t \cdot \exp[-\mu_\ell t] \cdot i_e \cdot a/L^2} .$$

Figure 5-7 is a typical intensity plot for polystyrene which shows the radially averaged small-angle scattering data of PS108 ($\overline{Mn}$ = 247,000, $\overline{Mw}$ = 267,000) in electron units. The SAXS intensity of amorphous polystyrene is very weak compared with semicrystalline Lupolen. The scattering curve has essentially the same characteristic features as the data obtained by Renninger and Uhlmann (atactic polystyrene provided by the American Optical Co., [167]): a sharp decrease of the intensity at small angles followed by slightly decrease of the intensity between about $s = 0.06\ \mathring{A}^{-1}$ and $s = 0.1\ \mathring{A}^{-1}$. However, this scattering behavior is very different from that of Hendricks et al. (163). In the latter work, the scattering curves show a continuous decrease of the intensity from small angle region to $s = 0.15\ \mathring{A}^{-1}$. The scattering intensity is also higher than ours. By

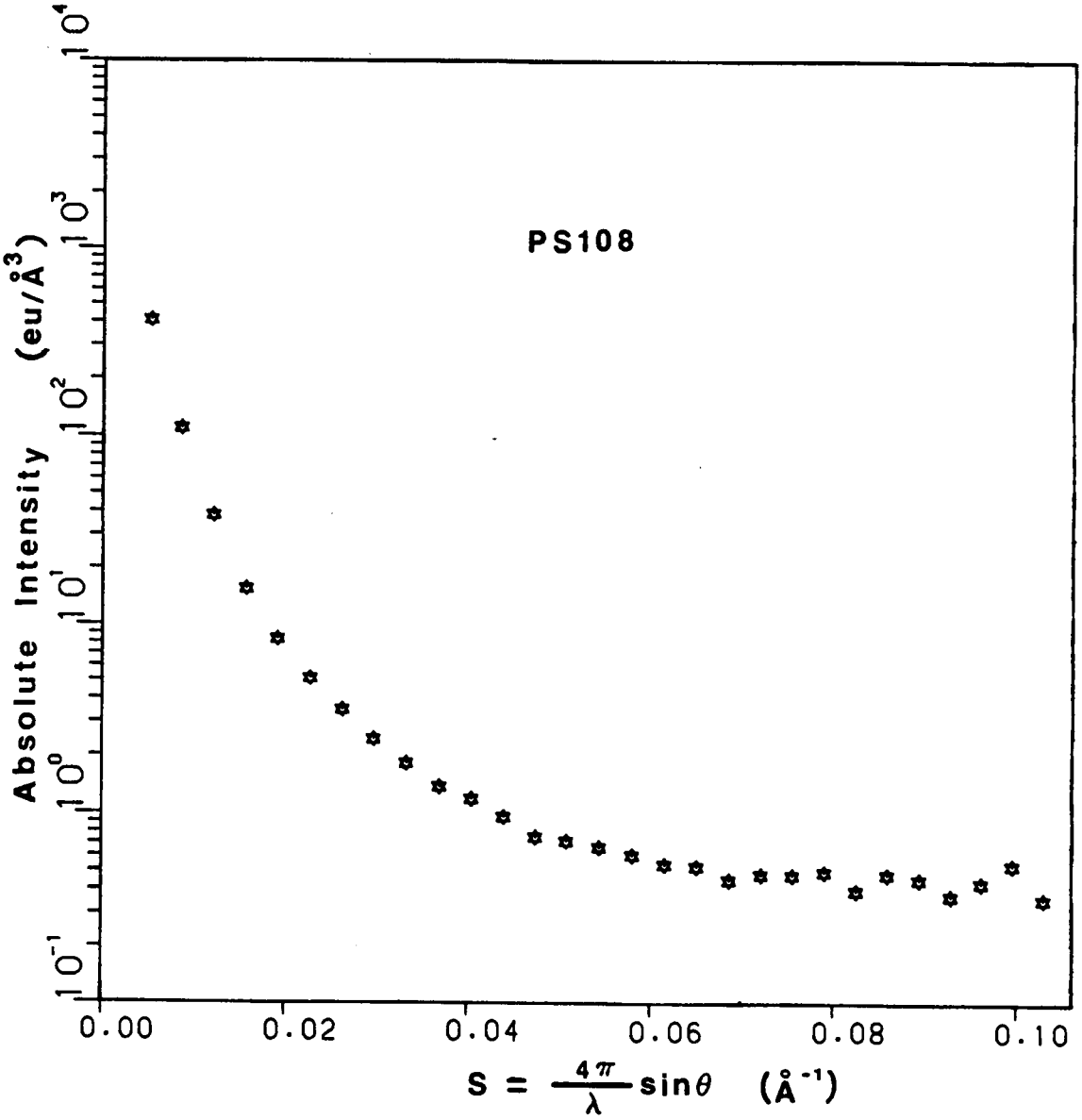


Figure 5-7. Dependence of the absolute scattering intensity for PS108 on s.

the WAXS technique the latter was proved to be isotactic polystyrene. Thus its semicrystallinity is responsible for the discrepancy.

Figure 5-8 is the Porod plot of PS108. The dashed line is the fitted curve of the type of Eq.(5-14) with n = 0. The frozen-in electron density fluctuation determined in this way is 0.403 eu/$\mathring{A}^3$. The experimental value is 0.8 eu/$\mathring{A}^3$ as determined by Rathje and Ruland (166) and about 0.5 eu/$\mathring{A}^3$ as measured by Renninger and Uhlmann (167) for their polystyrene. The solid line in Figure 5-9 is the molecular weight dependence of Fl_{el} for polystyrene. The linear regression results shows that Fl_{el} increases slightly with increases in number averaged molecular weight. The solid line in Figure 5-10 is the molecular weight distribution dependence of Fl_{el} for polystyrene and has a small negative slope.

The theoretical value for the electron density fluctuations Fl of a one-component equilibrium system can be deduced from the thermodynamic relationship

$$Fl_{el} = \rho_{el} k_B T \cdot \kappa(T) \qquad \text{Eq.(5-16)}$$

where ρ_{el} is the average electron density, k_B Boltzmann's constant, T the absolute temperature and κ the isothermal compressibility (98, 99). The dashed lines in Figure 5-9 and Figure 5-10 are calculated from the compressive modulus-molecular weight relationship obtained at room temperature and different nominal strain rates by Chapman (168). The values calculated according to Eq.(5-16) are about half of the experimental values. It has been pointed out that for glassy polymers Eq.(5-16) is true only above the glassy transition temperature (Tg), and for T < Tg, Eq.(5-16) changes to

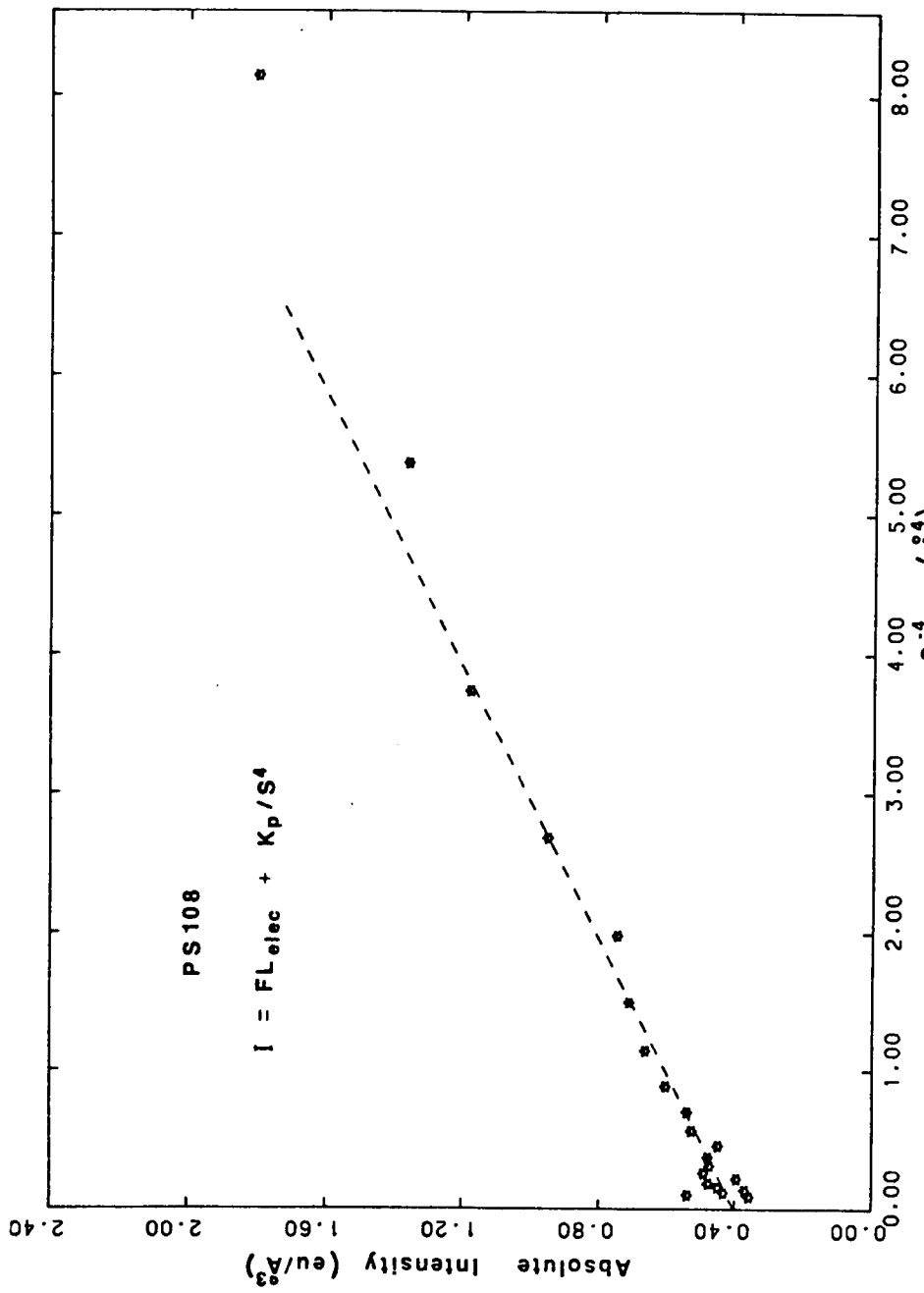


Figure 5-8. Porod plot of PS108: I(s) versus $1/s^4$.

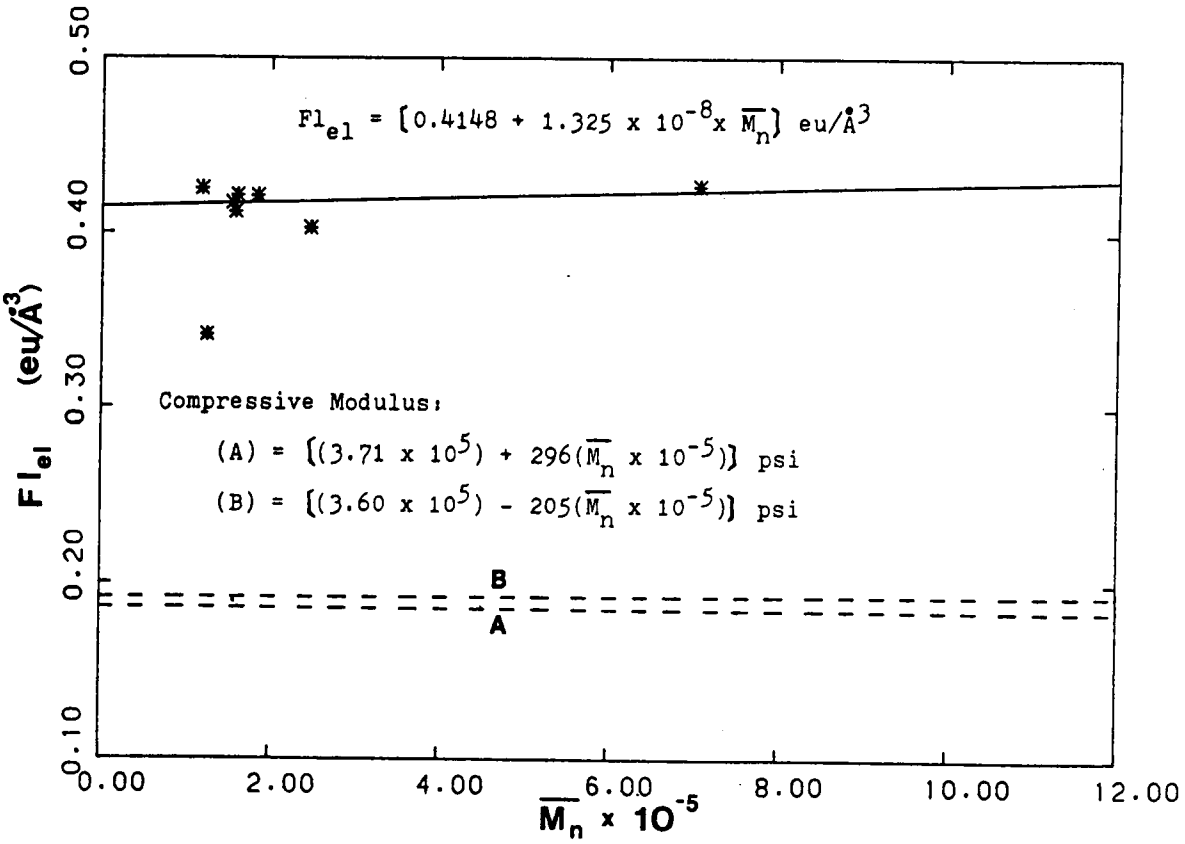


Figure 5-9. Molecular weight dependence of the thermal frozen-in electron density fluctuation for polystyrene at room temperature. ———: SAXS data; - - -: calculated from compressive modulus measured at room temperature and nominal strain rates of (A) 0.004/min and (B) 0.04/min.

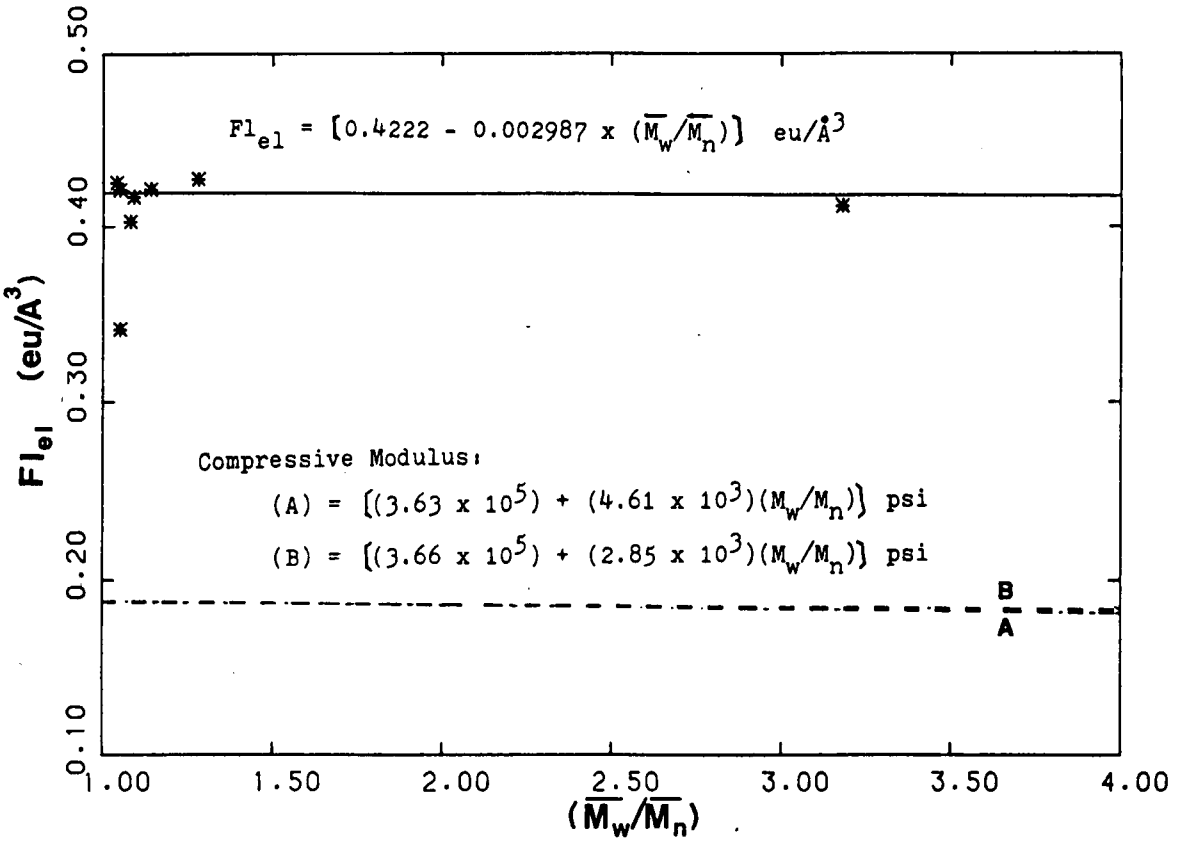


Figure 5-10. Molecular weight distribution dependence of the thermal frozen-in electron density fluctuation for polystyrene at room temperature. ———: SAXS data; - - -: calculated from compressive modulus at room temperature and nominal strain rates of (A) 0.004/min and (B) 0.04/min.

$$Fl_{el} = \rho_{el} k_B T \cdot \kappa(Tg) \qquad \text{Eq.(5-17)}$$

where $\kappa(Tg)$ is the isothermal compressibility at Tg (166, 169). If take $\kappa(Tg)$ = 5E-11 cm**2/dyne for polystyrene, the estimated value for the scattering intensity associated with thermal density fluctuations is about 0.3 eu/$\mathring{A}^3$.

After substracting the thermal density fluctuations, the invariant for PS108 is calculated as 0.971E-5 eu/$\mathring{A}^6$. Three possibilities may be envisaged for the origin of the scattering at small-angle range (167, 170):

(1) inherent structure of the pure polymer phase;

(2) microvoids presents in the polymer samples;

(3) foreign particles present in the polymer samples.

Using a two phase model, the concentration of various hetrogeneities can be evaluated by assuming a value for the electron density difference between the two phases. If a nodular model is assumed and $(\rho_1 - \rho_2)$ is taken as 0.023 electron/$\mathring{A}^3$, the inhomogeneity concentration is 1.459%. This high value and the steep rise of intensity at small angle exclude the first possibility (169, 170). If microvoids are assumed and $(\rho_1 - \rho_2)$ is taken as 0.34 electron/$\mathring{A}^3$, the concentration is 0.00841%. We also find that the invariant increases with decreasing molecular weight for monodispersed polystyrene, and it is true that molecular weight decreases with increasing concentration of initiator. Moreover, polydispersed polystyrene has lower scattering intensity near zero angle region and lower invariant than monodispersed polystyrene and this can be attributed to the different

source of initiator used for polymerization. Therefore, we can conclude that SAXS of amorphous polystyrene originates from foreign particles such as initiators and possibilly partly from trace amount of microvoids presents in the polymers.

5.8 Conclusion

Lupolen is an excellent calibration standard for long geometry. Because it has high scattering intensity at small angles, short measuring time (usually 1000 seconds is sufficient) and good reproducibility and thus reliable data can be obtained. For short geometry, the application of electron density fluctuation of Lupolen for the purpose of calibration is also proved to be successful.

The SAXS of amorphous polystyrene is source dependent. The steep rise at near zero angle region can be attributed mostly to foreign particles. The thermal frozen-in electron density fluctuation for polystyrene increases slightly with number averaged molecular weight and decreases slightly with polydispersity.

With conversion of arbitrary intensity to absolute values, we can easily combine the intensity measured with different camera geometries and make interlaboratory comparisons.

CHAPTER 6

SURFACE SCATTERING PHENOMENON AND THE SAXS STUDIES OF POLYSTYRENE CRAZES

In this chapter, the surface scattering phenomenon of electromagnetic waves by single or multiple layers of films are reviewed and a special treatment for the total reflection of x-rays is developed. This theory is applied to the analysis of the surface scattering observed in SAXS studies of two-phase matter in polymers having lamella stacks or a flat interfacial boundary structure. Important features of this vector theory are the ability to calculate the surface scattering invariant, the absolute scattering intensity, and surface roughness that gives rises to dispersion of specular reflection from perfectly smooth surfaces. By considering the interfacial surface roughness of polystyrene crazes, the surface scattering spectrum is calculated theoretically and compared to some experimental results. Also the theory is presented in such a way as to compare surface scattering to volume scattering, i.e. both two and three dimensional scattering events can be simultaneously treated. This provides a new basis for quantitative analysis of crazes in polystyrene.

6.1 Introduction

The scattering of electromagnetic waves from any type of a material object can originate from two sources. These are defects of homogeneity such as local variations of the properties in the interior

of the material, or irregularities of the surfaces and interfaces that form its external and internal boundaries. These two sources are classified as volume scattering and surface scattering, respectively. The latter can further be considered as the sum of two components; the specular component and the diffuse component (171). Specular reflection is the reflection from smooth surfaces; it is directional and obeys the laws of classical optics. If the surface is rough, regular reflection occurs at each point but the rays go off in many directions. Diffuse reflection (sometimes called scattering in reflection) is a phenomenon which consequently takes place over a much larger area of the surface than specular reflection.

In the wavelength region of x-rays, the values of the refractive indices of media through which the rays propagate differ very little from unity. Reflection and refraction are usually neglected in the treatment of SAXS theory. Roentgen (94) tried, but failed to detect any refraction on passing x-rays through slabs of various materials because of the extremely small magnitude of the effect. The refraction of x-rays was first observed by Stenstrom (172) in 1919 and total reflection by Compton (173) in 1922. Since then, many aspects of the optical analogous properties of x-rays have been studied. These previous investigations include the determinations of the refractive indices of x-rays by the total reflection method for various substances over a wide range of wavelengths (e.g. 173, 174, 175), the production of converging x-ray beams by total reflection (e.g. 176, 177, 178), surface studies of metal coated films (e.g. 179

- 184) and the nature of the surface of polymers and their solutions (185) by the total reflection method.

All the previous studies were limited to the total reflection phenomenon occuring at the external sample surface (i.e. the x-ray beam is directly incident on the sample external surface). Generally the surface scattering from interfaces in the interior of the matter has been neglected in SAXS studies. By SAXS, researchers usually have meant volume scattering caused by the inhomogeneity of electron density distributions in the matter (see Chapter 3). Schultz first indicated the possibility of total reflection occurring within lamellar stacked systems when their lamellar spacings are greater than a critical value (186). This critical value is related to the crystallinity and the refractive indices of the two phases composing the system. His calculations showed that for semicrystalline polymers such as polyethylene (PE) and polyoxymethylene (POM) their lamellar thickness is usually much lower than the critical value (960 Å and 710 Å for PE and POM of 70 volume percent crystallinity, respectively) and total reflection is thus insignificant. However, the critical value depends on the scattering system. It was realized only recently in the SAXS studies of crazes (82) that the two phenomena (surface scattering and volume scattering) do coexist and are superimposed. Because of the inherent microstructure of crazes, surface scattering in reflection is clearly evident under certain incident conditions (i.e. the x-ray is perpendicular to the tensile axis and thus nearly parallel to the craze plane). Among the SAXS studies of polymer

crazes, LeGrand, Kambour, and Haaf (73) first observed the anisotropic SAXS craze pattern. Brown and Kramer (81) have shown that by tilting the crazed polymer specimen toward the direction of tensile axis, it would greatly reduce the intensity of what they called the "anamolous streak" parallel to the tensile axis. They made a passing speculation that the anamolous streak could be partially due to total reflection. However, the majority of their interpretation and discussion of this streak of high intensity is that it arises from parallel craze fibrils. Westbrook et al. (82) also did tilting experiments on polystyrene crazes to show that the anisotropic character of the scattering function completely disappears when the sample is tilted beyond the critical angle for total reflection. Subsequent void fraction determinations (by invariant analysis of scattering patterns from tilted and untilted samples and comparison to bulk density determination) showed that the anisotropic scattering pattern is composed of superimposed scattering mechanisms. By modeling the crazes as reflecting media, it was shown that the entire anisotropic component of the scattering behavior is consistent with surface scattering, while the isotropic scattering behavior is consistent with volume scattering. However, the detailed character of the craze total reflection is still uncertain and its interpretation is still lacking.

Surface scattering of light is of considerable importance in optics and has been very extensively treated by numerous authors (e.g. 171, 187 - 201). This chapter consists of a brief review of electromagnetic optics, followed by the theory of scattering of

electromagnetic waves by an assembly of surfaces. This treatment is then used for the calculation of x-ray surface scattering spectra for several typical two-phase systems including a semicrystalline polymer (PE), a polymer with microvoids (PS crazes), and a metal alloy (78%Al-22%Zn). PE and 78%Al-22%Zn are chosen because they are typical two-phase systems investigated by SAXS and were examined previously by Schultz (186). The theoretical calculation for PS crazes will be compared with SAXS experimental results. Important interpretations about PS crazes are then made.

6.2 Theory

The basic theories which describe the behavior of electromagnetic radiation under various conditions are well established (124, 202 - 205). This section is composed of a brief summary of selected topics in order that a complete discussion of the application is achieved.

6.2.1 Refractive Index of X-Rays

When x-rays are propagated through a material, the theory of dispersion (124, 202, 203) gives an absolute refractive index. This is the ratio of the phase velocities in vacuum and in the medium, and appears in this theory as a complex number,

$$n = 1 - \zeta - i\beta. \qquad \text{Eq.(6-1)}$$

Under conditions that the wavelengths are much shorter than any critical absorption wavelength of the medium, the expression for ζ is

$$\zeta = \frac{Ne^2}{2\pi m\nu^2} = \frac{Ne^2}{2\pi mc^2} \qquad \text{Eq.(6-2)}$$

where N is the total number of mobile electrons per unit volume, ν the frequency and λ the wavelength of the radiation in vacuo, c the velocity of light in vacuo, e and m the charge and mass of the electron, respectively (124). ζ usually has a magnitude of 10^{-6}.

Eq.(6-2) indicates the existence of an index of refraction less than unity. This implies a wave motion with a velocity greater than that of light and contradicts the special theory of relativity which states that no signal can be transmitted with a velocity greater than that of light in vacuum. Nonetheless this result follows directly from the fact that with frequencies greater than the natural frequencies of the electrons in the medium, the displacements of electrons composing the medium are opposite in direction to the displacing force and hence $v > c$ and $n < 1$. A clear explanation for the significance of a refractive index less than one can be found in Ref.(203).

The imaginary part in Eq.(6-1) has to do with the absorption of waves in the medium,

$$\beta = \frac{\lambda}{4\pi}\mu_\ell \qquad \text{Eq.(6-3)}$$

where μ_ℓ is the ordinary linear absorption coefficient of the medium at wavelength λ (124). The absolute refractive index turns out to be smaller than unity and only dependent on the number of electrons per unit volume.

6.2.2 Electromagnetic Optics of Isotropic Media

6.2.2.1 The Laws of Reflection and Refraction

When a plane wave falls on to a boundary between two homogeneous transparent isotropic media of different optical properties, it is divided into two waves: a transmitted wave proceeding into the second medium and a reflected wave propagated back into the first medium (Figure 6-1). Let the propagation direction of the incident wave be specified by the wave vector $\vec{ko}$, and $\vec{kr}$ and $\vec{kt}$ denote wave vectors in the direction of propagation of the reflected and the transmitted wave. The plane specified by $\vec{ko}$ and the normal to the boundary (the z - axis) is called the plane of incidence. The boundary Σ is taken as the plane $z = 0$ and the plane of incidence as the xz-plane. Due to the boundary and continuity conditions for wave propagation, as shown in Figure 6-1, the following laws are established (197, 204, 205):

(1) The law of reflection: the incident and reflected rays lie symmetrically with respect to the normal at the point of incidence; i.e., the reflected wave vector $\vec{kr}$ is in the plane of incidence and the angle of reflection i_1' equals the angle of incidence i_1.

(2) The law of refraction (or Snell's law): the refracted wave vector $\vec{kt}$ is in the plane of incidence and

$$\frac{\sin i_1}{\sin i_2} = \frac{n_2}{n_1} = n_{12}. \qquad \text{Eq.(6-4)}$$

Here n_1 and n_2 denote the refractive indices of media 1 and 2, respectively, and n_{12} is called the relative refractive index of medium 2 with respect to medium 1.

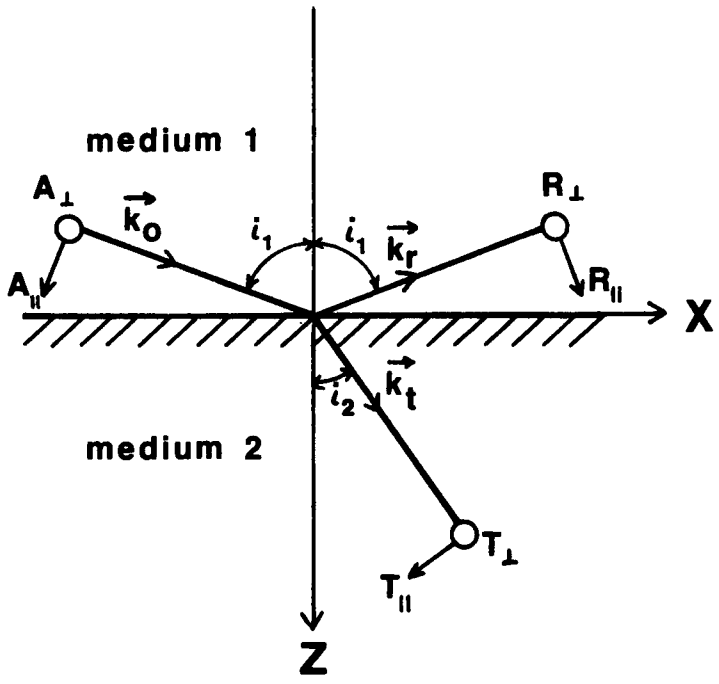


Figure 6-1. Reflection and refraction of an electromagnetic wave.

6.2.2.2 Fresnel Formulae

Consider now the amplitudes of the reflected and the transmitted waves. Let E, R, and T denote the amplitude of the electric vector of the incident, reflected and transmitted waves. Each wave can be resolved into components parallel (denoted by subscript $\parallel$) and perpendicular (subscript $\perp$) to the plane of incidence. The choice of the positive directions for the parallel components is indicated in Figure 6-1. The perpendicular components may be visualized at right angles to the plane of the paper. The Fresenel reflection coefficients r_{12} (ratio of reflected and incident amplitude) and transmission coefficients t_{12} (ratio of transmitted and incident amplitude) are (197, 204, 205):

$$r_{12_\perp} = \frac{R_\perp}{E_\perp} = \frac{n_1\cos i_1 - n_2\cos i_2}{n_1\cos i_1 + n_2\cos i_2} = -\frac{\sin(i_1 - i_2)}{\sin(i_1 + i_2)}, \quad \text{Eq.(6-5)}$$

$$t_{12_\perp} = \frac{T_\perp}{E_\perp} = \frac{2n_1\cos i_1}{n_1\cos i_1 + n_2\cos i_2} = \frac{2\cos i_1\sin i_2}{\sin(i_1 + i_2)}, \quad \text{Eq.(6-6)}$$

$$r_{12_\parallel} = \frac{R_\parallel}{E_\parallel} = \frac{n_1\cos i_2 - n_2\cos i_1}{n_1\cos i_2 + n_2\cos i_1} = -\frac{\tan(i_1 - i_2)}{\tan(i_1 + i_2)}, \quad \text{Eq.(6-7)}$$

$$t_{12_\parallel} = \frac{T_\parallel}{E_\parallel} = \frac{2n_1\cos i_1}{n_1\cos i_2 + n_2\cos i_1} = \frac{2\cos i_1\sin i_2}{\sin(i_1 + i_2)\cos(i_1 - i_2)}. \quad \text{Eq.(6-8)}$$

The subscript 12 of r_{12} and t_{12} indicates the incident wave is in medium 1. Eqs.(6-5) to (6-8) are called Fresnel formulae, having first been derived in a slightly less general form by Fresnel in 1823, on the basis of his elastic theory of light.

6.2.2.3 The Reflectance and Transmittance

In the reflection and transmission of an electromagnetic beam at the surface separating two media, the conservation of energy involves the incident flux Φ_i and its resulting fluences, that is,

$$\Phi_i = \Phi_r + \Phi_t + \Phi_a$$

or

$$1 = \mathcal{R} + \mathcal{T} + \mathcal{A}$$

where $\mathcal{R} = \Phi_r/\Phi_i$ is the reflection factor or the reflectance, $\mathcal{T} = \Phi_t/\Phi_i$ is the transmission factor or the transmittance, and $\mathcal{A} = \Phi_a/\Phi_i$ is the absorption factor (197). When the refractive index is real, $\mathcal{A} = 0$ and $\mathcal{R} + \mathcal{T} = 1$. The reflectance is given by

$$\mathcal{R} = r_{12} \cdot r_{12}^* \qquad \text{Eq.(6-9)}$$

where r* denotes the complex conjugate of r. If the incident wave is unpolarized, then

$$\mathcal{R} = (\mathcal{R}_{\parallel} + \mathcal{R}_{\perp})/2. \qquad \text{Eq.(6-10)}$$

6.2.2.4 Total Reflection

When $n_2 > n_1$, then $n_{12} > 1$, and this implies the second medium is optically denser than the first medium. In this case, by Eq.(6-4)

$$\sin i_2 = \sin i_1/n_{12} < \sin i_1,$$

so there is a real angle i_2 of refraction for every incident angle i_1 between 0 and $\pi/2$. If, however, the second medium is optically less dense than the first medium, one obtains a real value for i_2 only for those incident angles i_1 for which $\sin i_1 < n_{12}$. When the angle of incidence i_1 exceeds the critical value i_c given by

$$\sin i_c = n_{12}, \qquad \text{Eq.(6-11)}$$

there exists $\sin i_2 = \sin i_1 / n_{12} > 1$. No angle i_2 corresponds to this value and there is then no refracted wave to enter the second medium. All the incident wave is reflected back into the first medium; this is called total reflection. However, when the absorption effect is taken into account, ideal total reflection can no longer occur. Nevertheless the electromagnetic field in the second medium does not disappear. However there is no longer a flow of energy across the boundary, but it flows along the boundary in the plane of incidence (197). When total reflection occurs on the boundary, the terms involving i_2 in the Fresnel formulae should be replaced by

$$\cos i_2 = i\sqrt{(n_1/n_2)^2 \sin^2 i_1 - 1} \ .$$

Since the absolute refractive index for x-rays is always less than one and is dependent only on the electron density, it turns out that for SAXS from a multi-phase material, the significance of the surface total reflection phenomenon is governed by the electron density difference and the inherent structure of the boundary between the phases. Figure 6-2 shows the reflectance of a smooth interface as a function of glancing angle ϵ, $\epsilon = \pi/2 - i_1$, under CuKα x-ray radiation for three representative two-phase systems, as examined previously by Schultz (186), that are typical in SAXS investigations. They are a semicrystaline polymer represented by polyethylene, a polymer with microvoids represented by a polystyrene craze, and a metal alloy represented by 78%Al - 22%Zn. The material constants used for the calculation for each system are given in Table 6-1. From Figure 6-2 we can see how the electron contrast between two phases and the absorption of the reflecting media affect the reflectance curves.

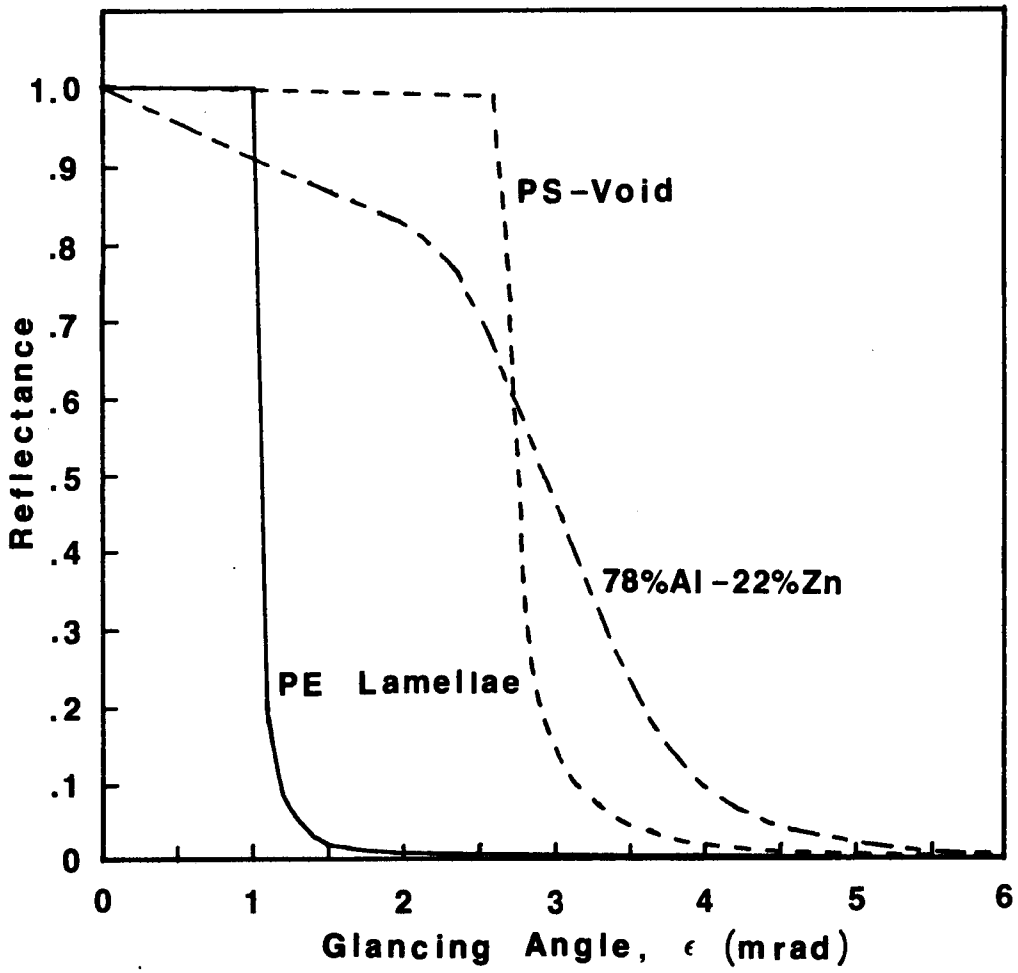


Figure 6-2. The reflectance curve calculated by Fresnel formulae for smooth surfaces of three representative material systems.

Table 6-1

Material constants used to calculate the critical angle of total reflection for three typical material systems

	At CuKα Radiation:		$\lambda = 1.5417$ Å			
	ρ_m (g/cm^3)		$\zeta \times 10^6$			
Material	Medium 1	Medium 2	Medium 1	Medium 2	$\beta \times 10^9$	ϵ_c(mrad)
PE Lamellae*	0.85	1.00	2.95	3.47	4.360+	1.020
PS Craze	0.0	1.049	0.0	3.63**	5.452+	2.693
78%Al-22%Zn++	2.70	6.51	9.68	15.49	355.6+	3.409

* from (186).

\+ calculated by Eq.(6-3).

** calculated by Eq.(6-2);
experimental value is 4.4×10^{-6} from Ref.(185).

++ from (186, 206).

6.2.2.5 Penetration of a Totally Reflected Electromagnetic Wave into the Film Between Two Media

In the above discussion the thickness of medium 2 is not considered. As a matter of fact, if medium 2 is a very thin film between two portions of medium 1, no reflection takes place, for in the limit, the thickness d of this film is zero, so that the incident wave must pass through undisturbed.

Consider a plate pictured in Figure 6-3 bounded by two parallel perfectly smooth surfaces Σ and Σ'. The reflection coefficient of the surface Σ is r_{12} for a wave in the medium of index n_1 falling on the medium with index n_2 and r_{21} is the reflection coefficient for the inverse process. The corresponding transmission coefficients are t_{12} and t_{21}. The analogous variables for the surface Σ' separating the plate from the medium with index n_3 are r_{23}, r_{32}, t_{23}, and t_{32}. The Fresnel formulas are (197, 204, 205):

$$r^{I} = \frac{r_{12} + r_{23}\exp(-i\Psi)}{1 + r_{12}r_{23}\exp(-i\Psi)}, \qquad \text{Eq.(6-12)}$$

$$t^{III} = \frac{t_{12}t_{23}}{1 + r_{12}r_{23}\exp(-i\Psi)}, \qquad \text{Eq.(6-13)}$$

where r^{I} and t^{III} are the reflection and transmission coefficients respectively, in the jth medium, and

$$\Psi = \frac{4\pi}{\lambda} n_2 d \cdot \cos i_2 \qquad \text{Eq.(6-14)}$$

is the phase difference between the wave reflected by surface Σ and the wave which passes Σ, reflected by Σ', and then passes Σ. The reflectance is then given by

$$\mathcal{R} = r^{I} \cdot r^{I*}. \qquad \text{Eq.(6-15)}$$

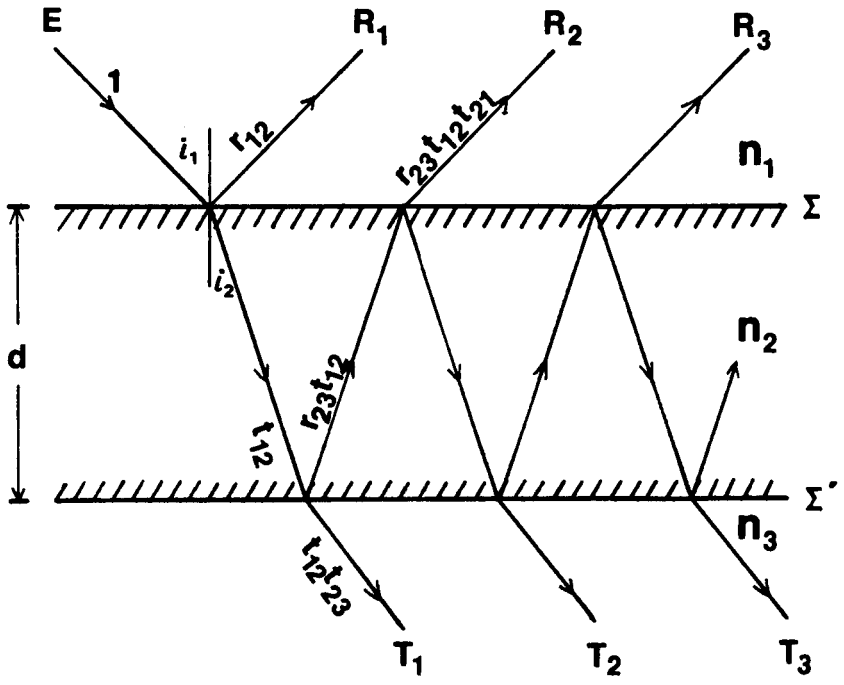


Figure 6-3. Penetration of the totally reflected electromagnetic wave into the film between two media.

By assuming media 1 and 3 to be air (void) and medium 2 to be polystyrene matrix, the reflectance for such a plate structure is plotted against the glancing angle ϵ in Figure 6-4. Previous optical microscopy measurements of craze density show that the distance between crazes ranges around 38 μm in highly crazed polystyrene (207). Thus in the following discussion of crazes, we can always assume "d" (thickness) to be infinity and consider the surface scattering phenomenon from the interface between two media of infinite depth.

6.2.3 Scattering of Electromagnetic Waves by Rough Surfaces

Electromagnetic waves reflected from a smooth homogeneous surface are found in the specular beam. Its intensity, given by Fresnel's equations, depends upon the polarization of the incident wave, the angle of incidence, and the optical properties of the bulk medium. When electromagnetic waves are reflected from rough surfaces, the condition of specularity is relaxed and scattered waves are found away from the specular direction, with a reduction in the specular intensity. Fresnel's equations are no longer valid. The transition from specular reflection to diffuse surface scattering from surfaces of various degrees of roughness is shown in Figure 6-5 (171). For a smooth surface, there is a single reflected wave in the specular direction. For a slightly rough surface, the specular term is still the dominating term with some side lobes. But for a very rough surface, the specular term has lost its privileged position altogether.

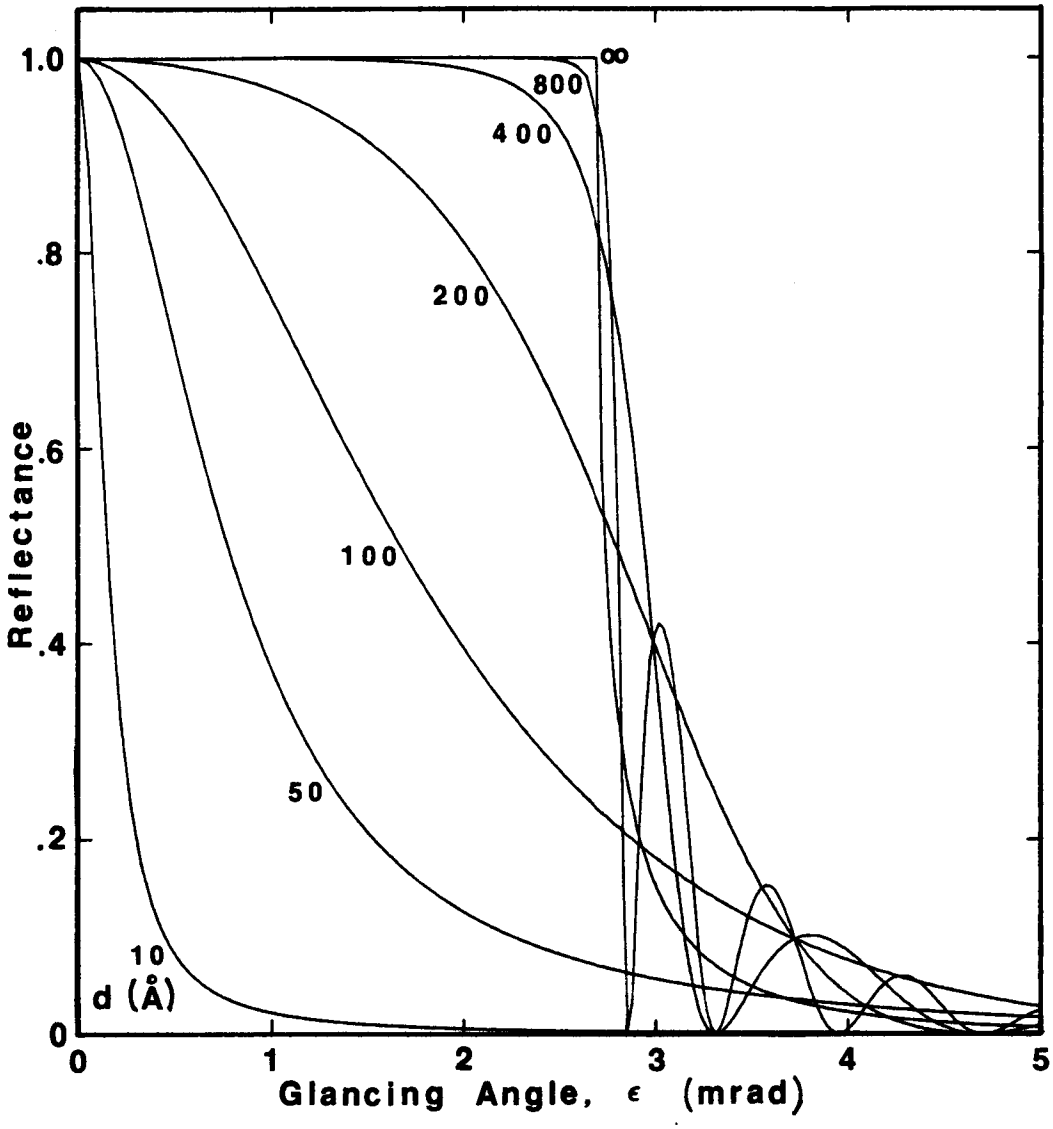


Figure 6-4. Reflectance of a polystyrene matrix film between void media as a function of glancing angle ϵ at various thickness d.

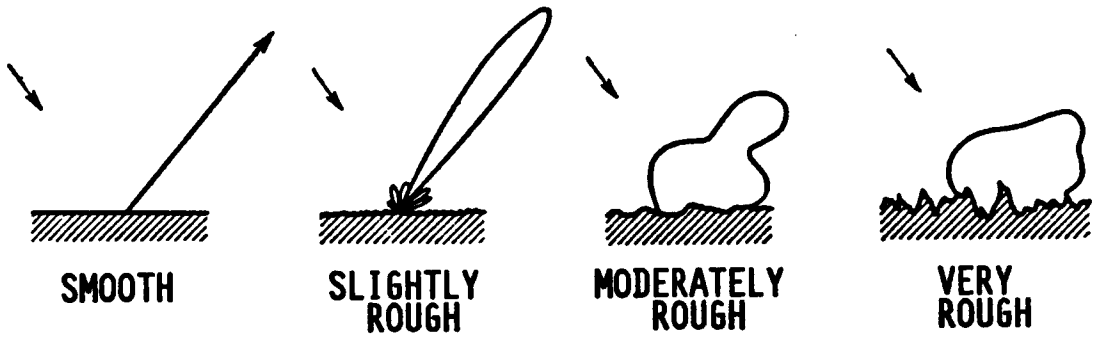


Figure 6-5. Transition from specular reflection to diffuse surface scattering from surfaces of various degree of roughness (171).

The simplest scalar scattering theory (171) gives a relation between the total integrated surface scattering and the surface roughness. The scalar scattering theory has been applied to the study of the surface irregularities and thickness of metal coated films using x-ray scattering (182, 183). Vector scattering theory (187 - 194) can be used to predict the angular distribution of scattered waves about the specular direction. Vector scattering theory is more complete in that it includes the vector nature of the incident and scattered waves. Since in this study of crazes via SAXS we are rather interested in the angular distribution of scattered waves, the vector scattering theory will be considered. In the following, the fundamental concepts about the vector surface scattering theory will be introduced and when appropriate, a comparison with volume scattering theory will be made.

6.2.3.1 A Rough Surface

A rough surface is defined as one which will scatter the energy of an incident plane wave into various directions, whereas a surface that reflects specularly will be called smooth (171). A rough surface is best described by the statistical distribution of the deviation of the surface height from its mean level. A Cartesian coordinate system is shown in Figure 6-6 with $\vec{e}_1$, $\vec{e}_2$, $\vec{e}_3$ as the orthogonal unit vectors. The system is taken to consist of two semi-infinite media: medium 1 with refractive index n_1 in the upper half space ($z > \delta(x,y)$) and medium 2 of refractive index n_2 in the lower half space ($z < \delta(x,y)$). The rough surface between the two media is defined by

$$z - \delta(x,y) = 0, \qquad \text{Eq.(6-16)}$$

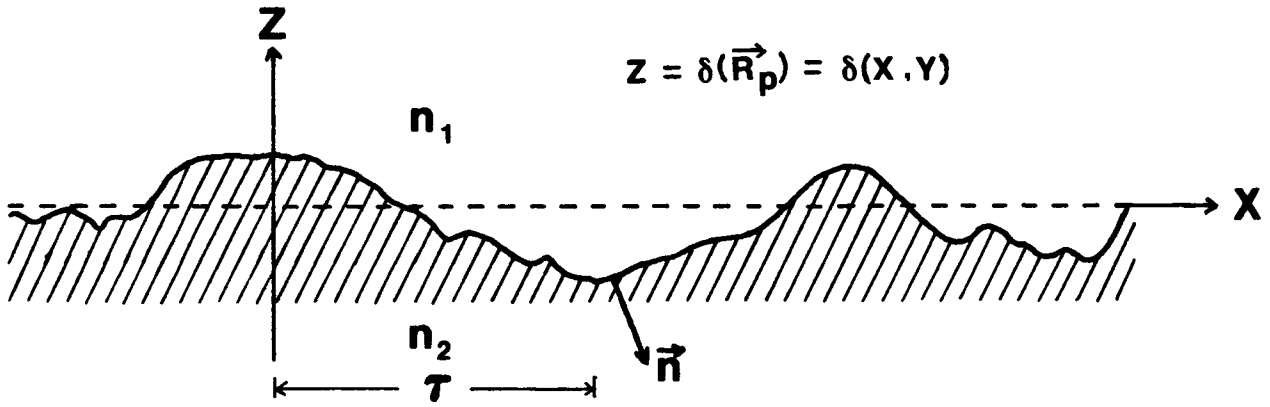


Figure 6-6. Schematic representation of a rough surface separating two media of refractive indices n_1 and n_2.

where $\delta(x,y)$ is a roughness function specifying the shape of the interface. The normal upon this interface is

$$\vec{n} = \left(\frac{\partial \delta}{\partial x}, \frac{\partial \delta}{\partial y}, -1\right). \qquad \text{Eq.(6-17)}$$

The interface is taken to be between $-X/2 \leq x \leq X/2$ and $-Y/2 \leq y \leq Y/2$, where in the final result the limit $XY \rightarrow \infty$ is taken. The dotted line represents the location of the $z = 0$ plane which is the average plane of the interface;

$$\langle \delta \rangle = \lim_{XY \rightarrow \infty} \frac{\int_{-X/2}^{X/2} \int_{-Y/2}^{Y/2} \delta(x,y)\,dxdy}{XY} = 0. \qquad \text{Eq.(6-18)}$$

The surface roughness function δ may be random in nature, in which case the interaction processes considered here can not be predicted in an exact manner but only on an average basis.

6.2.3.2 Surface Scattering Factor

For a surface without discontinuities, the complex amplitude for surface scattering is (194, 198, 200);

$$\xi(\vec{s}_p) = \int_o^\infty \delta(\vec{R}_p) \cdot \exp[-i \cdot \vec{s}_p \cdot \vec{R}_p] d^2R_p = \mathcal{F}_2[\,\delta(\vec{R}_p)], \qquad \text{Eq.(6-19)}$$

which is the two-dimensional Fourier transform of the two-dimensional surface profile. $R_p(x, y)$ is the projection of the position vector

$$\vec{R} = x \cdot \vec{e}_1 + y \cdot \vec{e}_2 + z \cdot \vec{e}_3$$

on the plane $z = 0$. $\vec{s}_p$ is the net change in the component of the wave-vector along the surface between the incident and scattered photon:

$$\vec{s}_p = \vec{k}_p - \vec{ko}_p, \qquad \text{Eq.(6-20)}$$

where $\vec{k}_p$ and $\vec{ko}_p$ are the components of the scattered and incident wave vectors which are parallel to the plane z = 0,

$$|\vec{k}| = |\vec{ko}| = 2\pi/\lambda$$

$$|\vec{k}_p| = |\vec{k}|\sin\phi$$

$$|\vec{ko}_p| = |\vec{ko}|\sin\phi_o$$

in which ϕ and ϕ_o are the polar angles of the scattered and incident waves, respectively.

The scattering factor is equal to the square of the modulus of the surface scattering amplitude $\xi(\vec{s}_p)$;

$$\begin{aligned} g(\vec{s}_p) &= |\xi(\vec{s}_p)|^2 \\ &= \left| \int_o^\infty \delta(\vec{R}_p)\cdot\exp[-i\cdot\vec{s}_p\cdot\vec{R}_p]d^2R_p \right|^2 \\ &= \int_o^\infty\int_o^\infty \delta(\vec{R}_p)\cdot\delta(\vec{R}_p')\cdot\exp[-i\cdot\vec{s}_p\cdot(\vec{R}_p' - \vec{R}_p)]d^2R_p d^2R_p' \\ &= \int_o^\infty\int_o^\infty \delta(\vec{R}_p)\cdot\delta(\vec{R}_p + \vec{r}_p)\cdot\exp[-i\cdot\vec{s}_p\cdot\vec{r}_p]d^2R_p d^2r_p \end{aligned} \qquad \text{Eq.(6-21)}$$

with

$$\vec{r}_p = \vec{R}_p' - \vec{R}_p.$$

In this equation, the integral $\int_o^\infty \delta(\vec{R}_p)\cdot\delta(\vec{R}_p + \vec{r}_p)d^2r_p$ depends uniquely on $\vec{r}_p$. It is a self-convolution of the surface roughness distribution function $\delta(\vec{R}_p)$. The surface correlation function can then be defined as

$$G(\vec{r}_p) = \frac{\int_o^\infty \delta(\vec{R}_p)\cdot\delta(\vec{R}_p + \vec{r}_p)d^2R_p}{\int_o^\infty \delta(R_p)\cdot\delta(R_p)d^2R_p} = \frac{\widetilde{\delta^2(\vec{R}_p)}}{\overline{\delta^2}S} \qquad \text{Eq.(6-22)}$$

where S = XY is the area of interface under irradiation and $\overline{\delta^2}$ is the average value of the square of the surface roughness. If no assumptions whatever are made about the nature of the irregularities

that gives rise to surface scattering from a surface, the only parameter that can be determined is $\overline{\delta^2}$, the average value of the square of the surface roughness, which determines the scattering power of the surface. Further, the correlation function $G(\vec{r}_p)$ tells us whether the hills and valleys of the surface are crowded close together or whether they are far apart. Normalizing by dividing by $\overline{\delta^2}S$ makes $G(\vec{r}_p)$ independent of the irradiated area S and the scattering power $\overline{\delta^2}$. In this case, $G(\vec{r}_p)$ will decrease monotonically from its maximum value $G(0) = 1$ to $G(\infty) = 0$.

From Eq.(6-21) and Eq.(6-22) the expression for the surface scattering factor is then

$$g(\vec{s}_p) = \overline{\delta^2}S \cdot \int_o^\infty G(\vec{r}_p) \cdot \exp[-i \cdot \vec{s}_p \cdot \vec{r}_p] d^2 r_p = \overline{\delta^2}S \cdot \mathcal{F}_2[G(\vec{r}_p)]. \qquad \text{Eq.(6-23)}$$

And the surface correlation is the inverse Fourier transform of $g(\vec{s}_p)$;

$$G(\vec{r}_p) = \frac{1}{\overline{\delta^2}S} \cdot \int_o^\infty g(\vec{s}_p) \cdot \exp[+i \cdot \vec{s}_p \cdot \vec{r}_p] d^2 s_p = \frac{1}{\overline{\delta^2}S} \cdot \mathcal{F}_2^{-1}[g(\vec{s}_p)]. \qquad \text{Eq.(6-24)}$$

$g(\vec{s}_p)$, the so-called "surface scattering factor," is a measure of the relative strength of the roughness wave-vector components $\vec{s}_p$. This term may also be called the spectral density function since it contains the spectrum of Fourier wave-vectors $\vec{s}$ contained in the surface roughness, and consequently determines the contributions of surface roughness to the distribution of scattered electromagnetic wave.

6.2.3.3 Comparison Between Surface Scattering and Volume Scattering

Comparing Sections 6.2.3.1 and 6.2.3.2 to Section 3.2 (in which a standard treatment of an electron density distribution function in a scattering volume is presented) we can see that surface scattering theory and volume scattering theory are very alike. The basic mechanism of volume scattering originates in the electron density distribution function $\rho(\vec{R})$ or the local electron density fluctuation function $\eta(\vec{R})$. The dimensionality in volume scattering is three. For surface scattering, the basic mechanistic factor is the surface roughness distribution function $\delta(\vec{R}_p)$ and the dimensionality is two.

By analogy to volume scattering, we can call the term $\overline{\delta^2}S$ the invariant of surface scattering, Ks. The subscript s indicates that it is the surface scattering invariant and distinguishes itself from the volume scattering invariant Kv defined by Eq.(3-27),

$$Kv = \frac{1}{(2\pi)^3} \cdot \int_o^\infty I(\vec{s}) dv_s = \overline{\eta^2} V.$$

The surface scattering invariant is given by

$$Ks = \frac{1}{(2\pi)^2} \cdot \int_o^\infty g(\vec{s}_p) d^2 s_p = \overline{\delta^2} S. \qquad \text{Eq.(6-25)}$$

The comparison of surface scattering theory to volume scattering theory is listed in Table 6-2.

6.2.3.4 Surface Scattering Intensity

The scattering factor discussed in Section 6.2.3.2 depends only on the statistical properties of the surface. However, the surface scattering is a phenomenon which also depends on the wavelength of

Table 6-2

Comparison of Volume Scattering and Surface Scattering

Volume Scattering	Surface Scattering
Dimensionality = 3	Dimensionality = 2
Position Vector $\vec{R} = x\cdot\vec{e}_1 + y\cdot\vec{e}_2 + z\cdot\vec{e}_3$	Position Vector $\vec{R}_p = x\cdot\vec{e}_1 + y\cdot\vec{e}_2$
Scattering Vector $\vec{s} = \vec{R} - \vec{ko} = s_1\cdot\vec{u}_1 + s_2\cdot\vec{u}_2 + s_3\cdot\vec{u}_3$	Scattering Vector $\vec{s}_p = \vec{k}_p - \vec{ko}_p = s_{p_1}\cdot\vec{u}_1 + s_{p_2}\cdot\vec{u}_2$
Electron Density Fluctuation Function $\eta(\vec{R})$	Surface Roughness Function $\delta(\vec{Rp})$
Correlation Function of Electron Density Fluctuation $\gamma(\vec{r}) = \frac{\overrightarrow{\eta(R)}^2}{\overline{\eta^2}_V}$	Correlation Function of Surface Roughness Distribution $G(\vec{r}_p) = \frac{\overrightarrow{\delta(Rp)}^2}{\overline{\delta^2}_S}$
$\overline{\eta^2}$ = mean square electron density fluctuation	$\overline{\delta^2}$ = mean square surface roughness
V = volume scattering volume	S = surface scattering area
Volume Scattering Intensity $I(\vec{s}) = \overline{\eta^2}_V \mathcal{F}[\gamma(\vec{r})]$	Surface Scattering Factor $g(\vec{s}_p) = \overline{\delta^2}_S \mathcal{F}_2[G(\vec{r}_p)]$

incident radiation, optical properties of the media, and angles of incidence and scattering. Thus, the total surface scattering intensity is the product of two terms, namely, the optical factor and the scattering factor. For an unpolarized electromagnetic wave incident at polar angle ϕ_o, the differential fraction dP of incident energy per unit solid angle $d\Omega = \sin\phi\, d\phi\, d\chi$, scattered into the direction specified by polar angle ϕ and azimuthal angle χ is given by (191)

$$\frac{dP}{d\Omega} = \left[\left(\frac{4\pi^2}{\lambda^4}\right)\cos^2\phi\right]\left|1 - n_{12}^2\right|^2\left(\frac{|\varphi_\phi|^2}{|v - iqn_{12}^2|^2} + \frac{|\varphi_\chi|^2}{|v - iq|^2}\right)]g(\vec{s_p})$$

Eq.(6-26)

where

$$\varphi_\phi = \frac{(v \cdot v_o \cdot \cos\chi + k_p \cdot k_{op} \cdot n_{12}^2)}{v_o - iq_o n_{12}^2} - \frac{i(1/\lambda)v \cdot \sin\chi}{v_o - iq_o} \qquad \text{Eq.(6-27)}$$

and

$$\varphi_\chi = \left(\frac{1}{\lambda}\right)\left(\frac{v_o \cdot \sin\chi}{v_o - iq_o n_{12}^2} + \frac{i(1/\lambda)\cdot\cos\chi}{v_o - iq_o}\right). \qquad \text{Eq.(6-28)}$$

In these equations, the polar angles ϕ_o and ϕ are measured from the normal of the average surface plane, the azimuthal angle χ is measured relative to the plane of incidence, q_o and q are the components of the wave vectors perpendicular to the average surface;

$q_o = |\vec{ko}|\cos\phi_o$, (incident wave)

$q = |\vec{k}|\cos\phi$, (scattered wave)

and

$$v_o = (2\pi/\lambda)[\sin^2\phi_o - n_{12}^2]^{1/2} = -(2\pi/\lambda)i[n_{12}^2 - \sin^2\phi_o]^{1/2},$$

$$v = (2\pi/\lambda)[\sin^2\phi - n_{12}^2]^{1/2} = -(2\pi/\lambda)i[n_{12}^2 - \sin^2\phi]^{1/2}.$$

The first term in Eq.(6-26) is the so-called "optical factor." It contains the polarizability and angular radiation characteristics of photons in the presence of an interface but without any effects of surface roughness.

6.2.3.5 Relations Between Theory and Experiment

In order to calculate the surface scattering intensity distribution on the two-dimensional detector plane, the coordinate system has to be redefined. Referring to Figure 6-7, the average plane of the interface is now parallel to the x′y′ plane and the normal to the average plane is parallel to the z′ axis. The x′, y′, and z′ Cartesian coordinates are called the sample axes. The scattered wave vector $\vec{k}$ can be considered as a point on a sphere with polar angle ϕ and azimuthal angle χ, or expressed in Cartesian coordinates:

$$\vec{k} = (2\pi/\lambda)[\sin\phi\cdot\cos\chi\cdot\vec{u_1'} + \sin\phi\cdot\sin\chi\cdot\vec{u_2'} + \cos\phi\cdot\vec{u_3'}] \qquad \text{Eq.(6-29)}$$

where $\vec{u_1'}$, $\vec{u_2'}$, $\vec{u_3'}$ are the orthogonal unit vectors along the x′, y′, and z′ axes, respectively. The reference axes are defined by the incident x-ray propagation direction, which is parallel to the x-axis, and the detector plane, which is parallel to the yz plane. So we have

$$\vec{ko} = (2\pi/\lambda)\vec{u_1'}. \qquad \text{Eq.(6-30)}$$

Upon parallel incidence, the incident x-ray beam is parallel to the average plane of the interface and the x′, y′, z′ axes coincide with the x, y, z axes. For a two-dimensional isotropic rough surface, the rotation of the surface around the z-axis has no effect on its

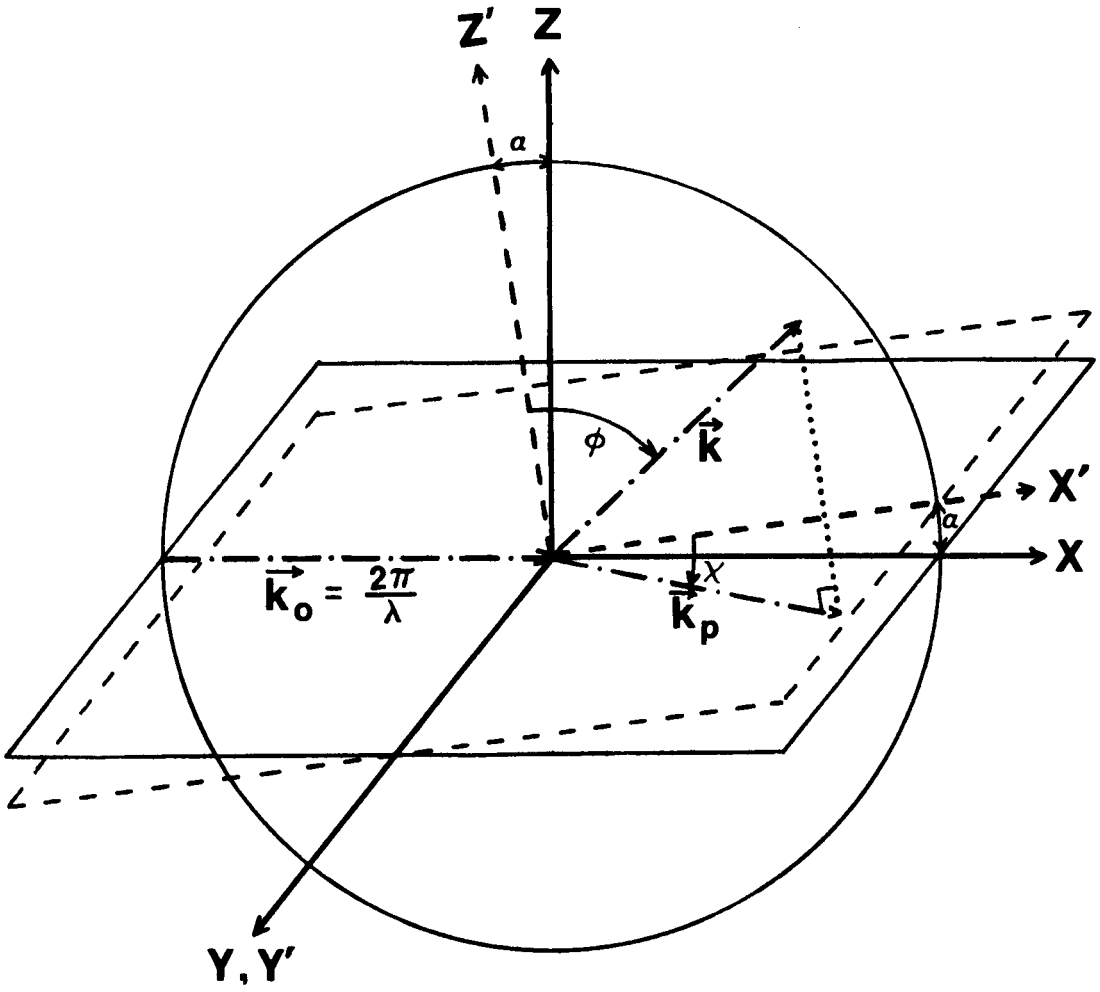


Figure 6-7. Sample axes with respect to laboratory reference axes.

scattering spectrum, but the rotation around the y-axis does affect the surface scattering spectrum. For the latter case we can say the surface is tilted toward the z-axis and the tilting angle α is the angle between the z- and z'-axis and also the x- and x'-axis while the y-axis always coincides with the y'-axis. The relationship between the unit vectors of the coordinate systems are

$$\vec{u_1'} = \cos\alpha \cdot \vec{u_1} + \sin\alpha \cdot \vec{u_3} \qquad \text{Eq.(6-31a)}$$

$$\vec{u_2'} = \vec{u_2} \qquad \text{Eq.(6-31b)}$$

$$\vec{u_3'} = -\sin\alpha \cdot \vec{u_1} + \cos\alpha \cdot \vec{u_3}. \qquad \text{Eq.(6-31c)}$$

The reciprocal space vector is

$$\vec{s} = \vec{k} - \vec{ko} = s_1 \cdot \vec{u_1} + s_2 \cdot \vec{u_2} + s_3 \cdot \vec{u_3} \qquad \text{Eq.(6-32)}$$

with

$$s_1 = (2\pi/\lambda)[\sin\phi \cdot \cos\chi \cdot \cos\alpha - \cos\phi \cdot \sin\alpha - 1],$$

$$s_2 = (2\pi/\lambda)[\sin\phi \cdot \sin\chi],$$

$$s_3 = (2\pi/\lambda)[\sin\phi \cdot \cos\chi \cdot \sin\alpha + \cos\phi \cdot \cos\alpha].$$

where s_2 and s_3 are the two components observed on the detector plane. To be consistent with the notation usually used in SAXS theory (see Section 3.2.2), the scattering angle, $\angle(\vec{k}, \vec{ko})$, is named as 2θ. So we have

$$\begin{aligned} s &= (s_1^2 + s_2^2 + s_3^2)^{1/2} \\ &= (4\pi/\lambda)[(1 - \sin\phi \cdot \cos\chi \cdot \cos\alpha + \cos\phi \cdot \sin\alpha)/2]^{1/2} \\ &= (4\pi/\lambda)\sin\theta. \end{aligned}$$

When $\alpha = 0$ and $\chi = 0$, $2\theta = \pi/2 - \phi$.

The net change in the wave vector component along the surface between the incident and scattered photon is

$$\vec{s}_p = \vec{k}_p - \vec{ko}_p = s_{p_1} \cdot \vec{u_1} + s_{p_2} \cdot \vec{u_2} \qquad \text{Eq.(6-33)}$$

where

$$s_{p_1} = (2\pi/\lambda)[\sin\phi\cdot\cos\chi - \cos\alpha\,],$$

$$s_{p_2} = (2\pi/\lambda)[\sin\phi\cdot\sin\chi\,].$$

It is also convenient to use the vectors

$$\vec{b} = \vec{s}/2\pi = (\vec{k} - \vec{ko})/2\pi, \qquad \text{Eq.(6-34)}$$

$$\vec{b}_p = \vec{s}_p/2\pi = (\vec{k}_p - \vec{ko}_p)/2\pi. \qquad \text{Eq.(6-35)}$$

When $\chi = 0$, $s_{p_2} = 0$, this corresponds to the intersection of the plane of incidence and the detector plane. In other words, the intensity observed along the meridional direction is the intensity of scattered x-xays which remain in the plane of incidence. The width of the meridional surface scattering intensity streak observed on the detector plane is an indication of the degree of deviation from the law of reflection for smooth surfaces.

6.2.3.6 Roughness Analysis of a Two-Dimensional Isotropic Surface

If the roughness distribution on the surface has circular symmetry about its average normal direction, the scattering factor $g(\vec{s}_p)$ has circular symmetry too. The phase factor $\exp[-i\cdot\vec{s}_p\cdot\vec{r}_p]$ can be replaced by its average,

$$\langle\exp[-i\cdot\vec{s}_p\cdot\vec{r}_p]\rangle = \frac{\sin(s_p\cdot r_p)}{s_p\cdot r_p}.$$

This means Eq.(6-19) and Eq.(6-20) can be reduced to:

$$g(s_p) = \overline{\delta^2}S\cdot\int_o^\infty 2\pi r_p G(r_p)\frac{\sin(s_p\cdot r_p)}{s_p\cdot r_p}dr_p, \qquad \text{Eq.(6-36)}$$

$$G(r_p) = \frac{1}{(2\pi)^2\cdot\overline{\delta^2}S}\cdot\int_o^\infty 2\pi\cdot s_p g(s_p)\frac{\sin(s_p\cdot r_p)}{s_p\cdot r_p}ds_p. \qquad \text{Eq.(6-37)}$$

The invariant of surface scattering now becomes

$$Ks = \overline{\delta^2}S = (1/2\pi)^2 \cdot \int_0^\infty 2\pi s_p g(s_p) ds_p . \qquad \text{Eq.(6-38)}$$

By the analogy to volume scattering, an important characterization factor called the correlation distance τ, can be defined as the distance at which the correlation function $G(r_p)$ drops to the value 1/e, where e = 2.71828... . $\tau = 0$ implies there will be no correlation between two different points on the surface, no matter how close to each other they may be. $\tau \rightarrow 0$ implies a surface with very densely packed irregularities. If τ is large, points on the surface will be correlated even if they are far apart. Hence a large τ implies gently rolling surfaces, i.e. large distances between hills and valleys. A surface with large τ is shown in Figure 6-8 (A) whereas Figure 6-8 (B) shows the profile of a surface with small τ.

If we take an isotropic Gaussian approach for the correlation function $G(r_p)$,

$$G(r_p) = \exp[-r_p^2/\tau^2], \qquad \text{Eq.(6-39)}$$

we get for the scattering factor

$$g(s_p) = \overline{\delta^2}S \cdot \pi \cdot \tau^2 \cdot \exp[-s_p^2 \cdot \tau^2/4]. \qquad \text{Eq.(6-40)}$$

If the correlation function is of an isotropic exponential form;

$$G(r_p) = \exp[-r_p/\tau], \qquad \text{Eq.(6-41)}$$

then

$$g(s_p) = \overline{\delta^2}S \frac{2 \cdot \pi \cdot \tau^2}{[1 + (s_p \cdot \tau)^2]^{3/2}} . \qquad \text{Eq.(6-42)}$$

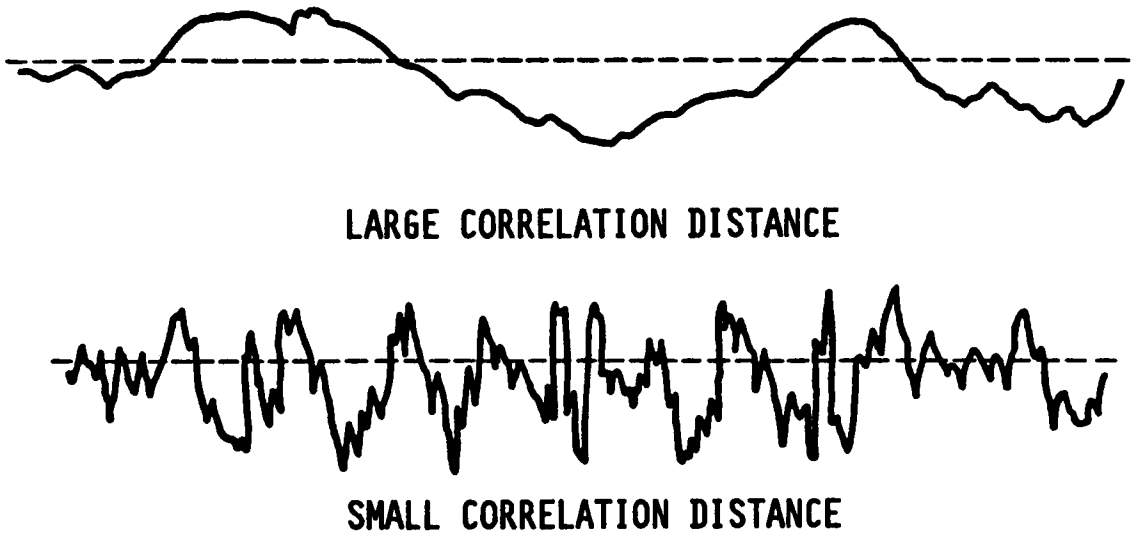


Figure 6-8. Profiles of surfaces with (A) large correlation distance and (B) small correlation distance (171).

6.3 Numerical Results

Eq.(6-26) can be used directly to calculate the surface scattering pattern of x-rays by any rough surface if the surface correlation function $G(\vec{r}_p)$ and subsequent spectral density function $g(\vec{s}_p)$ are known. On the other hand, if the scattering intensity is high enough to detect, it may be possible to determine $g(\vec{s}_p)$ and $G(\vec{r}_p)$ directly from the scattering pattern. In the following calculations, a perfect point-collimated parallel incident x-ray beam is assumed.

Figure 6-9 is a three-dimensional plot for the distribution of the optical factor on the detector plane (yz-plane) for a polystyrene-void (vacuum) interface upon parallel incidence. The optical factor is zero at $s_{p_3} = 0$, this indicates no scattered waves distribute along the equatorial direction. The ridges on Figure 6-9 correspond to the position where the scattering angle 2θ (angle between incident and scattered waves) equals the critical glancing angle for total reflection. The optical factor depends on the value of s_{p_3} only, i.e. it depends on the value of the polar angle ϕ and is independent of the azimuthal angle χ of the scattered wave (refer to Eq.(6-32) with $\alpha = 0$). In Figure 6-10 the optical factor distribution on the plane of incidence (the meridional direction, $s_{p_2} = 0$) for three different kinds of interfaces listed in Table 6-1 are plotted against the scattering angle 2θ, $2\theta = \pi/2 - \phi + \alpha$. From Eq.(6-26) we can see that when 2θ is less than the critical angle for total reflection, the optical factor increases with $\cos^2\phi$. When 2θ is greater than the critical angle, the optical factor falls off

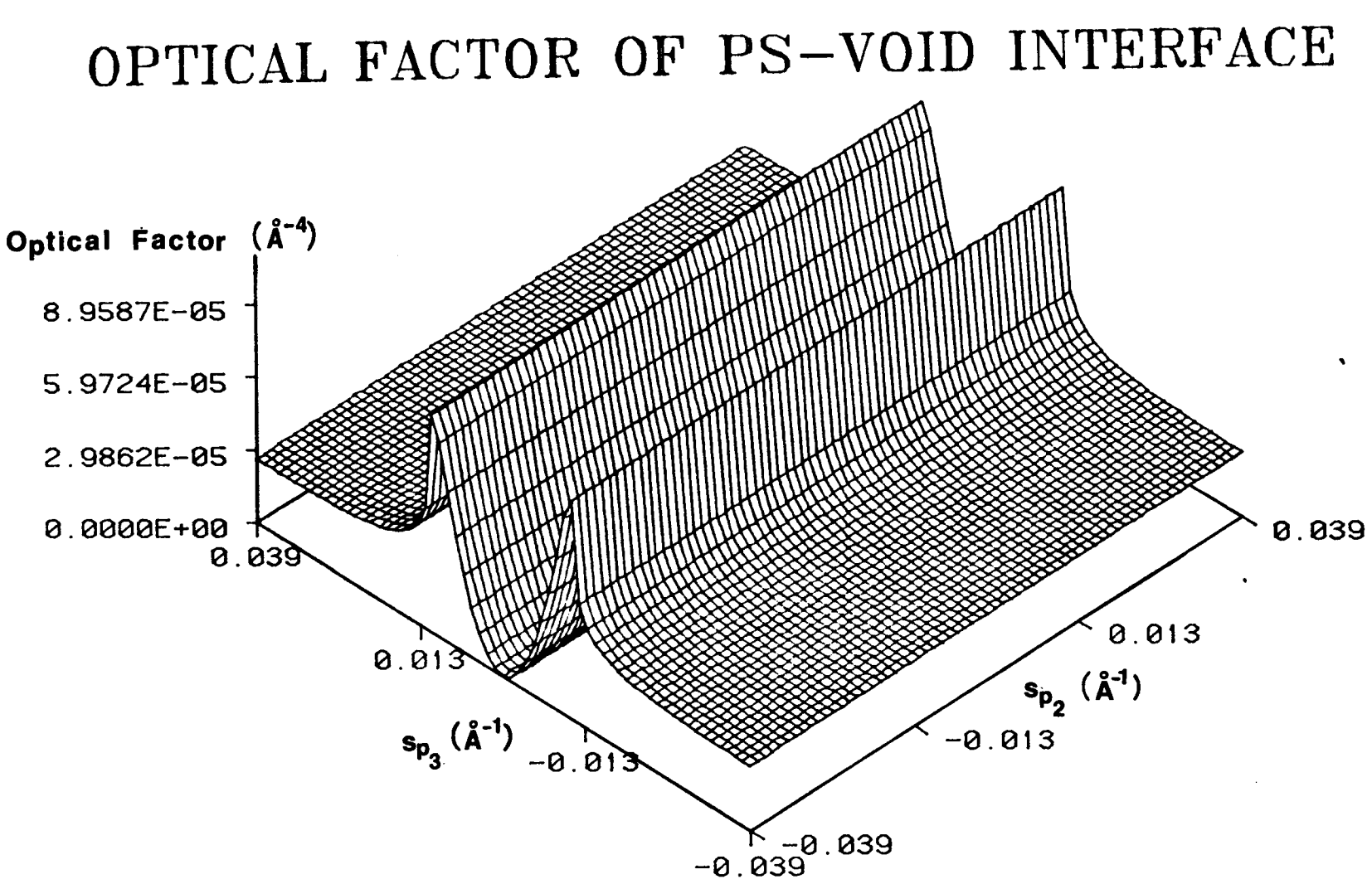


Figure 6-9. Three-dimensional plot for the calculated optical factor of PS-void interface upon parallel incidence of x-rays.

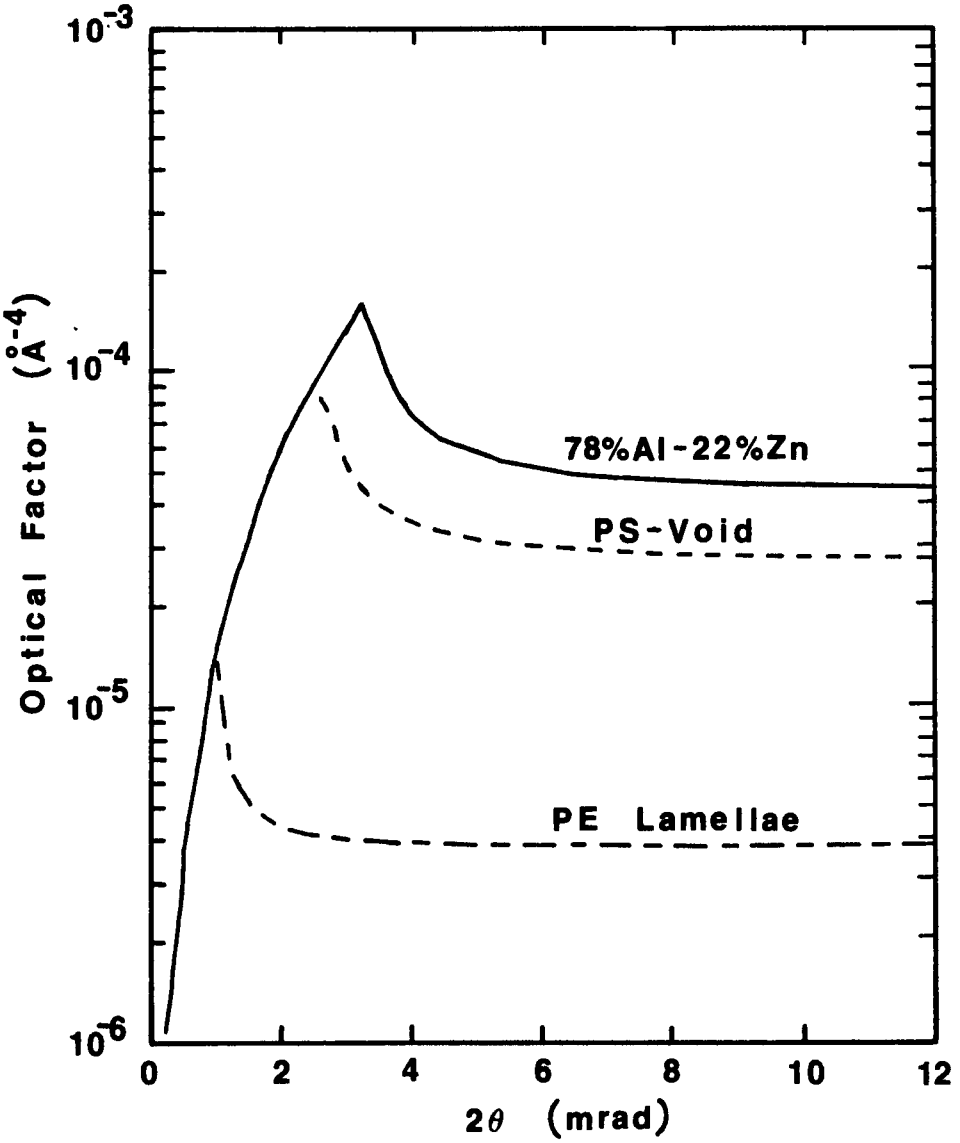


Figure 6-10. Calculated angular distribution of optical factor on the plane of incidence versus scattering angle 2θ for three kinds of interfaces.

sharply to an asymptotic value which is proportional to the term $|1 - n_{12}|^2$. Figure 6-10 clearly shows that the higher the interfacial electron contrast, the higher the optical factor for x-ray surface scattering.

The surface scattering intensity distribution on the two-dimensional detector plane for a polystyrene-void interface is calculated according to Eq.(6-26) by taking an isotropic Gaussian approach for the surface correlation function. The results are compared in Figure 6-11 for two different correlation distances τ in Eq.(6-39). τ = 10 μm and 0.1 μm for Figure 6-11 (A) and (B), respectively. These two values for τ are chosen because the typical value of τ for polystyrene crazes is about 5 μm, as we will show in the next section. Evidently when the correlation distance increases, many of the scattered waves are forced to remain in the plane of incidence. The other feature is the appearance of maximum peaks on the three-dimensional intensity plot. In Figure 6-12 the calculated surface scattering intensity distribution on the plane of incidence (i.e. along the meridional direction) is plotted against the scattering angle 2θ for various interfaces listed in Table 6-1 by assuming different values for the correlation distance τ in Eq.(6-39). Clearly as the correlation distance increases the scattered waves will be directed in the near specular direction, and the surface scattering intensity streak becomes narrower and sharper. The position of the maximum peak depends on both of the interfacial electron contrast and the correlation distance.

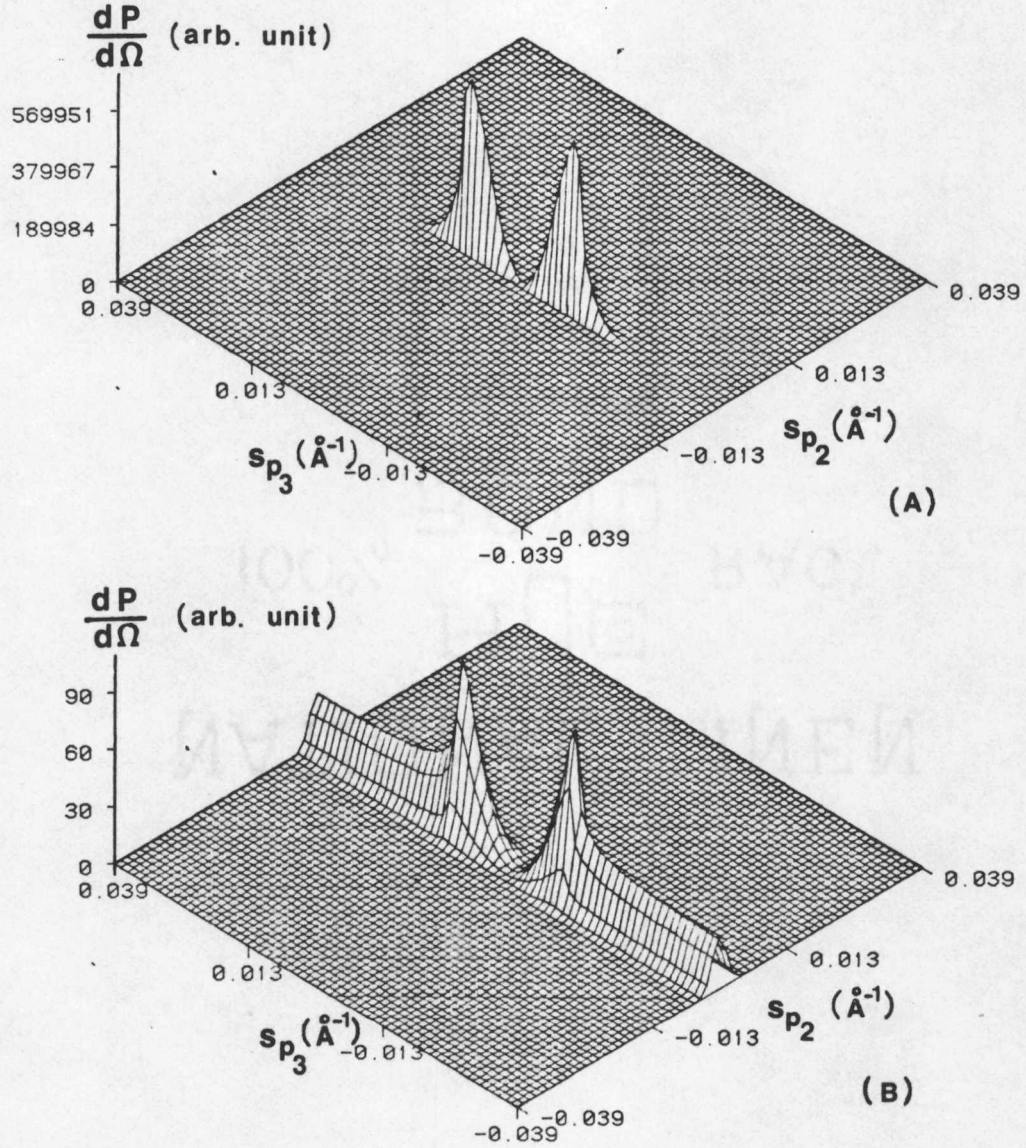


Figure 6-11. Three-dimensional plot for the calculated surface scattering intensity distribution on the detector plane by assuming an isotropic Gaussian correlation function for the PS-void interface. (A) τ = 10 μm; (B) τ = 0.1 μm.

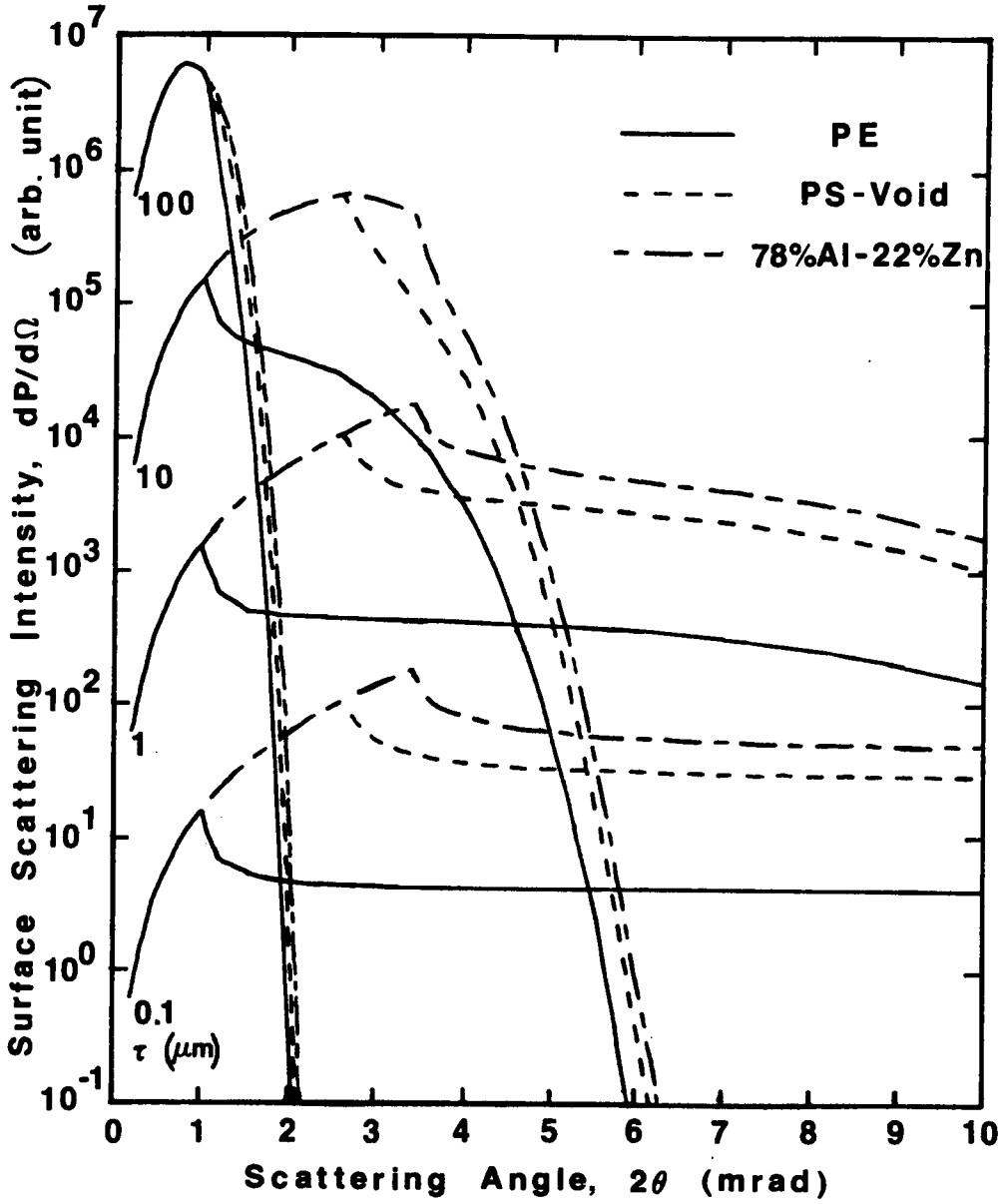


Figure 6-12. Comparison among the three calculated surface scattering intensity distribution on the plane of incidence for three kinds of interfaces with different Gaussian correlation lengths τ (0.1, 1, 10 and 100 μm).

Next, we consider the effect of tilting the surface on its scattering behavior. The surface scattering intensity distribution on the plane of incidence for various tilting angles α is compared in Figure 6-13. A PS-void interface with a Gaussian correlation distance $\tau = 1$ μm is employed in the calculation. The result shows when α is greater than the critical glancing angle for total reflection, the surface scattering intensity drops sharply and may be not high enough to detect in real experimental measurements.

6.4 Experimental Results

6.4.1 Laminated Polystyrene Samples

Westbrook et al. (82) modeled the interfaces between crazes and bulk polymer by a laminated sample constructed of stacked films of about 0.1 mm thickness. During the experimental runs, the planes of the films were placed parallel to the incident x-ray beam. The films were stacked in two ways to test the effect of varying interfacial electron contrast: mechanically clamping (PS-air) and glued together with epoxy (PS-epoxy). The SAXS patterns of each case obtained by Westbrook et al. (82) are shown in Figure 6-14 (A) and (B), respectively.

Comparing Figure 6-14 with Figure 6-11, the lack of scattering intensity along the equatorial direction indicates the predominant contribution to the SAXS from laminated film sample is surface scattering, whereas the volume scattering is negligible (or too low to be detected). The angular variations of the observed intensity on the

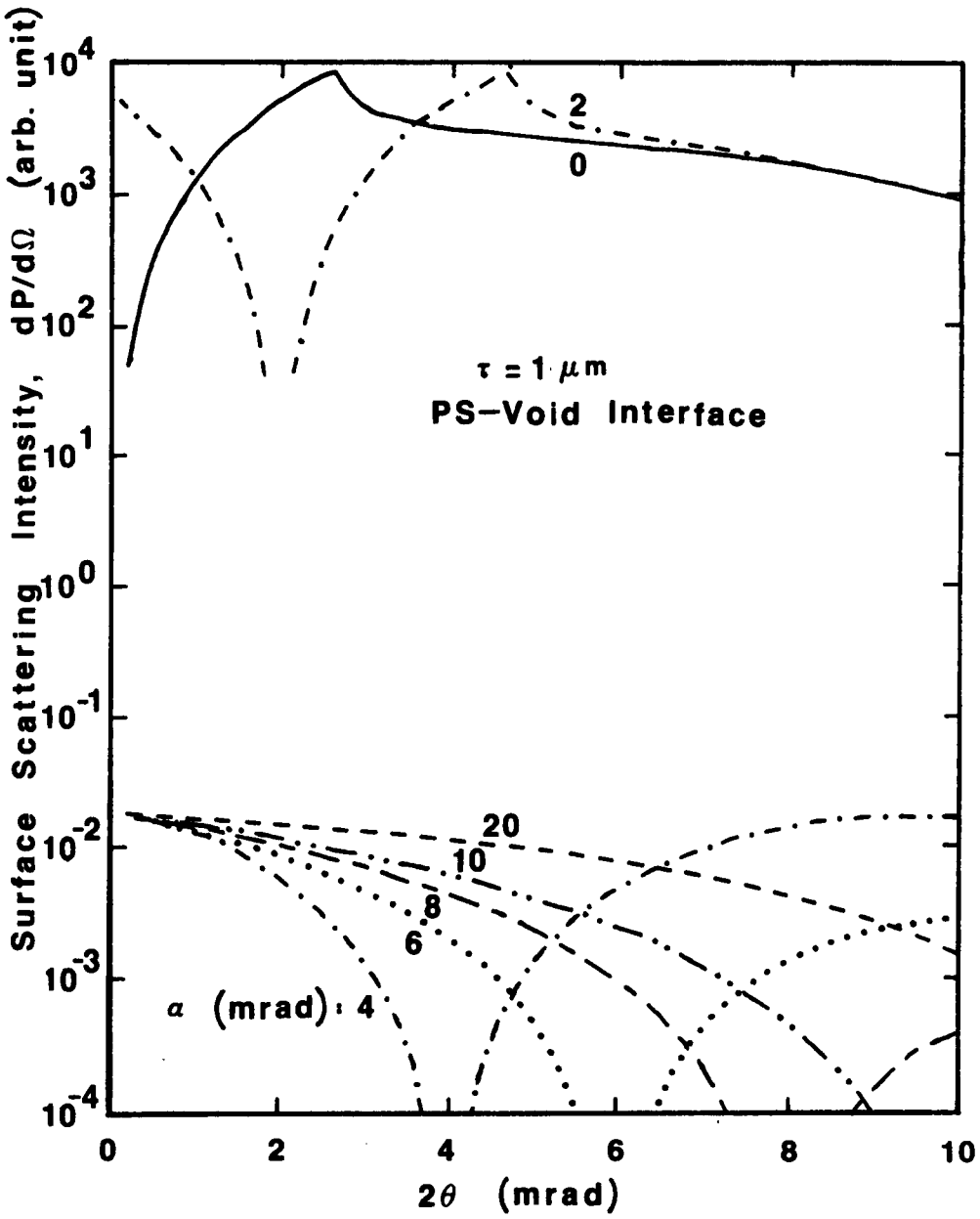


Figure 6-13. Calculated angular distribution of the surface scattering intensity on the plane of incidence for a PS-void interface at various tilting angles α.

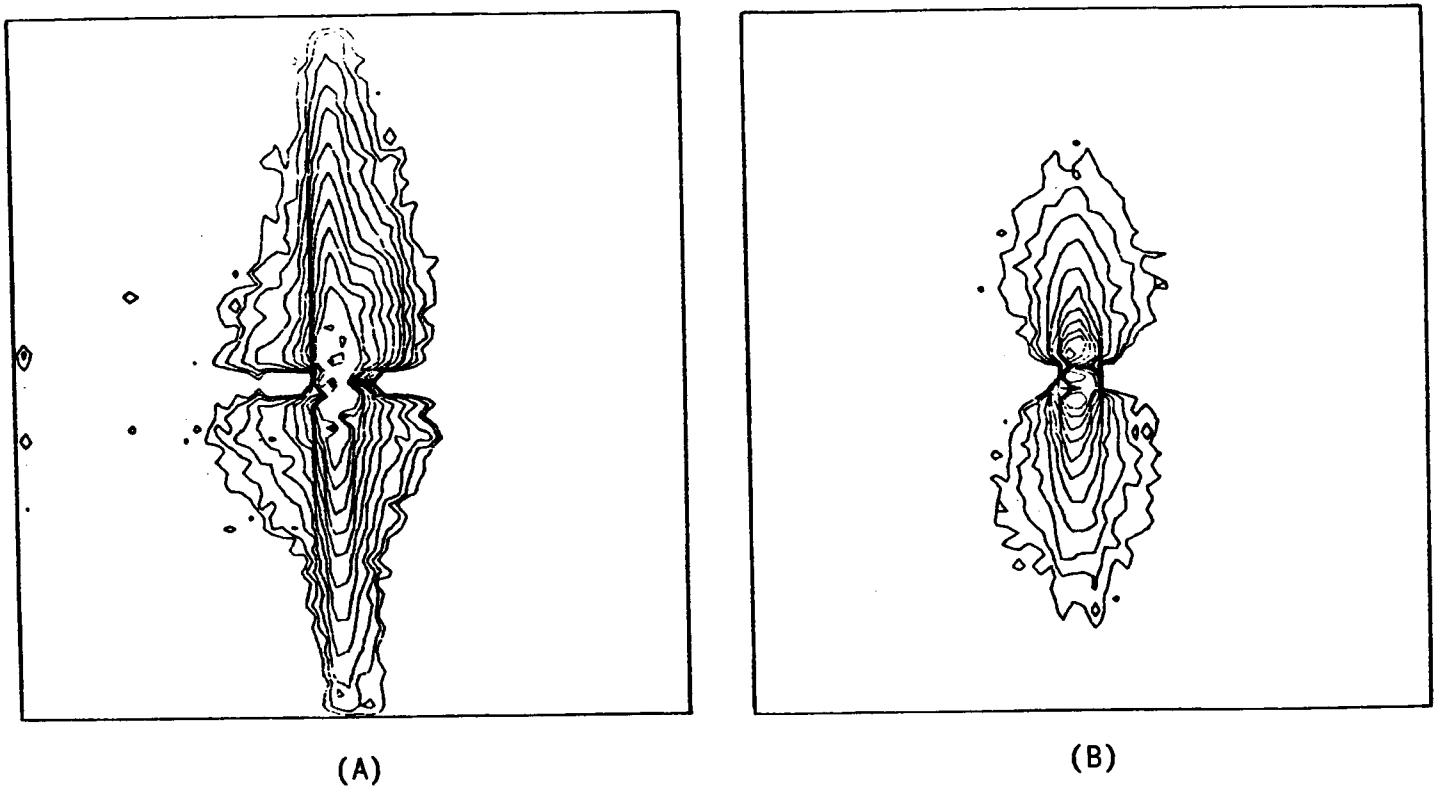


Figure 6-14. Effect of varying the interfacial electron contrast on the SAXS patterns from laminated PS film sample: (A) PS-air; (B) PS-epoxy.

plane of incidence (i.e. the meridional direction of the scattering pattern) are compared in Figure 6-15 for PS-air and PS-epoxy interfaces. The scattering factor calculated by applying Eq.(6-26) is also shown in Figure 6-15. When the scattering angle is greater than the critical glancing angle for total reflection, the scattering factor basically duplicates the shape of the observed scattering intensity distribution. Assuming the roughness distribution on the interfacial surface is isotropic in two-dimensions, Eq.(6-37) can be used to calculate the surface roughness correlation function $G(r_p)$. The results are shown in Figure 6-16 for PS-air and PS-epoxy interfaces. Because of the finite angular region of experimental measurements, the most accurate portion of Figure 6-16 is the initial portion. As can be seen in Figure 6-16, the initial portions of the two curves superimpose each other quite well. The correlation distance τ is 1.60 μm for PS-air interface and 2.50 μm for PS-epoxy interface.

6.4.2 Polystyrene Craze

Figure 6-17 (A) is a typical SAXS pattern of crazes in unoriented polystyrene. Also shown in Figure 6-17 (B) is the SAXS pattern of the simulated laminated PS-air interface. There is a striking resemblance between the two in the meridional direction. The major difference is that the meridional intensity streak from the crazes is superposed on a less intense diffuse background. This diffuse background can be attributed to the volume scattering component originating from local inhomogeneities in electron density distribution in the bulk polymer

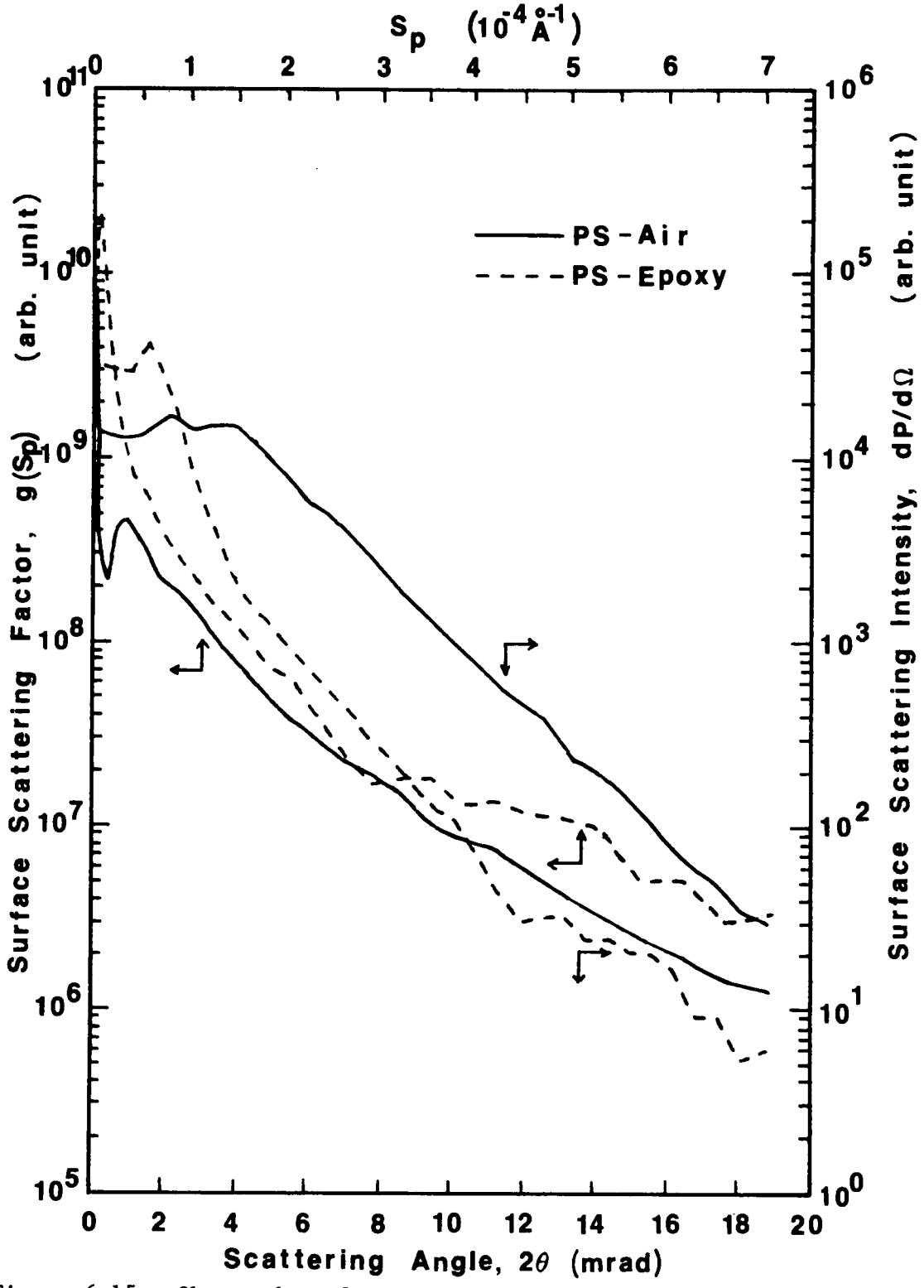


Figure 6-15. Observed surface scattering intensity and calculated surface scattering factor on the plane of incidence versus scattering angle 2θ for PS-air and PS-epoxy interfaces.

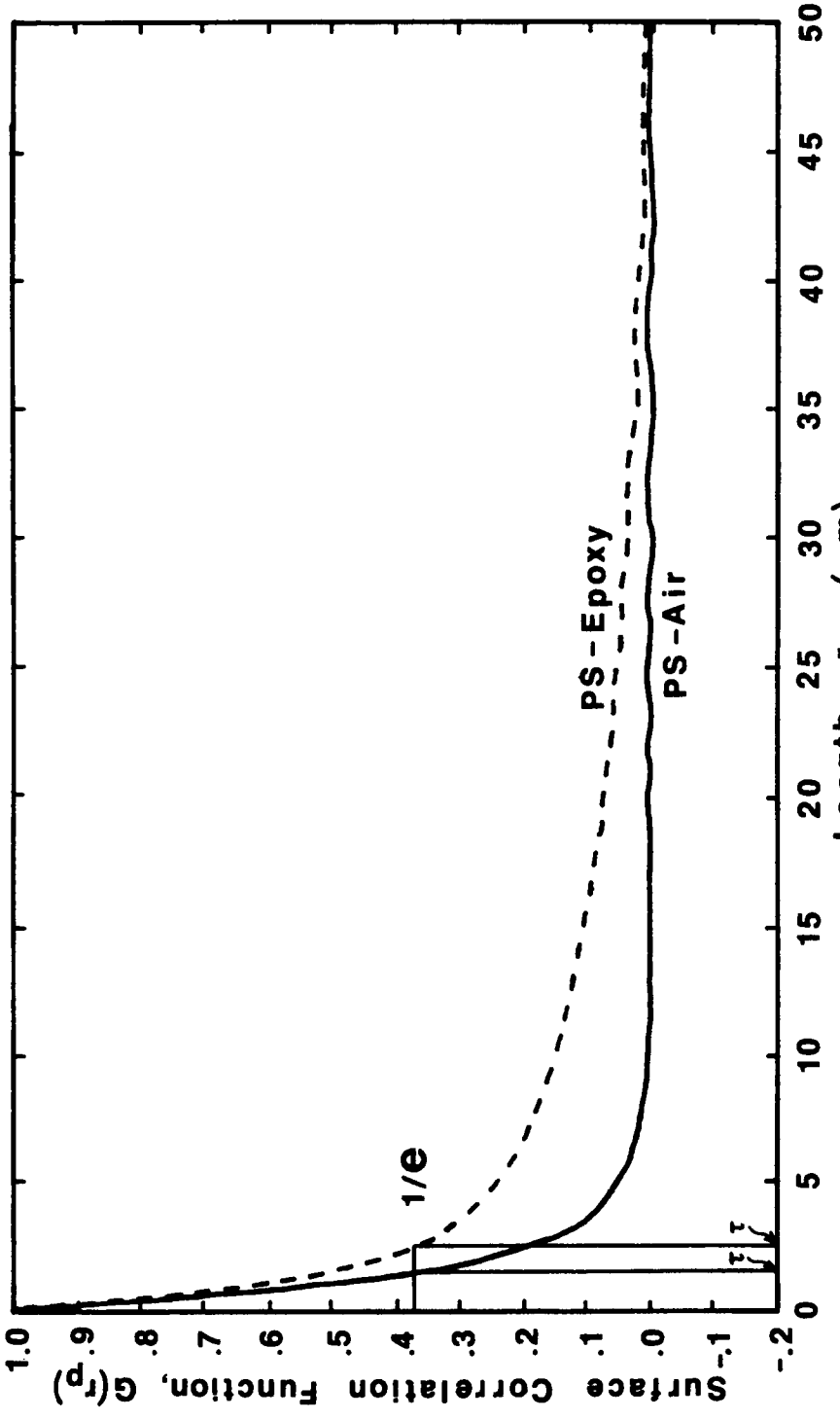


Figure 6-16. Surface roughness correlation function $G(r_p)$ of PS-air and PS-epoxy interfaces versus length r_p.

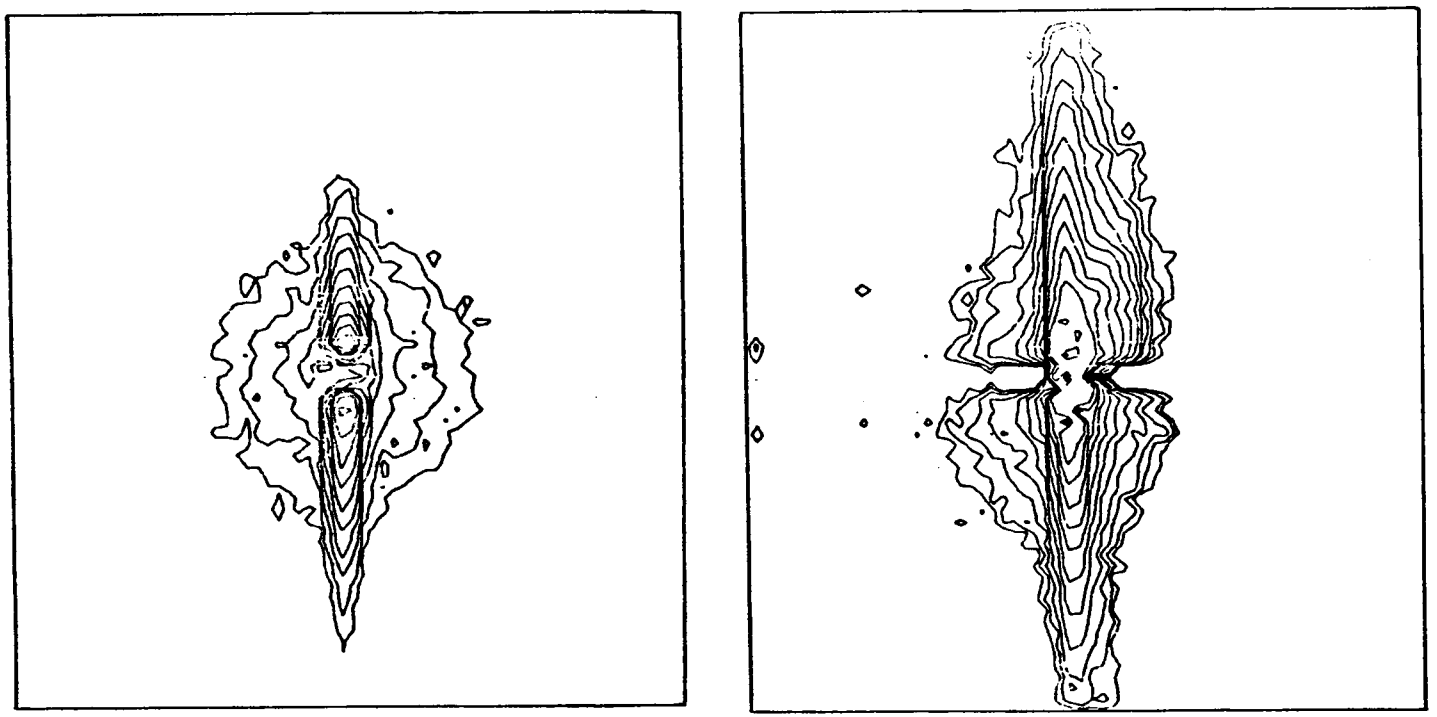


Figure 6-17. Comparison of SAXS patterns from: (A) typical polystyrene crazes; (B) laminated polystyrene film (PS-air) sample.

phase and the microvoids in the craze matter. The surface scattering component originates from the roughness of the surfaces forming the internal boundaries in crazed polystyrene.

Tilting experiments have been performed on crazes in unoriented polystyrene in previous work (81, 82). The work done by Westbrook et al. (82) is shown in Figure 6-18 in which (A) is parallel incidence ($\alpha = 0^{o}$), (B) is tilted incidence ($\alpha = 8^{o}$), and (C) is the pattern obtained by subtracting Figure 6-18 (B) from Figure 6-18 (A). In Figure 6-18 (B) the surface scattering intensity streak disappeared after tilted eight degrees toward the tensile axis. The remaining observed intensity can be attributed to volume scattering, which shows circular symmetry and corresponds to an isotropic distribution of the inhomogeneities that cause volume scattering. The net result shown in Figure 6-18 (C) is an intensity streak that lies along the direction parallel to the tensile axis, which corresponds to the average direction of the normals to the craze interface. This pattern resembles the shape in intensity contour predicted by the theory presented earlier (refer to Figure 6-11). In the latter case, the incident x-ray beam is assumed to be point-like. The collimation error may cause the ideal surface scattering pattern to smear somewhat. This is why the observed surface intensity streak is not so narrow as the calculated one.

Since both theory (Figure 6-11) and experiments (Figure 6-14) show the equatorial intensity is zero when only surface scattering phenomenon occurs, and that the volume scattering background shows a

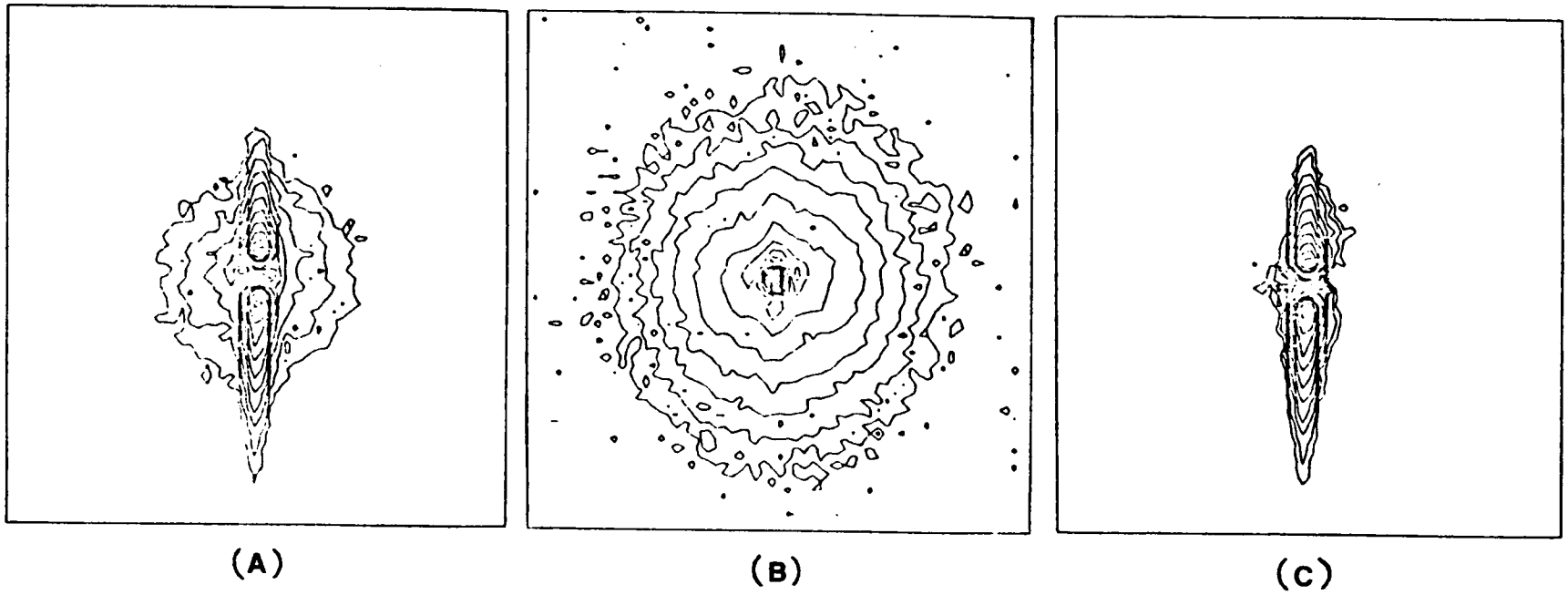


Figure 6-18. Effect of tilting on the SAXS patterns of crazes in initially unoriented polystyrene: (A) incident x-ray is normal to the tensile axis; (B) sample is tilted eight degrees toward the tensile axis; (C) contour pattern obtained by subtracting (B) from (A).

nearly circular pattern for crazes in unoriented polystyrene [Figure 6-18 (B)], the surface scattering intensity along the meridional direction for SAXS from crazes in unoriented polystyrene can then be approximated by

$$\frac{dP}{d\Omega}(\Phi, \chi = 0) = \frac{dP}{d\Omega}(s_{p_2} = 0) = I_{obs}(s_2 = 0) - I_{obs}(s_3 = 0)$$
$$= I_{obs}(\mu = 0^{o}) - I_{obs}(\mu = 90^{o}) \qquad \text{Eq.(6-43)}$$

where μ is the azimuthal angle measured from the meridional direction on the scattering pattern. The surface scattering theory can then be applied to the meridional intensity after correction for volume scattering. Volume scattering theory can be directly applied to the equatorial intensity.

In Figure 6-19 the surface scattering intensity and the surface scattering factor on the plane of incidence for the craze SAXS pattern shown in Figure 6-17 (A) are plotted against the scattering angle 2θ. By assuming an isotropic roughness distribution on the interface, the surface roughness correlation function $G(r_p)$ and the surface scattering invariant Ks can be calculated using Eq.(6-37) and Eq.(6-38), respectively. The calculated surface roughness correlation function of the PS craze is compared with that of the PS-air interface in Figure 6-20. The correlation distance of PS craze is 4.71 μm. Figure 6-21 shows the transmission electron micrographs of a fractured craze (66) and an air craze in the process of fracturing (208). It thus seems reasonable to postulate the correlation distance of PS crazes corresponds to the average length of the steps caused by the microcrack jumping from one craze-matrix interface to the other.

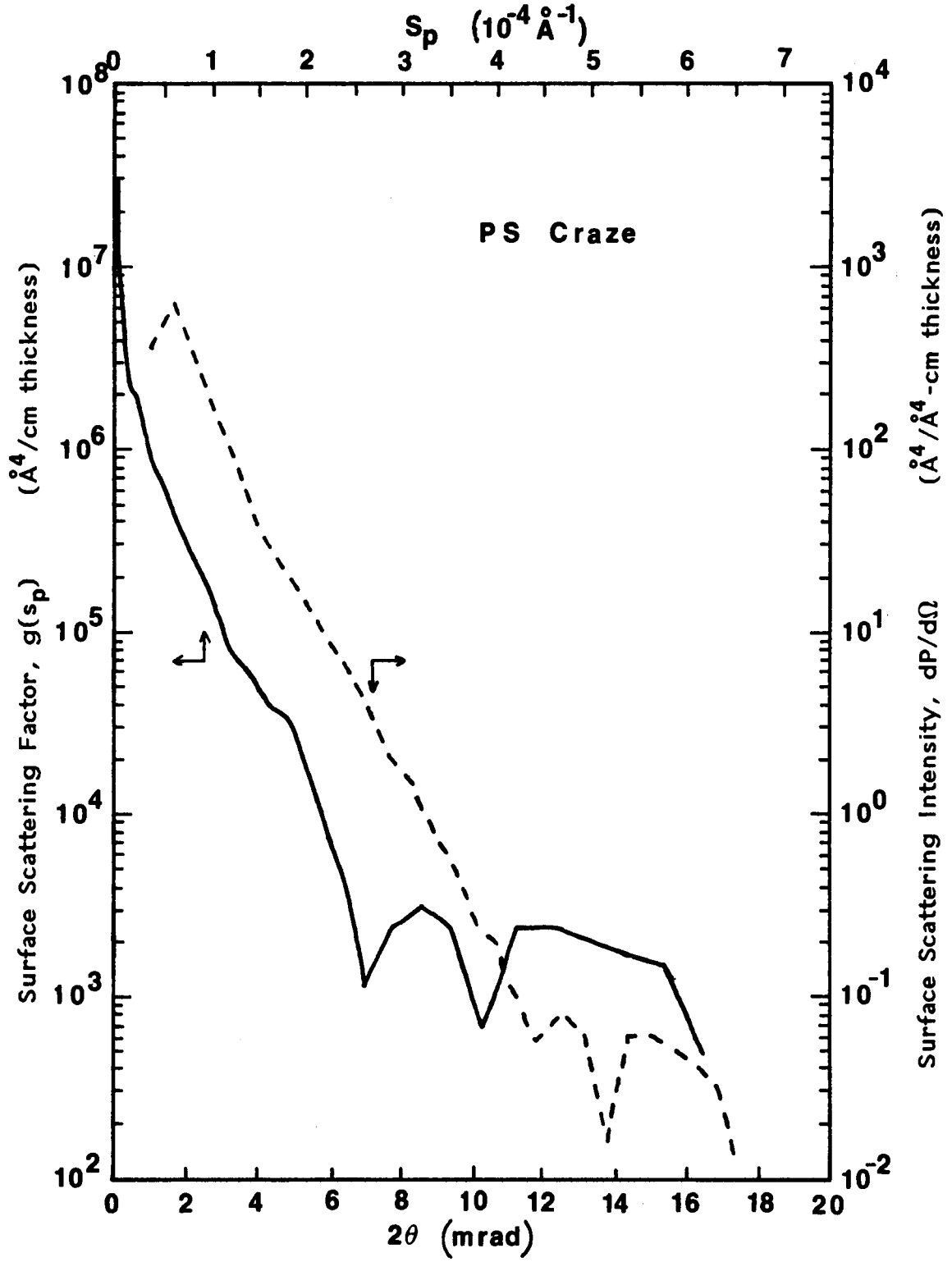


Figure 6-19. Surface scattering intensity and surface scattering factor on the plane of incidence versus scattering angle 2θ for polystyrene crazes.

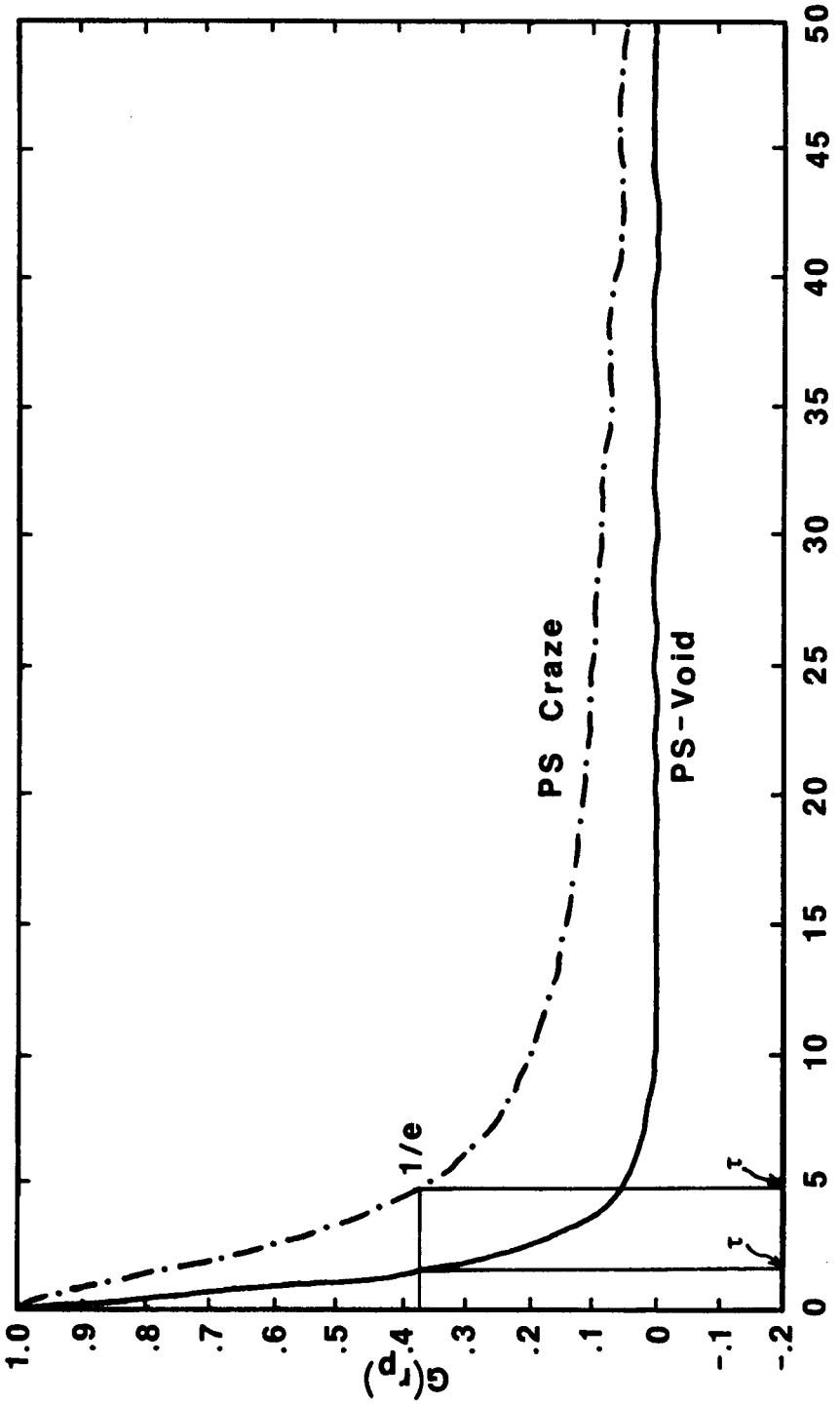


Figure 6-20. Comparison of the surface roughness correlation function of polystyrene crazes and PS-air interfaces.

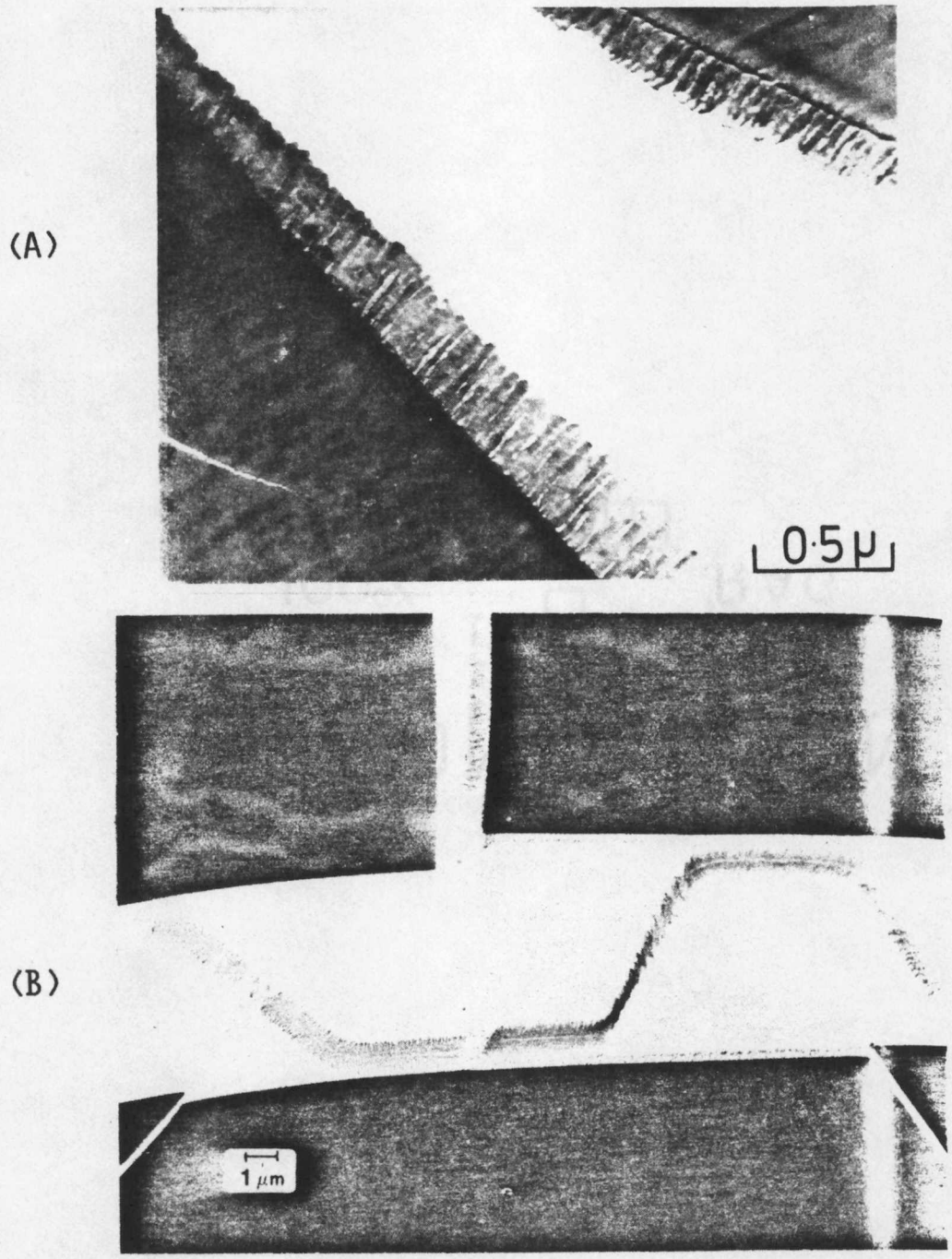


Figure 6-21. Transmission electron micrographs of (A) a fractured craze (66) and (B) an air craze in the process of fracturing (208).

6.5 Summary and Conclusions

In order to investigate the surface scattering phenomenon of polystyrene crazes by SAXS, theoretical calculations for various two-phase scattering systems such as PE, PS crazes, and 78%Al-22%Zn alloy were performed and experiments were carried out on crazed polystyrene. The following conclusions are important to the fundamental theory of SAXS.

(1) Surface scattering and volume scattering always coexist when x-rays (or electromagnetic waves of any wavelength) are scattered from any type of solid state material. The theories for surface scattering and volume scattering resemble each other in many ways. Generally speaking, surface scattering theory is similar to volume scattering theory for a slit collimated x-ray system. The former component has usually been neglected in the SAXS studies and when people talk about SAXS, they really mean volume scattering.

(2) For two-phase (also multi-phase) systems which have high electron contrasts and inherently flat interfacial structures, the surface scattering component is no longer negligible and sometimes even greater than the magnitude of the volume scattering component.

(3) The contribution of surface scattering to the total observed x-ray scattering depends on the arrangement of the specimen geometry, i.e. it depends on the glancing angle of x-rays on the average plane of the exterior surface or the interior interfaces.

(4) Most of the surface scattering intensity is limited to the specular direction, i.e. on the incidence plane formed by the propagation direction of incident x-rays and the normal direction to the average plane of surface. The magnitude of the surface scattering intensity streak depends on the surface roughness correlation distance, the mean square of the surface roughness, and the surface area.

(5) There is no surface scattering intensity along the direction perpendicular to the normal direction of the average interface plane. This feature enables the processing of SAXS data of polystyrene crazes. We can treat the intensity data in the equatorial direction by conventional small-angle x-ray (volume) scattering theory and the meridional direction intensity data after correction for the volume scattering component by surface scattering theory.

(6) The correlation distance of the surface roughness distribution function for PS crazes corresponds to the average length of the steps made by the microcrack jumping from one craze-matrix interface to the other.

(7) Small-angle x-ray surface scattering behavior can be used to study the surface structures of materials which need to be highly polished, for example, optical fibers, metal coated thin films, and chips used in the microcircuits of computers.

CHAPTER 7

SAXS OF CRAZES IN UNORIENTED POLYSTYRENE

Through concurrent observation of sample specimens by small-angle x-ray scattering (SAXS) during dynamic tensile tests, the microstructure changes and mechanical behavior of bulk specimens of unoriented polystyrene were investigated. The observed scattering intensity was resolved into two components: surface scattering and volume scattering. The propagation of microcracks can be deduced from the former component. The size and concentration of microvoids can be determined from the latter component. The crazing and fracture process is discussed in terms of microvoid formation and microcrack propagation as a function of the applied tensile stress and material parameters. The effects of material parameters were analyzed by altering the molecular weight and molecular weight distribution of polystyrene (PS), blending monodispersed PS, and using polydispersed PS samples.

7.1 General Description

Generally speaking, the change of shape variations of the SAXS patterns of crazes in unoriented PS with stress level is independent of the molecular weight and its distribution, while the scattering intensity does depend on molecular weight and its distribution. Figure 7-1 shows the typical changes of SAXS patterns of crazes in unoriented polystyrene (PSBI) as a function of the loading state. The last point in this figure corresponds to the point observed in the

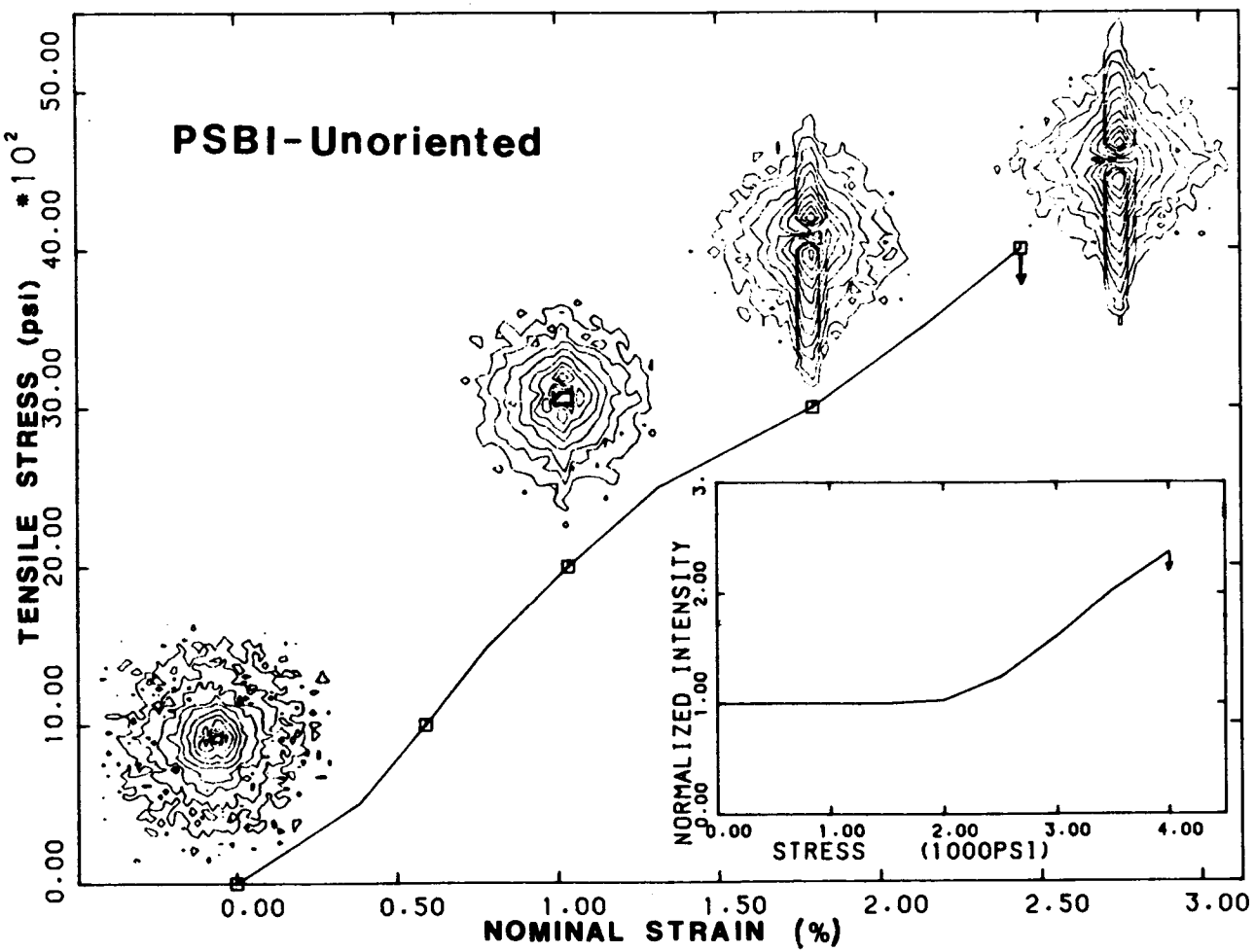


Figure 7-1. Variation of craze SAXS pattern in initially unoriented polystyrene with loading state. PSBI: $\overline{Mn}$ = 160,000; DP = 1.14.

specimen just before fracture. As described in Chapter 4, crazes were created in unoriented bulk specimen of thickness 1.6 mm using steps of 500 psi per 500 seconds increases in uniaxial tensile stress. The strain is converted from the digital reading according to a digital reading - gauge length calibration curve. The insert in Figure 7-1 is a plot of normalized scattering intensity versus stress level. The normalized scattering intensity is defined as the ratio of the total scattered counts for a sample at stress to that for an undeformed sample:

$$\text{Normalized Scattering Intensity} = \frac{P_{NET,\sigma}}{P_{NET,\sigma=0}} \qquad \text{Eq.(7-1)}$$

where

$$P_{NET} = [P_{RAW} - P_{DC} * \frac{SMON}{CMON}] - \frac{TS}{TBAC} * \frac{SMON}{BMON}(P_{BAC} - P_{DC} * \frac{BMON}{CMON})$$

P = total scattered counts registered by the 2DPSD

P_{NET} = dark current and background corrected counts of specimen

P_{RAW} = raw counts of specimen

P_{BAC} = background counts

P_{DC} = dark current counts

SMON = beam monitor counts during scattering run

BMON = beam monitor counts during background run

CMON = beam monitor counts during dark current run

TS = transmission coefficient of specimen

TBAC = transmission coefficient of background.

Since the strain of the sample is only several percent, the corrections for thickness and irradiated volume changes are neglected.

The basic features of the SAXS patterns from PS under load are that before crazing is initiated, the scattering pattern shows circular symmetry and the normalized scattering intensity stays equal to one. Once the crazing process starts, an anisotropic scattering pattern is observed and the normalized scattering intensity increases continuously until fracture. There exists a strong narrow intensity streak parallel to the tensile axis and superimposed on a less intense background. This can be seen clearly from Figure 7-2 in which the intensity distribution along different azimuthal slices are shown for a typical craze SAXS result. In the very small angle region the intensity falls off quickly (almost one order of magnitude) as the azimuthal angle μ changes from 0° to 90°, where μ is measured from meridional direction (tensile axis) toward the equatoral direction on the SAXS pattern. When 2θ is greater than eight milliradian (mrad) or μ is greater than 45 degrees there is almost no difference between intensity distribution along different azimuthal directions.

Figure 7-3 compares the effect of loading on the scattering intensity distribution of crazes along the meridional ($\mu = 0^{o}$) and the equatorial ($\mu = 90^{o}$) directions. Qualitatively, the shape of these curves does not change with stress level. The increase in the meridional intensity with stress is much more than the equatorial intensity increase. The increase in the equatorial intensity with stress is most significant at scattering angles greater than four milliradians.

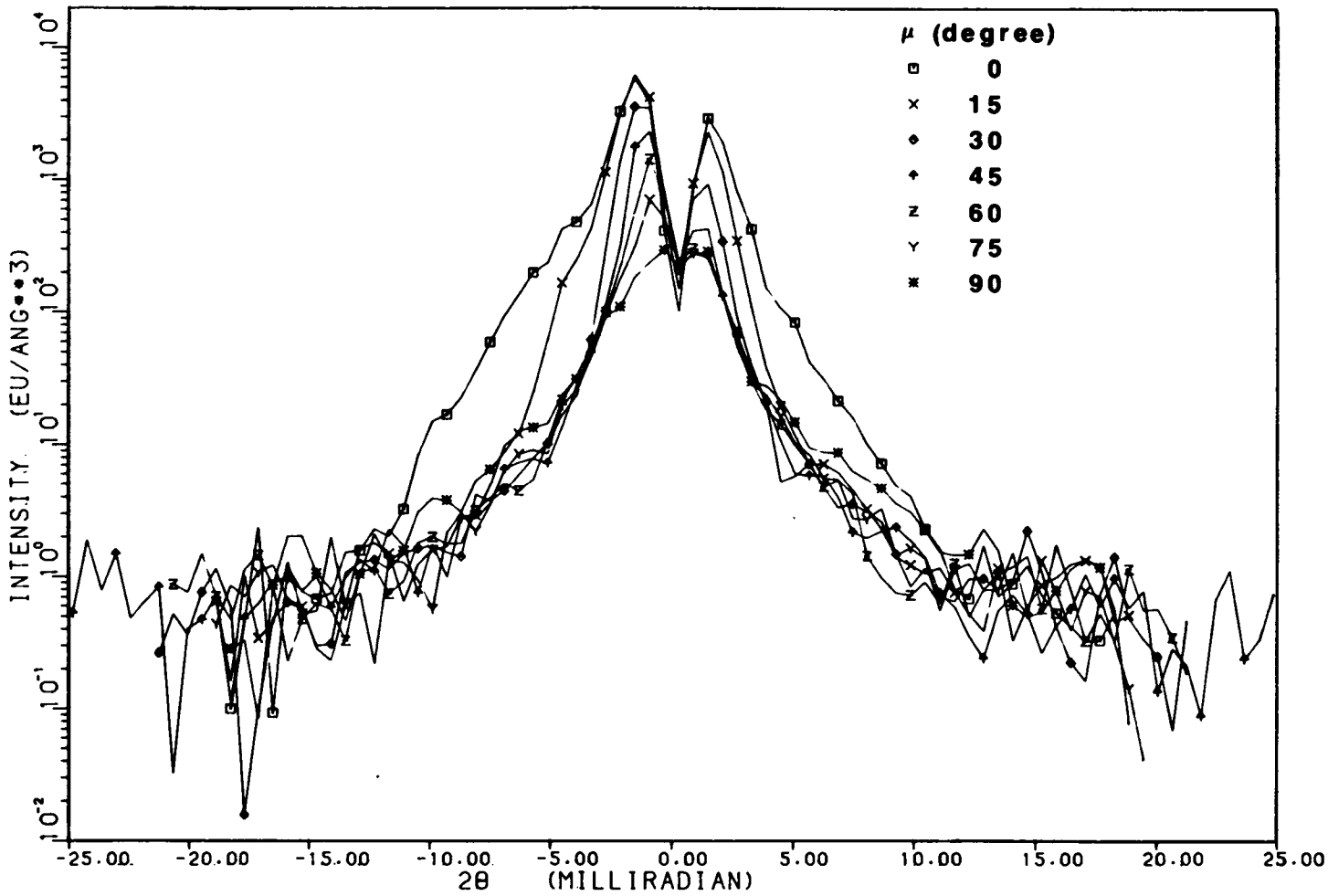


Figure 7-2. Logarithmic intensity distribution along different azimuthal slices for a typical craze SAXS pattern in unoriented polystyrene. PSBI: σ = 3500 psi.

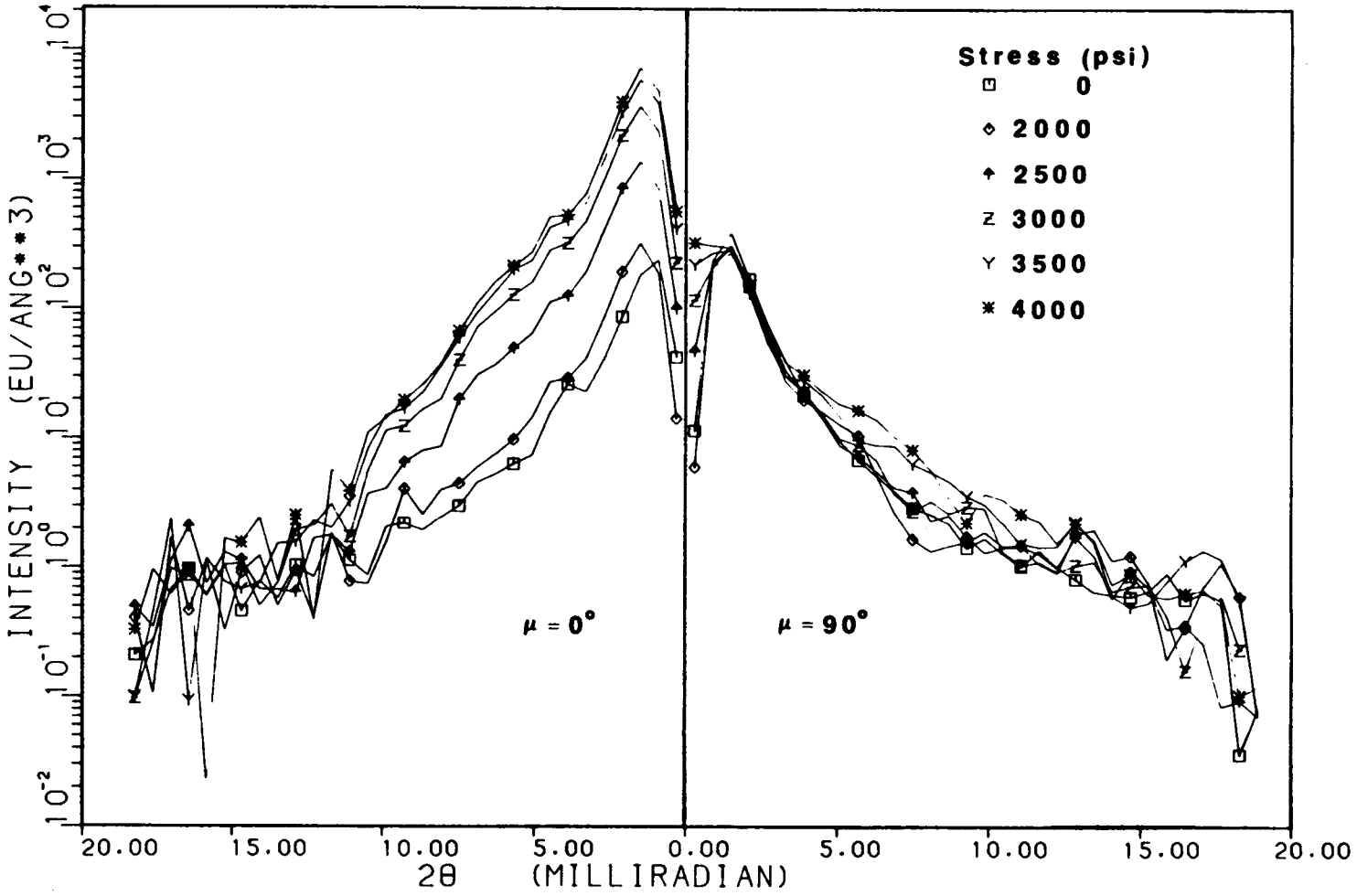


Figure 7-3. Intensity distribution along the meridional direction and the equatorial direction as a function of loading state. PSBI: $\overline{Mn}$ = 160,000; DP = 1.14.

7.2 Characterization of the Origin of SAXS from Crazed Polystyrene

As was described in section 2.3, it was agreed that the initial stages of crack propagation in polystyrene entail a slow growth process in which the crack propagates through the midrib of the mature craze (leaving behind a relatively smooth fracture surface) followed by a regime of increasing crack growth velocity in which material separation occurs at the craze/bulk polymer interfaces (40, 43, 47, 49, 64, 68). Murray and Hull (43) refer to the markings left on fracture surfaces by the latter process as mackerel or patch patterns depending on whether they are regular or irregular. Dramatic confirmation of both the mechanism postulated to give rise to the smooth and the mackerel or patch pattern can be seen in Figure 2-3.

Figure 6-21 (A) shows a transmission electron micrograph of a fractured craze taken by Beahan et al. (66) and Figure 6-21 (B) is an electron micrograph of an air craze caught in the process of fracture taken by Lauterwasser and Kramer (208). The two craze/polymer boundaries have become widely separated. There is a layer of highly drawn fibrils at both the craze surfaces and crack propagation occurs at the boundary of this layer. The inherent interconnection of the craze fibril structure is evidenced by the fact that the craze matter not only remains intact laterally, but apparently supports some amount of stress. As the crack propagates, regions of the craze immediately ahead of the advancing crack front experience a sudden and large increase in applied surface stress (208) and generate more craze matter at the tip of the running crack, leading to the large values of

fracture toughness conventionally measured on these polymeric materials.

Therefore, the microstructure of a crazed polystyrene can be considered to consist of three parts: a foam structure composed of fibrils and microvoids (usually called craze matter), a microcrack which grows through the midrib of craze and material separation occurs at the craze/bulk polymer interfaces, and the uncrazed bulk polymer matrix. The incident x-ray beam is parallel to the "average" plane of the interface of the microcracks. Upon arriving at the interface it is divided into three parts: the direct beam which is shielded by the beam-stop, the reflection scattering caused by the irregularities of the interfaces, and the diffuse scattering caused by the penetration of x-rays into the foam and polymer matrix. The observed scattering intensity is the sum of the latter two components. Since the meridional intensity is mainly caused by surface scattering occuring at interfaces in the crazed sample, the tremendous increase in the meridional intensity with stress can be attributed to the propagation of microcracks and the creation of more interfacial surface area.

7.3 Data Analysis

Since the origin of SAXS from crazed polystyrene is identified, we may now interpret the data in terms of the characterization parameters derived from the surface and volume scattering theories to describe the morphological features of crazes.

7.3.1 Surface Scattering Analysis

As discussed in Chapter 6, both the surface scattering theory and the simulated experiments by laminated samples of PS films show that the equatorial intensity is zero when only the surface scattering phenomenon occurs. Since the volume scattering background shows a circularly symmetric pattern for crazes in initially unoriented polystyrene, the surface scattering intensity along the meridional direction can then be approximated by

$$\frac{dP}{d\Omega}(\phi, \chi = 0) = \frac{dP}{d\Omega}(s_{p_2} = 0) = I_{obs}(s_2 = 0) - I_{obs}(s_3 = 0)$$

$$= I_{obs}(\mu = 0^{o}) - I_{obs}(\mu = 90^{o}) \qquad \text{Eq.(7-2)}$$

where ϕ and χ are the polar angle and azimuthal angle of the scattered wave (see Figure 6-7), respectively. The typical variation of surface scattering intensity distribution along the meridional direction with stress level is shown in Figure 7-4 for PSBI.

Referring to Eq.(6-26), the surface scattering intensity is composed of two parts: (i) an optical factor which depends on the wavelength, optical constants of the scattering interface, and angles of incidence and scattering, and (ii) a surface factor which depends only on the statistical properties of the interface. For the simplest case, the optical factor can be theoretically calculated by assuming the optical properties of the interfaces. Since the electron density of the fibrillar structure is not too different from that of the uncrazed polystyrene and the wavelength of x-rays is much smaller than the dimension of the broken fibrillar residuals on the interface, the

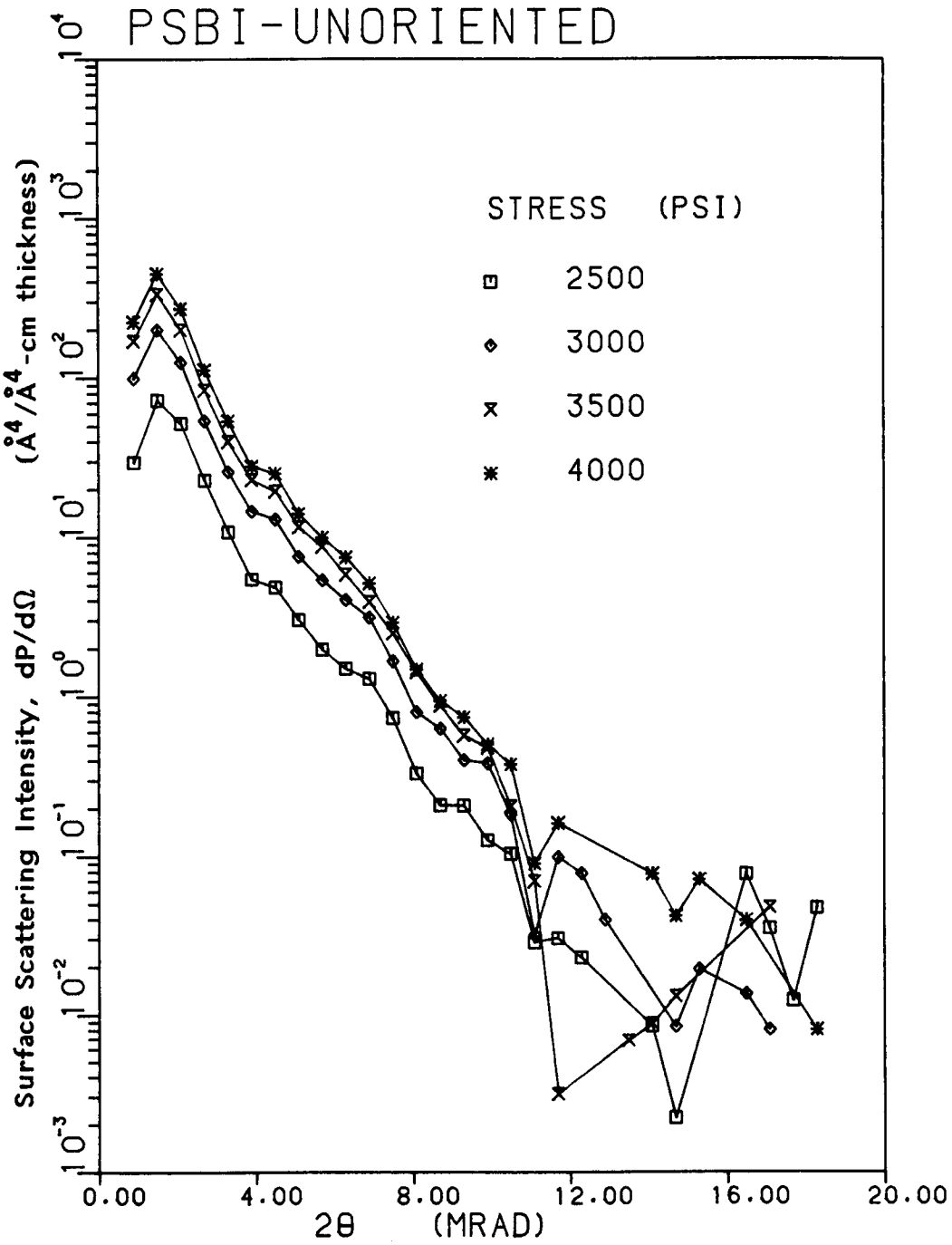


Figure 7-4. Typical variations of surface scattering intensity distribution along the meridional direction with stress levels.

interface between the microcracks and the polymers can then be approximated as the void (vacuum) and polystyrene interface. Further, the roughness distribution on the interfaces can be assumed to be isotropic on the radial direction for a scattering system with cylindrical symmetry. The scattering factor $g(s_p)$ can then be calculated from the meridional surface scattering intensity $dP/d\Omega$ according to Eq.(6-26). The results are plotted against the surface scattering reciprocal space vector $\vec{s}_p$ at various stress levels in Figure 7-5. The surface roughness correlation function $G(\vec{r}_p)$ calculated from Eq.(6-37) at different stress levels is plotted in Figure 7-6. From Figures 7-4 to 7-6 we can see that the basic qualitative features of each plot remain constant over all values of stress, but their quantitative features vary. The quantitative features may be described by two variables, namely, the surface scattering invariant Ks and the correlation distance τ of the surface roughness distribution.

The propagation of microcracks is proportional to the creation of microcrack interfaces. The latter can be analyzed if we compare the surface scattering invariant $\overline{\delta^2}S$ with the stress-strain behavior. The surface scattering invariant for a two-dimensional isotropic interface is given by Eq.(6-38)

$$Ks = \overline{\delta^2}S = (1/2\pi)^2 \cdot \int_o^\infty 2\pi s_p \cdot g(s_p) ds_p .$$

Figure 7-7 (A) shows the surface scattering invariant Ks, which is directly related to the microcrack interfacial area, as a function of the stress level for PSBI. By extrapolating the surface scattering

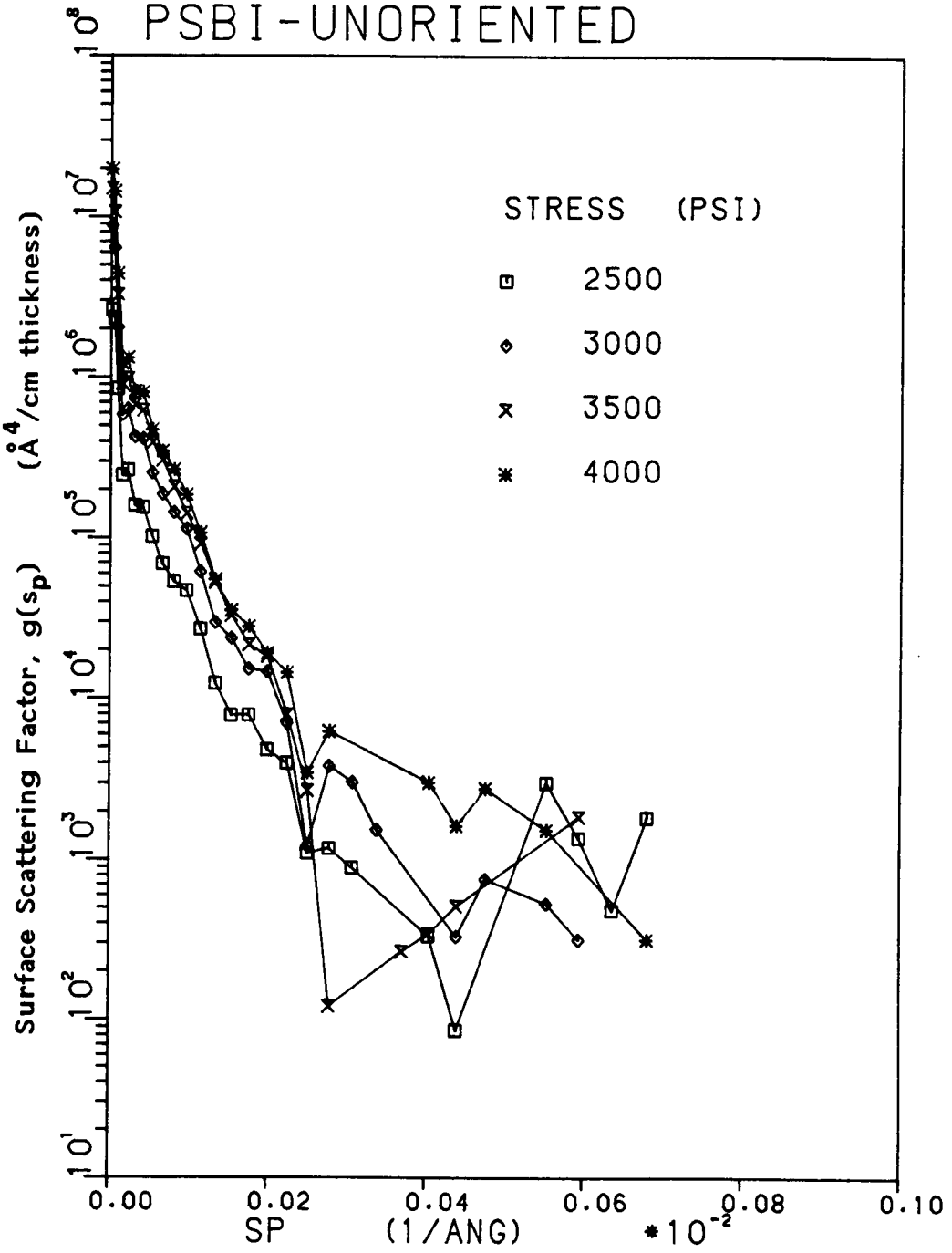


Figure 7-5. Surface scattering factor versus surface scattering reciprocal space vector $\vec{s}_p$ at various stress levels.

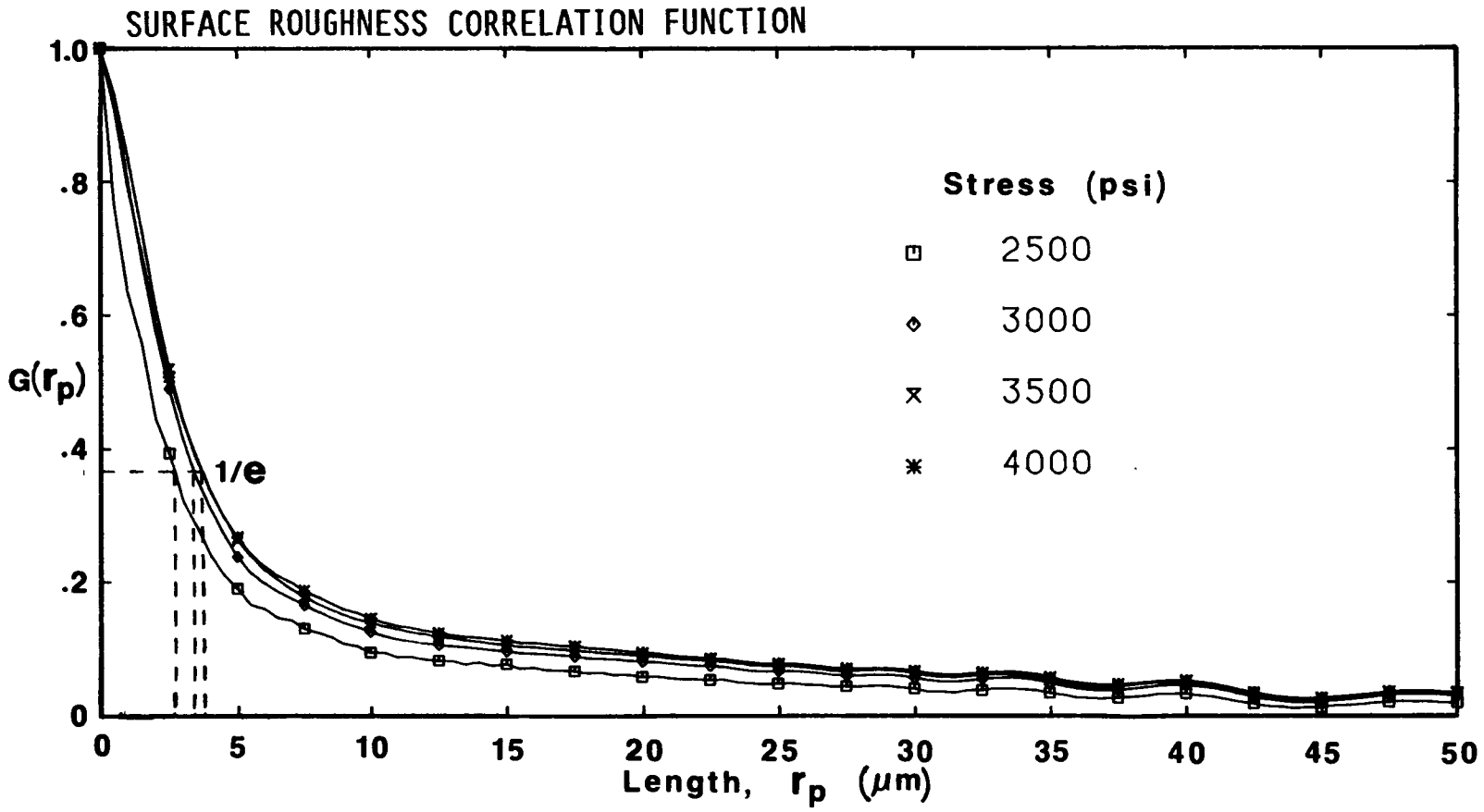


Figure 7-6. Variations of surface roughness correlation function $G(r_p)$ with stress levels.

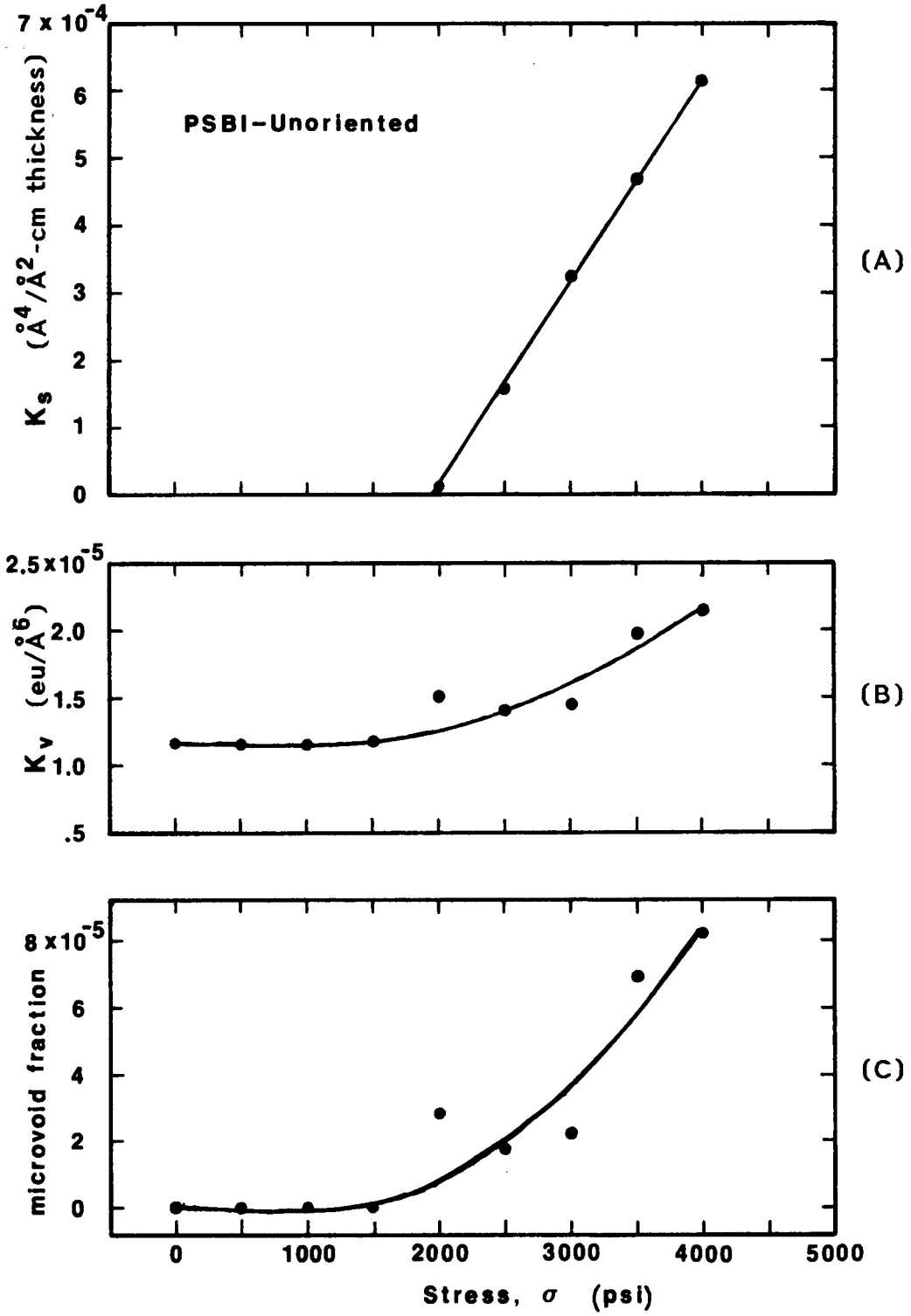


Figure 7-7. (A) Surface scattering invariant, (B) volume scattering invariant, and (C) microvoid fraction as a function of the stress level. PSBI: $\overline{Mn}$ = 160,000; DP = 1.14.

invariant to zero, the microcrack initiation stress can be estimated. After initiation, the surface scattering invariant rises monotonically until fracture occurs. Assuming the mean square surface roughness $\overline{\delta^2}$ is independent of the stress level, then the microcrack interfacial area is directly proportional to the surface scattering invariant. This is not a bad assumption since the surface scattering intensity distribution and the surface roughness correlation function do not vary with stress level. The continuing steady increase in microcrack interfacial area may indicate that microcracks propagate by chain disentanglement and/or chain scission and the continuous increase in strain must mostly be due to continuous drawing of uncrazed polymer matrix into fibrils. If the increase in strain is due to fibril extension, we would observe an increase in craze thickness instead of the increase in interfacial area. The polymer fractures because the density of microcracks exceeds a critical value and the hollow microcracks can no longer sustain local stress due to the lack of support from interconnected fibrils between the opposite boundaries.

The surface roughness correlation function $G(r_p)$ tells us whether the hills and valleys of the surfaces are crowded close together or whether they are far apart. It is characterized by the parameter named correlation distance, τ, which is defined as the distance at which $G(r_p)$ drops to the value 1/e. The meaning of τ is described in Figure 6-8. In Chapter 6 we have concluded that τ corresponds to the average length of the steps caused by the microcrack jumping from one craze-matrix interface to the other (see Figure 6-21). The

correlation distance determined from Figure 7-6 is plotted against stress in Figure 7-8 (A). It is clear the correlation distance increases steeply with stress level at first and then increases smoothly.

7.3.2 Volume Scattering Analysis

The first parameter to be discussed is the volume scattering invariant Kv defined by Eq.(3-27) (74)

$$Kv = \overline{\eta^2}V = (1/2\pi)^3 \int_0^\infty I(s)dv_s.$$

This equation is the integral of the volume scattering intensity over reciprocal space and is directly related to the mean square fluctuation of electron density, irrespective of special features of the structure. If parts of the system were shifted or deformed, the scattering pattern might be altered considerably, but the invariant must remain constant. If, however, new phase(s) with different electron density than original existing phase(s) is (are) produced, the invariant will change, and this is the case for crazing in polystyrene. When crazing starts, new phases (microvoids and fibrils) are created and the invariant increases.

The surface scattering theory and the simulated experiments show the equatorial intensity is constituted by volume scattering only and the tilting experiments show that the volume scattering background has spherical symmetry (see Figure 6-18). The volume scattering invariant can thus be calculated by Eq.(3-43) (74)

$$Kv = \overline{\eta^2}V = (1/2\pi)^3 \cdot \int_0^\infty 4\pi s^2 I(s)ds$$

$$= (1/2\pi)^3 \cdot \int_0^\infty 4\pi s^2 I_{\mu=90^o}(s)ds. \qquad \text{Eq.(7-3)}$$

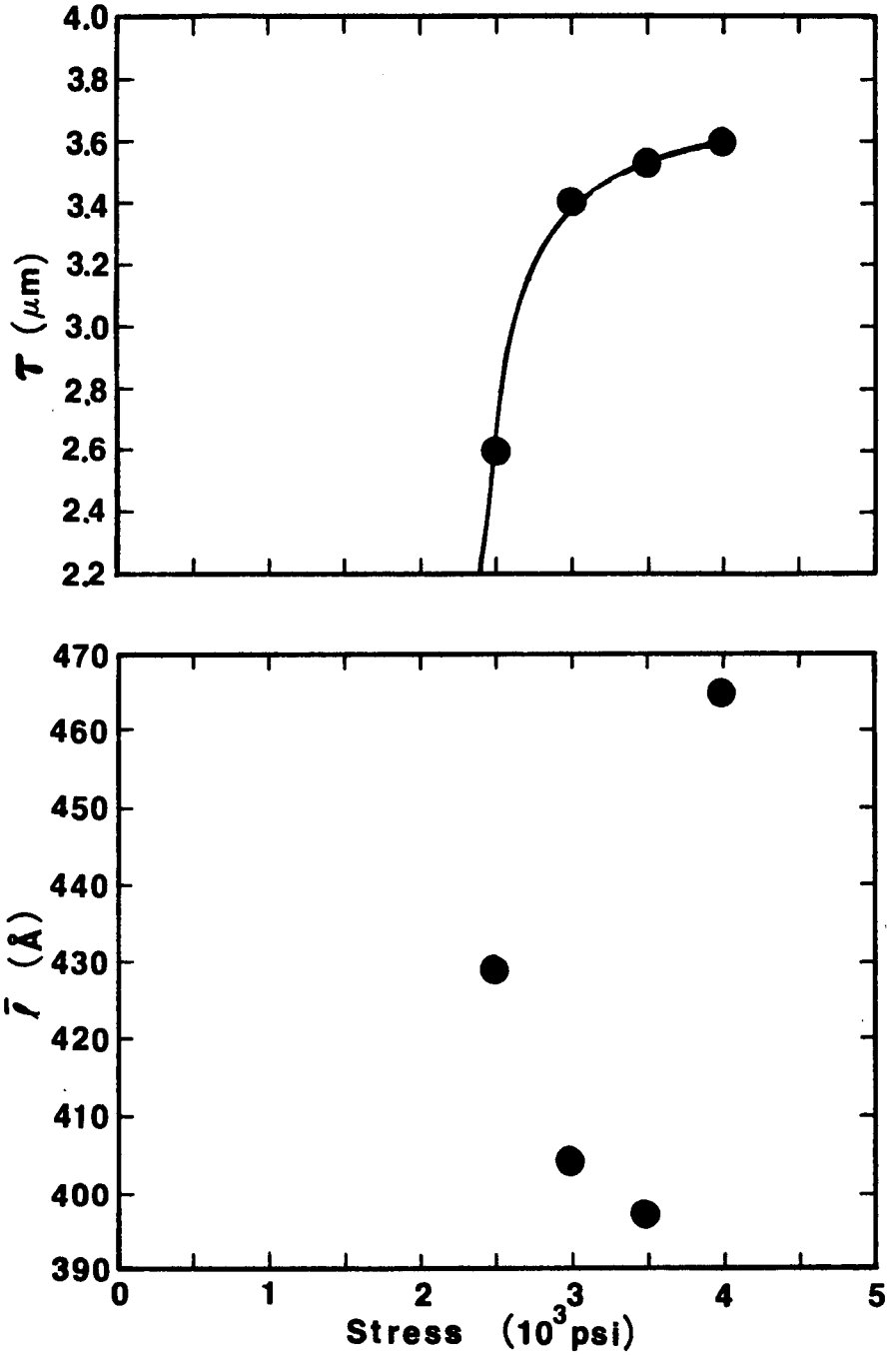


Figure 7-8. (A) Correlation distance τ of surface roughness distribution and (B) chord length $\bar{l}$ of microvoids as a function of stress. PSBI: $\overline{Mn}$ = 160,000, DP = 1.14.

Figure 7-7 (B) shows the variation of Kv with applied stress. By comparing Figure 7-7 (B) with Figure 7-1, it is found Kv stays constant as the scattering pattern shows circular symmetry. From Figures 7-7 (A) and (B) it is clear that Ks and Kv start increasing at the same stress. In the literature, it has usually been proposed that void and craze formation coincide in place and time and then the planar void propagates as a crack along the craze (e.g. 40, 43, 44, 45, 49, 50, 75, 81). If this is true, then surface scattering should originate from the interfaces of microvoids and polymer fibrils or matrix and Ks should increase at the same rate as Kv increases. However, the correlation distance of surface roughness is of the value of about three to five microns which is much larger than the size of microvoids which ranges 200 to 500 Å as revealed by electron microscopy studies (e.g. 66 - 69). Additionally Kv increases at a much lower rate than Ks increases. This result means that once the application of stress creates approximately spherical microvoids and craze matter forms, the microcrack propagates rapidly through the craze matter and makes jumping steps by tearing from one craze-matrix interface to the other. The volume fraction of craze matter (drawn fibrils interspersed with microvoids) increases slightly with stress while the volume fraction of microcracks (big voids of several microns) increases greatly. That is why the scattering intensity parallel to the meridional direction increases with stress much faster than that parallel to the equatorial direction does.

Strictly speaking, crazed polystyrene is a multi-phase system: microvoids (v), fibrils (f), uncrazed polymer matrix (p), and inherent scatters (i) which accounts for the SAXS in undeformed PS (see Chapter 5). If the electron densities in each phase are uniform and separated by sharp boundaries, then

$$\overline{\eta^2} = \sum_{i<j}\sum w_i w_j(\rho_i - \rho_j)^2$$
$$= w_v w_f(\rho_v - \rho_f)^2 + w_v w_p(\rho_v - \rho_p)^2 + w_v w_i(\rho_v - \rho_i)^2$$
$$+ w_f w_p(\rho_f - \rho_p)^2 + w_f w_i(\rho_f - \rho_i)^2 + w_p w_i(\rho_p - \rho_i)^2. \qquad \text{Eq.(7-4)}$$

To analyze the data, the method usually employed by previous workers (e.g. 75 - 82) is to subtract the scattering intensity of undeformed PS from that of crazed PS. By doing this, we obtain

$$\Delta Kv = Kv_{\sigma} - Kv_{\sigma=0}$$
$$= w_v w_f(\rho_v - \rho_f)^2 + w_v w_p(\rho_v - \rho_p)^2 + w_v w_i(\rho_v - \rho_i)^2$$
$$+ w_f w_p(\rho_f - \rho_p)^2 + w_f w_i(\rho_f - \rho_i)^2. \qquad \text{Eq.(7-5)}$$

The electron density difference between the solid phases and the microvoid phase is much larger than the difference betwen the solid phases. Since the electron density differences are squared in Eq.(7-5), it is easy to realize that the net invariant is mostly due to the electron density difference between the void phase ($\rho_v = 0$) and the solid phases (average ρ_p). Thus we have the following relation,

$$\Delta Kv = (\Delta\rho)^2 x_{void}(1 - x_{void}). \qquad \text{Eq.(7-6)}$$

The variation of microvoid fraction with stress level is plotted in Figure 7-7 (C). Although the microcrack propagates rapidly through the craze matter just created, the monotonic increase of the microvoid

fraction indicates the creation of new craze matter is slightly faster than the propagation of microcrack. The microvoid fraction determined by SAXS seems too low as compared to the density measurement result ($\sim$ 0.5%). This is because this SAXS experiment cannot detect the existence of either big planar voids in the microcracks or small microvoids ca. tens of Angstroms.

The second parameter to be discussed is the average size of the microvoids. Since we observe an interference peak on the equatorial scattering intensity curve (see Figure 7-3), it is not appropriate to apply Guinier analysis (72) to find the size of the particle. The correlation function of electron density fluctuations $\gamma(r)$ is determined by Eq.(3-40) (131)

$$\gamma(r) = \frac{1}{(2\pi)^3 \cdot \overline{\eta^2}_V} \cdot \int_0^\infty 4\pi s^2 \cdot I(s) \cdot \frac{\sin(s \cdot r)}{s \cdot r} ds$$

$$= \frac{1}{(2\pi)^3 \, \eta^2_V} \cdot \int_0^\infty 4\pi s^2 \cdot I_{\mu=90^o}(s) \cdot \frac{\sin(s \cdot r)}{s \cdot r} ds. \quad \text{Eq.(7-7)}$$

For clarity, the correlation function $\gamma(r)$ at only one stress level is shown in Figure 7-9. The basic qualitative features of this function at various stress level are the same, having the value unity at $r = 0$, and descending to zero as r increases. The chord length $\bar{\ell}$ (135) of the microvoids is determined by Eq.(3-48)

$$\bar{\ell} = -1/\gamma'(0)$$

where $\gamma'(0)$ is the derivative of $\gamma(r)$ at the origin. $\bar{\ell}$ is a measure of the size of the microvoids. The variation of the chord length $\bar{\ell}$ with stress is plotted in Figure 7-8 (B) for PSBI. It seems that the size of the microvoids does not vary with loading conditions.

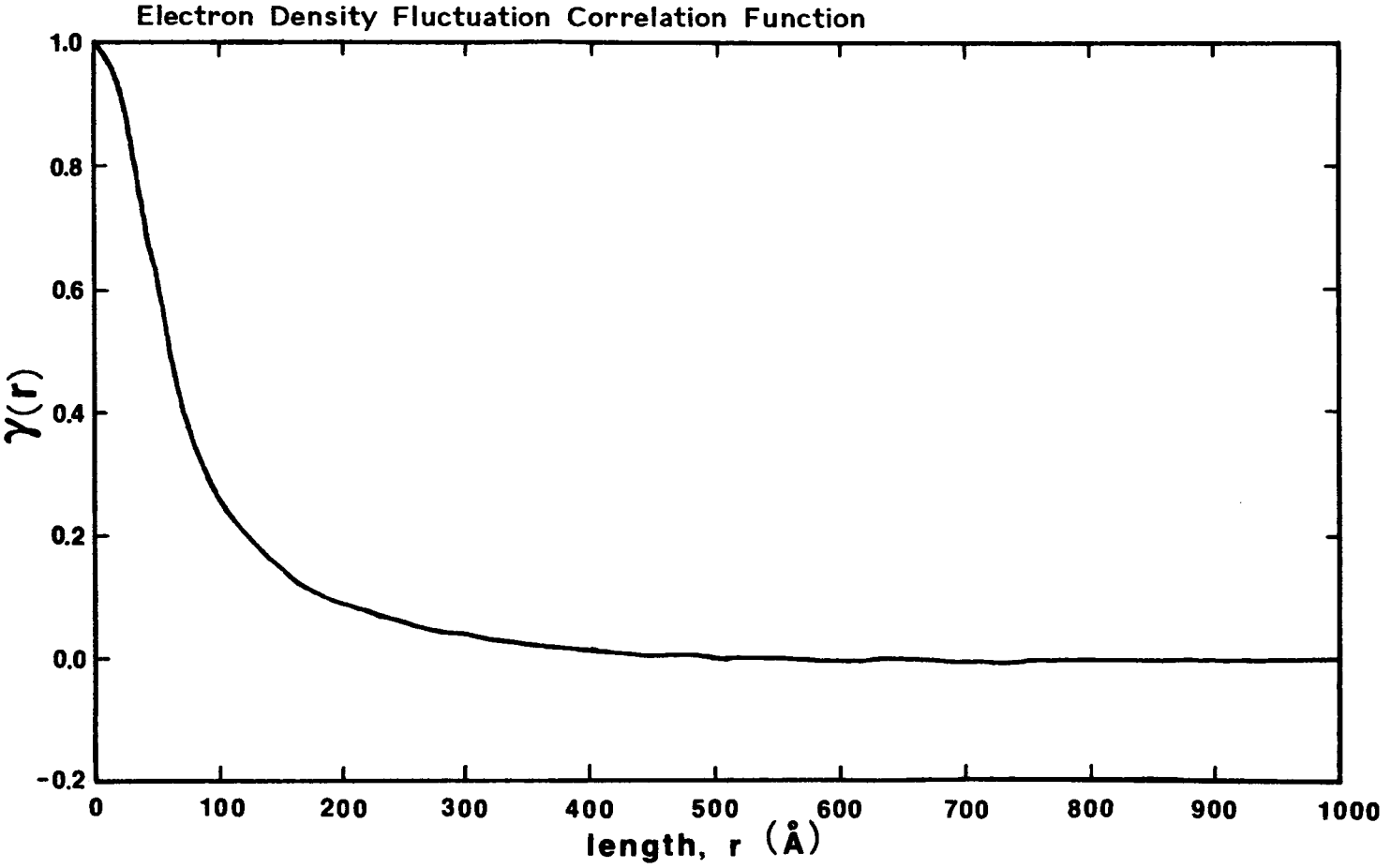


Figure 7-9. Typical correlation function of electron density fluctuation of polystyrene craze. PSBI: σ = 4000 psi.

7.4 Results and Discussion

7.4.1 Effect of Stress

The first variable to be discussed here is the stress level. Generally speaking, the behavior of polystyrenes with different molecular weights are qualitatively the same. For simplicity, one polystyrene (PSBI) is discussed. PSBI is a 50/50 bimodal blend of two monodispersed polystyrene with $\overline{Mn}$ = 118,000 and $\overline{Mn}$ = 247,000, respectively. The number averaged molecular weight of PSBI is 160,000 and the polydispersity ($\overline{Mw}/\overline{Mn}$) is 1.14.

The effect of stress on the SAXS patterns and the intensity distributions along the meridional and equatorial directions are illustrated in Figures 7-1 and 7-3, respectively. Before crazing is initiated, the scattering pattern shows circular symmetry and the normalized scattering intensity stays close to one. Once the crazing process starts, an anisotropic scattering pattern is observed and the normalized scattering intensity increases continuously until fracture. The scattering intensity along the meridional direction is much higher (almost one order of magnitude) and much faster than that along the equatorial direction. The former is mostly contributed by surface scattering originating from the microcrack/polymer matrix interfaces. The latter is caused by the electron density fluctuations in the craze matter composed of microvoids and polymer fibrils. Since the angular range of 2θ used in the SAXS experiments was two to twenty milliradians, we can only say that microvoids of sizes smaller than several tens of Ångstroms are not observed before the SAXS pattern

changes from circular symmetry to anisotropic and the normalized scattering intensity starts to increase.

As before, the structural characterization parameters calculated from surface scattering phenomenon include the surface scattering invariant Ks and correlation distance τ of the surface roughness distribution. The structural characterization parameters calculated from volume scattering phenomenon include the volume scattering invariant Kv, microvoid fraction, and chord length $\bar{\ell}$ of microvoids. The variation of these parameters with stress are shown in Figure 7-7 and Figure 7-8. By comparing Figures 7-7 (A) and (B), it is found Ks and Kv start increasing at the same stress level. Since the measured variable is the scattering intensity accumulated within a certain time period, 500 seconds in this case, it means the time lag between the microcrack propagation and the creation of microvoids of the size with the SAXS resolution limit is less than 500 seconds. However, in the synchrotron radiation studies of crazes by Martinson et al. (83, 84) with a measurement period of 30 seconds, it was also observed that the scattering intensity parallel to the strain direction increased with time much faster than that perpendicular to the strain direction does. Therefore we can say the surface scattering phenomenon and volume scattering phenomenon occur nearly simultaneously. Additionally, the volume fraction of microvoids calculated from the volume scattering invariant is much lower than that determined by density measurement and increases with stress slower than the surface scattering invariant does. This result may indicate the propagation of microcracks through

created microvoids is slightly slower than the formation of new microvoids. If the former is equal to or faster than the latter, then we would observe no increase with stress for the latter. Figure 7-8 (A) shows the correlation distance τ of surface roughness distribution increases steeply with stress level at first and than increases slowly. τ corresponds to the average length of the steps caused by the microcrack jumping from one craze-matrix interface to the other. The increase in τ may indicate some of the polymer fibrils contained in the jump steps of microcracks are broken so the average length increases. Figure 7-8 (B) shows the variation of chord length $\bar{\ell}$ of microvoids with stress. This plot indicates the average size of microvoids formed at different stress stays approximately the same.

Combining the conclusions obtained above, a model for crazing and fracture is proposed in Figure 7-10. When there is no tensile stress, the polystyrene has a random coil structure with distributions in entanglement densities. At stress less than the crazing initiation stress (the latter is defined as the stress at which SAXS pattern changes from circular symmetry to anisotropic), small microvoids of size ca. 10 $\mathring{A}$ may form at the weakest point (i.e., lowest entanglement density or chain ends). At stress equals to the crazing initiation stress, crazes start to form. For clarity, only one single craze is shown in Figure 7-10. The newly formed craze has microvoids ca. 400 $\mathring{A}$ interspersed with fibrils at the craze tip and nearly simultaneously microcrack propagates through the craze by making jumps

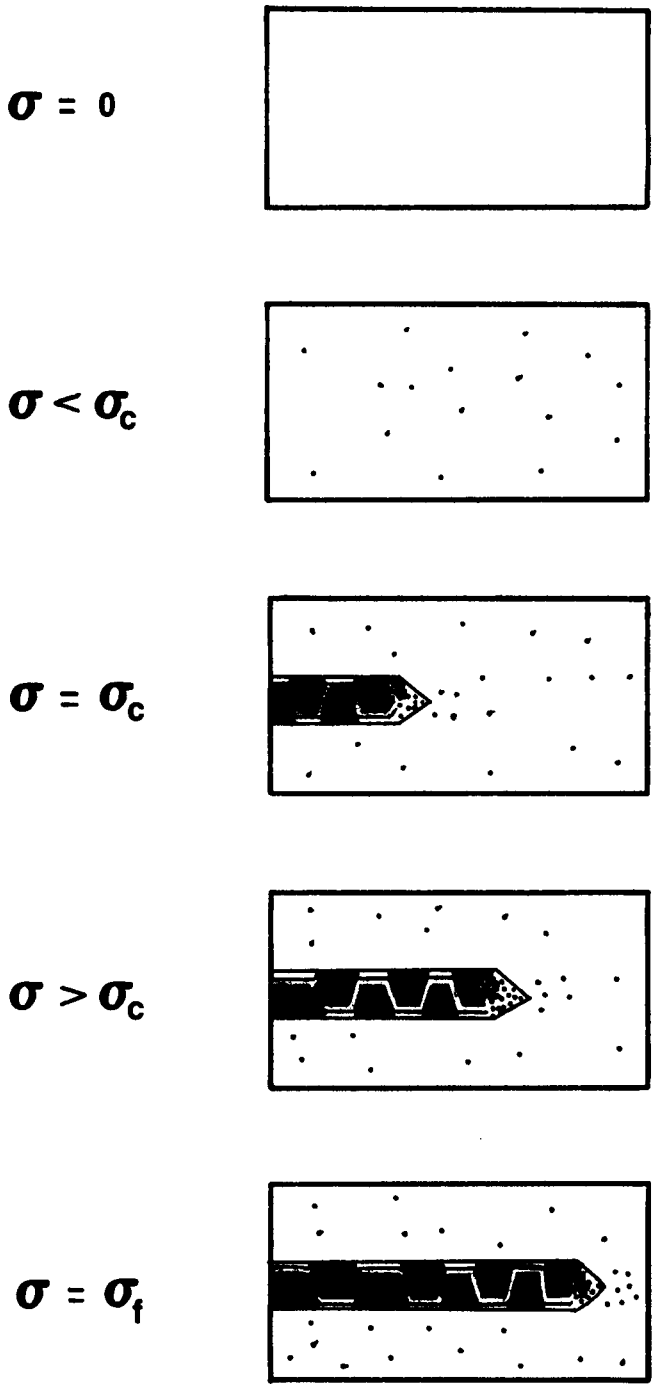


Figure 7-10. Proposed model for crazing and fracture.

from one craze/matrix interface to the other. As stress (time) increases, the old craze/microcrack keeps growing in length and more and more new crazes/microcracks form. Finally, the polymer fractures because the number of microcracks exceeds a critical value and the hollow microcracks can no longer sustain local stress due to the lack of support from interconnected fibrils between the opposite boundaries.

7.4.2 Effect of Molecular Weight

The second variable to be discussed here is the molecular weight. Three different monodispersed molecular weights were examined: 118,000 (PS103), 186,000 (PS109), and 247,000 (PS108). The stress-strain behavior of these samples together with the variation of normalized scattering intensity with stress are presented in Figure 7-11. While the general shapes of the curves are similar, the tensile strength and the normalized scattering intensity at fracture are significantly different. The morphology of the microcrack interfaces at fracture, which can be represented by the surface scattering intensity distribution, are compared in Figure 7-12 for different molecular weights. This plot indicates for the range of molecular weight studied, the microcrack interface morphology does not vary with molecular weight and shows a mirror-like smooth fracture plane. Therefore we can deduce the mean square surface roughness τ is independent of the molecular weight. The surface scattering invariant calculated using Eq.(6-38) by assuming a two-dimensional isotropic surface roughness is plotted in Figure 7-13 as a function of stress

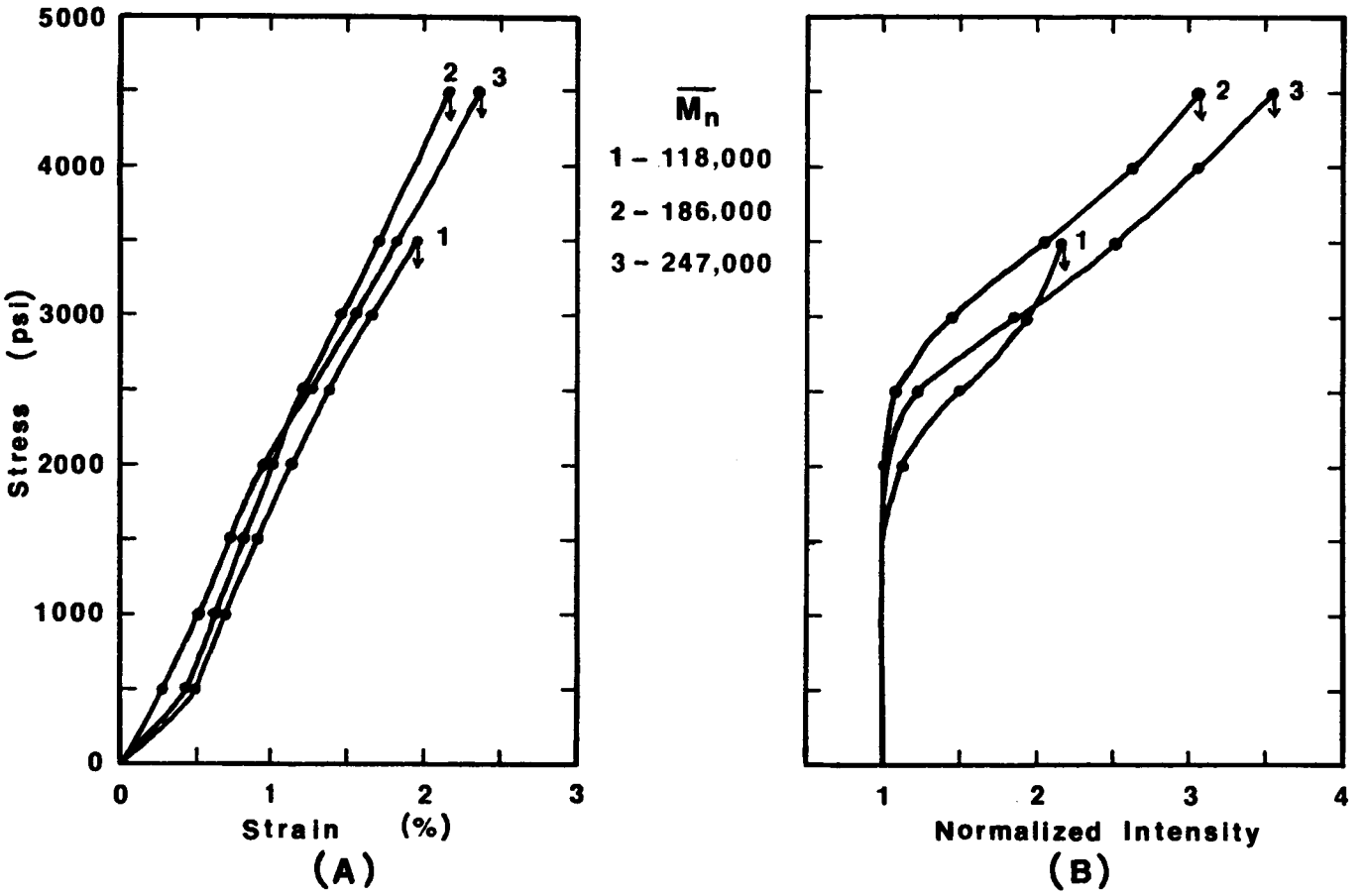
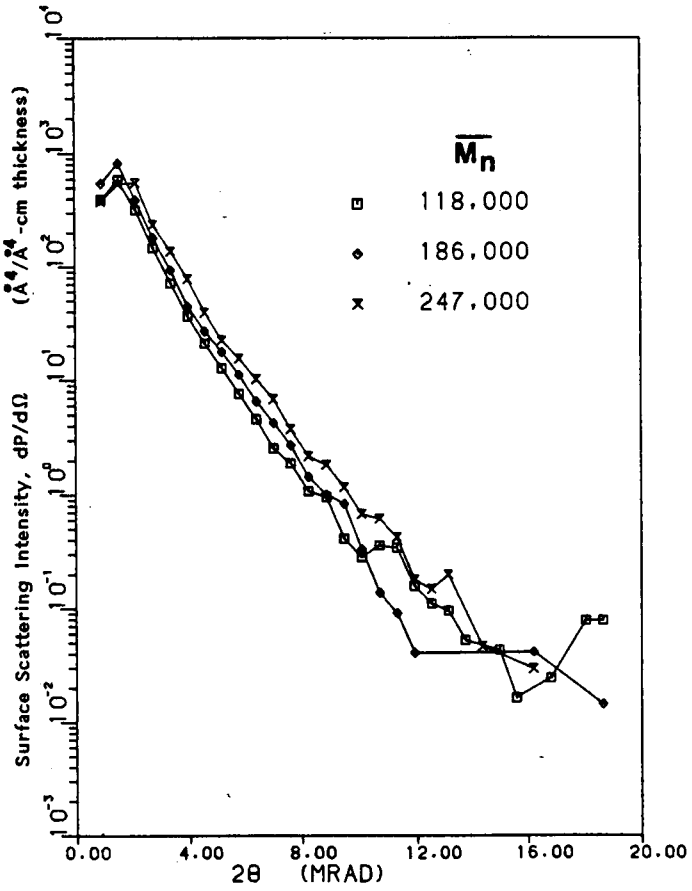
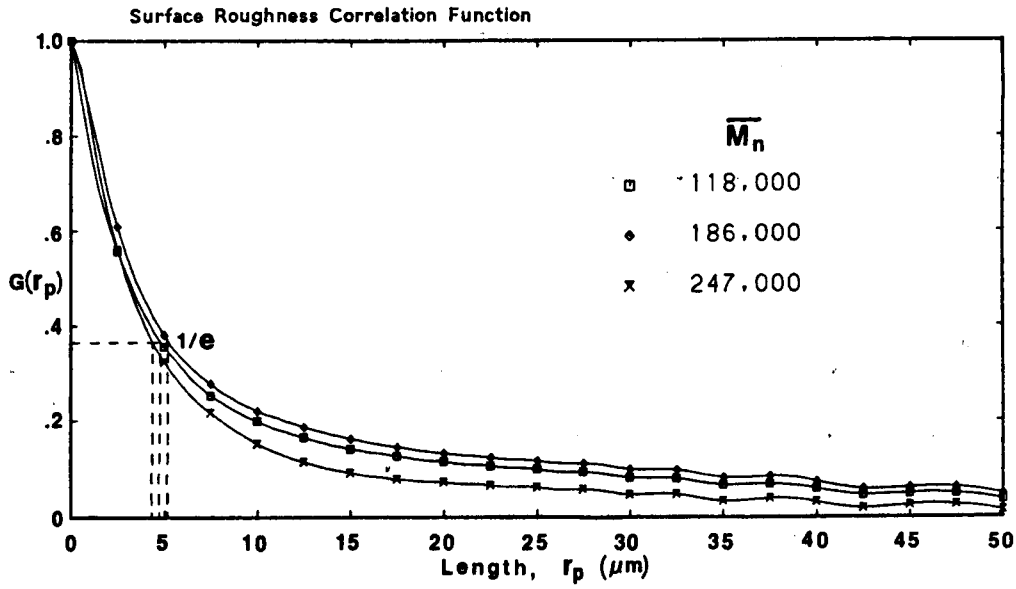


Figure 7-11. (A) Stress-strain behavior and (B) the variation of nomalized intensity with stress for monodisperse polystyrene of different molecular weights.



(A)



(B)

Figure 7-12. Comparision of (A) the surface scattering intensity and (B) the surface roughness correlation function at fracture for monodisperse polystyrene of different molecular weights.

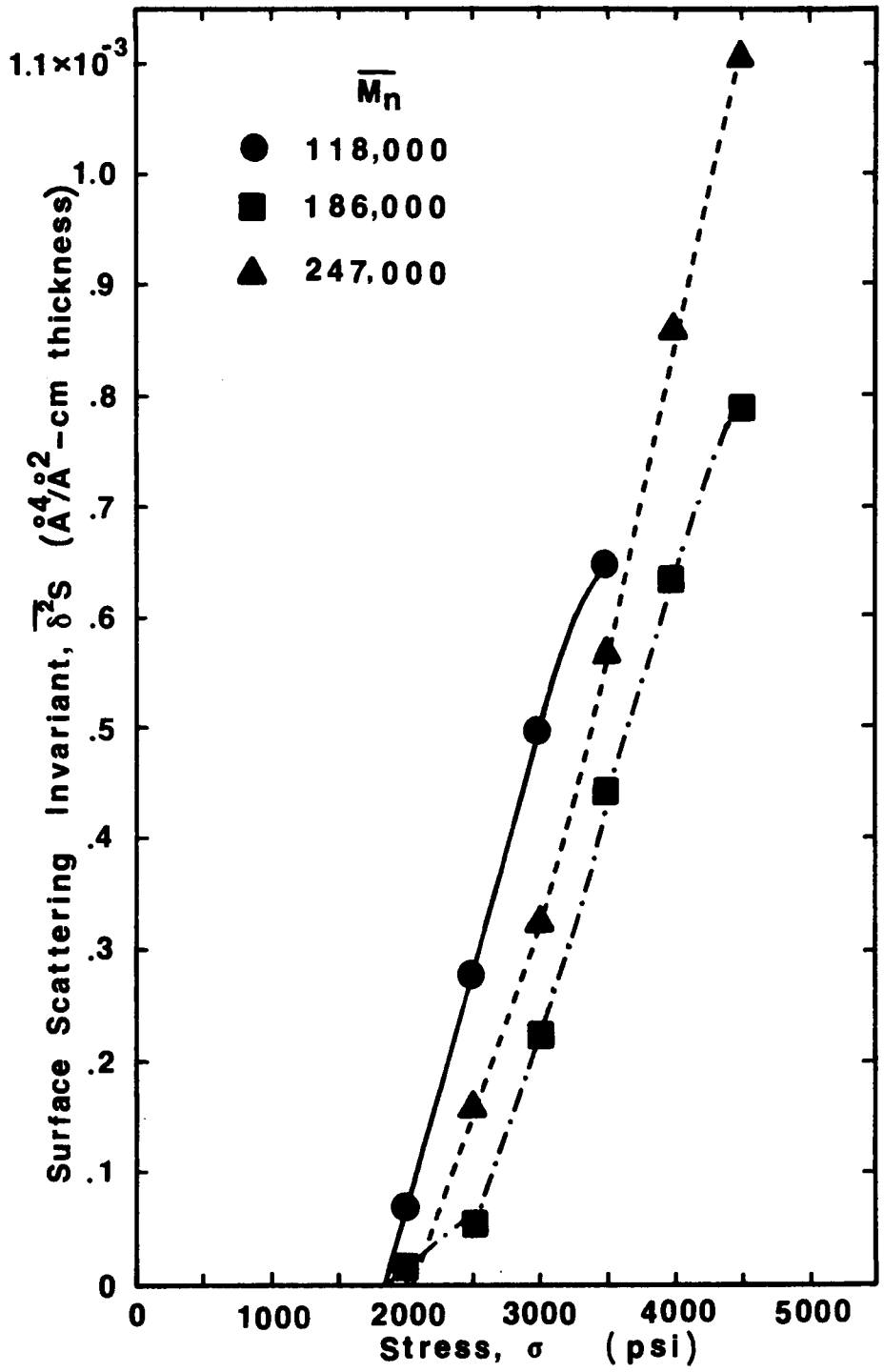


Figure 7-13. Surface scattering invariant versus stress level for monodisperse polystyrene of different molecular weights.

for different molecular weights. Since the mean square surface roughness $\overline{\delta^2}$ is also stress independent, the surface scattering invariant is directly proportional to the microcrack interfacial area. Figure 7-13 shows the microcracks grow steadily with stress until fracture and the slope does not vary with molecular weight. New microcrack interfaces can be created either by the break-down of the fibrils in the crazed matter through disentanglement of molecular coils or by chain scission of entangled coils. The former is a molecular weight dependent process. The molecular weight independence of the slope may indicate the occurence of chain scission in craze break-down. This has also been infered from thermal, mechanical, and acoustical evidence (55:Chapter 9). Figures 7-14 (A) and (B) compares the surface scattering invariant value at fracture and the correlation distance τ of surface roughness distribution at fracture for different molecular weights, respectively. The microcrack density at fracture represented by the surface scattering invariant value increases with molecular weight significantly. This result indicates the strength of PS to support local stress increases with molecular weight. Within experimental error, the average length of the microcrack jumps at fracture as represented by τ can be said to be independent of molecular weight. The independence also indicates the occurence of chain scission in craze break-down.

The stress induced variation of the volume scattering invariant and the void fraction are compared in Figures 7-15 (A) and (B) respectively for different molecular weights. It is observed that the

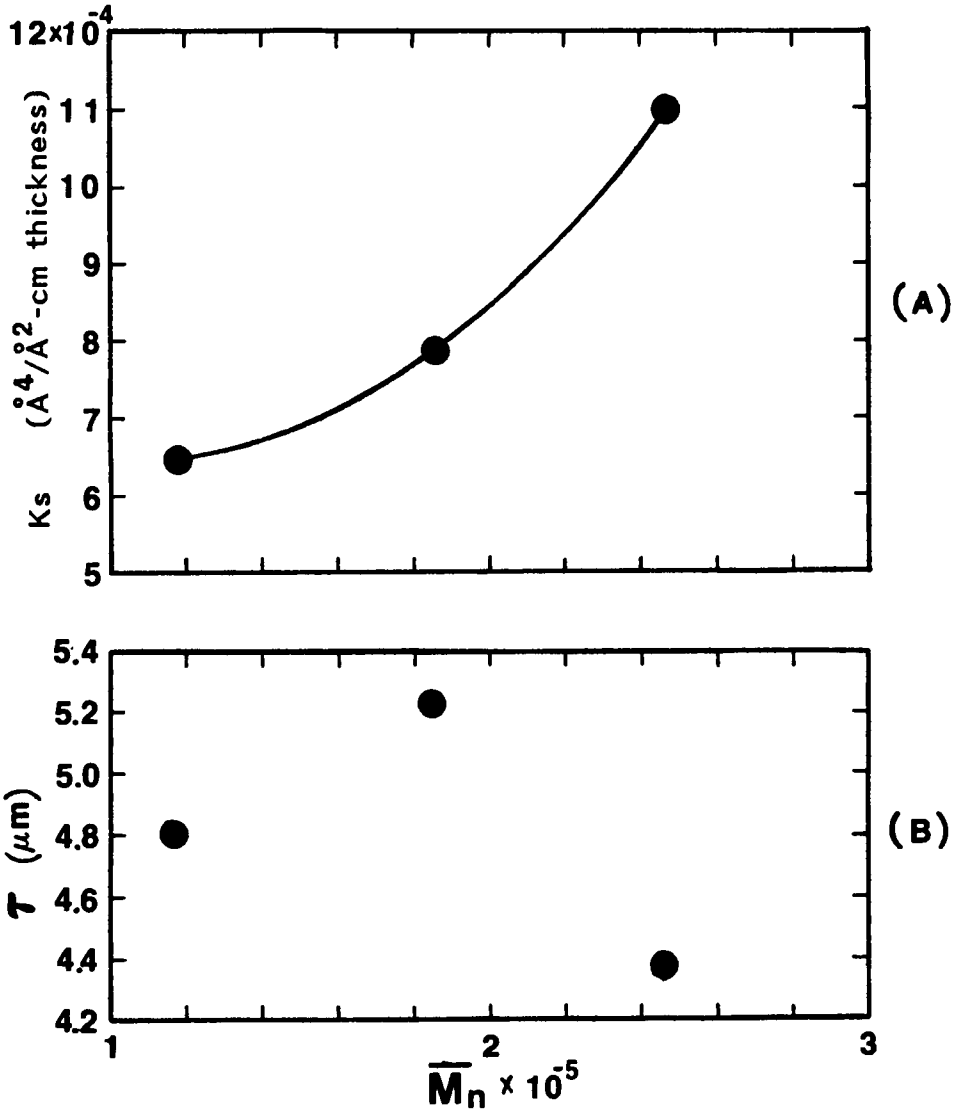


Figure 7-14. Comparison of (A) surface scattering invariant Ks at fracture and (B) correlation distance τ of surface roughness distribution at fracture for monodisperse polystyrene of different molecular weights.

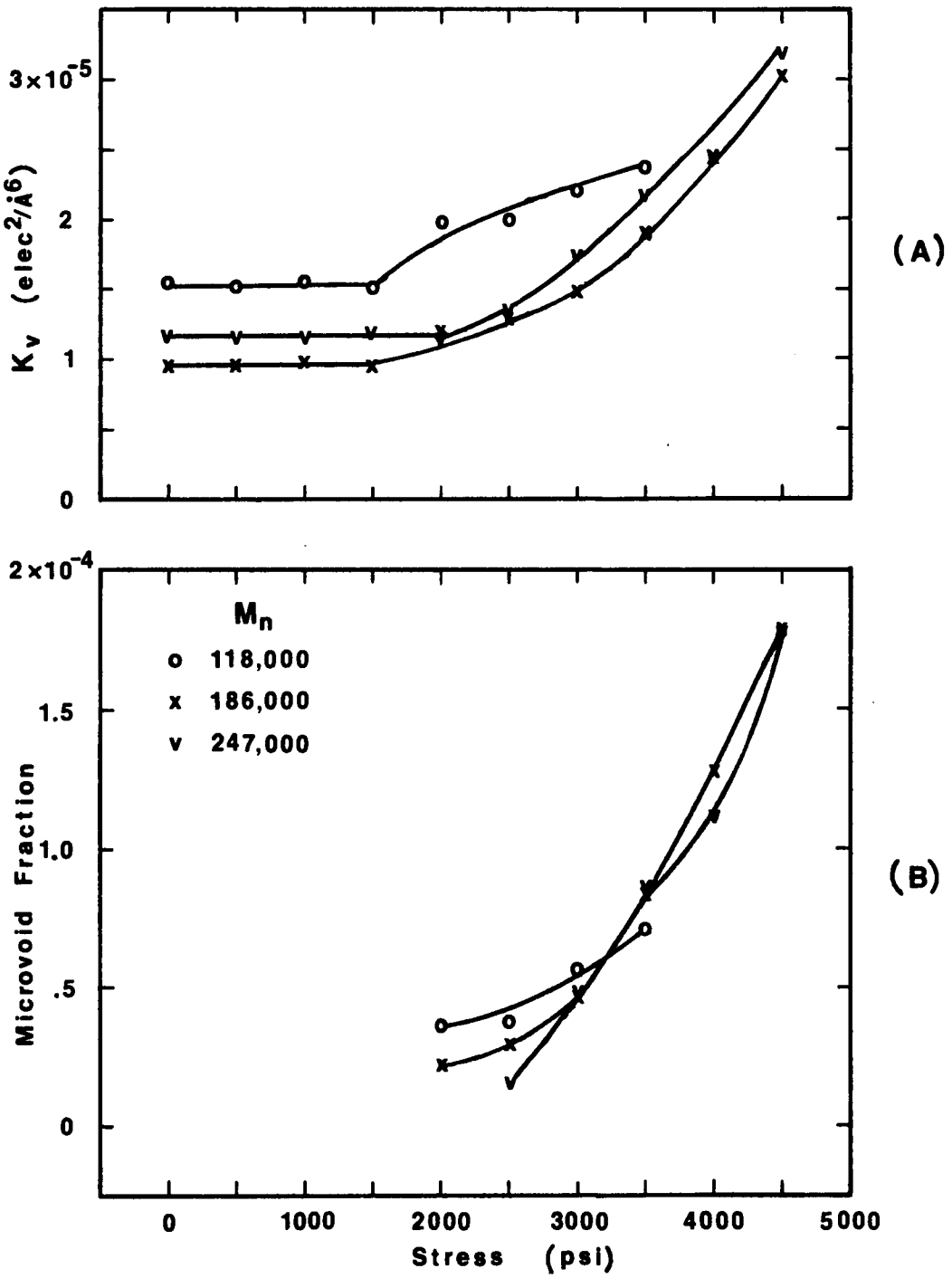


Figure 7-15. (A) Volume scattering invariant and (B) microvoid fraction versus stress level for monodisperse polystyrene of different molecular weights.

void fraction increases steadily with stress in the range crazes exist. Comparing Figure 7-15 (A) with Figure 7-13, it is easy to realized the growth of microcrack starts at the same time when crazing initiates. It is also observed that the void fraction at fracture increases with molecular weight and then decreases slightly. The slight decrease may be either attributed to experimental error or to the fact that in higher molecular weight more craze matter develop into microcracks. Therefore the microcrack density at fracture increases with molecular weight significantly while the craze matter that remained unbroken increases and then decreases with molecular weight. Figure 7-16 compares the chord length $\bar{l}$ of microvoids for monodisperse polystyrene of different molecular weights at fracture. Note that the average size of microvoids decreases with molecular weight.

7.4.3 Effect of Molecular Weight Distribution

Next the effect of molecular weight distribution on the crazing behavior is discussed. Two samples with same number average molecular weight but different polydispersity were studied: an artificial bimodal blend (PSBI: $\overline{Mn}$ = 160,000, DP = 1.14) and a commercial polydispersed polystyrene (PS685D: $\overline{Mn}$ = 160,000, DP = 1.91). The effect of increasing the polydispersity on the crazing and fracture process is the same as the effect of increasing molecular weight. This is a natural consequence since for samples of same number averaged molecular weight, the portion of high molecular weight tails increases with the polydispersity. The variation of surface

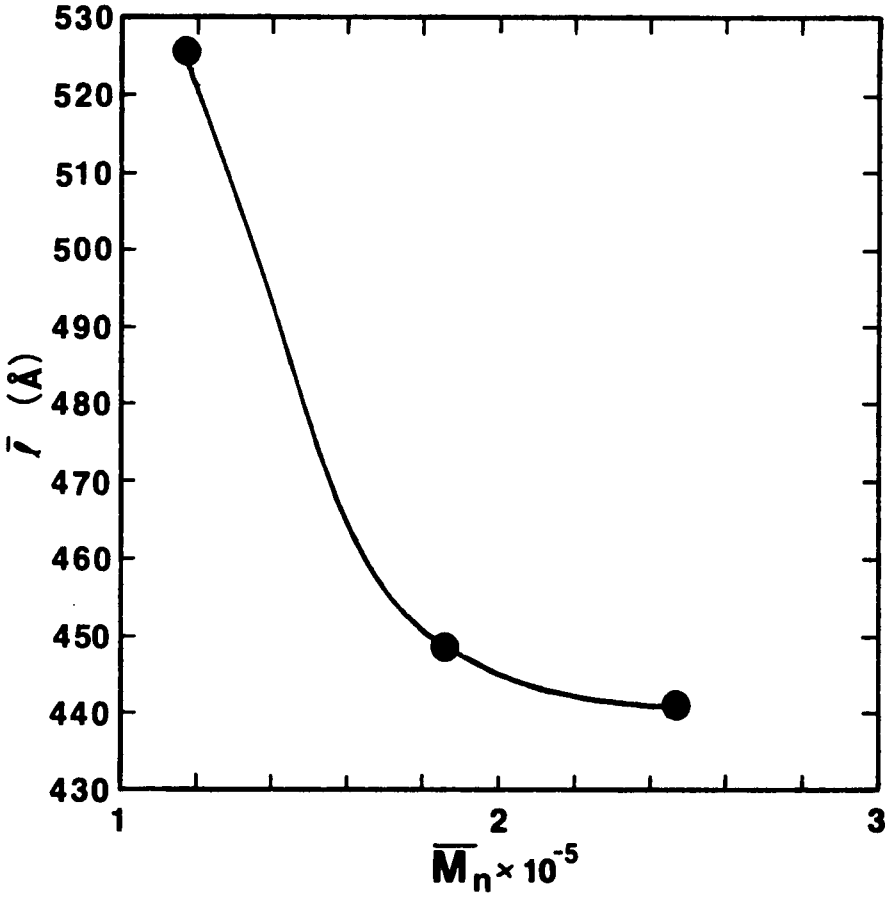


Figure 7-16. Comparison of the chord length $\bar{\ell}$ of microvoids at fracture for monodisperse polystyrene of different molecular weights.

scattering invariant Ks, volume scattering invariant Kv, and microvoid fraction with stress are plotted in Figures 7-17 (A), (B), and (C), respectively, for different polydispersities. The volume scattering invariant of uncrazed PS685D is much lower than that of PSBI. This may be because PS685D was polymerized differently than others (see Section 5.7). Clearly, the microcrack density and the microvoid fraction at fracture, and the fracture stress increase with polydispersity. It is found the correlation distance τ of surface roughness distribution and the chord length $\bar{\ell}$ of microvoids are independent of the polydispersity.

7.5 Summary and Conclusions

The small-angle x-ray volume scattering (SAXVS) theory discussed in Chapter 3 and the small-angle x-ray surface scattering (SAXSS) theory introduced in Chapter 6 are both applied to analyze the SAXS results of unoriented polystyrene during dynamic tensile tests. The microstructure changes are discussed in terms of the five following characterization parameters: the surface scattering invariant Ks, which is related to the interfacial area between microcracks and matrix; the correlation distance τ of surface roughness distribution, which corresponds to the average length of the steps caused by the microcrack jumping from one craze-matrix interface to the other; the volume scattering invariant Kv, which is directly related to the mean square fluctuation of electron density; the microvoid fraction; and the chord length $\bar{\ell}$ of microvoids. The following important conclusions are drawn from the results.

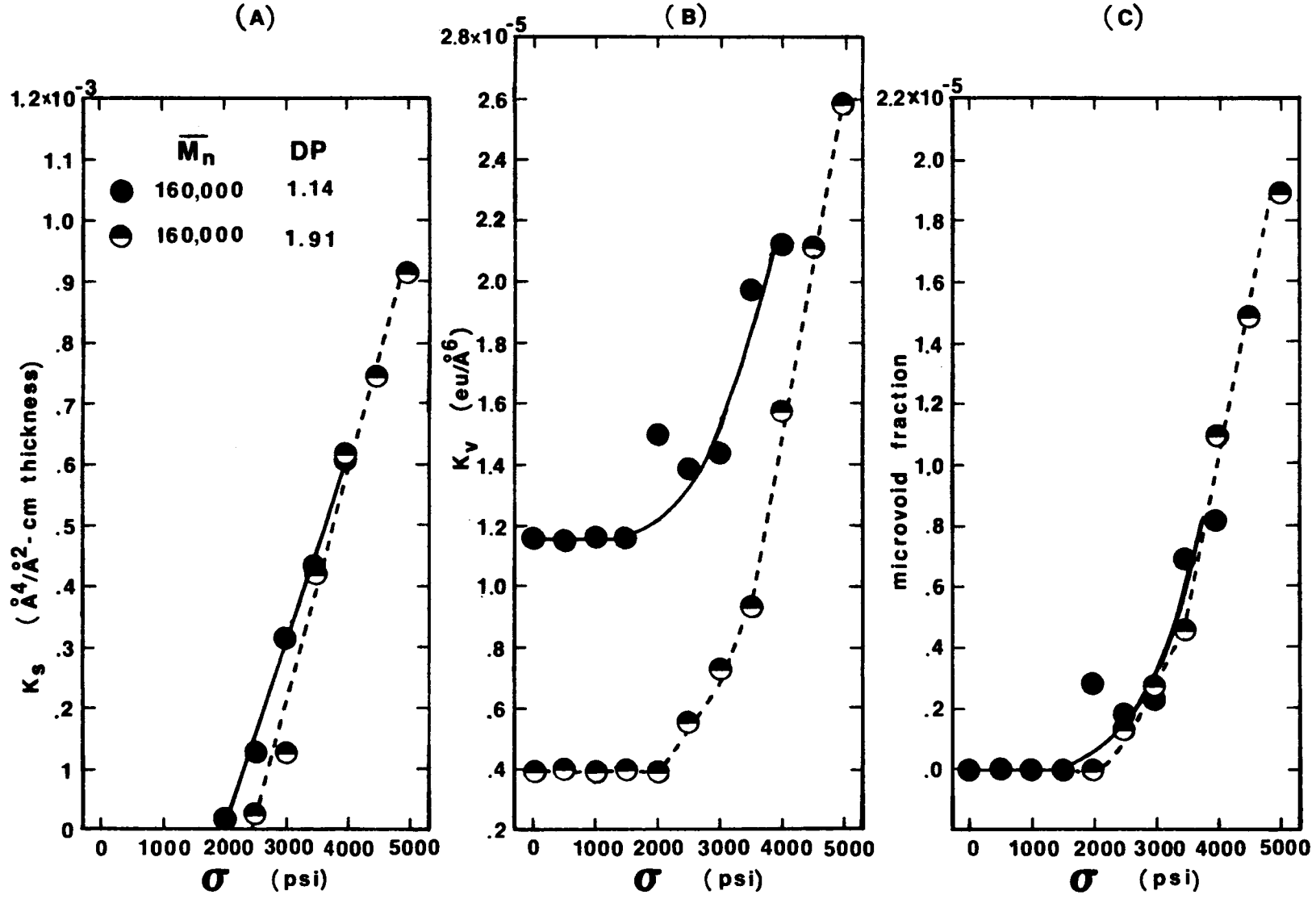


Figure 7-17. (A) Surface scattering invariant Ks; (B) volume scattering invariant Kv; and (C) microvoid fraction as a function of the stress level for two polystyrenes with different molecular weight distributions.

(1) The surface scattering phenomenon and the volume scattering phenomenon occur nearly simultaneously. Or in other words, the microcrack starts to propagate soon after the microvoids formed.

(2) The volume fraction of microvoids increases with stress less faster than Ks does. This indicates the propagation of microcracks through created microvoids is slightly slower than the formation of new microvoids.

(3) The average length of the jump steps in the microcracks increases steeply with stress at first and then increases smoothly, whereas the average size of microvoids formed at different stress stays approximately the same.

(4) The microcrack density at fracture and the fracture stress increase with number averaged molecular weight and polydispersity.

(5) At fracture, the average length of the jump steps in the microcracks, which ranges about 4 μm, is independent of the number average molecular weight and the polydispersity.

(6) The average size of microvoids in crazed polystyrene decreases with molecular weight in monodispersed polystyrene.

CHAPTER 8

SAXS OF CRAZES IN ORIENTED POLYSTYRENE

The deformation and fracture of oriented polystyrene have been studied as a function of the degree of molecular orientation and the relation between the applied tensile direction and the initial molecular orientation direction (MOD, i.e., the hot-stretching direction). The degree of birefringence (Δn) was used as a parameter of molecular orientation. The results show that: (1) The degree of birefringence is not a unique parameter to characterize the molecular orientation state and depends strongly on the molecular weight and the hot-stretching temperature. (2) when the applied tension is parallel to the MOD, the crazing initiation stress increases with the degree of orientation until the specimen fractures without formation of crazes and if crazes formed, the direction of the craze plane is perpendicular to that of the applied tension; (3) when the applied tension forms various angles with the MOD, the specimen fractures with crazing at all angles, but the crazing stress and amount of crazes vary significantly with angle.

8.1 Introduction

There has been considerable interest for many years in the effect of molecular orientation on the mechanical properties of glassy polymers. This is mainly due to practical consequences arising from unintentionally introduced orientation from industrial production processes such as extrusion, injection molding, blow molding, etc.

Work on polystyrene has been concerned primarily with mechanical properties either parallel or perpendicular to the main direction of orientation. The major conclusions from previous works are:

(1) Stretching at different temperatures and strain rates introduces varying degrees of orientation (23).

(2) Birefringence is a better measure of the degree of orientation than draw ratio and reversion ratio (23, 209, 210). However, physical properties are not uniquely related to birefringence because the latter also depends on the number and type of entanglements present in the polymer structure and the processing condition producing orientation.

(3) The tensile strength parallel to the MOD generally increases as the degree of orientation increases and decreases with increasing orientation perpendicular to the MOD (23, 32, 210, 211, 212). For commercial polystyrenes (Styron 666 with $\overline{Mw}$ = 202,000 and $\overline{Mw}/\overline{Mn}$ = 2.5, Styron 679 with $\overline{Mw}$ = 184,000 and $\overline{Mw}/\overline{Mn}$ = 2.8) the brittle-to-ductile transition point occurs at $\Delta n = -0.002$ (32, 212).

(4) Young's modulus varies only slightly with both birefringence and the angle of testing with respect to the MOD (213).

(5) The fracture surface energy decreases with increasing degree of orientation when applied stress parallel to the MOD and the fracture surface becomes increasingly smooth (211, 214). Oriented specimens tend to fail by splitting or fibrillation rather than by transverse fracture when tension is applied parallel to the MOD (211).

(6) In tensile tests with applied stress parallel to the MOD, the crazing strength increases with the amount of orientation and above a critical amount of orientation, crazing is suppressed and the material deforms by shear yielding and cold drawing (90).

(7) The crazing stress decreases rapidly with increasing angle between MOD and tensile direction (90). Crazes produced by straining parallel to the MOD have higher fibril volume fraction (V_f = 0.45) than crazes in unoriented PS (V_f = 0.25), and the crazes produced by straining perpendicular to the MOD have a much lower fibril volume fraction (V_f = 0.05) (91).

This chapter deals with the effect of varying the degree of orientation under various process conditions, the molecular weight, and the direction of orientation on the microstructural changes during tensile deformation of polystyrene.

8.2 Experimental

The polystyrene samples were molded from pellets, obtained from the Dow Chemical Co., to a thickness of 1.6 mm in a hot press. The molecular orientation was introduced by stretching specimens of length 50 mm and width 7 to 10 mm at a constant cross-head speed using an Instron, equipped with a specially constructed environmental oven, to a predetermined length and subsequent rapid cooling in the extended state to room temperature by opening doors of the oven. The birefringence was used as an arbitrary scale to represent the amount of orientation in the final specimen. The actual extension ratio L/L_o and birefringence Δn were measured at the central portion where the

deformation was uniform. The central portion was then well insulated and the two ends were soaked in a silicon oil bath at atemperature of 180°C to let them shrink back so as to form a test piece with dumbbell ends. This treatment is necessary because it is difficult to drill holes in oriented polystyrene to fit them to the sample holder of the deformation device of the ORNL 10-m SAXS instrument. It was found that the birefringence and extension ratio of the insulated region did not change before and after this treatment.

Additionally, the molded polystyrene sheet was cut into dimensions of 48 mm by 48 mm and uniaxially stretched with free width at constant temperature and constant cross-head speed using a T. M. Long Biaxial Stretcher. Tensile specimens were then cut from the uniformly deformed central part of the drawn sheet at various angles to the initial MOD.

8.3 Results and Discussion

A series of specimens with different degrees of orientation were obtained by controlling three variables; namely, hot-stretching temperature Ts, total extension ratio L/L_o, and polystyrene molecular weight, while varying one of them and maintaining the other two constant. The characteristics of the specimens for each series of experiments are listed in Table 8-1. The specimen was deformed by applying uniaxial tensile stress in a stepwise manner with increments of 500 psi per 500 seconds using the dynamic device of the ORNL 10-m SAXS instrument (147, 148). All measurements were done at room temperature.

Table 8-1

Sample characterization for the study of orientation effects on crazing

	Polymer	$\overline{Mn}$	$\overline{Mw}/\overline{Mn}$	Ts	$\dot{\gamma}$	L/L_o	Δn	ψ_m
I.	PSBI	160,000	1.14			1.0	0.0	0°
	PSBI	160,000	1.14	115^oC	500%/min	3.0	-0.005205	0°
	PSBI	160,000	1.14	115^oC	500%/min	6.0	-0.01224	0°
	PSBI	160,000	1.14	115^oC	500%/min	8.5	-0.022432	0°
II.	PS103	118,000	1.05	115^oC	500%/min	3.0	-0.003972	0°
	PSBI	162,000	1.14	115^oC	500%/min	3.0	-0.005208	0°
	PS109	186,000	1.05	115^oC	500%/min	3.0	-0.007695	0°
III-1.	PS103	118,000	1.05			1.0	0.0	0°
	PS103	118,000	1.05	115^oC	500%/min	3.0	-0.003972	0°
	PS103	118,000	1.05	110^oC	500%/min	3.0	-0.009233	0°
III-2.	PS109	186,000	1.05			1.0	0.0	0°
	PS109	186,000	1.05	120^oC	500%/min	3.0	-0.00487	0°
	PS109	186,000	1.05	115^oC	500%/min	3.0	-0.007695	0°
IV.	PS108	247,000	1.08	115^oC	500%/min	2.0	-0.00497	0°
	PS108	247,000	1.08	115^oC	500%/min	2.0	-0.00497	15°
	PS108	247,000	1.08	115^oC	500%/min	2.0	-0.00497	30°
	PS108	247,000	1.08	115^oC	500%/min	2.0	-0.00497	45°
	PS108	247,000	1.08	115^oC	500%/min	2.0	-0.00497	60°
	PS108	247,000	1.08	115^oC	500%/min	2.0	-0.00497	75°
	PS108	247,000	1.08	115^oC	500%/min	2.0	-0.00497	90°

8.3.1 Varying Extension Ratio

Tests were done on specimens having extension ratio values equal to 1, 3, 6, and 8.5. The polystyrene is a 50/50 bimodal mixture (PSBI: $\overline{Mn}$ = 160,000; DP = 1.14) of two monodispersed polystyrenes: PS103 ($\overline{Mn}$ = 118,000) and PS108 ($\overline{Mn}$ = 247,000). The stress-strain curves are plotted in Figure 8-1. The insert in Figure 8-1 is a plot of the normalized scattering intensity versus stress level. The normalized scattering intensity is defined as the ratio of total scattered counts registered by the 2DPSD after being corrected for dark current and empty beam background for a sample at stress to that at zero stress. The start of the crazing process is indicated by the abrupt increase in the normalized scattering intensity and the craze initiation points are indicated by solid circles on the stress-strain curves of Figure 8-1. The SAXS patterns at fracture is also shown for comparison.

Apparently, when the degree of molecular orientation increases, both the fracture strength and strain increase. Crazes were observed for L/L_o = 1, L/L_o = 3, and L/L_o = 6. The craze initiation stress and strain increase with the degree of molecular orientation. The main characteristics of crazes formed in these specimens with tensile direction parallel to MOD was that they always formed with the craze plane perpendicular to the tensile axis, as indicated by the fact that the surface scattering streak is parallel to the tensile axis. Specimen of L/L_o = 8.5 fractured at 6% strain without the formation of crazes. There was no evidence for shear yielding of this specimen.

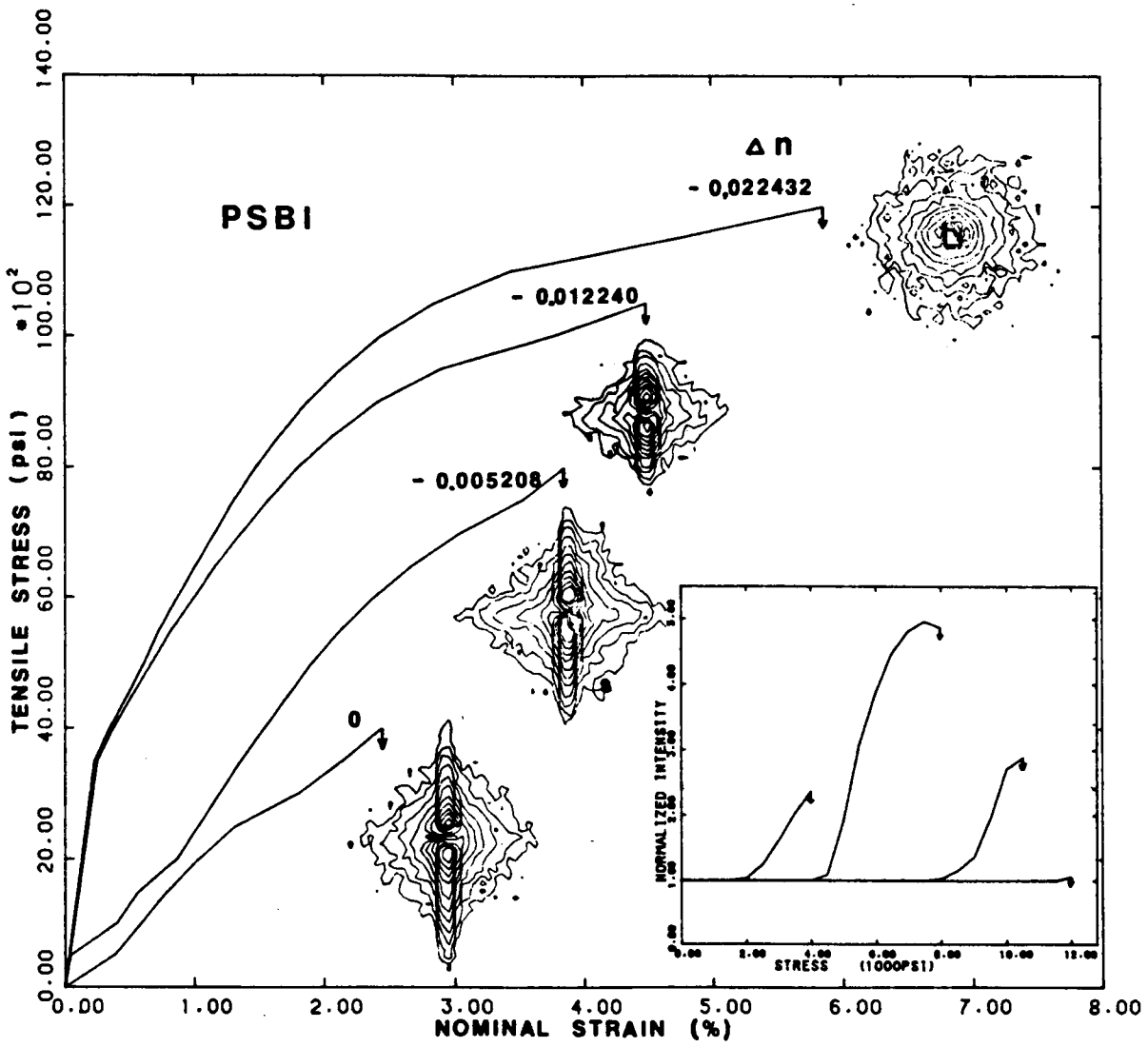


Figure 8-1. Stress-strain curves for uniaxially oriented polystyrene with various extension ratios prepared at the same stretching temperature Ts and cross-hear speed $\dot{\gamma}$. PSBI: $\overline{Mn}$ = 160,000; DP = 1.14; Ts = 115°C; $\dot{\gamma}$ = 500%/min.

Hull and Hoare (90) reported that when above a critical value of orientation ($\Delta n = -0.005$, draw ratio = 2.6, $\overline{Mn} = 69{,}000$, $\overline{Mw}/\overline{Mn} = 3.18$), crazing is suppressed, and the polystyrene deforms by shear yielding and cold drawing. This may be due to the difference in molecular weights between their and our studies.

In Figure 8-2 the SAXS patterns at various deformation stages for the specimens studied in Figure 8-1 are compared. It is observed that even for polystyrene with an extension ratio as high as 8.5 and birefringence -0.0224 the scattering pattern and the (volume) scattering invariant are not much different from that of unoriented one in the unstressed state. This indicates (1) no new phase (microvoids) has been created during the orientation process, and stretching polystyrene above its glassy transition temperature results in homogeneous deformation, (2) stretching does not cause shape changes of the scatters (e.g. foreign particles, initiator residuals, etc.) which are the main sources of SAXS from unstressed polystyrene (see section 5.7).

Generally speaking, the SAXS pattern for crazes in oriented polystyrene is similar to that in unoriented polystyrene: it consists of a surface scattering streak superposed on the volume scattering background. However, the differences among the the SAXS patterns of crazes in specimens with various degrees of orientation are obvious. In Figure 8-3 the scattering intensity distribution along the meridional direction (i.e., tensile direction) and the equatorial direction at the fracture point are compared separately for the

Figure 8-2. Comparison of the SAXS patterns at different deformation stages for the specimens studied in Figure 8-1. (A) No stress; (B) craze initiation; (C) fracture; and (D) relaxed for 10^7 seconds after fracture.

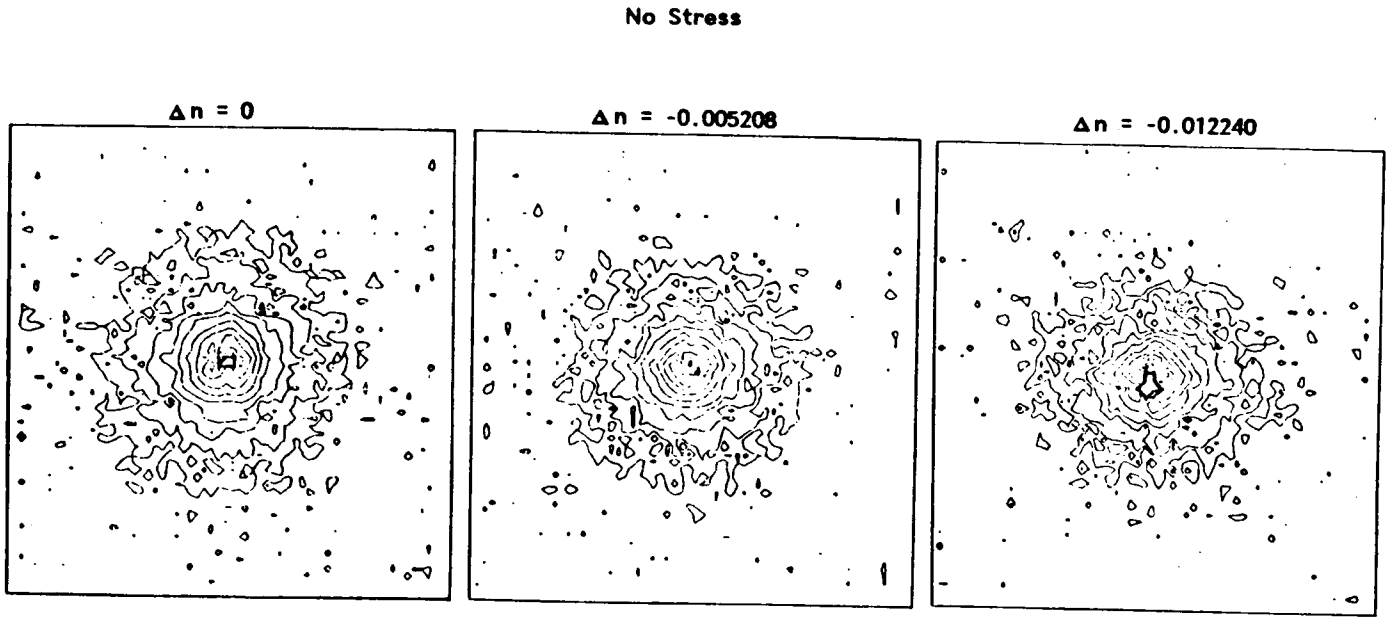


Figure 8-2 (A).

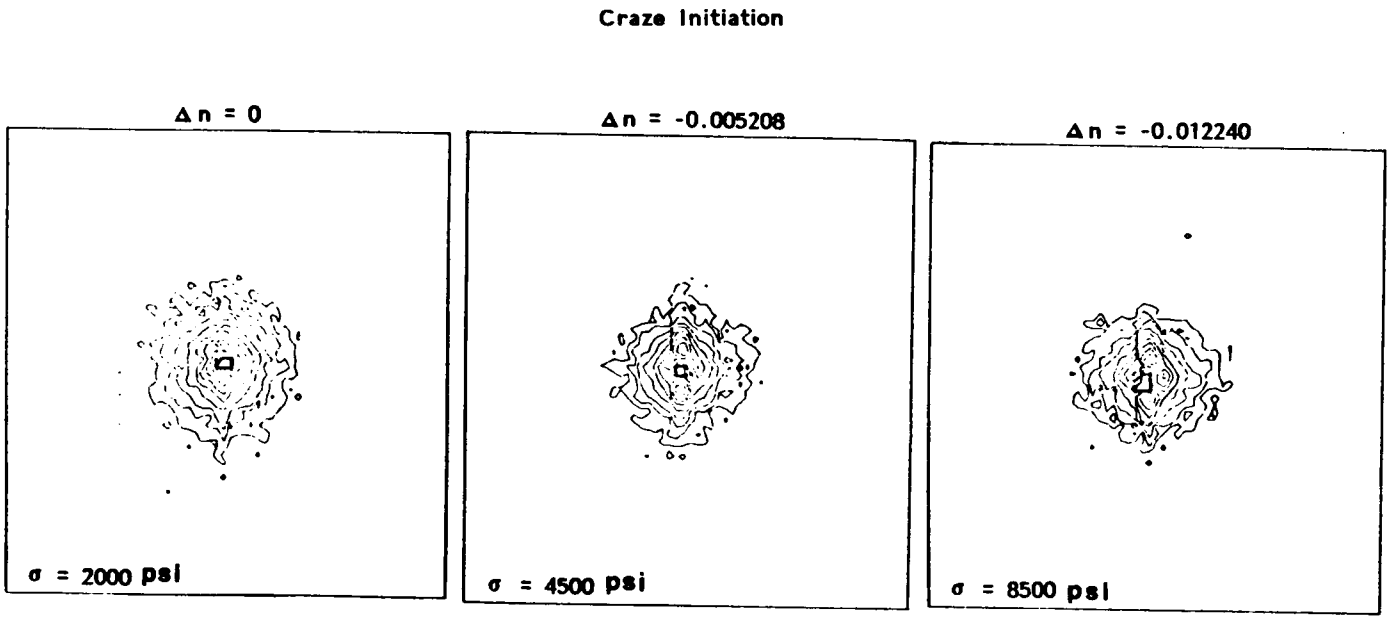

Craze Initiation
Δn = 0
Δn = -0.005208
Δn = -0.012240
σ = 2000 psi
σ = 4500 psi
σ = 8500 psi

Figure 8-2 (B).

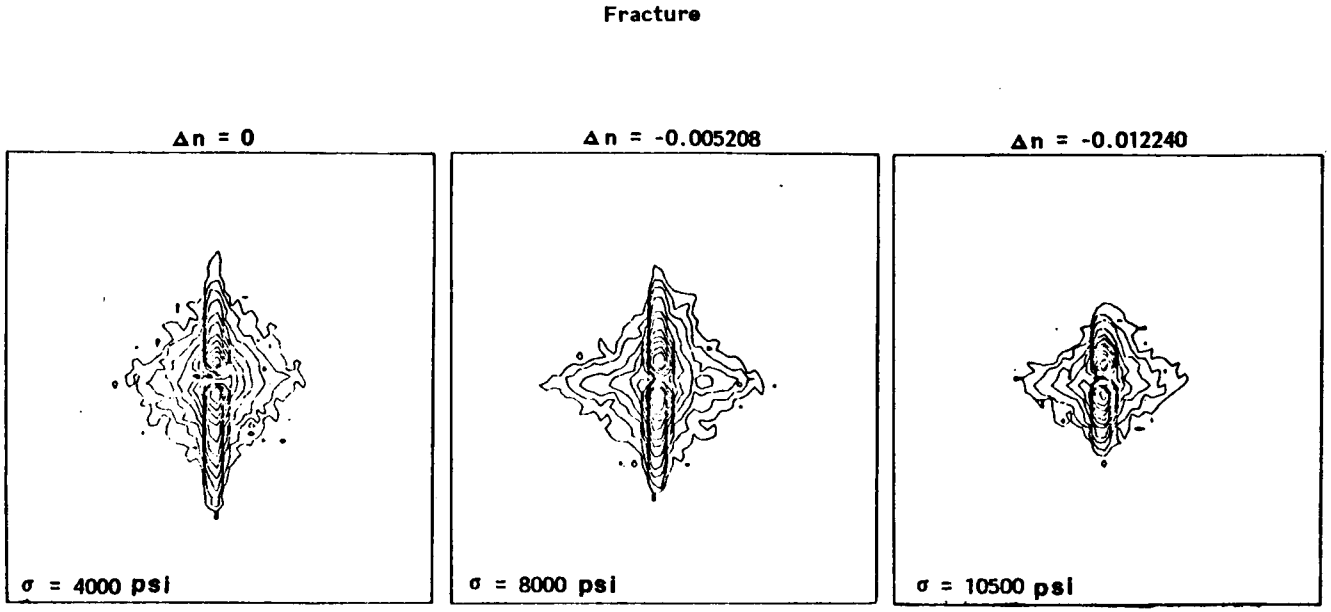

Fracture
Δn = 0
Δn = -0.005208
Δn = -0.012240
σ = 4000 psi
σ = 8000 psi
σ = 10500 psi

Figure 8-2 (C).

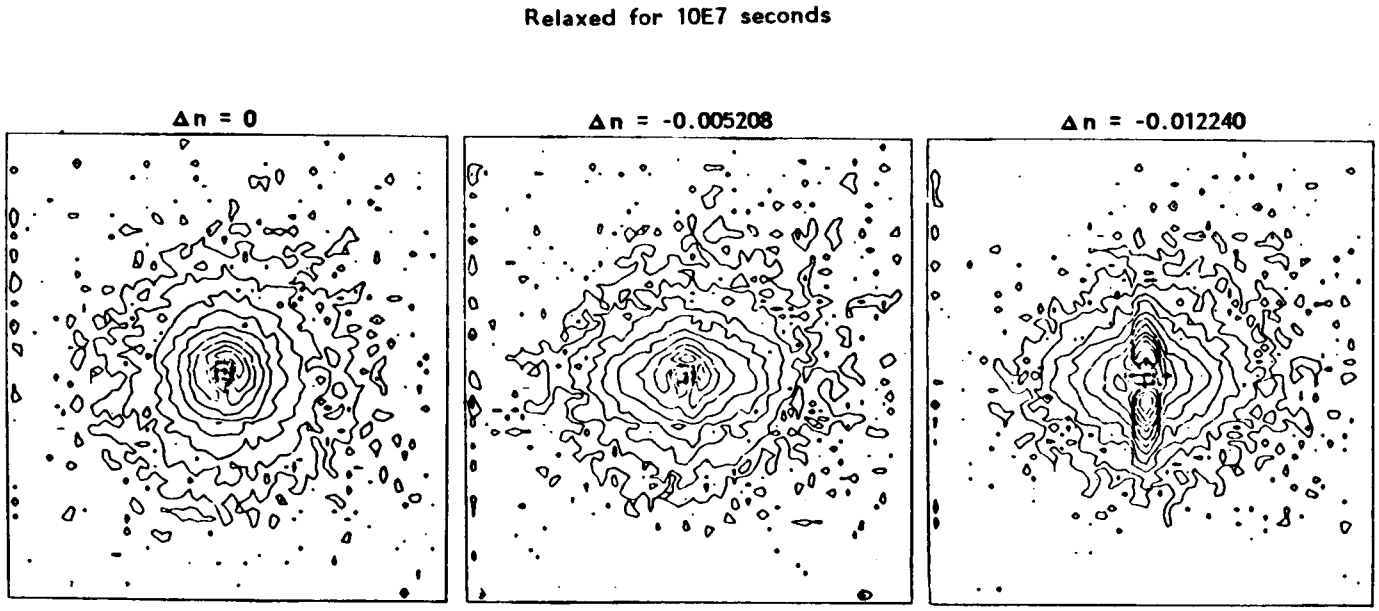


Figure 8-2 (D).

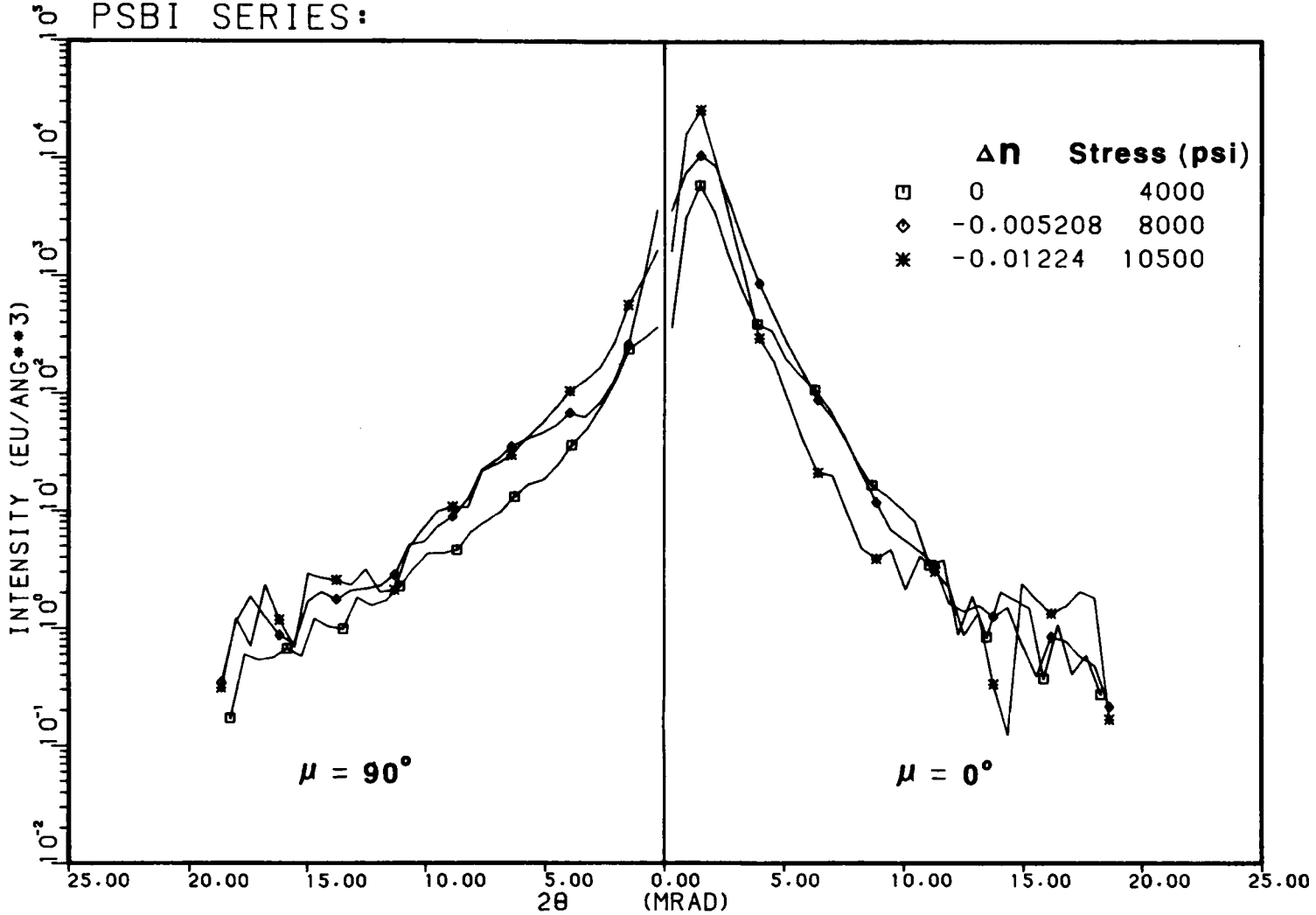


Figure 8-3. Comparison of the meridional and equatorial scattering intensity distributions at the fracture point for the specimens studied in Figure 8-1.

specimens with various degrees of orientation. Although the normalized scattering intensity at fracture increases with orientation and then drops (see the insert in Figure 8-1), the intensity distribution along the meridional direction and equatorial direction do not show the same trend. The equatorial scattering intensity at the fracture point increases with the degree of orientation at all measured 2θ regions. But the meridional scattering intensity increases with degree of orientation only at very small 2θ regions and the distribution curve versus 2 becomes steeper with increases in orientation. In Chapter 6, we have shown theoretically that as the correlation distance τ of the surface roughness distribution increases, the scattered waves will be directed in the near specular direction, and the surface scattering streak observed on the two-dimensional detector plane becomes narrower and sharper (see Figure 6-11). τ corresponds to the average length of the steps made by the microcrack jumping from one craze-matrix to the other (see Figure 6-21). Therefore, it can be concluded from Figure 8-3 that the average length of the steps made by the microcrack jumps increases with the degree of orientation.

In Figure 8-4, the comparison for meridional intensity and equatorial intensity is made for each specimen individually. For the unoriented sample, the meridional intensity is always higher than the equatorial intensity in the region of 2θ = 0 to 12 milliradians (mrad) and beyond 12 mrad the two are roughly equal indicating an isotropic volume scattering background. When the degree of

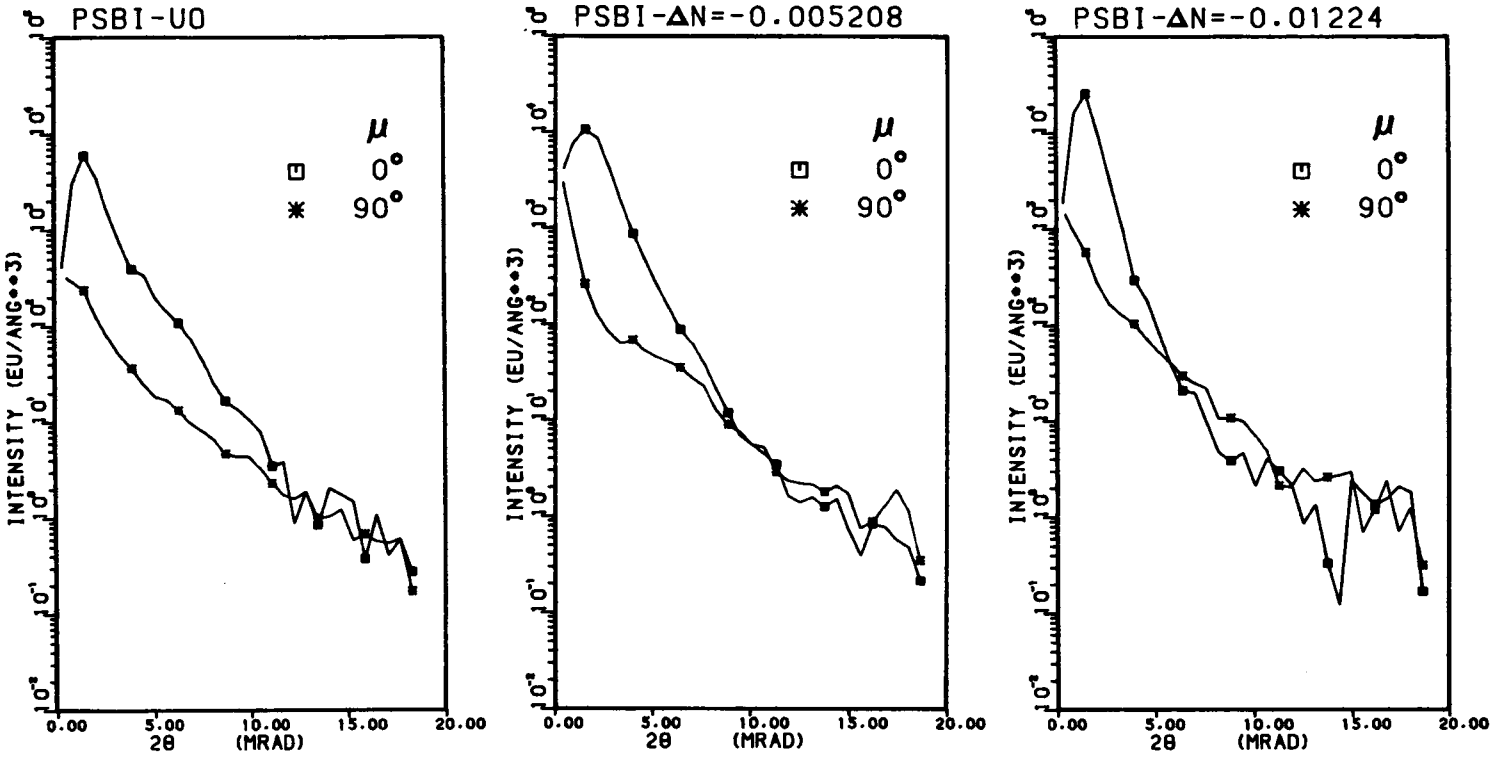


Figure 8-4. Comparison of the meridional and equatorial scattering intensity distributions for each specimen studied in Figure 8-1 at the fracture point.

orientation increases, the range of 2θ within which the equatorial intensity is lower than the meridional intensity decreases. Furthermore, beyond that 2θ limit the former exceeds the latter. This suggests the shape of the scatters which cause volume scattering changes from sphere to ellipsoid with their longer axis parallel to the tensile direction as the degree of orientation increases. The fact that the scatterer's shape changes from sphere in crazed unoriented polystyrene to ellipsoid in crazed oriented polystyrne is also evidenced by the SAXS pattern of crazes in polystyrene relaxed for 10^7 seconds after fracture (see Figure 8-2).

Since the volume scattering background is no longer isotropic, the analysis technique for surface scattering employed in Chapter 7 can not be applied. Instead, the intensity at two specified scattering angles, namely, 2θ = 1.5 mrad and 2θ = 5 mrad, are used to describe the craze and microcrack growth behavior with stress. 2θ = 1.5 mrad corresponds to the peak location on the meridional scattering intensity curve and 2θ = 5 mrad corresponds to the location at which the equatorial scattering intensity begins to increase drastically when crazing starts.

The variation of the scattering intensity at 2θ = 1.5 mrad and 2θ = 5 mrad with stress are shown in Figure 8-5 for PSBI series. For all samples, the equatorial intensity at 2θ = 1.5 mrad stays constant at all stress levels. The increases with stress for the equatorial intensity at 2θ = 5 mrad becomes more significant when the degree of orientation increases. In the unoriented sample, the meridional

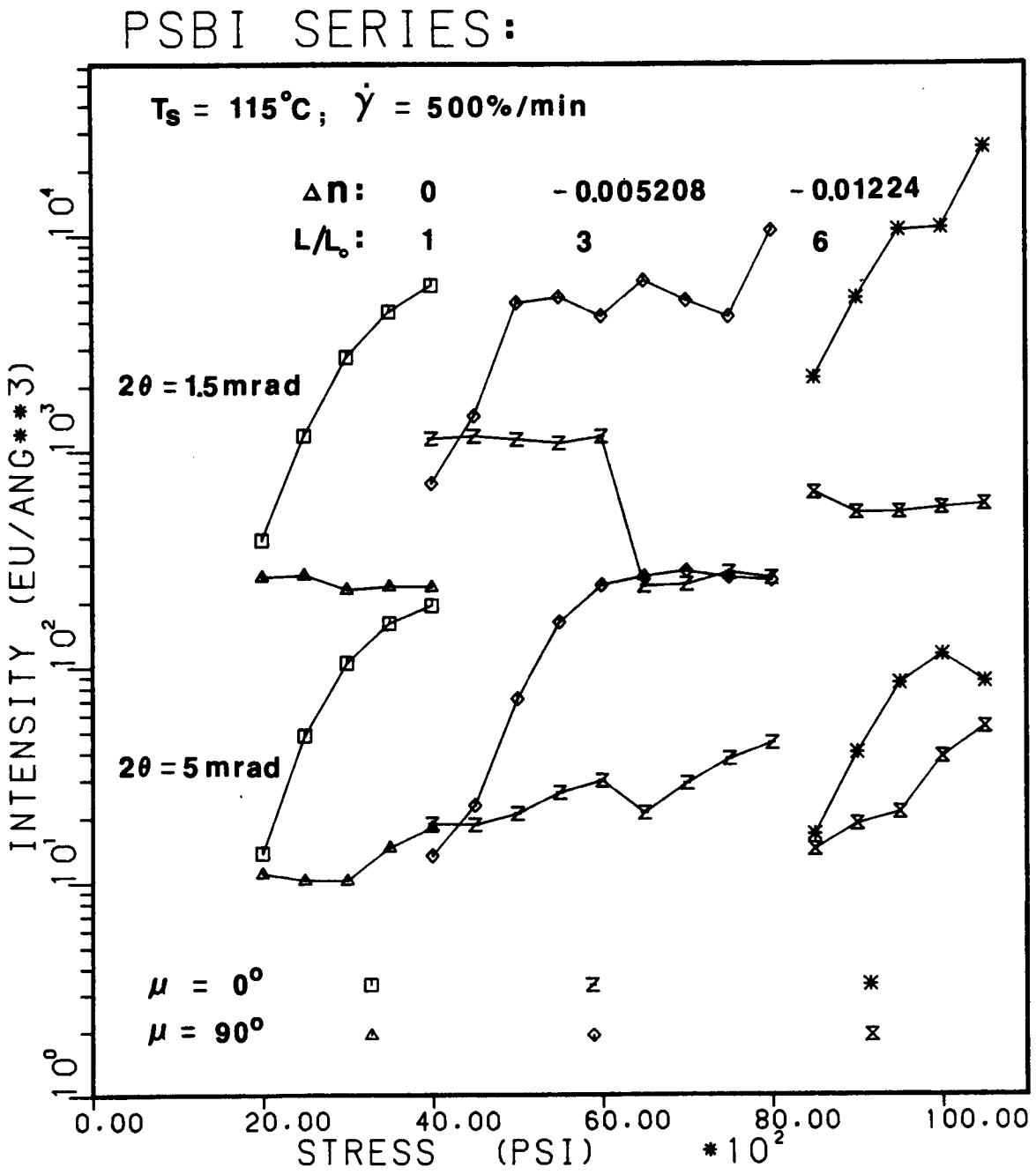


Figure 8-5. Variation of the meridional and equatorial scattering intensity at 2θ = 1.5 mrad and 2θ = 5 mrad with stress for the specimens studied in Figure 8-1.

intensity at both 2θ = 1.5 mrad and 2θ = 5 mrad increases monotonically with stress until fracture. But in the oriented samples, the meridional intensity at both 2θ = 1.5 mrad and 2θ = 5 mrad increases with stress monotonically at the beginning when crazing initiates and then reaches a transition point beyond which the increase with stress is much smoother. This behavior may be explained by the transition in the craze thickening mechanisms.

The craze thickness is thought to grow by a combination of drawing bulk polymer into the fibrils at the craze-matrix interface (surface drawing mechanism) and elongating the pre-existing craze (fibril creep mechanism). Electron microscope observations have shown surface drawing to be the dominant thickening mechanism for isolated air crazes in polystyrene films (48, 208, 215, 216). To a first order approximation one might expect the surface scattering intensity to increase monotonically with stress if crazes thicken by surface drawing and new interfaces continuously form by fibril break-down. This is the case for unoriented polystyrene and at the begining of the crazing process in oriented polystyrene. If crazes thicken by fibril creep rather than break-down, no new interfacial area would be created and the surface scattering intensity would stay constant. In the meanwhile, microvoids are generated continuously at the crack tip and new crazes are initiated and propagate, therefore the equatorial scattering intensity increases continuously with stress but the meridional scattering intensity increases with stress less rapidly than before the transition in the craze thickening mechanism. The

other evidence for the fibril creep mechanism is the fibrous appearance of the fractured oriented polystyrene. Since our tensile tests were conducted in a stepwise manner with incremental increase of 500 psi per 500 seconds and the stress at each measurement period was kept constant, the yield point which is usually defined by the maximum of the stress-strain curve was not observed in our stress-strain curves as shown in Figure 8-1. However, we indeed observed that for some of the oriented polystyrene specimens the load tended to drop while the strain increased continuously when the stress was above a certain value, and this gave us some trouble in keeping the load at a constant level. Although no obvious yield point can be observed in the stress-strain curves shown in Figure 8-1, it is reasonable to correlate the transition in the craze thickening mechanisms to the inherent yielding behavior of polystyrene.

Referring to Figure 8-2, the difference in the SAXS patterns from crazes in polystyrene with various degrees of orientation relaxed for 10^7 seconds after fracture can be explained in the same way. In unoriented polystyrene, the specimen fractured by local crazing before plastic creep of the craze fibrils took place. The highly extended craze fibrils relax back visco-elastically while the whole body strain recovers in the time period of 10^7 seconds so that the microcracks were cured and the surface scattering streak in SAXS pattern disappeared. In the oriented polystyrene, the specimens fractured after craze fibril creep. The creeped craze fibrils could not relaxed back completely in the time period of 10^7 seconds at room temperature.

The degree of relaxation is inversely proportional to the degree of creep of the fibrils, which depends on the degree of orientation of the specimens. In the highest oriented specimen fractured with craze formation, the surface scattering streak on the SAXS pattern still can be seen clearly.

8.3.2 Varying Molecular Weight

Examples of stress-strain curves and stress-normalized scattering intensity curves for uniaxially oriented polystyrene of various molecular weights having the same extension ratio prepared at the same stretch temperature Ts and cross-head speed $\dot{\gamma}$ are plotted in Figure 8-6 (A) and (B), respectively. PSBI ($\overline{Mn}$ = 160,000) is a bimodal mixture, while PS103 ($\overline{Mn}$ = 118,000) and PS109 ($\overline{Mn}$ = 186,000) are monodispersed polystyrene. Clearly, the birefringence is dependent on the molecular weight of the polystyrene being stretched. For specimens with the same extension ratio prepared under the same stretch conditions, the resultant birefringence increases with polystyrene molecular weight. Both the fracture stress and strain increase with Δn. The crazing stress is the same for PS103 and PSBI, but it is much higher for PS109. This indicates craze initiation is closely related to the low molecular weight component in a polydispersed polystyrene.

The SAXS patterns at various deformation stages for the specimens studied as shown in Figure 8-6 are compared in Figure 8-7. The comparison for meridional intensity and equatorial intensity at fracture are made for each specimen individually in Figure 8-8. The

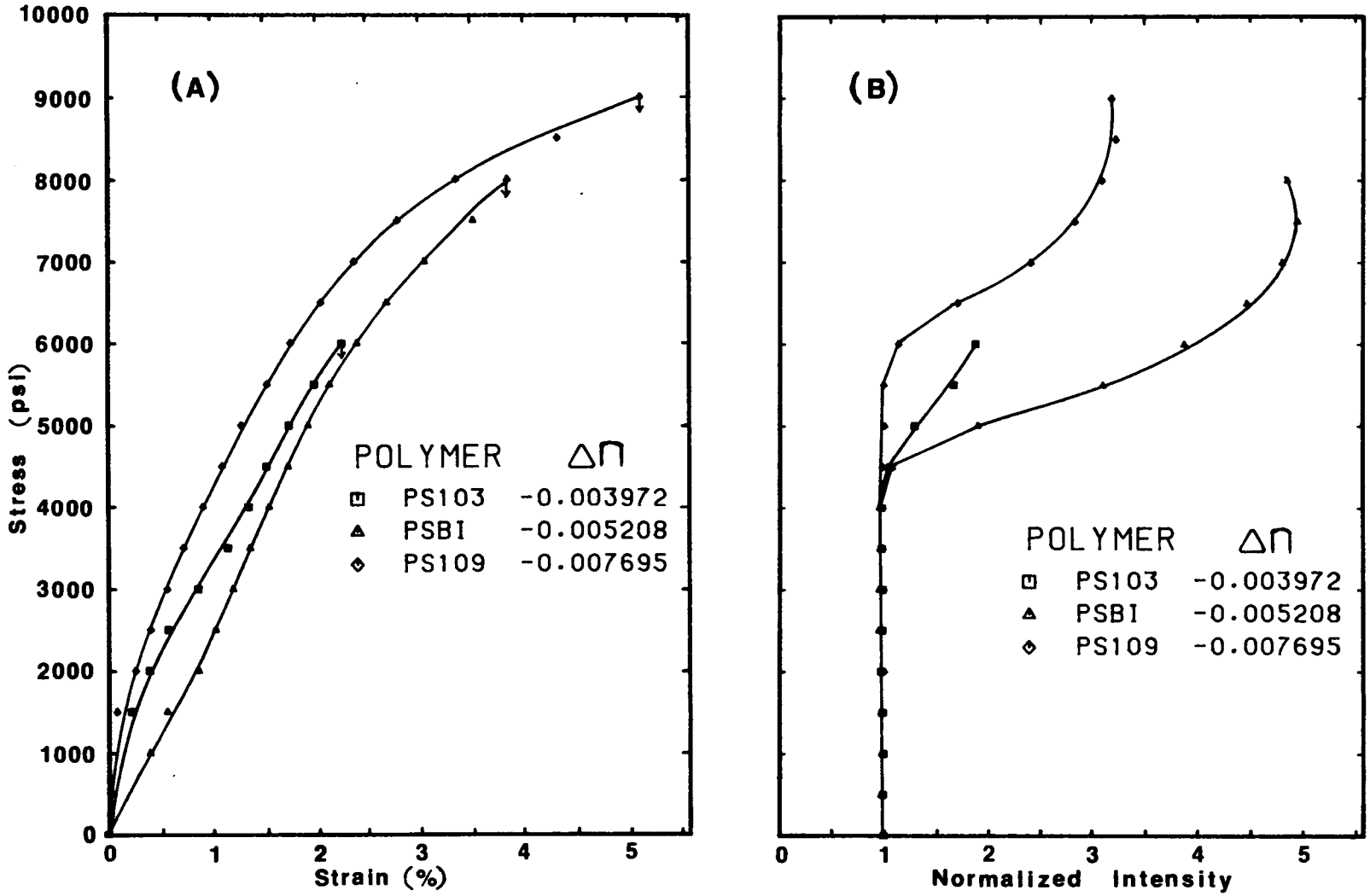


Figure 8-6. (A) Stress-strain curves and (B) stress-normalized intensity curves for uniaxially oriented polystyrenes of various molecular weight prepared using the same conditions. Ts =115°C; $\dot{\gamma}$ = 500%/min; L/L_o = 3.0.

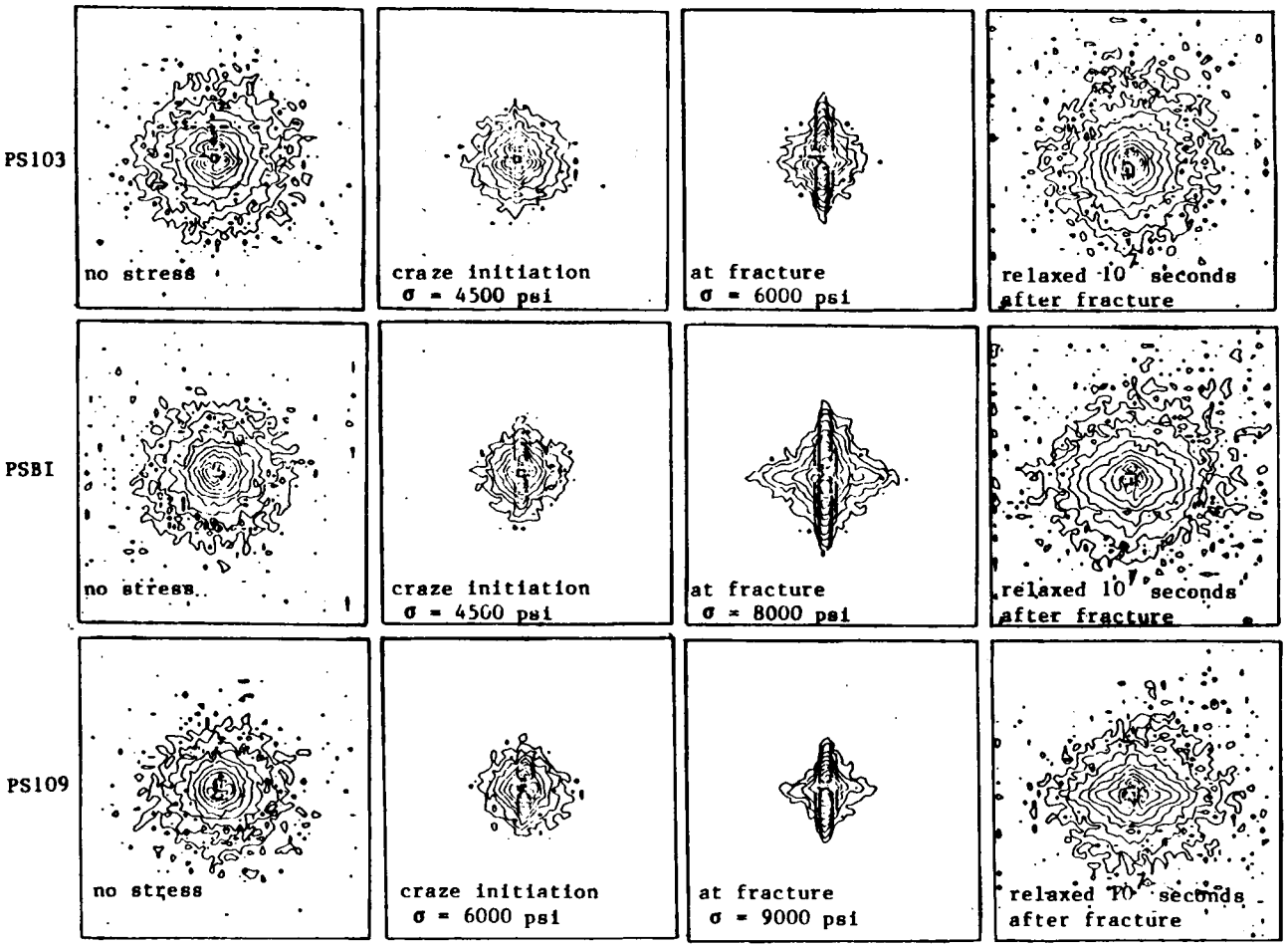


Figure 8-7. Comparison of the SAXS patterns at different deformation stages for the specimens studied in Figure 8-6.

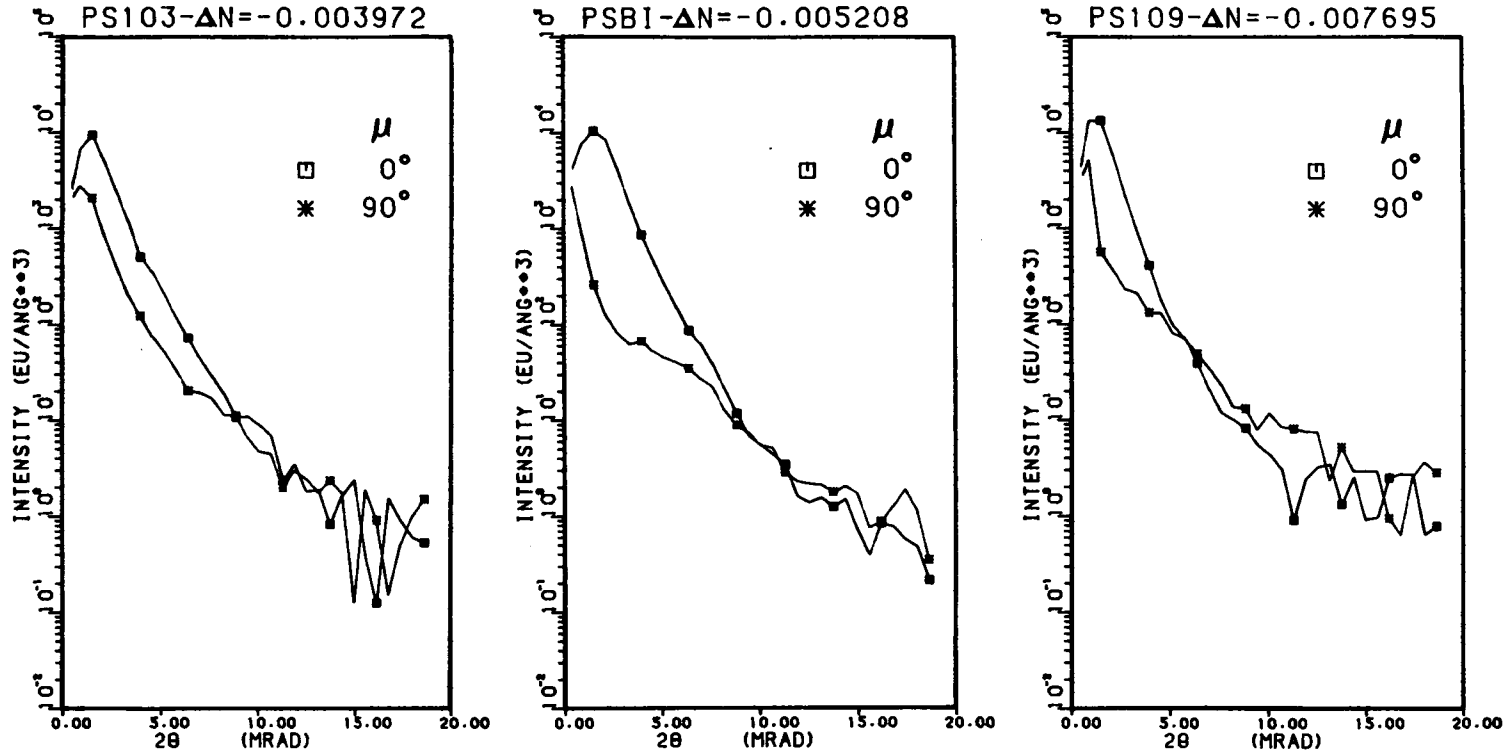


Figure 8-8. Comparison of the meridional and equatorial scattering intensity distributions for each specimen studied in Figure 8-6 at the fracture point.

variations of the scattering intensity at 2θ = 1.5 mrad and 2θ = 5 mrad with stress are shown in Figure 8-9. These three plots indicate that the oriented PS103 specimen has a different fracture mode from the other two polystyrenes: PS103 fractured with local crazing before craze fibrils creep and PSBI and PS109 fractured after craze fibril creep. The oriented PS103 specimen still has an isotropic volume scattering background as shown in Figure 8-8 (A), while the other two have an elliptically shaped volume scattering background. Therefore, both the molecular weight and the degree of molecular orientation affect the value of stress (i.e., the yielding stress) at which the craze thickening mechanism changes from surface drawing to fibril creep.

8.3.3 Varying Stretching Temperature

Two monodispersed polystyrenes, PS103 ($\overline{Mn}$ = 118,000) and PS109 ($\overline{Mn}$ = 186,000), were studied to determine the effect of orientation introduced at different stretch temperatures Ts. The SAXS patterns at various deformation stages and the variations of the scattering intensity at 2θ = 1.5 mrad and 2θ = 5 mrad with stress are shown in Figure 8-10 and Figure 8-11, respectively, for the PS103 series. Both plots suggest that the PS103 series fractured with crazing formation but without craze fibril creep at all oriented states. However, there is a different behavior for the PS109 series which has a higher molecular weight.

The SAXS patterns at various deformation stages and the variations of the scattering intensity at 2θ = 1.5 mrad and 2θ = 5

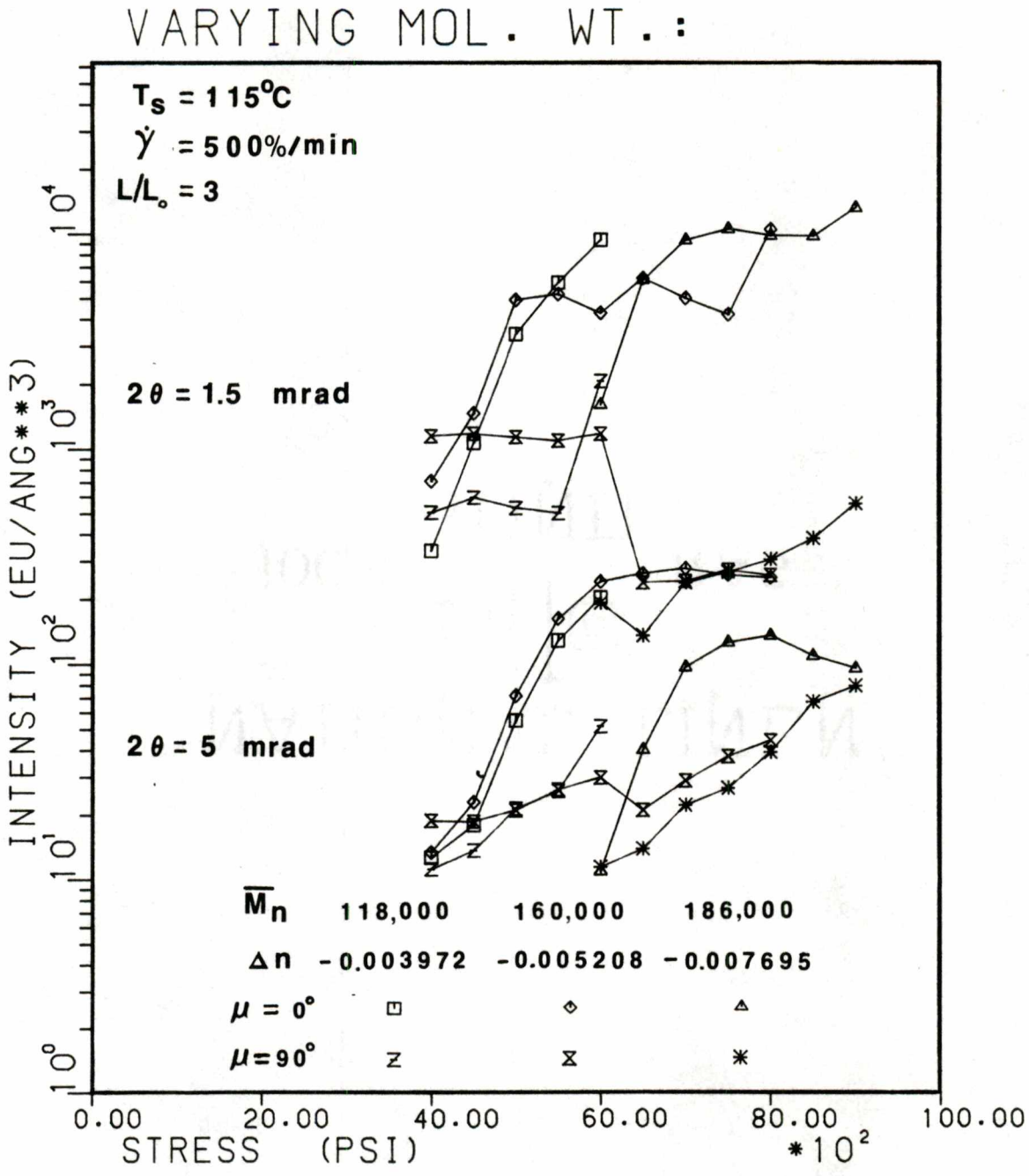


Figure 8-9. Variation of the meridional and equatorial scattering intensity at 2θ = 1.5 mrad and 2θ = 5 mrad with stress for the specimens studied in Figure 8-6.

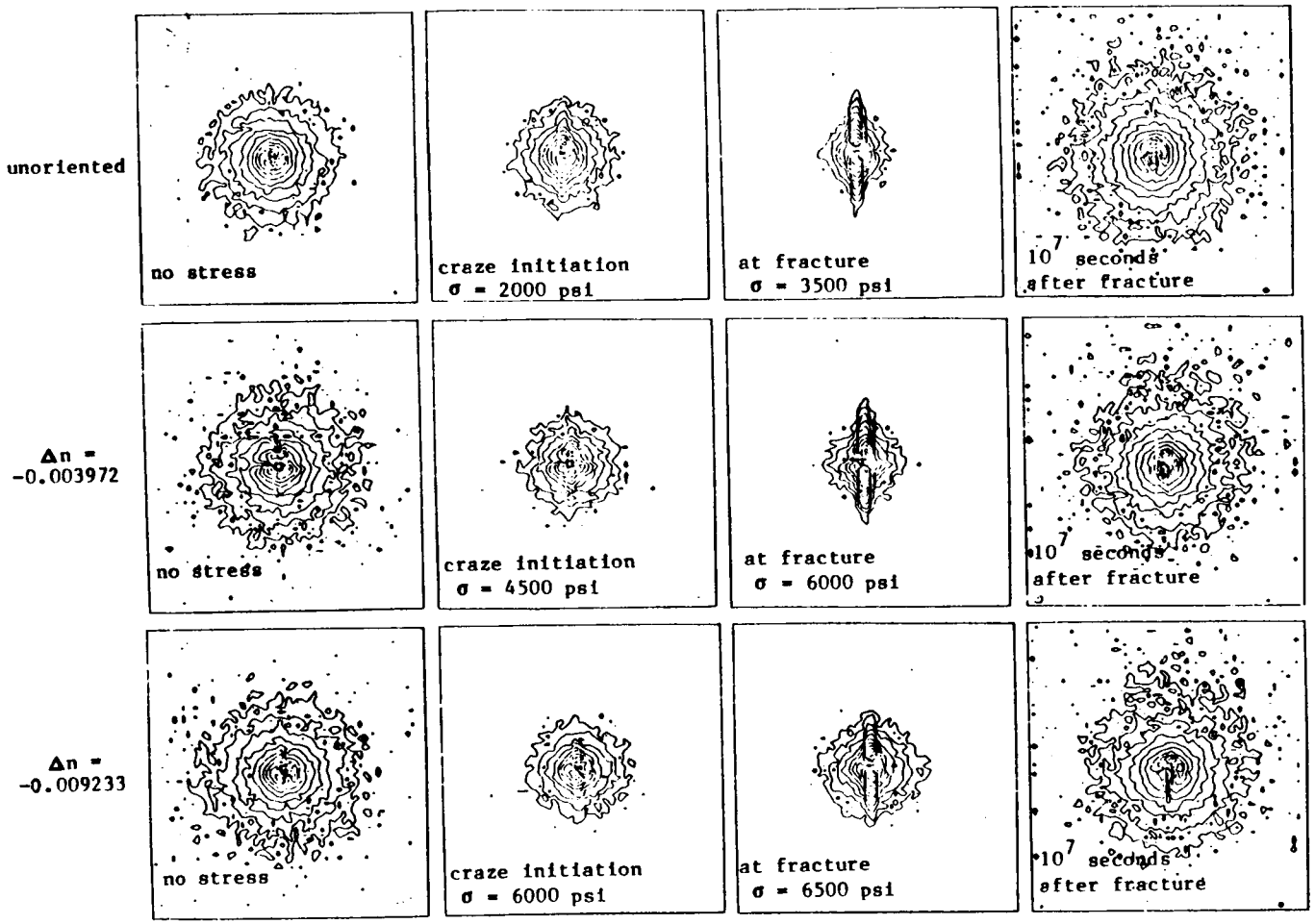


Figure 8-10. Comparison of the SAXS patterns at different deformation stages for the PS103 series. $\overline{Mn}$ = 118,000; $\dot{\gamma}$ = 500%/min; L/L_o = 3.0.

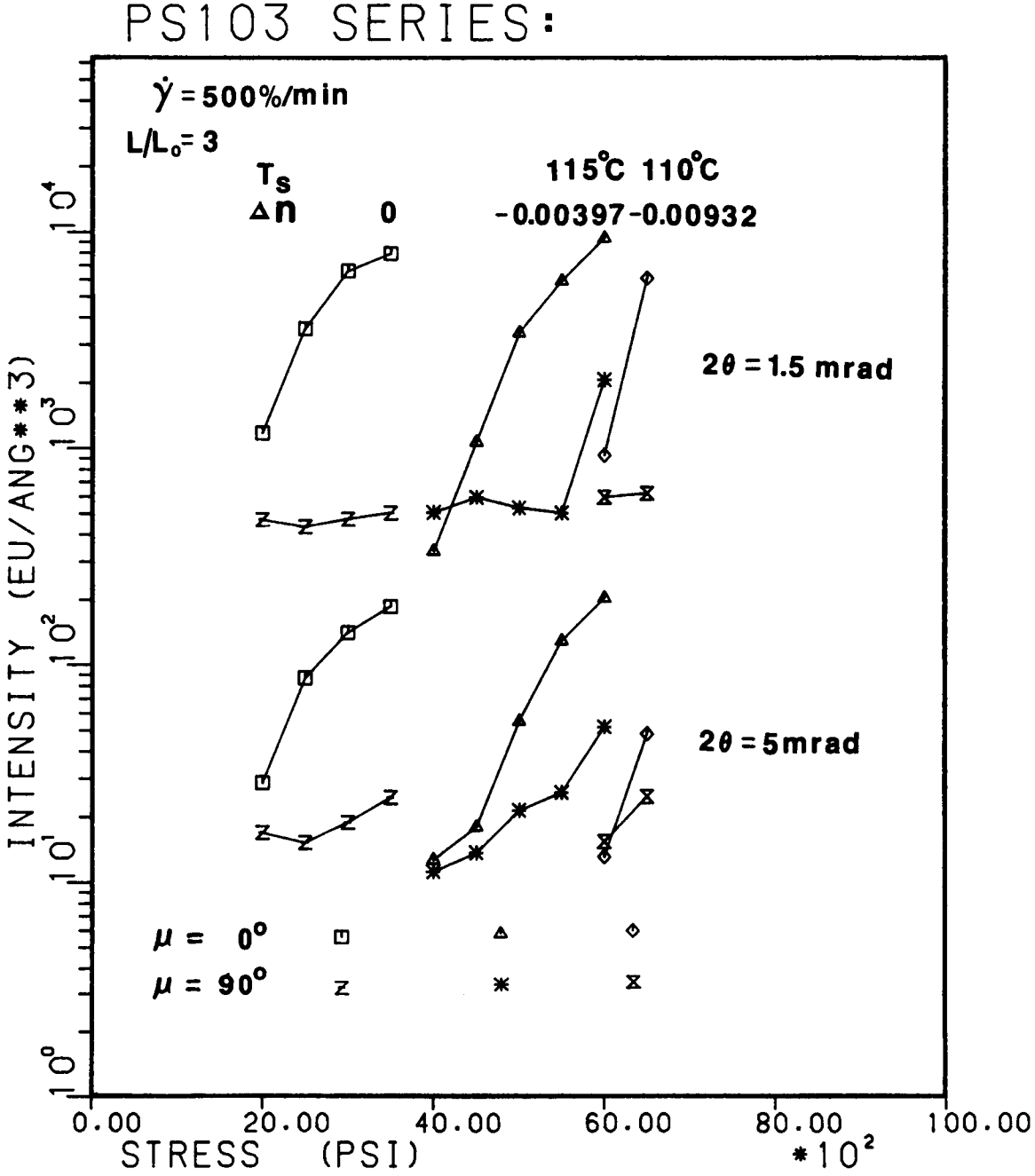


Figure 8-11. Variation of the meridional and equatorial scattering intensity at 2θ = 1.5 mrad and 2θ = 5 mrad with stress for the PS103 series.

mrad with stress are shown in Figure 8-12 and Figure 8-13, respectively. The unoriented PS109 fractured before craze fibril creep. However the two oriented PS109 specimens fractured with yielding of the crazes. If the orientation is introduced at higher temperatures, although the birefringence is lower, the specimen has more ability for craze fibril creep. This behavior may be due to the fact that at higher stretching temperatures more high molecular weight components are oriented than at lower stretching temperatures and thus increase the ability for the yielding of craze fibrils.

8.3.4 Varying Test Angle

A set of stress-strain curves for tensile tests on specimens cut at different angles (ψ_m) from the uniaxially oriented polystyrene sheet are shown in Figure 8-14 (A), and the corresponding stress-normalized scattering intensity curves are shown in Figure 8-14 (B). The results show crazes always developed prior to fracture, irrespective of the angular relationship between the tensile axis and the original MOD. The SAXS patterns taken prior to fracture for various ψ_m are shown in Figure 8-15. Figure 8-16 defines the craze directions in reciprocal space and real space: ψ_m (the angle between the original MOD and tensile axis), ψ_s (the angle between the normal to the craze plane, $\vec{n}_s$, and the tensile axis - for $\psi_m = 0^o$, $\psi_s = 0^o$), and ψ_v (the angle between the transverse axis of the microvoids, $\vec{n}_v$, and the tensile axis - for $\psi_m = 0^o$, $\psi_v = 90^o$).

At $\psi_m \leq 45^o$, the specimens crazed at much higher stresses and fractured at much higher strengths and strains than in unoriented

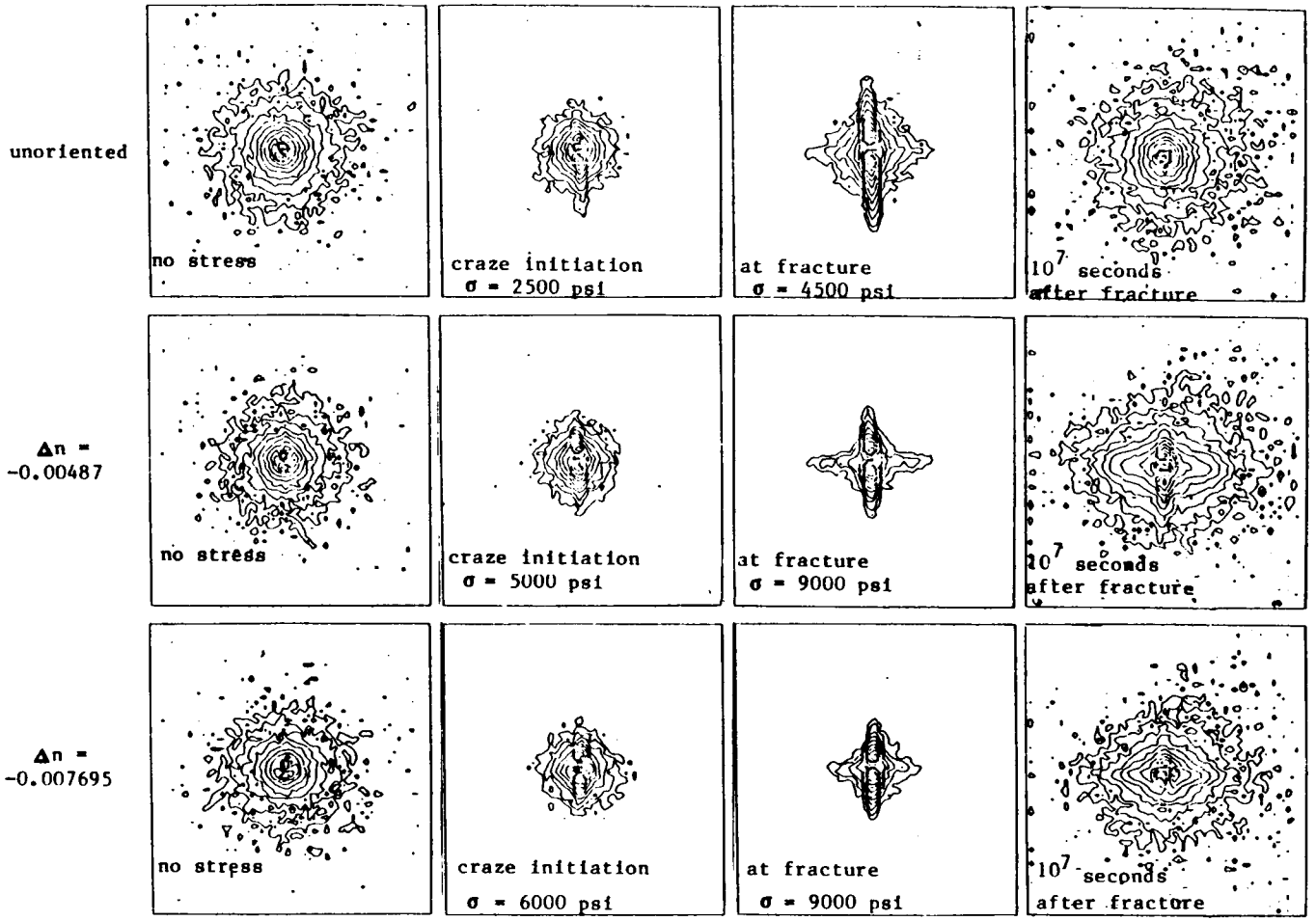


Figure 8-12. Comparison of the SAXS patterns at different deformation stages for the PS109 series. $\overline{Mn}$ = 186,000; $\dot{\gamma}$ = 500%/min; L/L_o = 3.0.

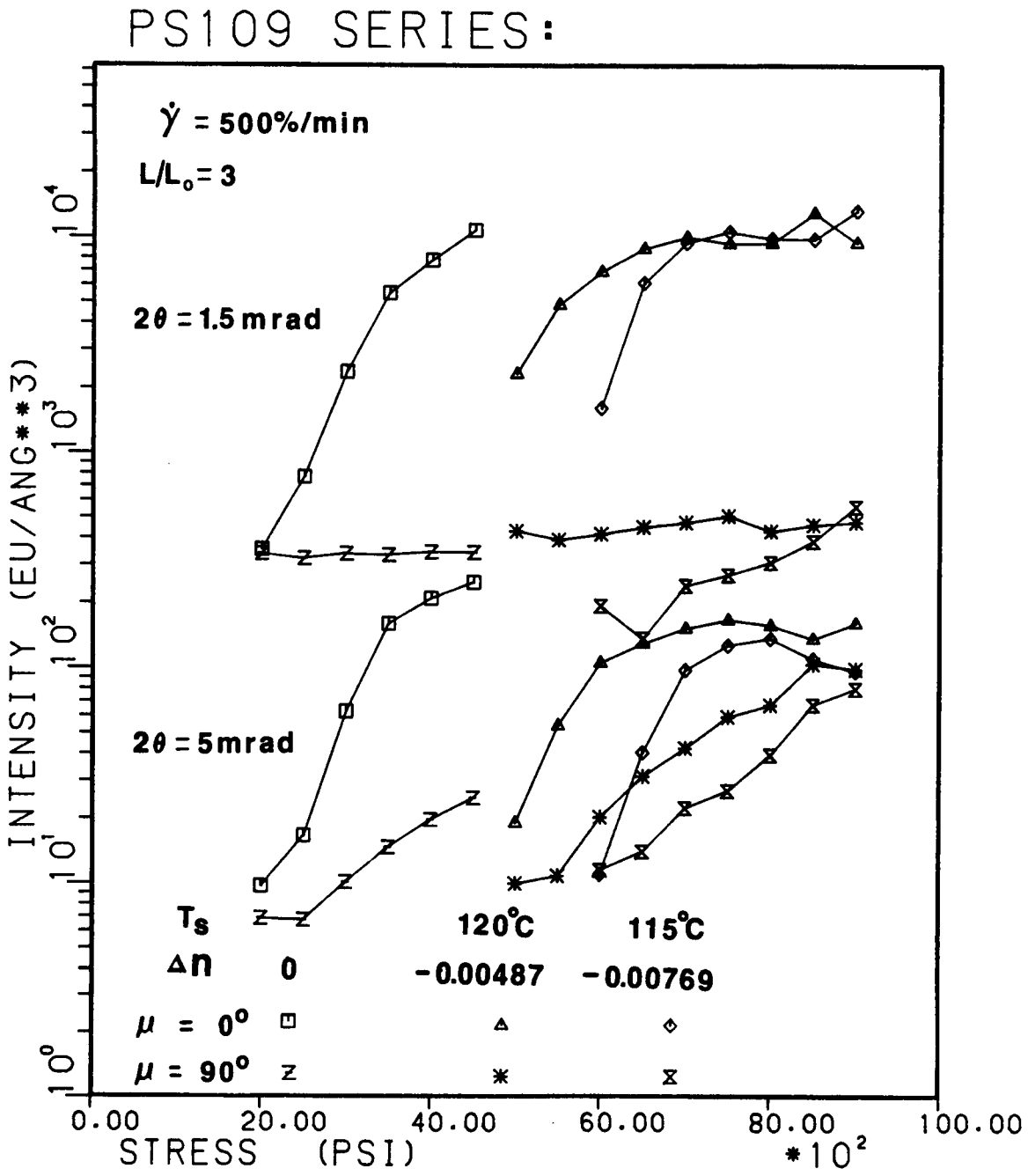


Figure 8-13. Variation of the meridional and equatorial scattering intensity at 2θ = 1.5 mrad and 2θ = 5 mrad with stress for the PS109 series.

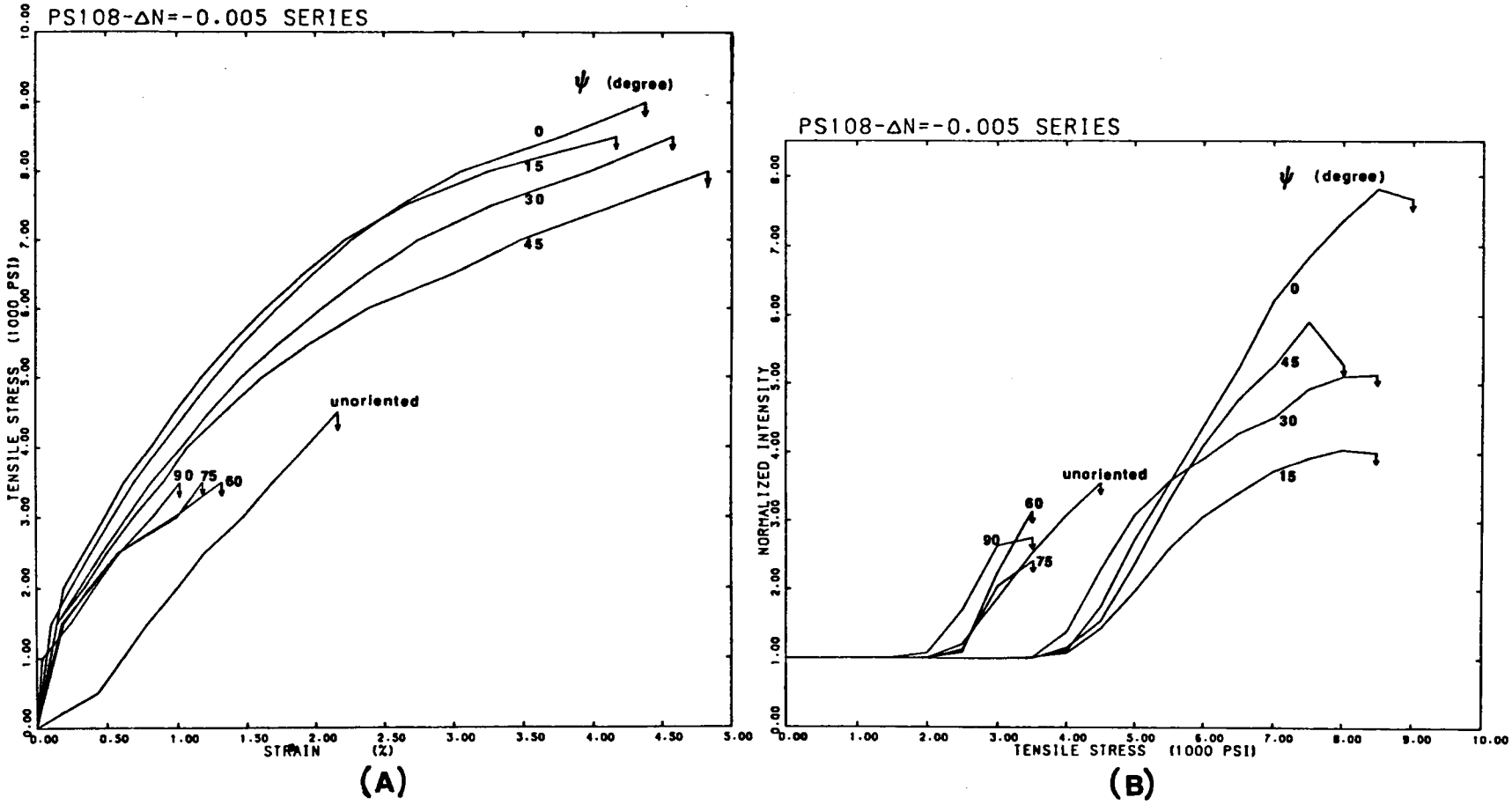


Figure 8-14. (A) Stress-strain curves and (B) stress-normalized intensity curves for tensile tests on specimens cut at different angles from uniaxially oriented polystyrene sheet.

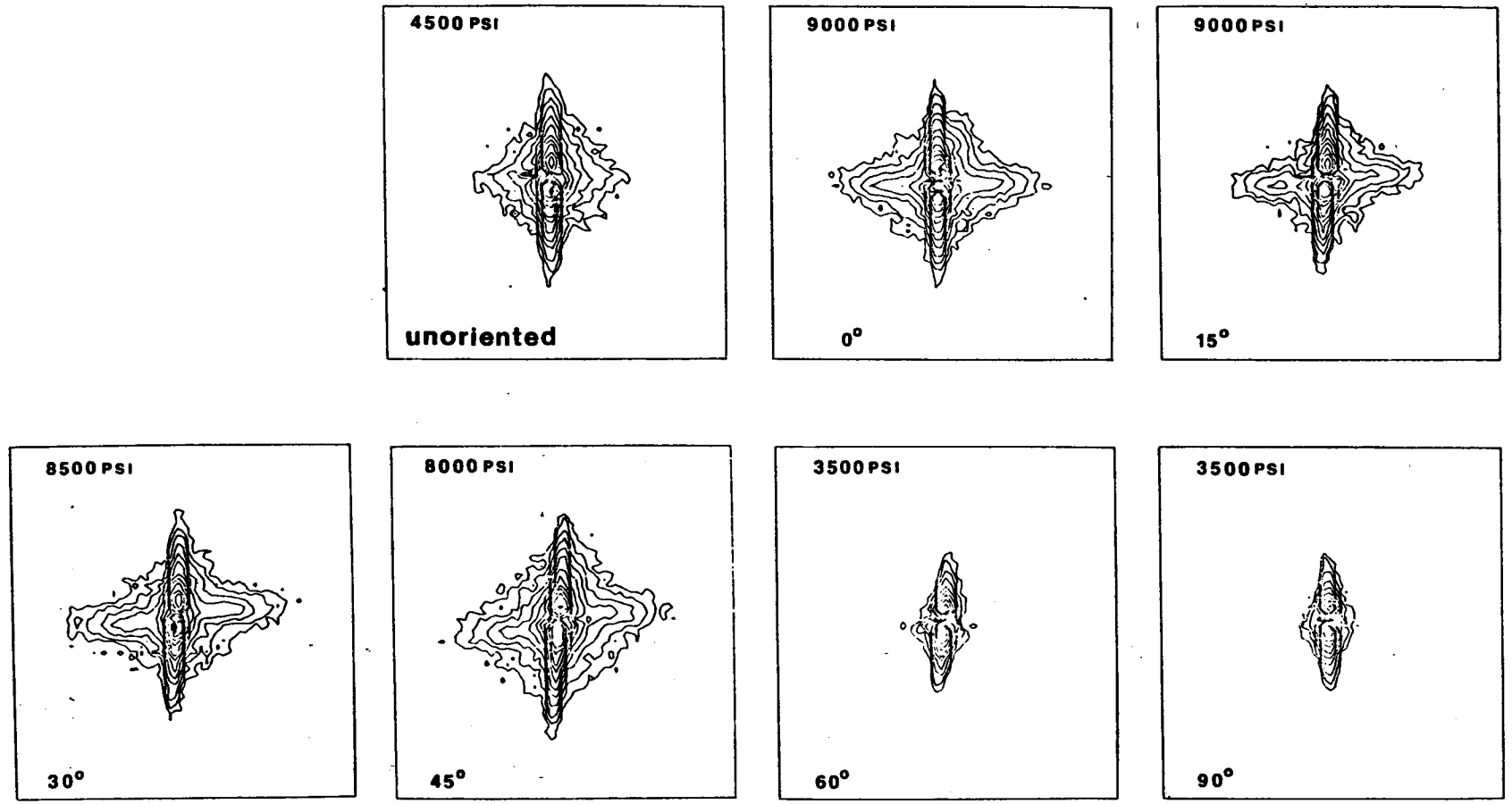


Figure 8-15. Comparison of the SAXS patterns taken prior to fracture for various ψ_m.

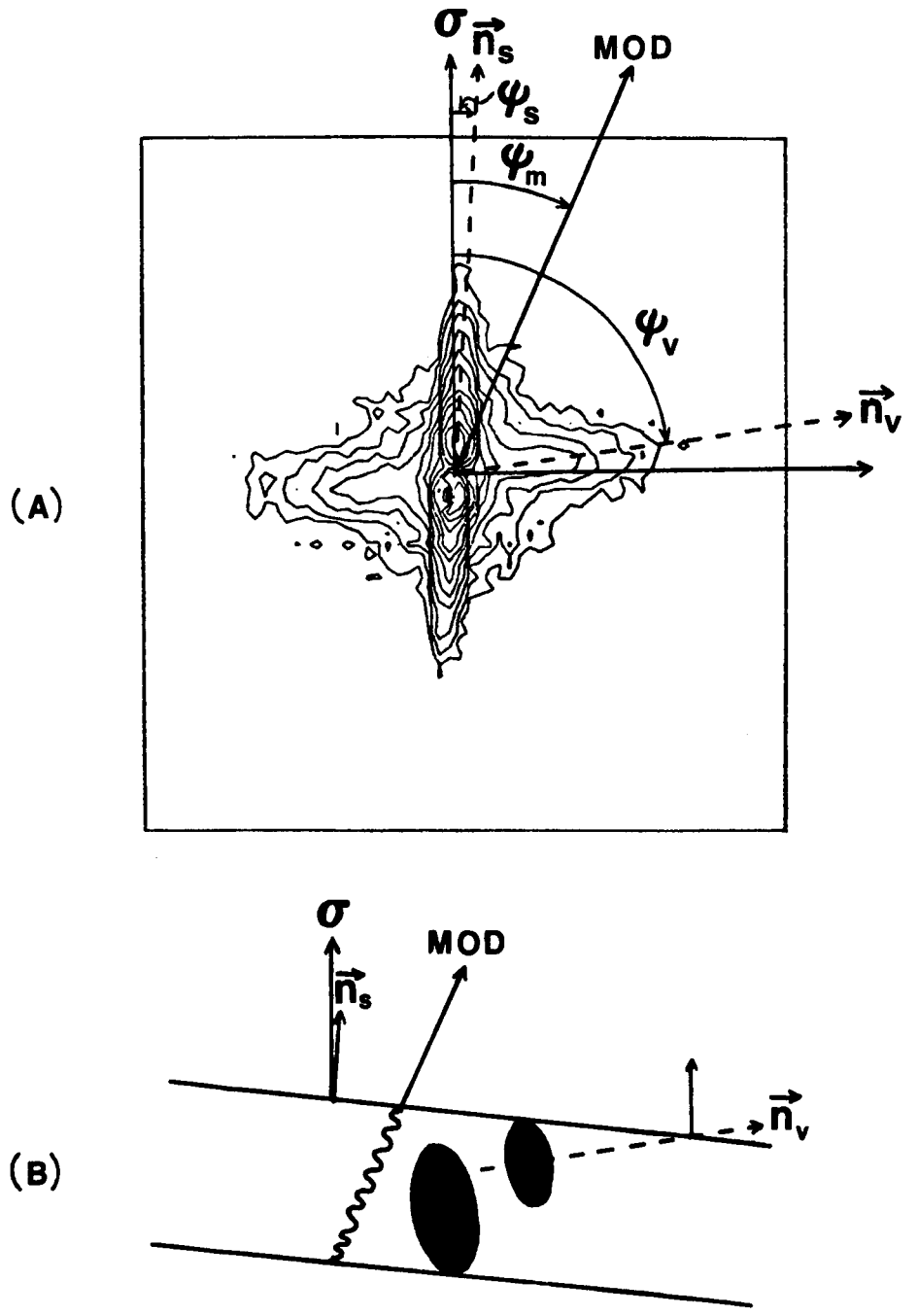


Figure 8-16. Definition of craze directions in (A) reciprocal space and (B) real space.

polystyrene. At $\psi_m > 45^o$, the strength of the specimens and the density of crazes formed prior to fracture were relatively low. Except when the applied tensile force is parallel ($\psi_m = 0^o$) or perpendicular ($\psi_m = 90^o$) to the MOD, the craze plane is not always perpendicular to the tensile axis, as revealed in Figure 8-15 by the fact that the surface scattering streak is not parallel (a deviation of 3° to 4°) to the tensile axis. The craze directions defined by angles ψ_s and ψ_v are plotted against ψ_m in Figures 8-17 (A) and (B), respectively. Except for $\psi_m = 0^o$ and $\psi_m = 90^o$, the plane of the crazes inclines slightly (3° to 4°) towards the MOD and the value of ψ_s does not vary with the value of ψ_m. In the studies of polystyrenes by Hull and Hoare (90), ψ_s is reported to be 2 degrees for specimens with $L/L_o = 1.5$ ($\Delta n = -0.0025$) and 9 degrees for specimens with $L/L_o = 2.6$ ($\Delta n = -0.005$) and $L/L_o = 3.9$ ($\Delta n = -0.008$). The disagreement may be caused by the difference in polystyrene molecular weights and sample preparations.

Previous experiments performed under uniaxial tension have led to stress-based (217, 218) and strain-based criterion (219 - 223) for crazing. The former has generally been interpreted as no crazing will occur if the scalar difference in principal stresses remains below a limiting value. It follows that crazing must occur perpendicular to the maximum stress direction, which is parallel to the tensile axis. The strain-based criteria has generally been interpreted as no crazing will occur if the largest principal strain remains below a limiting value. In a biaxial stress field Oxborough and Bowden (223) pointed

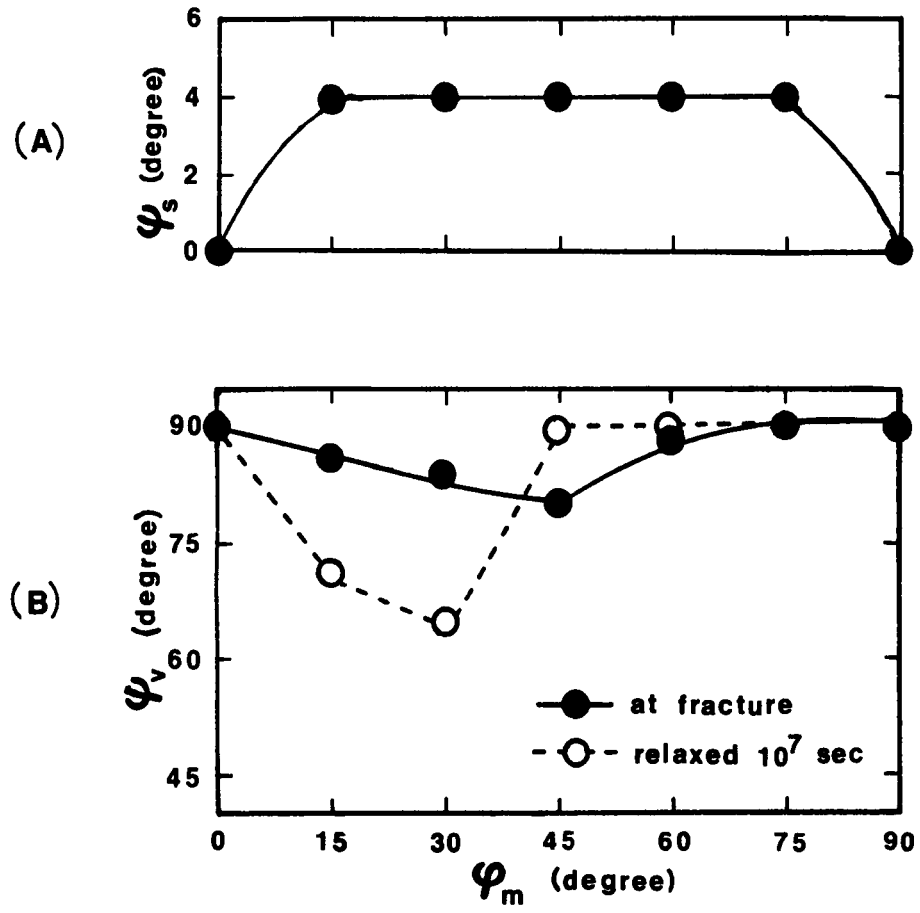


Figure 8-17. Variation of craze directions defined by (A) angle ψ_s and (B) angle ψ_v with test angle ψ_m.

out the stress-based and strain-based criterion for isotropic polymers differ only a little. However, the direction of crazes varies in a more complex manner in an anisotropic material than in an isotropic material. Paying attention to the fact that the craze plane is not always perpendicular to the tensile axis, as revealed in Figure 8-17 (A), it is reasonable to infer that the strain-based criterion is more suitable for crazing. The strain due to the applied stress and the frozen-in strain due to the internal stress along the MOD both play important roles for crazing.

Next, the anisotropy of the microvoids will be discussed. In unoriented specimens, the microvoids are of spherical shape. In oriented specimens with the tensile axis parallel to the MOD, the microvoids are of elliptical shape with the principal axes coinciding with the principal molecular axis, i.e., the longer axis of the ellipsoid is parallel to the MOD and the tranverse axis is perpendicular to the MOD. However, when ψ_m is not equal to 0° nor 90°, the transverse axis of the microvoids is no longer perpendicular to the tensile axis. Using $\psi_m = 0^o$ as the starting condition, as ψ_m is increased the inclination of the microvoid transverse axis to the MOD increases and then decreases with a minimum of $\psi_v = 80^o$ at $\psi_m = 45^o$. More surprisingly is that $\vec{n}_v$ (i.e., the transverse axis of microvoids) is not perpendicular to $\vec{n}_s$ (i.e., the direction of surface scattering streak). This indicates that the surface scattering phenomena does not arise from the microvoid-matrix interfaces but from the microcrack-matrix interfaces.

The variations of the scattering intensity along the directions of $\vec{n}_s$ (i.e., the surface scattering streak) and $\vec{n}_v$ (i.e., the tranverse axis of microvoids) at 2θ = 1.5 mrad and 2θ = 5 mrad with stress are shown in Figure 8-18 and Figure 8-19, respectively. These plots show the yielding of craze fibrils occurs in specimens with ψ_m < 45°. The SAXS patterns of the fractured specimens relaxed for 10^7 seconds are shown in Figure 8-20. The remaining surface scattering streak can be observed clearly in the specimens fractured with the yielding of craze fibrils. Compared to the SAXS patterns taken prior to fracture, the plane of the crazes does not vary during the relaxation for all the values of ψ_m, but the anisotropy of the microvoids changes significantly during the relaxation of the specimens with ψ_m = 15°, ψ_m = 30°, and ψ_m = 45°. Figure 8-21 shows the SAXS patterns of the specimens with ψ_m = 30° and ψ_m = 45° at various stages after fracture. This plot indicates that the shape changes of the microvoids are mostly due to the elastic recovery after the removal of tensile force (specimen fracture), and the viscous recovery which is time dependent does not cause shape change of the microvoids further. The direction of microvoids in relaxed crazes shown in Figure 8-20 is plotted against ψ_m in Figure 8-17 (B) as dashed line.

8.4 Conclusions

Atactic polystyrene specimens having various degrees of orientation were obtained by uniaxially stretching the polystyrene above its glass transition temperature. The microstructural changes

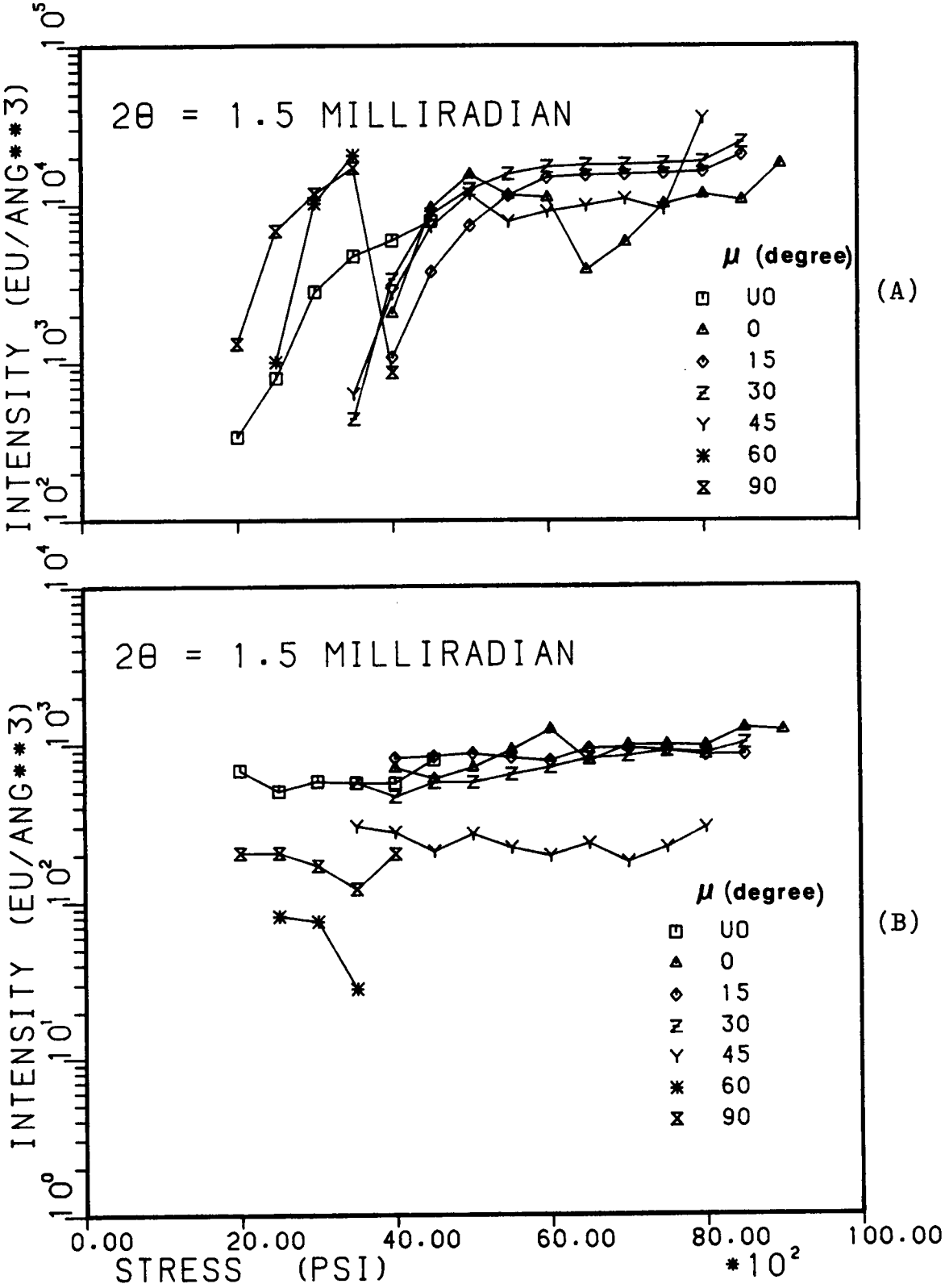


Figure 8-18. Variation of the scattering intensity along (A) $\vec{n}_s$ and (B) $\vec{n}_v$ at 2θ = 1.5 mrad with stress.

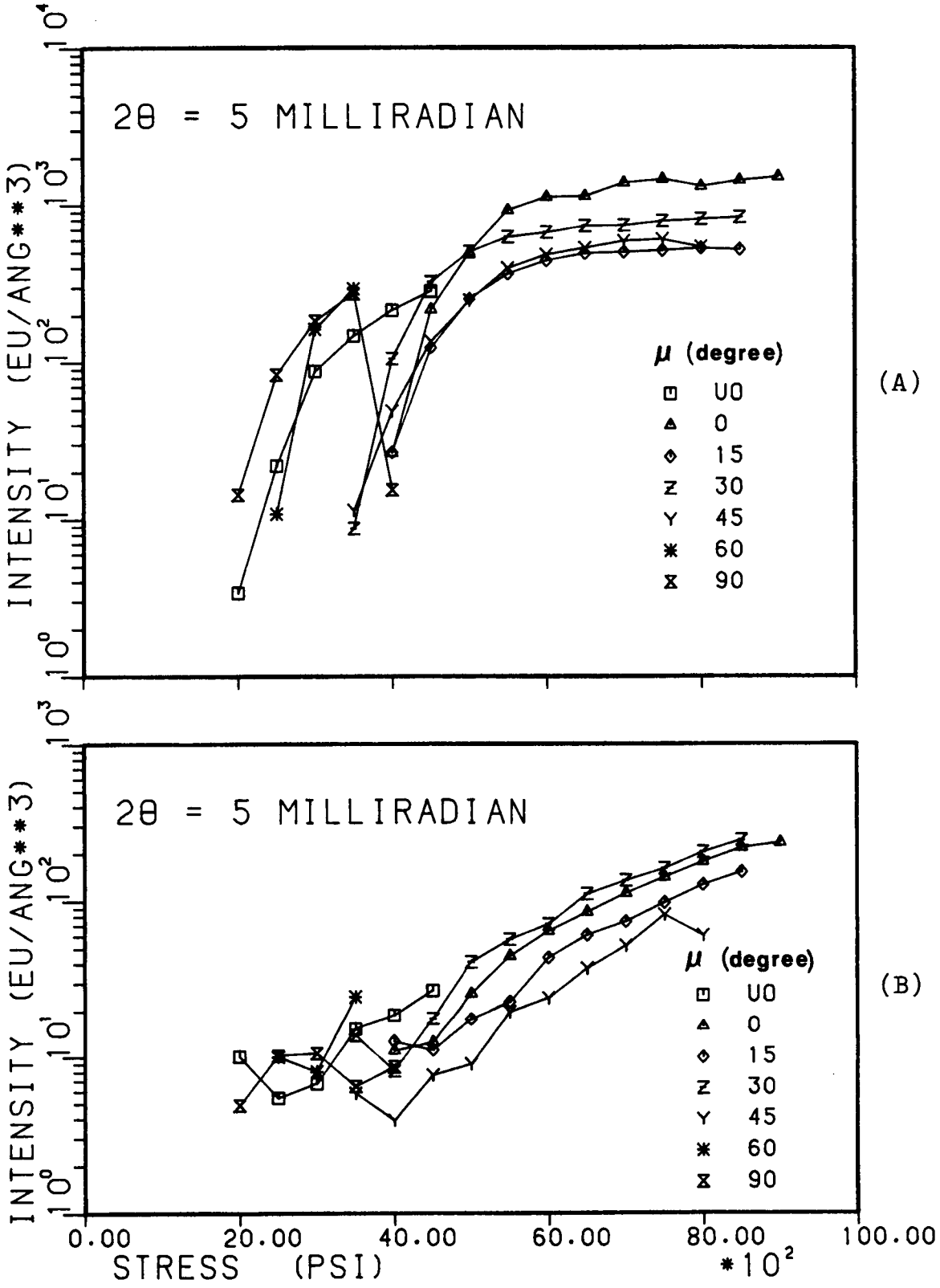


Figure 8-19. Variation of the scattering intensity along (A) $\vec{n}_s$ and (B) $\vec{n}_v$ at 2θ = 5 mrad with stress.

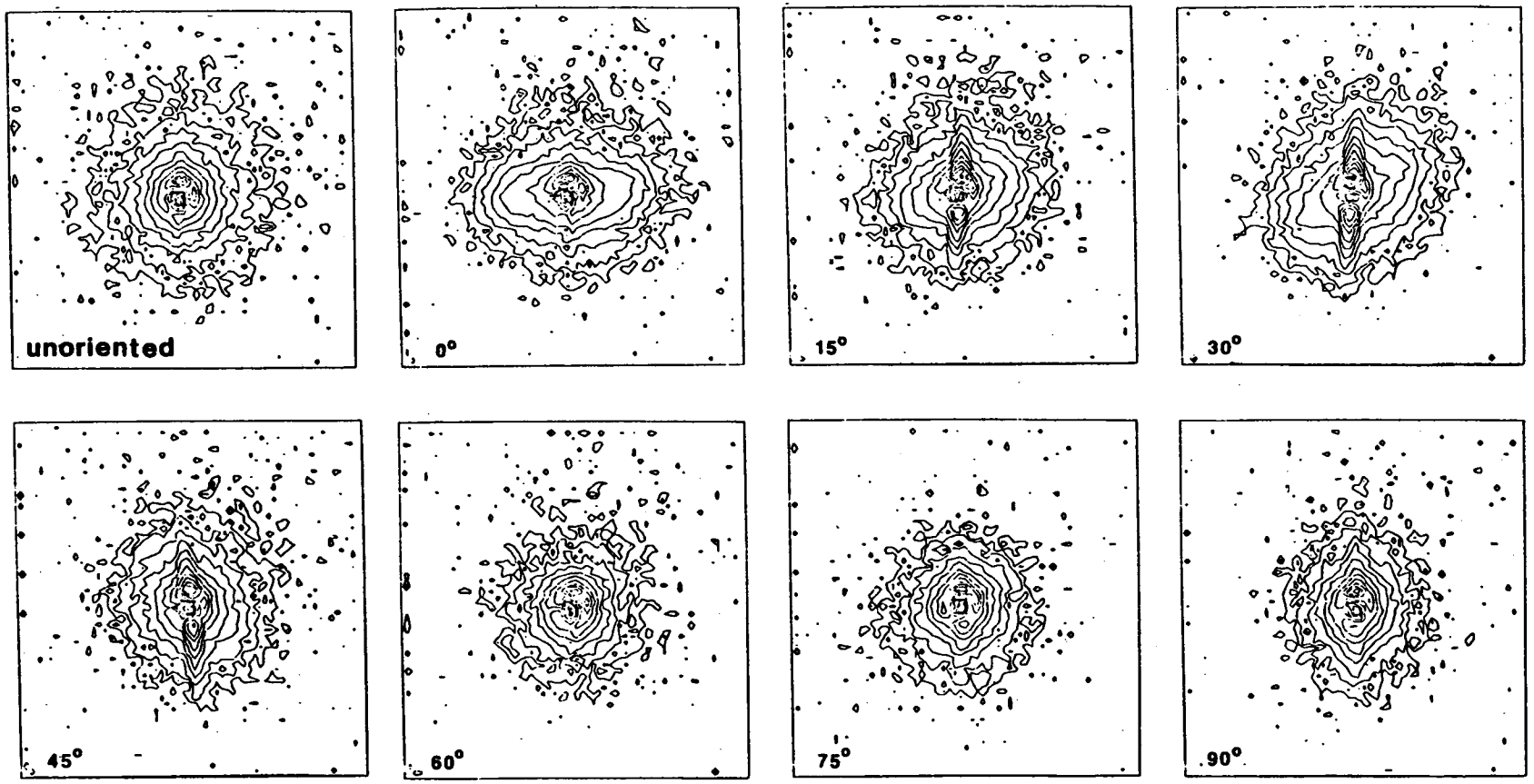


Figure 8-20. Comparison of the SAXS patterns of the fractured specimens relaxed for 10^7 seconds for various ψ_m.

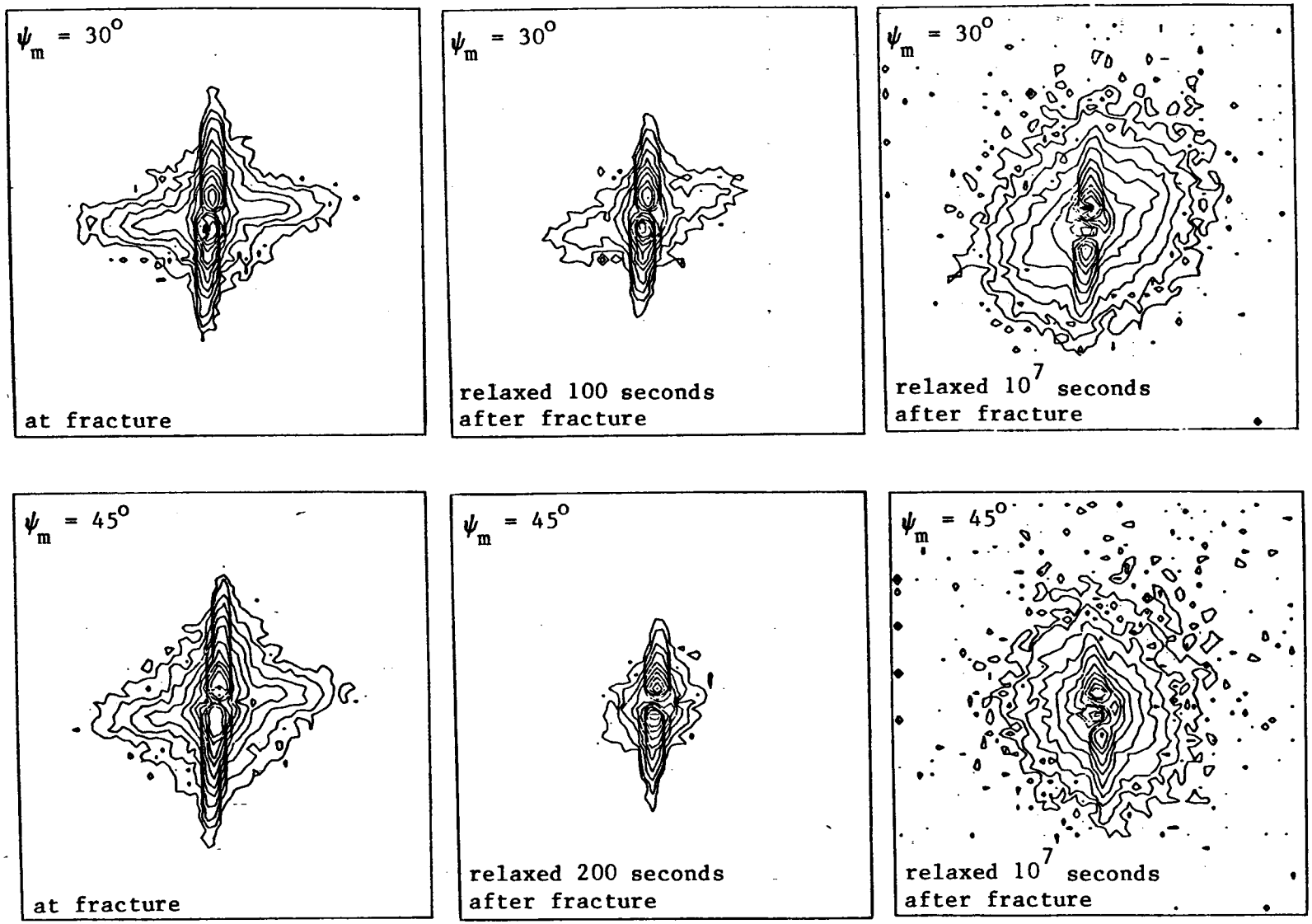


Figure 8-21. Relaxations of the specimens with (A) $\psi_m = 30^\circ$ and (B) $\psi_m = 45^\circ$ at various stages after fracture.

during the tensile tests of oriented polystyrene were investigated concurrently with SAXS. The following conclusions are drawn from the results.

(1) When the applied tensile stress is parallel to the MOD, the craze initiation stress increases with the degree of orientation until the specimen fractures without the formation of crazes. If crazes formed, the direction of the craze plane is perpendicular to that of the applied stress. The average length of the steps made by microcrack jumping from one craze-matrix interface to the other increases with the degree of orientation. The shape of the microvoids in crazes changes from spheres in crazed unoriented polystyrene to ellipsoids in crazed oriented polystyrene.

(2) The inherent yielding behavior of polystyrene is indicated by the transition of the craze thickening mechanism from surface drawing to craze fibril creep. For low molecular weight polystyrene (PS103, $\overline{Mn}$ = 118,000), the specimens fractured with crazing formation show no evidence for yielding of craze fibrils at all orientation states. For high molecular weight polystyrenes (PSBI, $\overline{Mn}$ = 160,000; PS109, $\overline{Mn}$ = 186,000; PS108, $\overline{Mn}$ = 247,000), the yielding of craze fibrils occurs as the degree of orientation increases.

(3) Craze initiation is closely related to the low molecular weight component. The yielding behavior is closely related to the high molecular weight component.

(4) The degree of birefringence can not be used as a unique parameter to identify the orientation state of polystyrene. At higher

stetching temperatures, more high molecular weight components tend to be oriented than at lower stretching temperatures.

(6) When the applied stress froms various angles ψ_m with the MOD, the specimens still fracture with crazing but the craze initiation, the amount of crazes, and the directions of crazes vary significantly with angle ψ_m. This indicates the strain-based criteria for crazing is more suitable than stress-based criteria.

CHAPTER 9

RECOMMENDATIONS

(1) The dynamic SAXS experiments can be conducted using shorter sample to detector distances (e.g. 1 meter and 3 meters). With shorter geometry, (A) the surface scattering phenomenon limited to the region where scattering angle less than five milliradians will not be observed; and (B) the possible small microvoids of size ca. 10 $\mathring{A}$ created at stress less than creazing initiation stress may be detected.

(2) A special sample holder can be designed so that the dynamic tensile tests can be conducted with the incident x-ray forming an angle slightly larger (or smaller) than 90 degrees. Then the total observed scattering intensity is due to the volume scattering phenomenon.

(3) At room temperature, polystyrenes with number averaged molecular weight ranges between 118,000 and 247,000 fracture through microcrack propagation by chain scission. Experiments can be conducted to study the crazing mechanism as a function of the loading history and test temperature. Various amounts of plastizer can be added to the polystyrene to change the glass transition temperature and to study the effects on crazing mechanism.

(4) More detailed experiments should be performed to study the fracture mechanism of oriented polystyrene. The birefringence is related to the microscopic structure with the range of light

wavelengths. The microscopic structure changes in the molecular level introduced by hot-stretching at various process conditions can be studied with small-angle neutron scattering and related to the transition in the crazing mechanism.

(5) Experiments can be conducted on various kinds of amorphous polymers to study the surface scattering phenomenon arising in crazes as a function of the van der Waals surface energy and the strength of main chain bond.

(6) Craze relaxation and interface healing in unloaded crazed polymers can be studied as a function of time, temperature, and loading history.

(7) Dynamic SAXS experiments can be performed with synchrotron radiation source. High radiation power reduces the necessary measurement time and is most beneficial for the highly time dependent relaxation studies.

(8) The application of small-angle x-ray surface scattering phenomenon to the study of the surface structures of optical surface which need to be highly polished or very thin (several hundreds Angstroms) can be explored. Such material includes optical fibers, metal coated thin films, and chips used in the microcircuits for computers.

LIST OF REFERENCES

LIST OF REFERENCES

1. P. J. Flory, "Statistical Mechanics of Chain Molecules," Wiley, New York, 1969.

2. G. S. Y. Yeh, J. Macromol. Sci.-Phys., B6, 464 (1972).

3. W. R. Pechhold and S. Blasenbrey, Kolloid Z. Z. Polym., 241, 955 (1970).

4. P. J. Flory, "Spatial Configuration of Macromolecular Chains," The 1974 Nobel Lecture, J. Polym, Sci.-Polym. Symp., 54, 19 (1976).

5. P. J. Flory, Faraday Discussions, 68, 14 (1979).

6. H. Hayashi, F. Hamada, and A. Nakajima, Macromolecules, 9, 543 (1976); Makromol. Chem., 178, 827 (1977); J. Appl. Cryst., 11, 514 (1978).

7. H. Kim, J. Appl. Polym. Sci., 22, 889 (1978).

8. G. D. Wignall, D. G. H. Ballard, and J. Schelten, Eur. Polym. J., 9, 965 (1973); ibid., 10, 861 (1974).

9. H. Benoit, J. Macromol. Sci.-Phys., B12, 27 (1976).

10. A. Maconnachie and R. W. Richard, Polymer, 19, 739 (1978).

11. G. S. Y. Yeh, Crit. Rev. Macromol. Chem., 1, 173 (1972).

12. P. H. Geil, "Morphology of Amorphous Polymers," Final Report USAROD, Contract DAHC04-70C-0032.

13. D. R. Uhlmann, Faraday Discussions, 68, 87 (1979).

14. W. R. Pechhold in "Deformation and Fracture of High Polymers," ed. by H. H. Kausch, J. A. Hassel, and R. I. Jaffee, Plenum Press, New York, 1972.

15. W. R. Pechhold and H. P. Grossmann, Faraday Discussions, 68, 57 (1979).

16. L. Hoare and D. Hull, Polym. Eng. Sci., 17, 204 (1977).

17. D. A. Carey, C. J. Wust, and D. C. Bogue, J. Appl. Polym. Sci., 25, 575 (1980).

18. A. J. de Vries, C. Bonnebat, and J. Beautemps, J. Polym. Sci.-Polym. Symp., 58, 109 (1977).

19. K. Oda, J. L. White, and E. S. Clark, Polym. Eng. Sci., 18, 53 (1978).

20. W. Kuhn and F. Grun, Kolloid Z., 101, 248 (1942).

21. L. R. G. Treloar, "The Physics of Rubber Elasticity," Oxford, 1958.

22. J. F. Rudd and R. D. Andrews, J. Appl. Phys., 29, 1421 (1958).

23. T. T. Jones, Pure and Appl. Chem., 45, 39 (1976).

24. T. Matsumoto and D. C. Bogue, J. Polym. Sci.-Polym. Phys. Ed., 15, 1663 (1977).

25. C. Picot, R. Duplessix, D. Decker, H. Benoit, F. Boue, J. P. Cotton, M. Farnoux, G. Jannink, M. Nierlich, A. J. de Vries, and P. Pincus, Macromolecules, 10, 436 (1977).

26. F. Boue, M. Nierlich, G. Jannink, and R. Ball, J. Physique, 43, 137 (1982).

27. J. R. Kaze, Trans. Faraday Soc., 32, 77 (1936).

28. S. M. Wecker, T. Davidson, and J. B. Cohen, J. Mat. Sci., 7, 1249 (1972).

29. T. E. Brady and G. S. Y. Yeh, J. Macromol. Sci.-Phys., B7, 243 (1973).

30. A. Colebrooke and A. H. Windle, J. Macromol. Sci.-Phys., B12, 373 (1976).

31. M. May, J. Polym. Sci.-Polym. Symp., 58, 23 (1977).

32. Y. Tanabe and H. Kanetsuna, J. Appl. Polym. Sci., 22, 1619 (1978).

33. B. Jasse and J. Koenig, J. Polym. Sci.-Polym. Phys., 17, 799 (1979).

34. J. Hoare and D. Hull, Phil. Mag., 26, 443 (1972).

35. I. Narisawa, J. Polym. Sci., A-2, 10, 1789 (1972).

36. K. Matsushige, S. V. Radcliffe, and E. Baer, J. Appl. Polym. Sci., 20, 1853 (1976).

37. A. S. Argon, R. D. Andrews, J. A. Godrick, and W. Whitney, J. Appl. Phys., 39, 1899 (1968).

38. R. P. Kambour, J. Polym. Sci., Macromol. Rev., 7, 1 (1973).

39. R. J. Bird, J. Mann, G. Pogany, and G. Rooney, Polymer, 7, 307 (1966).

40. J. Murray and D. Hull, Polymer, 10, 451 (1969).

41. P. Beardmore, Phil. Mag., 19, 389 (1969).

42. R. N. Haward and I. Brough, Polymer, 10, 724 (1969).

43. J. Murray and D. Hull, J. Polym. Sci. A-2, 8, 583 (1970).

44. J. Murray and D. Hull, J. Polym. Sci., A-2, 8, 1521 (1970).

45. J. Murray and D. Hull, J. Polym. Sci.-Polym. Lett., 8, 159 (1970).

46. R. J. Bird, G. Rooney, and J. Mann, Polymer, 12, 742 (1971).

47. M. J. Doyle, A. Maranci, E. Orowan, and S. T. Stork, Proc. Roy. Soc. London, A329, 137 (1972).

48. P. Beahan, M. Bevis, and D. Hull, Polymer, 14, 96 (1973).

49. P. Beahan, M. Bevis, and D. Hull, Proc. Roy. Soc. London, A343, 525 (1975).

50. M. J. Doyle, J. Mat. Sci., 10, 300 (1975).

51. S. Wellinghoff and E. Baer, J. Macromol. Sci.-Phys., B11, 367 (1975).

52. J. A. Sauer, J. Martin, and C. C. Hsiao, J. Appl. Phys., 20, 507 (1949).

53. C. C. Hsiao and J. A. Sauer, J. Appl. Phys., 21, 1071 (1950).

54. S. Rabinowitz and P. Beardmore, CRC Critical Reviews, 1, 1 (1973).

55. H. H. Kausch, "Polymer Fracture," Springer-Verlag, Berlin, 1978.

56. R. P. Kambour, Nature, 195, 1299 (1962).

57. R. P. Kambour, Polymer, 5, 143 (1964).

58. R. P. Kambour, J. Polym. Sci., A-2, 2, 4159 (1964).

59. M. J. Doyle, J. Mat. Sci., 8, 1185 (1973).

60. H. R. Brown, J. Polym. Sci.-Polym. Phys., 17, 1417 (1979).

61. H. R. Brown, J. Polym. Sci.-Polym. Phys., 17, 1431 (1979).

62. H. R. Brown, Ultramicroscopy, 7, 263 (1982).

63. R. P. Kambour, J. Polym. Sci., A-2, 7, 1393 (1969).

64. D. Hull, J. Mat. Sci., 5, 357 (1970).

65. M. Bevis and D. Hull, J. Mat. Sci., 5, 983 (1970).

66. P. Beahan, M. Bevis, and D. Hull, Phil. Mag., 24, 1267 (1971).

67. R. P. Kambour and R. R. Russel, Polymer, 12, 237 (1971).

68. P. Beahan, M. Bevis, and D. Hull, J. Mat. Sci., 8, 162 (1973).

69. T. E. Brady and G. S. Y. Yeh, J. Mat. Sci., 8, 1083 (1973).

70. D. Hull in "Molecular Behavior and the Development of Polymeric Materials," ed. by A. Ledwith and A. M. North, Chapman and Hall, London, 1975.

71. S. N. Zhurkov, V. S. Kuksenko, and A. I. Slutsker in "Fracture," Proc. Int. Symp. on Fracture, Brighton, England (1969), p. 531, Chapman and Hall, London, 1969.

72. A. Guinier and G. Fournet, "Small-Angle Scattering of X-Rays," Wiley, New York, 1955.

73. D. G. LeGrand, R. P. Kambour, and W. R. Haaf, J. Polym. Sci., Part A2, 10, 1565 (1972).

74. G. Porod, Kolloid Z., 124, 83 (1951); Correction: ibid., 133, 51 (1953).

75. T. R. Steger and L. E. Nielsen, J. Polym. Sci.-Polym. Phys., 16, 613 (1978).

76. J. H. Wendorff, Ang. Makromol. Chem., 74, 203 (1978).

77. J. H. Wendorff, Prog. Colloid & Polym. Sci., 66, 135 (1979).

78. J. H. Wendorff, Polymer, 21, 553 (1980).

79. U. Biskup, L. Morbitzer, and E. H. Muller, Ang. Makrompl. Chem., 75, 167 (1979).

80. E. Parades and E. W. Fischer, Makromol. Chem., 180, 2707 (1979).

81. H. R. Brown and E. J. Kramer, J. Macromol. Sci.-Phys., B19, 487 (1981).

82. P. A. Westbrook, Master Thesis, University of Tennessee, August, 1982;
also P. A. Westbrook, J. F. Fellers, M. Cakmak, and J. S. Lin, J. Polym. Sci.-Phys. Ed., 21, 1913 (1983).

83. W. S. Rothwell, R. H. Martinson, and R. L. Gorman, Appl. Phys. Lett., 42(5), 422 (1983).

84. R. H. Martinson and W. S. Rothwell, Polymer Prints, 24(2), 232 (1983).

85. J. F. Rudd, J. Polym. Sci.-Polym. Lett., 1, 1 (1963).

86. R. P. Kambour, Polym. Eng. Sci., 8, 281 (1968).

87. J. C. Bray and H. B. Hopfenberg, J. Polym. Sci.-Polym. Lett., 7, 679 (1969).

88. J. F. Fellers and B. F. Kee, J. Appl. Polym. Sci., 18, 2355 (1974).

89. R. N. Haward, B. M. Murphy, and E. F. T. White in "Fracture," Proc. Int. Symp. on Fracture, Brighton, England (1969), Chapman and Hall, London, 1969, Paper no. 45.

90. D. Hull and L. Hoare, Plastics and Rubber, Materials and Appl., 5, 65 (1976).

91. N. R. Farrar and E. J. Kramer, Polymer, 22, 691 (1981).

92. J. S. Harris and I. M. Ward, J. Mat. Sci., 5, 573 (1970).

93. P. Beardmore and S. Rabinowitz, J. Mat. Sci., 10, 1763 (1975).

94. W. C. Roentgen, Sitzungsber der Wurzburger physik-Medic. Gesellsch. Jahrg. 1895, reprinted in Ann. der Phys., 64, 1 (1898). Translation by A. Stanton in Science, 3, 227 (1896).

95. M. von Laue, F. Friedrich, and P. Knipping, Sitz. Math. Phys. Klasse Bayer. Akad. Wiss., p. 303 (1912); Ann. Phyk., 41, 971 (1913).

96. C. V. Raman and P. Krishnamurti, Nature, 124, 53 (1929).

97. M. V. Smoluchowski, Ann. Phys., 25, 205 (1908).

98. A. Einstein, Ann. Phys., 33, 1275 (1910).

99. F. S. Ornstein and F. Zernike, Proc. Acad. Sci. Amsterdam, 17, 797 (1914).

100. A. Guinier, Ann. Phys., 12, 161 (1939).

101. O. Kratky, Naturwissenschaften, 26, 94 (1938).

102. R. Hosemann, Z. Physik, 113, 751 (1938); ibid., 114, 133 (1939).

103. R. S. Bear, J. Amer. Chem. Soc., 64, 727 (1942); ibid., 65, 1784 (1943).

104. O. Kratky and A. Sekora, J. Makromol. Chem., 1, 113 (1943).

105. Papers from the Small Angle Scattering Meeting, Kansas City, Missouri, USA, 1958. J. Appl. Phys., 30, 601 - 674 (1959).

106. Papers from the First International Conference on Small-Angle X-Ray Scattering, Syracuse, New York, USA, 1965. "Small-Angle X-Ray Scattering," H. Brumberger (editer), Gordon and Breach, New York, 1967.

107. Papers from the Second International Conference on Small-Angle X-Ray Scattering, Graz, Austria, 1970. J. Appl. Cryst., 4, 408 - 426 (1971).

108. Papers from the Third International Conference on Small-Angle Scattering, Grenoble, France, 1973. J. Appl. Cryst., 7, 95 - 239 (1974).

109. Papers from the Fourth International Conference on Small-Angle Scattering of X-Rays and Neutrons, Gatlinburg, TN, USA, 1977. J. Appl. Cryst., 11, 295 - 674 (1978).

110. Papers from the Fifth International Conference on Small-Angle Scattering, Berlin, Germany, 1980. Program and Abstracts.

111. A. J. Renouprez, "Diffusion des Rayons X aus Petits Angles," Intern. Union Cryst. Bibliography 4 (1970).

112. P. F. van Hutten, "Small-Angle X-Ray Scattering Studies of Macromolecules and Colloidal Systems," Krips Repro., Meppel, Netherlands, 1981.

113. O. Glatter and O. Kratky (Editers), "Small Angle X-ray Scattering," Academic Press, New York, 1982.

114. W. W. Beeman, P. Kaesberg, J. W. Anderegg, and Webb, "Size of Particle and Lattice Defects," Handbuch der Physik, 32, 321 - 442 (1956).

115. O. Kratky in "Progress in Biophysics," Vol. 13, pp. 105 - 173, Pergamon Press, Oxford, 1963.

116. O. Kratky and I. Pilz in "Quarterly Reviews of Biophysics," Vol. 27, pp. 151 - 209, Academic Press, New York, 1972.

117. I. Pilz in "Physical Principles and Techniques of Protein Chemistry," Part C, pp. 141 - 243, Academic Press, New York, 1973.

118. I. Pilz, O. Glatter, and O. Kratky in "Methods of Enzymology," Vol. 61, pp. 148 - 249, Academic Press, New York, 1979.

119. R. Hosemann and S. N. Bagchi, "Direct Analysis of Diffraction by Matter," North-Holland, Amsterdam, 1962.

120. L. E. Alexander; "X-Ray Diffraction Methods in Polymer Science," Wiley, New York, 1969; and reprinted, Robert E. Krieger, New York, 1979.

121. M. Kakudo and N. Kasai, "X-Ray Diffraction by Polymers," Elsevier, New York, 1972.

122. P. Debye and A. M. Bueche, J. Appl. Phys., 20, 518 (1949).

123. R. Perret and W. Ruland J. Appl. Cryst., 4, 444 (1971).

124. A. H. Compton and S. K. Allison, "X-Rays in Theory and Experiment," Macmillan, London, 1935.

125. M. Roth, J. Appl. Cryst., 10, 172 (1977).

126. B. K. Vainshtein, "Diffraction of X-Rays by Chain Molecules," Elsevier, New York, 1966.

127. J. J. Thomson, Proc. Cambr. Phil. Soc., 9, 393 (1898).

128. R. W. Hendricks, J. Appl. Cryst., 5, 315 (1972).

129. A. L. Patterson, Z. Krist., 90, 517 (1935).

130. P. P. Ewald, Physik. Z., 14, 465 (1913).

131. P. Debye, Ann. Physik, 46, 809 (1915).

132. V. Gerold, Z. Elektrochem., 60, 405 (1956).

133. R. Bramer and H. G. Kilian, Kolloid Z. Z. Polym., 250, 410 (1972).

134. P. Debye, H. R. Anderson, and H. Brumberger, J. Appl. Phys., 28, 679 (1957).

135. L. Kahovec, G. Porod, and H. Ruck, Kolloid Z., 133, 16 (1953).

136. A. Guinier, Compt. Rend., 204, 1115 (1937).

137. A. Guinier, J. Chim. Physique, 40, 133 (1943).

138. W. Ruland, Colloid & Polym. Sci., 256, 932 (1978).

139. W. Wu, J. Polym. Sci.-Polym. Phys., 18, 1659 (1980).

140. D. Wrinch, "Fourier Transforms and Structure Factors," ASXRED Monograph No.2, 10, 1946.

141. G. H. Vineyard, Acta Cryst., 4, 281 (1951).

142. H. P. Klug and L. E. Alexander, "X-Ray Diffraction Procedures," Wiley, New York, 1954, pp. 204 - 206.

143. M. Matsui and D. C. Bogue, Trans. Soc. Soc. Rheol., 21, 133 (1977);
also M. Matsui, M. S. Thesis, University of Tennessee, Knoxville, 1976.

144. T. Matsumoto and D. C. Bogue, Trans. Soc. Rheol., 21, 453 (1977).

145. C. J. Wust, Jr., M. S. Thesis, University of Tennessee, Knoxville, 1979.

146. R. S. Stein, J. Polym. Sci., 24, 383 (1957).

147. R. W. Hendricks, J. Appl. Cryst., 11, 15 (1978).

148. S. Suehiro, R. W. Hendricks, J. S. Lin, T. Kyu, P. Young, and R. S. Stein, "A Dynamic Small-Angle Scattering System for the Study of Material Deformation and Relaxation," to be published.

149. C. J. Borkowski and M. K. Kopp, IEEE Trans. Nucl. Sci. NS 19, 161 (1972).

150. C. G. Vonk, J. Appl. Cryst., 8, 340 (1975).

151. V. Luzzati in "X-Ray Optics and X-Ray Microanalysis," p.133, Academic press, New York, 1963.

152. O. Kratky, Z. Anal. Chem., 201, 161 (1964).

153. O. Kratky, I. Pilz and P. J. Schmitz, J. Colloid and Interface Sci., 21, 24 (1966).

154. B. E. Warren, "X-Ray Diffraction," Addison-Wesley, Reading, Mass., 1969.

155. R. B. Leighton, "Principles of Modern Physics," p.577, McGraw-Hill, New York, 1959.

156. D. R. Chipman, Acta Cryst., 25, 209 (1969).

157. O. Kratky and H. Wawra, Mh. Chem., 94, 981 (1963).

158. R. W. Hendricks and L. B. Shaffer, "Some Properties of Octafluorocyclobutane (C4F8) of Interest in X-Ray Absolute Intensity Experiments," USAEC Report ORNL-TM-3407, Oak Ridge National Laboratory, Oak Ridge, Ttennessee.

159. I. S. Patel and P. W. Schmidt, J. Appl. Cryst., 4, 50 (1971).

160. I. Pilz and O. Kratky, J. Colloid and Interface Sci., 24, 211 (1967).

161. I. Pilz, J. Colloid and Interface Sci., 30, 140 (1969).

162. R. Perret and W. Ruland, J. Appl. Cryst., 5, 116 (1972).

163. R. W. Hendricks et al., J. Appl. Cryst., 11, 196 (1978).

164. W. Wiegand and W. Ruland, Prog. Colloid Polym. Sci., 66, 355 (1979).

165. C. G. Vonk, J. Appl. Cryst., 6, 81 (1973).

166. J. Rathje and W. Ruland, Colloid & Polym. Sci., 254, 358 (1976).

167. A. L. Renninger and D. R. Uhlmann, J. Polym. Sci. Polym. Phys. Ed., 16, 2237 (1978).

168. T. F. Chapman, Master Thesis, University of Tennessee, December, 1976.

169. J. H. Wendorff and E. W. Fischer, Kolloid Z. Z. Polym., 251, 876 (1973).

170. J. H. Wendorff and E. W. Fischer, Kolloid Z. Z. Polym., 251, 884 (1973).

171. P. Beckmann and A. Spizzichino, "The Scattering of Electromagnetic Waves from Rough Surfaces," Chapter 12, Macmillan, New York, 1963.

172. W. Stenstrom, Dissertation, Lund, 1919.

173. A. H. Compton, Bull. Nat. Res. Counc. U.S.A., 20, 48 (1922); Phil. Mag., 45, 1121 (1923).

174. H. E. Stauss, Phys. Rev., 31, 491 (1928).

175. E. Dershem and M. Schein, Phys. Rev., 37, 1246 (1931).

176. P. Kirkpatrick and A. V. Baez, J. Opt. Soc. Am., 38, 766 (1948).

177. W. Ehrenberg, J. Opt. Soc. Am., 39, 741 (1949).

178. B. L. Henke and J. W. M. DuMond, J. Appl. Phys., 26, 903 (1955).

179. L. G. Parratt, Phys. Rev., 95, 359 (1954).

180. A. N. Nigam, Phys. Rev., 138, A1189 (1965).

181. D. S. Kapp and N. Wainfan, Phys. Rev., 138, A1490 (1965).

182. P. Croce, G. Devant, M. G. Sere, and M. F. Verhaeghe, Surface Sci., 22, 173 (1970).

183. P. Croce and L. Nevot, J. Appl. Cryst., 7, 125 (1974).

184. Y. Nakano, T. Fukamachi, and K. Hayakawa, Japanese J. Appl. Phys., 17, Supplement 17-2, 329 (1978).

185. G. L. Gaines, Jr. and D. G. LeGrand, J. Colloid & Inter. Sci., 55, 274 (1976).

186. J. M. Schultz, Acta Cryst., A27, 179 (1971).

187. E. Kroger and E. Kretschmann, Z.Phys., 237, 1 (1970).

188. D. Beaglehole and O. Hunderi, Phys. Rev., B2, 309 (1970); ibid., B2, 321 (1970).

189. J. M. Elson and R. H. Ritchie, Phys. Rev., B4, 4129 (1971).

190. J. M. Elson and R. H. Ritchie, Phys. Status Solidi, B62, 461 (1974).

191. J. M. Elson, Phys. Rev., B12, 2541 (1975).

192. E. Kretschmann and E. Kroger, J. Opt. Soc. Am., 65, 150 (1975).

193. J. M. Elson and J. M. Bennett, J. Opt. Soc. Am., 69, 31 (1979).

194. J. M. Elson, J. Opt. Soc. Am., 66, 682 (1976).

195. F. Abeles, Ann. de Physique, 5, 596 (1950); ibid., 5, 706 (1950).

196. R. Jacobsson, Progress in Optics, 5, 247 (1965).

197. M. Born and E. Wolf, "Principles of Optics," 3rd ed., Chapter 1, Pergamon Press, New York, 1965.

198. J. M. Elson, Appl. Optics, 16, 2872 (1977).

199. J. M. Elson, J. Opt. Soc. Am., 69, 48 (1979).

200. J. M. Elson, J. P. Rahn, and J. M. Bennett, Appl. Optics, 19, 669 (1980).

201. P. Boussquet, F. Flory, and P. Roche, J. Opt. Soc. Am., 71, 1115 (1981).

202. H. A. Lorentz, "The Theory of Electrons," p.159, 1916.

203. A. H. Compton, "X-Rays and Electrons," Chapter 7, D. Van Nostrand Company, New York, 1926.

204. P. Drude, "Theory of Optics," English translation by C. R. Mann and R. A. Millikan, Longmans, New York, 1902.

205. J. P. Mathieu, "Optics," translated by J. W. Blaker, Chapters 5 and 7, Pergamon Press, New York, 1975.

206. C. S. Barrett and T. B. Massalski, "Structure of Metals," Table A-6. McGraw Hill, New York, 1966.

207. J. Hoare and D. Hull, Phil. Mag., 26, 443 (1972).

208. B. D. Lauterwasser and E. J. Kramer, Phil. Mag., 39A, 469 (1979).

209. L. E. Nielsen and R. Buchdahl, J. Appl. Phys., 21, 488 (1950).

210. K. J. Cleereman, H. J. Karam, and J. L. Williams, Modern Plastics, May, 119 (1953).

211. J. W. Curtis, J. Phys. D: Appl. Phys., 3, 1413 (1970).

212. H. Kanetsuna and Y. Tanabe, J. Appl. Polym. Sci., 22, 2707 (1978).

213. H. Wright, C. S. N. Faraday, E. F. T. White, and L. R. G. Treloar, J. Phys. D: Appl. Phys., 4, 2002 (1971).

214. L. J. Broutman and F. J. McGarry, J. Appl. Polym. Sci., 9, 609 (1965).

215. H. R. Brown, J. Mat. Sci., 14, 237 (1979).

216. T. Chan, A. M. Donald, and E. J. Kramer, J. Mat. Sci., 16, 676 (1981).

217. S. S. Sternstein, L. Ongchin, and A. Silverman, Appl. Polym. Symp., 7, 175 (1968).

218. S. S. Sternstein and F. A. Myers, J. Macromol. Sci.-Phys., B8, 539 (1973).

219. G. Menges and H. Schmidt, Plastics & Polymers, 38, 13 (1970).

220. J. Pohrt, J. Macromol. Sci.-Phys., B5, 299 (1971).

221. H. Schmidt, Kunststoff-Rundschau, 19, 1(1972); ibid., 19, 56 (1972).

222. G. Menges and E. Alf, Kunststoffe, 62, 259 (1972).

223. R. J. Oxborough and P. B. Bowden, Phil. Mag., 28, 547 (1973).

APPENDICES

APPENDIX A

PROGRAM SAXS.FOR

```
C     ************************************************************************
C     PROGRAM SAXS.FOR
C     ************************************************************************
C     MAIN PROGRAM
C     THIS PROGRAM IS WRITTEN FOR ANALYZING THE SAXS DATA
C     MEASURED USING THE 10-METER SAXS CAMERA AT NCSASR, ORNL.
C     IT IS DESIGNED TO DIALOGUE INTERACTIVELY ON DEC-10.
C     HOWEVER, BY CHANGING ASSIGNED LOGIC UNIT (IWRITE = 6),
C     IT CAN ALSO WORK ON IBM.
C     ************************************************************************
C     NOMENCLATURE:
C             IDATA:  OBSERVED INTENSITY DATA IN TOTAL COUNTS
C             DATA1:  ABSOLUTE INTENSITY DATA IN ELECTRON UNITS
C             DATA2:  PURE SCATTERED INTENSITY
C             DATA3:  SPECULAR REFLECTED INTENSITY
C             DATA1 = DATA2 + DATA3
C              HEAD:  HEAD RECORD
C              ISEQ:  SEQUENCE NUMBER OF DATA SET IN ORNL DISC
C              TIME:  TOTAL MEASURING TIME IN SECONDS
C       XCENT, YCENT:  COORDINATES OF CONTOUR CENTER
C              TRAN:  TRANSMISSION COEFFICIENT
C              WAVE:  X-RAY WAVELENGTH IN ANGSTRAM
C              ABSF:  ABSOLUTE INTENSITY CONVERSION FACTOR
C            TWOTHE:  SCATTERING ANGLE
C              SCAT:  SCATTERING INTENSITY
C             DIST1:  X-RAY SOURCE TO SAMPLE DISTANCE IN MM
C             DIST2:  SAMPLE TO DETECTOR DISTANCE IN MM
C            DXCHAN:  X-CHANNEL CONVERSION FACTOR (CHANNEL/MM)
C            DYCHAN:  Y-CHANNEL CONVERSION FACTOR (CHANNEL/MM)
C            IWRITE:  LOGIC UNIT TO WRITE DATA - 5 IS TERMINAL
C             IREAD:  LOGIC UNIT TO READ DATA - 5 IS TERMINAL
C            IFILER:  FILE NUMBER TO READ INTENSITY DATA
C            IFILEW:  FILE NUMBER TO STORAGE CALCULATED DATA
C     ************************************************************************
C     COMMON BLOCK DEFINITION:
C             COMMON /BLOCK1/IWRITE,IREAD,IFILER,IFILEW
C             COMMON /BLOCK2/HEAD
C             COMMON /BLOCK3/DATA1
C             COMMON /BLOCK4/DATA2
C             COMMON /BLOCK5/DTAT3
C             COMMON /BLOCK6/NI,NF,TWOTHE,SCAT
C     ************************************************************************
      INTEGER ANS(3)
      COMMON /BLOCK1/IWRITE,IREAD,IFILER,IFILEW
```

```
      IWRITE=5
      IREAD=5
      WRITE(IWRITE,10)
10    FORMAT(' ***  PROGRAM SAXS RUNNING ***')
20    WRITE(IWRITE,30)
30    FORMAT(' >> SELECT FUNCTION (3A1)')
      READ(IREAD,40) ANS
40    FORMAT(3A1)
      IF(ANS(1).EQ.'?'.OR.ANS(1).EQ.'F'.AND.ANS(2).EQ.'N') GO TO 60
      IF(ANS(1).EQ.'F'.AND.ANS(2).EQ.'E') GO TO 70
      IF(ANS(1).EQ.'R'.AND.ANS(2).EQ.'E') GO TO 80
      IF(ANS(1).EQ.'A'.AND.ANS(2).EQ.'N') GO TO 90
      IF(ANS(1).EQ.'A'.AND.ANS(2).EQ.'Z') GO TO 100
      IF(ANS(1).EQ.'I'.AND.ANS(2).EQ.'N') GO TO 110
      IF(ANS(1).EQ.'E'.AND.ANS(2).EQ.'X') GO TO 999
      WRITE(IWRITE,50)
50    FORMAT(' ... INVALID ... TRY AGAIN ...')
      GO TO 20
60    CALL FNCLST
      GO TO 20
70    CALL FETCH
      GO TO 20
80    CALL REFLEC
      GO TO 20
90    CALL QANGLE
      GO TO 20
100   CALL AZMUTH
      GO TO 20
110   CALL QINVAR
      GO TO 20
999   CONTINUE
      STOP
      END
      SUBROUTINE FNCLST
C     ********************************************************************************
C     SUBROUTINE TO LIST FUNCTIONS OF SAXS PROGRAM
C     ********************************************************************************
      COMMON /BLOCK1/IWRITE,IREAD
      WRITE(IWRITE,10)
10    FORMAT('  ¬¬¬  THE FUNCTIONS ARE: '/
     1 '       FNC:  LIST FUNCTIONS OF SAXS PROGRAM'/
     2 '       FET:  READ DATA SET FROM DISK FILE'/
     3 '       REF:  CORRECT SPECULAR REFLECTION EFFECT'/
     4 '       ANG:  CALCULATE INTENSITY AT CERTAIN AZMUTHAL ANGLE'/
     5 '       AZM:  CALCULATE INTENSITY AT CERTAIN SCATTERING ANGLE'/
     6 '       INV:  CALCULATE INVARIANT AT CERTAIN AZMUTHAL ANGLE'/
     7 '       EXI:  EXIT FROM SAXS PROGRAM')
      RETURN
      END
```

```
      SUBROUTINE FETCH
C     ****************************************************************
C     SUBROUTINE TO READ DATA SET FROM LOGIC UNIT IFILER
C     AND CONVERT THE OBSERVED INTENSITY INTO ABSOLUTE UNIT
C     (EU/ANG**3).
C     ****************************************************************
      DIMENSION IDATA(64,64),HEAD(100),DATA1(64,64)
      COMMON /BLOCK1/IWRITE,IREAD,IFILER,IFILEW
      COMMON /BLOCK2/HEAD
      COMMON /BLOCK3/DATA1
      EQUIVALENCE (ISEQ,HEAD(1)),(TIME,HEAD(34)),(XCENT,HEAD(37)),
     1 (YCENT,HEAD(38)),(TRAN,HEAD(42)),(FACT,HEAD(43)),
     2 (WAVE,HEAD(44)),(ABSF,HEAD(45)),(DIST2,HEAD(47)),
     3 (DXCHAN,HEAD(50)),(DYCHAN,HEAD(51))
      DATA IFILEW/1/
      THOMSN=7.94E-26
      WRITE(IWRITE,1010)
1010  FORMAT(' >> ENTER IFILER (I2)')
      READ(IREAD,1020) IFILER
1020  FORMAT(I2)
C***
C***  READ HEAD RECORD
C***
      READ(IFILER,20010) HEAD
20010 FORMAT(2I5,A5,13I5/15I5/5F10.1,3F10.4/8F10.4/6F10.4/47A1)
      WRITE(IWRITE,20020) HEAD(1),(HEAD(I),I=54,100)
20020 FORMAT('  SEQ. NO. =',I6/'     TITLE = ',47A1)
      IF(ABSF.NE.1.0) GO TO 20060
C***
C***  CALCULATE ABSOLUTE INTENSITY CONVERSION FACTOR
C***
      WRITE(IWRITE,20030)
20030 FORMAT('  >> ENTER SAMPLE THICKNESS IN INCH (G15.6)')
      READ(IREAD,20040) THICK
20040  FORMAT(G15.6)
      WRITE(IWRITE,20050)
20050 FORMAT('  >> ENTER INCIDENT BEAM INTENSITY IN CPS (G15.6)')
      READ(IREAD,20040) PO
      ABSF=(DIST2*DXCHAN)**2/(PO*THICK*2.54*TRAN*THOMSN*TIME*1.E24)
20060 CONTINUE
C***
C***  READ IDATA
C***
      DO 20090 J=1,64
      DO 20070 III=1,8
      II=III-1
      IS=(II*8)+1
      ISS=IS+7
20070 READ(IFILER,20080) (IDATA(I,J),I=IS,ISS)
20080 FORMAT(8I8)
```

```
20090  CONTINUE
C***
C***   CALCULATE DATA1
C***
       DMAX=1.0
       DO 20100 I=1,64
       DO 20100 J=1,64
       DATA1(I,J)=IDATA(I,J)*ABSF
       IF(DATA1(I,J).GT.DMAX) DMAX=DATA1(I,J)
20100  CONTINUE
       DD=ALOG10(DMAX)
       WRITE(IWRITE,20110) DMAX,DD
20110  FORMAT('  MAX. INTENSITY = ',G15.6 '(ELEC**2/ANG**3)'/
     & '  LOG(MAX. INTENSITY) =',G15.6)
       WRITE(IWRITE,20120)
20120  FORMAT(' >> SAVE IT? (N/Y)')
       READ(IREAD,20130) ANS
20130  FORMAT(A1)
       IF(ANS.EQ.'N') RETURN
C***
C***   SAVE DATA
C***
       WRITE(IWRITE,20132)
20132  FORMAT('  >> ENTER FILE NUMBER (I2)')
       READ(IREAD,1020) IFILEW
       WRITE(IFILEW,20010) HEAD
       DO 20140 J=1,64
       DO 20140 III=1,8
       II=III-1
       IS=(II*8)+1
       ISS=IS+7
20140  WRITE(IFILEW,20080) (IDATA(I,J),I=IS,ISS)
20150  CONTINUE
       RETURN
       END
       SUBROUTINE QANGLE
C      ********************************************************************************
C      ENTER PARAMETERS FOR SUBROUTINE ANGLE CALL
C      ********************************************************************************
       COMMON /BLOCK1/IWRITE,IREAD,IFILER,IFILEW
       WRITE(IWRITE,10)
10     FORMAT('  >> (1) OVERALL OR (2) AT CERTAIN AZMU. ANGLE? (1/2)')
       READ(IREAD,20) IANS
20     FORMAT(I1)
       WRITE(IWRITE,30)
30     FORMAT('  >> SAVE THE ANGULAR DATA? (Y/N)')
       READ(IREAD,40) ANS
40     FORMAT(A1)
       IF(ANS.EQ.'N') GO TO 70
```

```
      WRITE(IWRITE,50)
50    FORMAT('  >> ENTER FILE NUMBER TO SAVE ANGULAR DATA (I2)')
      READ(IREAD,60) IFILEW
60    FORMAT(I2)
70    IF(IANS.EQ.1) GO TO 140
80    WRITE(IWRITE,90)
90    FORMAT('  >> ENTER ANGLE OF SLICE (G15.6)')
      READ(IREAD,100) AZMU
100   FORMAT(G15.6)
      IF(AZMU.LE.90.0.AND.AZMU.GE.-90.0) GO TO 120
      IF(AZMU.GT.90.0.OR.AZMU.LT.-90.0) WRITE(IWRITE,110)
110   FORMAT(' ... INVALID ... TRY AGAIN ...')
      GO TO 80
120   WRITE(IWRITE,130)
130   FORMAT('  >> ENTER CHANNEL WIDTH OF THE SLICE (G15.6)')
      READ(IREAD,100) W2
      IF(W2.LE.0.0) W2=2.0
      CALL ANGLE(AZMU,W2,ANS)
      RETURN
140   WRITE(IWRITE,150)
150   FORMAT('  >> ENTER ANGLE INCREMENT (G15.6)')
      READ(IREAD,100) ANGINC
      IF(ANGINC.LE.0.0) ANGINC=10.
      NANGLE=180./ANGINC+1
      WRITE(IWRITE,130)
      READ(IREAD,100) W2
      IF(W2.LE.0.0) W2=2.0
      DO 160 KKKK=1,NANGLE
      AZMU=ANGINC*(KKKK-1)-90.0
      CALL ANGLE(AZMU,W2,ANS)
160   CONTINUE
      RETURN
      END
      SUBROUTINE ANGLE(AAAA,W2,ANS)
C     ************************************************************************
C     SUBROUTINE TO PERFORM LINEAR AVERAGING AT SPECIFIED
C     AZMUTHAL ANGLE
C     REFERENCE:  ORNL PROGRAM CONTOUR - SUBROUTINE ANGLE
C     ************************************************************************
C        TWOTHE:  SCATTERING ANGLE IN MILIRADIAN
C          AZMU:  AZMUTHAL ANGLE IN DEGREE
C          SCAT:  SCATTERING INTENSITY
C     ************************************************************************
      DIMENSION DATA1(64,64),HEAD(100)
      DIMENSION SCAT(100),TWOTHE(100),ES(100)
      DIMENSION U(4),V(4),X(4),Y(4)
      DIMENSION WORK(100),NIUS(2,1),XIU(10),YIU(10)
      INTEGER OTYPE
      DOUBLE PRECISION TOTAL,ETOTAL,ZTOT,ETOT,PART
```

```
      COMMON /BLOCK1/IWRITE,IREAD,IFILER,IFILEW
       COMMON /BLOCK2/HEAD
      COMMON /BLOCK3/DATA1
      COMMON /BLOCK6/NI,NPT,TWOTHE,SCAT
      EQUIVALENCE (ISEQ,HEAD(1)),(TIME,HEAD(34)),(XCENT,HEAD(37)),
     1 (YCENT,HEAD(38)),(TRAN,HEAD(42)),(FACT,HEAD(43)),
     2 (WAVE,HEAD(44)),(ABSF,HEAD(45)),(DIST2,HEAD(47)),
     3 (DXCHAN,HEAD(50)),(DYCHAN,HEAD(51))
C***
C***   SET PARAMETERS
C***
      PI=4.0*ATAN(1.0)
      TWOPI=8.0*ATAN(1.0)
      M=64
      N=64
      XF=FLOAT(M)
      YF=FLOAT(N)
      XFF=XF+0.5
      YFF=YF+0.5
      NA=4
      NB=4
      DIST=DIST2*DXCHAN
      W=W2/2.
      AZMU=AAAA
      DO 50010 I=1,100
      SCAT(I)=0.0
50010 TWOTHE(I)=0.0
      AZMUR=AZMU*PI/180.
      IF(AZMU.EQ.0.0) GO TO 50040
      IF(AZMU.EQ.-90.0) AZMU=-AZMU
      IF(AZMU.EQ.90.0) GO TO 50050
      CT=COS(AZMUR)/SIN(AZMUR)
      IF(AZMU.LE.45.0.AND.AZMU.GE.0.0) GO TO 50020
      IF(AZMU.GE.-45.0.AND.AZMU.LT.0.0) GO TO 50030
      SL=ABS((XCENT-0.5)/SIN(AZMUR)-W*CT)
      GO TO 50060
50020 SL=(YCENT-0.5)/COS(AZMUR)-W/CT
      GO TO 50060
50030 SL=(YFF-YCENT)/COS(AZMUR)+W/CT
      GO TO 50060
50040 SL=YCENT-0.5
      GO TO 50060
50050 SL=XCENT-0.5
50060 CONTINUE
      LP=IFIX(SL)
      NPT=0
      SLF=FLOAT(LP)
      C1=((SLF)**2.0+W**2.0)**0.50
```

```
      ATO=ATAN(W/SLF)
      APO=AZMUR+ATO
      AMO=AZMUR-ATO
      DELU=ABS(SIN(AZMUR))
      DELV=COS(AZMUR)
      IF(AZMUR.GE.0.0) GO TO 50070
      DELV=-DELV
50070 CONTINUE
      IF(AZMUR.LT.0.0) GO TO 50080
      U(1)=XCENT-C1*SIN(APO)
      U(2)=XCENT-C1*SIN(AMO)
      U(3)=U(2)+DELU
      U(4)=U(1)+DELU
      V(1)=YCENT-C1*COS(APO)
      V(2)=YCENT-C1*COS(AMO)
      V(3)=V(2)+DELV
      V(4)=V(1)+DELV
      GO TO 50090
50080 U(1)=XCENT+C1*SIN(APO)
      U(2)=XCENT+C1*SIN(AMO)
      U(3)=U(2)+DELU
      U(4)=U(1)+DELU
      V(1)=YCENT+C1*COS(APO)
      V(2)=YCENT+C1*COS(AMO)
      V(3)=V(2)+DELV
      V(4)=V(1)+DELV
50090 CONTINUE
      NWORK=100
      OTYPE=2
      IF(AZMUR.EQ.0.0) GO TO 50110
      IF(AZMU.EQ.90.0) GO TO 50110
      SM=(V(2)-V(1))/(U(2)-U(1))
50100 CA=V(2)-SM*U(2)
      CB=V(3)-SM*U(3)
50110 IF(AZMUR.LT.0.0) GO TO 50120
      IMIN=IFIX(U(1)+0.5)
      IMAX=IFIX(U(3)+0.5)
      JMIN=IFIX(V(2)+0.5)
      JMAX=IFIX(V(4)+0.5)
      IF(IMAX.GT.M.OR.JMAX.GT.N) GO TO 50320
      GO TO 50130
50120 IMIN=IFIX(U(2)+0.5)
      IMAX=IFIX(U(4)+0.5)
      JMIN=IFIX(V(3)+0.5)
      JMAX=IFIX(V(1)+0.5)
      IF(IMAX.GT.M.OR.JMIN.LT.1) GO TO 50320
50130 CONTINUE
      NPT=NPT+1
      IF(NPT.GT.100) GO TO 50350
```

```
      AREA=0.0
      TOTAL=0.0D0
      ETOTAL=0.0D0
      DO 50290 J=JMIN,JMAX
      Y(1)=J-0.5
      Y(2)=Y(1)
      Y(3)=J+0.5
      Y(4)=Y(3)
      DO 50280 I=IMIN,IMAX
      X(1)=I-0.5
      X(2)=I+0.5
      X(3)=X(2)
      X(4)=X(1)
      IF(AZMU.EQ.0.0) GO TO 50160
      IF(AZMU.EQ.90.0) GO TO 50160
      IF(AZMU.LT.0.0) GO TO 50140
      AA=Y(3)-SM*X(3)
      BB=Y(1)-SM*X(1)
      GO TO 50150
50140 AA=Y(2)-SM*X(2)
      BB=Y(4)-SM*X(4)
      IF(AA.GE.CA.OR.BB.LE.CB) GO TO 50270
      GO TO 50160
50150 IF(AA.LE.CA.OR.BB.GE.CB) GO TO 50270
50160 CONTINUE
      CALL IUCALC(X,Y,NA,U,V,NB,OTYPE,WORK,NWORK,NONIU,NIUS,XIU,YIU)
50170 FORMAT('  NONIU =',I3,'  I = ',I3,'  J = ',I3)
      IF(NONIU.LT.-1) WRITE(IWRITE,50180)
50180 FORMAT('  WORK SPACE IS INSUFFICIENT')
      IF(NONIU.EQ.-1) WRITE(IWRITE,50190)
50190 FORMAT('  THE TWO FIGURES ARE NOT SIMPLY CONNECTED')
      IF(NONIU.GT.1) WRITE(IWRITE,50200) NONIU
50200 FORMAT('  THERE ARE ',I5,'  OVERLAYS')
50210 IF(NONIU.EQ.0) GO TO 50270
      KOFF=NIUS(1,1)
      LEN=NIUS(2,1)
      CALL IAREA(XIU,YIU,KOFF,LEN,PART)
C***
C***  CALCULATE TWOTHE, INTENSITY, AND ERRORS
C***
      ZTOT=DBLE(DATA1(I,J))
      ETOT=DBLE(DATA1(I,J)**2)
      ETOTAL=ETOTAL+PART*ETOT
      TOTAL=TOTAL+PART*ZTOT
      AREA=AREA+SNGL(PART)
      TOTALS=SNGL(TOTAL)
      ETOTLS=SNGL(ETOTAL)
50270 CONTINUE
50280 CONTINUE
50290 CONTINUE
```

```
        SCAT(NPT)=TOTALS/AREA
        CC=-LP+NPT-0.5
        RAD=ABS(CC)
        TWOTHE(NPT)=1000.0*ATAN(CC/DIST)
        ES(NPT)=SQRT(AREA*ETOTLS-TOTALS**2)/AREA
        IF(AZMUR.LT.0.) DELV=-ABS(DELV)
        DO 50310 I=1,4
        U(I)=U(I)+DELU
50310   V(I)=V(I)+DELV
        IF(U(3).GT.XFF.OR.V(4).GT.YFF) GO TO 50320
        IF(U(4).GT.XFF.OR.V(3).LT.1.) GO TO 50320
        IF(AZMUR.EQ.0.0) GO TO 50110
        GO TO 50100
50320   CONTINUE
        NI=1
        NF=NPT
        IF(ANS.EQ.'N') GO TO 50370
        POINT=FLOAT(NPT)
        WRITE(IFILEW,50330) AZMU,POINT
50330   FORMAT(1X,F6.1,T16,G15.6)
        IF(NPT.LE.0) GO TO 50370
        WRITE(IFILEW,50340) ((TWOTHE(K),SCAT(K)),K=1,NF)
50340   FORMAT(2G15.6)
        GO TO 50370
50350   WRITE(IFILEW,50360) AZMU
50360   FORMAT('  AZMU = ',F6.2,' DEGREE,  NPT GREATER THAN 100, DUMP')
50370   CONTINUE
        RETURN
        END
        SUBROUTINE IAREA (X,Y,K,N,TSUM)
C***
C***    SUBROUTINE IAREA OF SUBROUTINE ANGLE
C***
        DIMENSION X(N),Y(N)
        DOUBLE PRECISION TSUM
        COMMON /BLOCK1/IWRITE,IREAD,IFILER,IFILEW
        IF(N.LT.3) GO TO 51020
        TSUM=0.0D0
        AY=Y(K+2)-Y(K+1)
        AX=X(K+2)-X(K+1)
        DO 51010 J=3,N
        BY=Y(K+J)-Y(K+1)
        BX=X(K+J)-X(K+1)
        TSUM=TSUM+BY*AX-AY*BX
        AX=BX
51010   AY=BY
        TSUM=DABS(TSUM)/2.0D0
        RETURN
51020   WRITE(IWRITE,51030)
51030   FORMAT('  INSUFFICIENT POINTS IN FIGURE')
        RETURN
        END
```

```
      SUBROUTINE AZMUTH
C     ***********************************************************************
C     SUBROUTINE TO PERFORM AZMUTHAL AVERAGING AT SPECIFIED
C     TWOTHETA.
C     REFERENCE:  ORNL PROGRAM CONTOUR - SUBROUTINE ANGLE
C     ***********************************************************************
C        TWOTHE:  SCATTERING ANGLE IN MILIRADIAN
C        AZMUDD:  AZMUTHAL ANGLE IN DEGREE
C          SCAT:  SCATTERING INTENSITY
C     ***********************************************************************
      DIMENSION DATA1(64,64),HEAD(100)
      DIMENSION SCAT(200),AZMUDD(200),ES(200)
      DIMENSION U(4),V(4),X(4),Y(4)
      DIMENSION WORK(100),NIUS(2,1),XIU(10),YIU(10)
      INTEGER OTYPE
      DOUBLE PRECISION TOTAL,ETOTAL,ZTOT,ETOT,PART
      COMMON /BLOCK1/IWRITE,IREAD,IFILER,IFILEW
       COMMON /BLOCK2/HEAD
      COMMON /BLOCK3/DATA1
      EQUIVALENCE (ISEQ,HEAD(1)),(TIME,HEAD(34)),(XCENT,HEAD(37)),
     1 (YCENT,HEAD(38)),(TRAN,HEAD(42)),(FACT,HEAD(43)),
     2 (WAVE,HEAD(44)),(ABSF,HEAD(45)),(DIST2,HEAD(47)),
     3 (DXCHAN,HEAD(50)),(DYCHAN,HEAD(51))
C***
C***  SET PARAMETERS
C***
      PI=4.0*ATAN(1.0)
      TWOPI=8.0*ATAN(1.0)
      M=64
      N=64
      XF=FLOAT(M)
      YF=FLOAT(N)
      XFF=XF+0.5
      YFF=YF+0.5
      NA=4
      NB=4
      DIST=DIST2*DXCHAN
      DO 50010 I=1,200
       AZMUDD(I)=0.0
50010  SCAT(I)=0.0
C***
C***  ENTER PARAMETERS
C***
      WRITE(IWRITE,10)
10    FORMAT('  >> (1) OVERALL OR (2) AT CERTAIN TWOTHETA? (1/2)')
      READ(IREAD,20) IANS
20    FORMAT(I1)
      WRITE(IWRITE,30)
30    FORMAT('  >> ENTER ANGLE INCREMENT (G15.6)')
      READ(IREAD,50340) ANGINC
      IF(ANGINC.LE.0.0) ANGINC=5.
```

```
        NANGLE=360.0/ANGINC+1
       WRITE(IWRITE,40)
40     FORMAT('  >> SAVE THE AZMUTHAL DATA? (Y/N)')
       READ(IREAD,50) ANS
50     FORMAT(A1)
       IF(ANS.EQ.'N') GO TO 80
       WRITE(IWRITE,60)
60     FORMAT('  >> ENTER FILE NUMBER TO STORE DATA (I2)')
       READ(IREAD,70) IFILES
70     FORMAT(I2)
80     IF(IANS.EQ.1) GO TO 140
90     WRITE(IWRITE,100)
100    FORMAT('  >> ENTER SCATTERING ANGLE IN MRADIAN (G15.6)')
       READ(IREAD,50340) TWOTHE
       IF(TWOTHE.LE.16.0.AND.TWOTHE.GE.0.0) GO TO 120
       IF(TWOTHE.GT.16.0.OR.TWOTHE.LT.0.0) WRITE(IWRITE,110)
110    FORMAT(' ... INVALID ... TRY AGAIN ...')
       GO TO 90
120    WRITE(IWRITE,130)
130    FORMAT('  >> ENTER CHANNEL WIDTH OF THE SLICE (G15.6)')
       READ(IREAD,50340) W2
       IF(W2.LE.0.0) W2=2.0
       GO TO 160
140    WRITE(IWRITE,150)
150    FORMAT('  >> ENTER SCATTERING ANGLE INCREMENT (G15.6)')
       READ(IREAD,50340) THEINC
       IF(THEINC.LE.0.0) THEINC=2.
       NTHE=10.0/THEINC
       WRITE(IWRITE,130)
       READ(IREAD,50340) W2
       IF(W2.LE.0.0) W2=2.0
C***
C***   STARTING CALCULATING ANGULAR AVERAGE
C***
        DO 50380 IIII=1,NTHE
        TWOTHE=THEINC*IIII
160    CONTINUE
       W=W2/2.0
       NPT=0
       DO 50370 KKKK=1,NANGLE
        AZ=ANGINC*(KKKK-1)
        IF(AZ.GE.0.0.AND.AZ.LE.90.0) GO TO 50012
        IF(AZ.GT.90.0.AND.AZ.LE.180.0) GO TO 50014
        IF(AZ.GT.180.0.AND.AZ.LE.270.0) GO TO 50016
        AZMU=AZ-360.0
        ABSO=-1.0
        GO TO 50018
50012   AZMU=AZ
        ABSO=1.0
        GO TO 50018
50014   AZMU=AZ-180.0
```

```
        ABSO=1.0
        GO TO 50018
50016   AZMU=AZ-180.0
        ABSO=-1.0
        GO TO 50018
50018   AZMUR=AZMU*PI/180.0
       IF(AZMU.EQ.0.0) GO TO 50040
       IF(AZMU.EQ.-90.0) AZMU=-AZMU
       IF(AZMU.EQ.90.0) GO TO 50050
       CT=COS(AZMUR)/SIN(AZMUR)
       IF(AZMU.LE.45.0.AND.AZMU.GE.0.0) GO TO 50020
       IF(AZMU.GE.-45.0.AND.AZMU.LT.0.0) GO TO 50030
       SL=ABS((XCENT-0.5)/SIN(AZMUR)-W*CT)
       GO TO 50060
50020  SL=(YCENT-0.5)/COS(AZMUR)-W/CT
       GO TO 50060
50030  SL=(YFF-YCENT)/COS(AZMUR)+W/CT
       GO TO 50060
50040  SL=YCENT-0.5
       GO TO 50060
50050  SL=XCENT-0.5
50060  CONTINUE
       LP=IFIX(SL)
       SLF=FLOAT(LP)
       C1=((SLF)**2.0+W**2.0)**0.50
       ATO=ATAN(W/SLF)
       APO=AZMUR+ATO
       AMO=AZMUR-ATO
       DELU=ABS(SIN(AZMUR))
       DELV=COS(AZMUR)
       IF(AZMUR.GE.0.0) GO TO 50070
       DELV=-DELV
50070  CONTINUE
       IF(AZMUR.LT.0.0) GO TO 50080
       U(1)=XCENT-C1*SIN(APO)
       U(2)=XCENT-C1*SIN(AMO)
       U(3)=U(2)+DELU
       U(4)=U(1)+DELU
       V(1)=YCENT-C1*COS(APO)
       V(2)=YCENT-C1*COS(AMO)
       V(3)=V(2)+DELV
       V(4)=V(1)+DELV
       GO TO 50090
50080  U(1)=XCENT+C1*SIN(APO)
       U(2)=XCENT+C1*SIN(AMO)
       U(3)=U(2)+DELU
       U(4)=U(1)+DELU
       V(1)=YCENT+C1*COS(APO)
       V(2)=YCENT+C1*COS(AMO)
       V(3)=V(2)+DELV
       V(4)=V(1)+DELV
```

```
50090  CONTINUE
        CCF=TAN(TWOTHE/1000.0)*DIST*ABSO
        TNPT=CCF+LP+0.5
        IF(AZMUR.LT.0.0) DELV=-ABS(DELV)
        DO 50095 KL=1,4
        U(KL)=U(KL)+DELU*TNPT
50095   V(KL)=V(KL)+DELV*TNPT
       IF(U(3).GT.XFF.OR.V(4).GT.YFF) GO TO 50320
       IF(U(4).GT.XFF.OR.V(3).LT.1.) GO TO 50320
       NWORK=100
       OTYPE=2
       IF(AZMUR.EQ.0.0) GO TO 50110
       IF(AZMU.EQ.90.0) GO TO 50110
       SM=(V(2)-V(1))/(U(2)-U(1))
50100  CA=V(2)-SM*U(2)
       CB=V(3)-SM*U(3)
50110  IF(AZMUR.LT.0.0) GO TO 50120
       IMIN=IFIX(U(1)+0.5)
       IMAX=IFIX(U(3)+0.5)
       JMIN=IFIX(V(2)+0.5)
       JMAX=IFIX(V(4)+0.5)
       IF(IMAX.GT.M.OR.JMAX.GT.N) GO TO 50320
       GO TO 50130
50120  IMIN=IFIX(U(2)+0.5)
       IMAX=IFIX(U(4)+0.5)
       JMIN=IFIX(V(3)+0.5)
       JMAX=IFIX(V(1)+0.5)
       IF(IMAX.GT.M.OR.JMIN.LT.1) GO TO 50320
50130  CONTINUE
       NPT=NPT+1
       IF(NPT.GT.200) GO TO 50350
       AREA=0.0
       TOTAL=0.0D0
       ETOTAL=0.0D0
       DO 50290 J=JMIN,JMAX
       Y(1)=J-0.5
       Y(2)=Y(1)
       Y(3)=J+0.5
       Y(4)=Y(3)
       DO 50280 I=IMIN,IMAX
       X(1)=I-0.5
       X(2)=I+0.5
       X(3)=X(2)
       X(4)=X(1)
       IF(AZMU.EQ.0.0) GO TO 50160
       IF(AZMU.EQ.90.0) GO TO 50160
       IF(AZMU.LT.0.0) GO TO 50140
       AA=Y(3)-SM*X(3)
       BB=Y(1)-SM*X(1)
       GO TO 50150
50140  AA=Y(2)-SM*X(2)
```

```
      BB=Y(4)-SM*X(4)
      IF(AA.GE.CA.OR.BB.LE.CB) GO TO 50270
      GO TO 50160
50150 IF(AA.LE.CA.OR.BB.GE.CB) GO TO 50270
50160 CONTINUE
      CALL IUCALC(X,Y,NA,U,V,NB,OTYPE,WORK,NWORK,NONIU,NIUS,XIU,YIU)
50170 FORMAT('  NONIU =',I3,'  I = ',I3,'  J = ',I3)
      IF(NONIU.LT.-1) WRITE(IWRITE,50180)
50180 FORMAT('  WORK SPACE IS INSUFFICIENT')
      IF(NONIU.EQ.-1) WRITE(IWRITE,50190)
50190 FORMAT('  THE TWO FIGURES ARE NOT SIMPLY CONNECTED')
      IF(NONIU.GT.1) WRITE(IWRITE,50200) NONIU
50200 FORMAT('  THERE ARE ',I5,'  OVERLAYS')
50210 IF(NONIU.EQ.0) GO TO 50270
      KOFF=NIUS(1,1)
      LEN=NIUS(2,1)
      CALL IAREA(XIU,YIU,KOFF,LEN,PART)
C****
C****  CALCULATE TWOTHE, INTENSITY, AND ERRORS
C****
      ZTOT=DBLE(DATA1(I,J))
      ETOT=DBLE(DATA1(I,J)**2)
      ETOTAL=ETOTAL+PART*ETOT
      TOTAL=TOTAL+PART*ZTOT
      AREA=AREA+SNGL(PART)
      TOTALS=SNGL(TOTAL)
      ETOTLS=SNGL(ETOTAL)
50270 CONTINUE
50280 CONTINUE
50290 CONTINUE
      SCAT(NPT)=TOTALS/AREA
       AZMUDD(NPT)=AZ
      ES(NPT)=SQRT(AREA*ETOTLS-TOTALS**2)/AREA
50320 CONTINUE
50370 CONTINUE
      NI=1
      NF=NPT
      IF(ANS.EQ.'N') GO TO 50380
       POINT=FLOAT(NPT)
      WRITE(IFILES,50330) TWOTHE,POINT
50330 FORMAT(1X,F6.1,T16,G15.6)
      IF(NPT.LE.0) GO TO 50380
      WRITE(IFILES,50340) ((AZMUDD(K),SCAT(K)),K=1,NF)
50340 FORMAT(2G15.6)
      GO TO 50380
50350 WRITE(IFILES,50360) AZMU
50360 FORMAT('  AZMU = ',F6.2,' DEGREE,  NPT GREATER THAN 200, DUMP')
50380  CONTINUE
      RETURN
      END
```

```
      SUBROUTINE IUCALC(APX,APY,NOAP,BCX,BCY,NOBC,OTYPE,WORK,
     & WRKMAX,NORC,INORC,RCX,RCY)
C     ************************************************************************
C     REFERENCE: ORNL IUCALC SUBROUTINE
C     THIS PROGRAM (1) DETERMINES THE POLYGONS DEFINING THE UNION,
C     INTERSECTION, OR RELATIVE DIFFERENCE OF TWO GIVEN POLYGONS,
C     OR (2) DETERMINES WHAT PORTIONS OF A CHAIN OF LINE SEGMENTS
C     LIE ON THE BOUNDARY, INTERIOR, OR EXTERIOR TO A GIVEN POLYGON.
C     ************************************************************************
      INTEGER NOAP,NOBC,OTYPE
      REAL APX(NOAP),APY(NOAP),BCX(NOBC),BCY(NOBC)
C     ********************  USER SPECIFIED VARIABLES  *********+*********
C     APX   A REAL ARRAY OF THE X COORDINATES OF A, THE 1ST POLYGON
C     APY   A REAL ARRAY OF Y COORDINATES OF THE A POLYGON
C     NOAP  AN INTEGER COUNT OF THE NUMBER OF POINTS DEFINING THE A
C     POLYGON.
C     THE POLYGON CONSISTS OF LINE SEGMENTS FROM APX(1), APY(1) TO
C     APX(2), APY(2) TO ... TO APX(NOAP),APY(NOAP) TO APX(1), APY(1).
C****
C     IF OTYPE IS FOUR OR LESS:
C     BCX   A REAL ARRAY OF THE X COORDINATES OF B, THE 2ND POLYGON
C     BCY   A REAL ARRAY OF Y COORDINATES OF THE B POLYGON
C     NOBC  AN INTEGER COUNT OF THE NUMBER OF POINTS DEFINING THE B
C     POLYGON.
C     OTYPE   AN INTEGER SPECIFYING THE DESIRED TYPE OF OVERLAY
C             OTYPE=1  UNION OF A AND B
C             OTYPE=2  INTERSECTION OF A AND B
C             OTYPE=3  RELATIVE DIFFERENCE OF A TO B
C             OTYPE=4  RELATIVE DIFFERENCE OF B TO A
C****
C     IF OTYPE IS GREATER THAN FOUR, BCX, BCY IS AN OPEN CHAIN OF
C     SEGMENTS (RATHER THAN A CLOSED POLYGON) FROM BCX(1), BCY(1) TO
C     BCX(2), BCY(2) TO ... TO BCX(NOBC), BCY(NOBC)
C             OTYPE=5  SUBCHAINS OF B ON THE BOUNDARY OF A
C             OTYPE=6  SUBCHAINS OF B EXTERIOR TO A
C             OTYPE=7  SUBCHAINS OF B INTERIOR TO A
C             OTYPE=8  SUBCHAINS OF B ECTERIOR TO OR ON THE BOUNDARY
C                      OF A
C             OTYPE=9  SUBCHAINS OF B INTERIOR TO OR ON THE BOUNDARY
C                      OF A
C****
      INTEGER WRKMAX,WORK(WRKMAX)
      INTEGER NORC,INORC(2,1)
      REAL RCX(1),RCY(1)
      LOGICAL NOFILE,FILOUT
      NOFILE=.TRUE.
       NORC=0
```

```
      CALL IUSUB1(APX,APY,NOAP,BCX,BCY,NOBC,OTYPE,WORK(1),WORK(1),
     &  WRKMAX,NONXT,NORC)
      IF(NORC.LT.0) RETURN
      CALL IUSUB2(APX,APY,IABS(NOAP),BCX,BCY,IABS(NOBC),OTYPE,
     &  WORK(1),WORK(1),WRKMAX,NONXT,WORK(NONXT*2+1),
     &  NORC,INORC,INOMAX,RCX,RCY,NRCMAX,FILOUT,NOFILE)
      RETURN
      END
      SUBROUTINE IUSUB1(X,Y,NAS,U,V,NBS,OTYPE,NXT,XYT,NWORK,
     &  NONXT,ERROR)
C     ******************************************************************
C     SUBROUTINE IUSUB1
C     ******************************************************************
      DIMENSION X(NAS),Y(NAS),U(NBS),V(NBS)
      INTEGER OTYPE,ERROR
C***
C     ERROR=-11      XT,YT  OVER-RUN
C     ERROR=-12      SEG  OVER-RUN
C     ERROR=-13           NXT  OVER-RUN
C***
      INTEGER NXT(2,1)
      REAL XYT(2,1)
      LOGICAL ASENSE,BSENSE,SENSE,INTER
      DOUBLE PRECISION ZERO,ONE
      DOUBLE PRECISION AX,AY,BX,BY,B2,DX,DY,
     &  AXB,AXD,BXD,D,Q,DMIN,DOTJM,DOTJNM,DOTJN,DOTJNN
      DATA ZERO/0.0D0/,ONE/1.0D0/
      DATA ASENSE/.TRUE./,BSENSE/.TRUE./
      NA=IABS(NAS)
      NB=IABS(NBS)
      NXYEND=NWORK/2+1
      IF(OTYPE.LE.4.AND.NAS.GT.0) ASENSE=SENSE(X,Y,NA)
      IF(OTYPE.LE.4.AND.NBS.GT.0) BSENSE=SENSE(U,V,NB)
      NBT=NB
      IF(OTYPE.GT.4) NBT=NB-1
      IF(OTYPE.EQ.3) BSENSE=.NOT.BSENSE
      IF(OTYPE.EQ.4) ASENSE=.NOT.ASENSE
      NONXT=0
      NXYT=0
      DO 5 I=1,NA
      IF(.NOT.ASENSE) NXT(2,I)=MOD(I+NA-2,NA)+1
      IF(ASENSE) NXT(2,I)=MOD(I,NA)+1
5     NXT(1,I)=I
      DO 10 I=1,NB
      IF(BSENSE) NXT(2,I+NA)=MOD(I,NB)+NA+1
      IF(.NOT.BSENSE) NXT(2,I+NA)=MOD(I+NB-2,NB)+NA+1
10    NXT(1,I+NA)=I+NA
```

```
      NONXT=NA+NB
      J=1
      XJN=X(1)
      YJN=Y(1)
      DO 65 I=1,NBT
      N=NXT(2,I+NA)
      UOLD=U(I)
      VOLD=V(I)
      NOLD=I+NA
C***  START OF LOOP ON J
11    BX=U(N-NA)-UOLD
      BY=V(N-NA)-VOLD
      B2=BX**2+BY**2
      INTER=.FALSE.
14    XJ=XJN
      YJ=YJN
      JN=NXT(2,J)
      IF(JN.LE.NA) GO TO 20
      JZ=-NXT(1,JN)-NA-NB
      IF(JZ.LE.0) GO TO 16
      XJN=XYT(1,NXYEND-JZ)
      YJN=XYT(2,NXYEND-JZ)
      GO TO 22
16    JZ=JZ+NB
      XJN=U(JZ)
      YJN=V(JZ)
      GO TO 22
20    XJN=X(JN)
      YJN=Y(JN)
22    DX=XJ-UOLD
      DY=YJ-VOLD
      AX=XJN-XJ
      AY=YJN-YJ
      AXB=AX*BY-AY*BX
      BXD=BX*DY-BY*DX
      IF(AXB.EQ.ZERO) GO TO 30
      Q=BXD/AXB
      IF(Q.LE.ZERO.OR.Q.GT.ONE) GO TO 45
      AXD=AX*DY-AY*DX
      D=AXD/AXB
      IF(D.LE.ZERO.OR.D.GT.ONE) GO TO 45
      K=0
      L=0
      XI=SNGL(UOLD+D*BX)
      YI=SNGL(VOLD+D*BY)
      IF(XI.NE.UOLD.OR.YI.NE.VOLD) GO TO 24
      K=NOLD
24    IF(XI.NE.U(N-NA).OR.YI.NE.V(N-NA)) GO TO 26
```

```
          K=N
26        XP=SNGL(XJ+Q*AX)
          YP=SNGL(YJ+Q*AY)
          IF(XP.NE.XJ.OR.YP.NE.YJ) GO TO 28
          L=J
28        IF(XP.NE.XJN.OR.YP.NE.YJN) GO TO 40
          L=JN
          GO TO 40
30        IF(BXD.NE.ZERO) GO TO 45
          K=0
          L=0
          DOTJM=DX*BX+DY*BY
          DOTJNM=(XJN-UOLD)*BX+(YJN-VOLD)*BY
          DOTJN=(XJ-U(N-NA))*BX+(YJ-V(N-NA))*BY
          DOTJNN=(XJN-U(N-NA))*BX+(YJN-V(N-NA))*BY
C***      IS J OUTSIDE M-N AND JN OUTSIDE M-N AND
C***         N OUTSIDE J-JN AND M OUTSIDE J-JN
          IF(DOTJN*DOTJM.GT.ZERO.AND.DOTJNM*DOTJNN.GT.ZERO.AND.
     &    DOTJN*DOTJNN.GT.ZERO.AND.DOTJM*DOTJNM.GT.ZERO) GO TO 45
C***      IS N INSIDE J-JN AND M INSIDE J-JN
          IF(DOTJN*DOTJNN.LE.ZERO.AND.DOTJM*DOTJNM.LE.ZERO) GO TO 36
C***      IS J OUTSIDE M-N AND JN INSIDE M-N
C***      OR J INSIDE M-N AND JN INSIDE M-N
C***      AND JN RATHER THAN J FURTHER FROM M
          IF(DOTJM*DOTJN.GE.ZERO.AND.DOTJNM*DOTJNN.LE.ZERO.OR.
     &    DOTJM*DOTJN.LE.ZERO.AND.DOTJNM*DOTJNN.LE.ZERO.AND.
     &    DOTJNM.GT.DOTJM) GO TO 38
          IF(DOTJM.EQ.ZERO) GO TO 45
          D=DOTJM/B2
          L=J
          IF(DOTJN.EQ.ZERO) K=N
          GO TO 40
36        D=ONE
          K=N
          IF(DOTJN.EQ.ZERO) L=J
          IF(DOTJNN.EQ.ZERO) L=JN
          GO TO 40
38        IF(DOTJNM.EQ.ZERO) GO TO 45
          D=DOTJNM/B2
          L=JN
          IF(DOTJNN.EQ.ZERO) K=N
40        IF(INTER.AND.D.GT.DMIN) GO TO 45
          IF(K.NE.0.AND.NXT(1,K).LT.0.OR.
     &    L.NE.0.AND.NXT(1,L).LT.0) GO TO 45
          DMIN=D
          XMIN=XI
          YMIN=YI
          KMIN=K
          LMIN=L
          JI=J
```

```
        INTER=.TRUE.
45      J=NXT(2,J)
        IF(J.NE.1) GO TO 14
C***    END OF LOOP ON J
        IF(.NOT.INTER) GO TO 65
C***   LINK THE NEW POINT INTO THE UU,V POLYGON
        IF(KMIN.NE.0) GO TO 54
        NONXT=NONXT+1
        IF(NONXT.LE.NWORK-2*NXYT) GO TO 46
        ERROR=-13
        GO TO 402
46      IF(LMIN.GT.0) GO TO 52
        NXYT=NXYT+1
        IF(NXYT.LE.(NWORK-NONXT)/2) GO TO 47
        ERROR=-11
        GO TO 402
47      XYT(1,NXYEND-NXYT)=XMIN
        XYT(2,NXYEND-NXYT)=YMIN
        NXT(1,NONXT)=-NXYT-NA-NB
        UOLD=XMIN
        VOLD=YMIN
        GO TO 53
52      NXT(1,NONXT)=-LMIN
        UOLD=X(LMIN)
        VOLD=Y(LMIN)
53      NXT(2,NONXT)=NXT(2,NOLD)
        NXT(2,NOLD)=NONXT
        NOLD=NONXT
        GO TO 55
54      NXT(1,KMIN)=-KMIN
        IF(LMIN.GT.0) NXT(1,KMIN)=-LMIN
C***    LINK THE NEW POINT INTO THE X,Y POLYGON
55      IF(LMIN.GT.0) GO TO 59
        NONXT=NONXT+1
        IF(NONXT.LE.NWORK-2*NXYT) GO TO 56
        ERROR=-13
        GO TO 402
56      IF(KMIN.GT.0) GO TO 57
        NXT(1,NONXT)=NXT(1,NONXT-1)
        GO TO 58
57      NXT(1,NONXT)=-KMIN
58      NXT(2,NONXT)=NXT(2,JI)
        NXT(2,JI)=NONXT
        GO TO 60
59      NXT(1,LMIN)=-NXT(1,LMIN)
60      IF(KMIN.NE.N) GO TO 11
65      CONTINUE
402     RETURN
        END
```

```
      SUBROUTINE IUSUB2(X,Y,NA,U,V,NB,OTYPE,NXT,XYT,NWORK,
     & NONXT,SEG,NONIU,NIUS,NIUMAX,XIU,YIU,NXYMAX,NIUBUL,NOFILE)
C     ***************************************************************************
C     SUBROUTINE IUSUB2
C     ***************************************************************************
      DIMENSION X(NA),Y(NA),U(NB),V(NB)
      INTEGER OTYPE
C***
C     SEG  AN INTEGER MATRIX DIMENSIONED (3,MAX2) WHERE MAX2-2
C     EQUALS THE NUMBER OF INTERSECTIONS OF THE TWO FIGURES.
C***
      INTEGER NXT(2,1),SEG(3,1)
      REAL XYT(2,1),XIU(1),YIU(1)
      REAL SENTNL
      INTEGER NIUS(2,1)
      INTEGER NIUMAX
      LOGICAL NIUBUL,NOFILE
      LOGICAL IDENT
      LOGICAL PTS
      DATA SENTNL/0.0E-78/
      NSEG=0
      NXYT=NONXT-NA-NB
      IF(OTYPE.LE.4) GO TO 68
      IF(NXT(1,NA+1).GT.0) NXT(1,NA+1)=-NXT(1,NA+1)
      IF(NXT(1,NA+NB).GT.0) NXT(1,NA+NB)=-NXT(1,NA+NB)
      GO TO 69
68    CALL SEGDEF(U,V,NB,X,Y,NA,0,OTYP,
     & SEG,NSEG,NXT,NONXT,XYT,NWORK)
      IF(NSEG.LT.0) GO TO 400
69    CALL SEGDEF(X,Y,NA,U,V,NB,NA,OTYPE,
     & SEG,NSEG,NXT,NONXT,XYT,NWORK)
      IF(NSEG.LT.0) GO TO 400
      IDENT=.TRUE.
      DO 70 I=1,NSEG
      IF(SEG(1,I).NE.4) IDENT=.FALSE.
      IZ=SEG(2,I)
70    IF(NXT(1,IZ).LT.0) NXT(1,IZ)=-NXT(1,IZ)
      IZ=SEG(3,NSEG)
      IF(NXT(1,IZ).LT.0) NXT(1,IZ)=-NXT(1,IZ)
C***  TAKE CARE OF UNION AND INTERSECTION OF IDENTICAL POLYGONS
C***  AS A SPECIAL CASE
      IF(.NOT.IDENT.OR.OTYPE.GT.2) GO TO 80
      NONIU=1
      NIUS(2,NONIU)=NB
      NIUS(1,NONIU)=0
      DO 71 I=1,NB
      XIU(I)=U(I)
71    YIU(I)=V(I)
      RETURN
```

```
C***
C***   LINK THE SEGMENTS AND GENERATE THE RESULT VARIABLES
C***
80      NIU=1
        NONIU=0
        NIUBUL=.FALSE.
C***
C       SEG(1,I)=1  SEGMENT I OF A IS ON THE BOUNDARY OF B
C       SEG(1,I)=2  SEGMENT I OF A IS OUTSIDE B
C       SEG(1,I)=3  SEGMENT I OF A IS INSIDE B
C       SEG(1,I)=4  SEGMENT I OF B IS ON THE BOUNDARY OF A
C       SEG(1,I)=5  SEGMENT I OF B IS OUTSIDE A
C       SEG(1,I)=6  SEGMENT I OF B IS INSIDE A
C***
90      DO 100 I=1,NSEG
        GO TO (91,92,93,94,95,96,97,98,99), OTYPE
91      IF(SEG(1,I).EQ.2.OR.SEG(1,I).EQ.5) GO TO 110
        GO TO 100
92      IF(SEG(1,I).EQ.3.OR.SEG(1,I).EQ.6) GO TO 110
        GO TO 100
93      IF(SEG(1,I).EQ.2.OR.SEG(1,I).EQ.6) GO TO 110
        GO TO 100
94      IF(SEG(1,I).EQ.3.OR.SEG(1,I).EQ.5) GO TO 110
        GO TO 100
95      IF(SEG(1,I).EQ.4) GO TO 110
        GO TO 100
96      IF(SEG(1,I).EQ.5) GO TO 110
        GO TO 100
97      IF(SEG(1,I).EQ.6) GO TO 110
        GO TO 100
98      IF(SEG(1,I).EQ.4.OR.SEG(1,I).EQ.5) GO TO 110
        GO TO 100
99      IF(SEG(1,I).EQ.4.OR.SEG(1,I).EQ.6) GO TO 110
100     CONTINUE
        IF(NIUBUL) WRITE(21,9999) SENTNL,SENTNL
        RETURN
110     IP=SEG(2,I)
        I1=NXT(1,IP)
        NONIU=NONIU+1
        IF(NOFILE.OR.NONIU.LE.NIUMAX) GO TO 111
        NINIU=.TRUE.
        CALL PNT001(NONIU,NIUS,XIU,YIU,NIUMAX)
111     PTS=.FALSE.
        IF(NIUBUL) GO TO 112
        NIUS(1,NONIU)=NIU-1
        NIUS(2,NONIU)=0
        GO TO 120
112     WRITE(21,9999) SENTNL,SENTNL
9999    FORMAT(2G15.6)
```

```
120     IF(IP.EQ.SEG(3,I).AND.NXT(1,IP).EQ.I1.AND.PTS) GO TO 310
        IF(.NOT.NIUBUL) NIUS(2,NONIU)=NIUS(2,NONIU)+1
        IF(NOFILE.OR.NIU.NE.NXYMAX) GO TO 121
1201    NIUBUL=.TRUE.
        CALL PNT001(NONIU,NIUS,XIU,YIU,NIUMAX)
121     IF(NIUBUL) CALL PNTALT(X,Y,NA,U,V,NB,XYT,NWORK,NXT(1,IP))
        IF(.NOT.NIUBUL) CALL PNTGET(X,Y,NA,U,V,NB,XYT,NWORK,
     & NXT(1,IP),XIU(NIU),YIU(NIU))
        PTS=.TRUE.
        NIU=NIU+1
        IF(IP.EQ.SEG(3,I)) GO TO 125
122     IP=NXT(2,IP)
        GO TO 120
125     IF(OTYPE.GT.4) GO TO 310
        DO 160 J=1,NSEG
        JP=SEG(2,J)
        IF(J.NE.I.AND.SEG(1,I).EQ.SEG(1,J).AND.
     & NXT(1,IP).EQ.NXT(1,JP)) GO TO 300
160     CONTINUE
        DO 180 J=1,NSEG
        JP=SEG(2,J)
        IF(NXT(1,IP).NE.NXT(1,JP)) GO TO 180
        GO TO (171,172,173,174), OTYPE
171     IF(SEG(1,J).EQ.2.OR.SEG(1,J).EQ.5) GO TO 300
        GO TO 180
172     IF(SEG(1,J).EQ.3.OR.SEG(1,J).EQ.6) GO TO 300
        GO TO 180
173     IF(SEG(1,J).EQ.2.OR.SEG(1,J).EQ.6) GO TO 300
        GO TO 180
174     IF(SEG(1,J).EQ.3.OR.SEG(1,J).EQ.5) GO TO 300
180     CONTINUE
        DO 190 J=1,NSEG
        JP=SEG(2,J)
        IF(NXT(1,IP).EQ.NXT(1,JP)) GO TO 300
190     CONTINUE
300     SEG(1,I)=0
        IP=SEG(2,J)
        I=J
        GO TO 122
310     SEG(1,I)=0
        GO TO 90
400     NONIU=-12
402     RETURN
        END
```

```
      LOGICAL FUNCTION SENSE(X,Y,N)
C     ************************************************************
C     LOGICAL FUNCTION SENSE
C     SENSE IS TRUE IF THE X, Y POLYGON CLOSES CLOCKWISE,
C     FALSE IF IT CLOSES COUNTERCLOCKWISE
C     ************************************************************
      INTEGER N
      REAL X(N),Y(N)
      DOUBLE PRECISION TSUM
      IF(N.LT.3) RETURN
      TSUM=0.0D0
      AY=Y(2)-Y(1)
      AX=X(2)-X(1)
      DO 2 J=3,N
      BY=Y(J)-Y(1)
      BX=X(J)-X(1)
      TSUM=TSUM+BY*AX-AY*BX
      AX=BX
2     AY=BY
      SENSE=.FALSE.
      IF(TSUM.LT.0.0D0) SENSE=.TRUE.
      RETURN
      END
      SUBROUTINE SEGDEF(X,Y,NXY,U,V,NUV,OFFSET,OTYPE,
     &  SEG,NSEG,NXT,NONXT,XYT,NWORK)
C     ************************************************************
C     SUBROUTINE SEGDEF
C     SEGDEF GENERATES THE SEG MATRIX.  A SEGMENT IS A SERIES OF
C     SUCCESSIVE SIDES OF ONE OF THE POLYGONS ALL LYING INSIDE
C     OR ALL OUTSIDE THE OTHER POLYGON, OR A SIDE OF ONE POLYGON L
C     LYING ON THE BOUNDARY OF THE OTHER.  IF THE POLYGONS
C     INTERSECT, THE END POINTS OF THE SEGMENTS LIE OF THE
C     BOUNDARY OF THE OTHER POLYGON.  IF THE POLYGONS DON'T
C     INTERSECT OR ARE IDENTICAL, EACH POLYGON IS A SINGLE
C     SEGMENT.  EACH TRIPLET OF THE SEG MATRIX DEFINES A
C     SEGMENT.  THE FIRST NUMBER IN THE ITH TRIPLET CONTAINS A
C     CODE, 1 - 6 (SEE COMMENTS IN SUBROUTINE IUSUB2).
C     SEG(2,I) IS THE INDEX IN THE NXT ARRAY OF THE FIRST POINT
C     OF SEGMENT I.  SEG(3,I) IS THE INDEX IN THE NXT ARRAY OF
C     THE LAST POINT OF SEGMENT I.
C     ************************************************************
      INTEGER NXY,NUV,OFFSET,NSEG,NXYT,OTYPE
      REAL X(NXY),Y(NXY),U(NUV),V(NUV)
      INTEGER NXT(2,1),SEG(3,1)
      REAL XYT(2,1)
      INTEGER SOLD
      LOGICAL SUMLNK
      MAX2=NWORK-(3*NONXT+1)/2-2*(NONXT-NXY-NUV)
      KK=2
      IF(OFFSET.NE.0) KK=5
      SUMLNK=.FALSE.
      IOLD=OFFSET+1
```

```
      MSTART=IOLD
      IOF=-1
      IF(NXT(1,IOLD).GT.0) GO TO 40
      SUMLNK=.TRUE.
      SOLD=IOLD
      MSTART=IOLD
      IF(OTYPE.GT.4) MSTART=NXY+NUV
40    INEW=NXT(2,IOLD)
      IF(NXT(1,INEW).LT.0) GO TO 42
      IF(.NOT.SUMLNK.OR.IOF.GE.0) GO TO 49
      IOF=INSYD2(U(INEW-OFFSET),V(INEW-OFFSET),X,Y,NXY)
      GO TO 49
42    IF(SUMLNK) GO TO 43
      MSTART=INEW
      SUMLNK=.TRUE.
      SOLD=INEW
      GO TO 60
43    NSEG=NSEG+1
      IF(NSEG.GT.MAX2) GO TO 51
      SEG(2,NSEG)=SOLD
      SEG(3,NSEG)=INEW
      SOLD=INEW
      IF(IOF.LT.0) GO TO 45
      SEG(1,NSEG)=KK+IOF
      IOF=-1
      GO TO 49
45    IF(OFFSET.EQ.0) GO TO 46
      CALL PNTGET(X,Y,NXY,U,V,NUV,XYT,NWORK,
     &  -NXT(1,IOLD),XOLD,YOLD)
      CALL PNTGET(X,Y,NXY,U,V,NUV,XYT,NWORK,
     &  -NXT(1,INEW),XNEW,YNEW)
      GO TO 47
46    CALL PNTGET(U,V,NUV,X,Y,NXY,XYT,NWORK,
     &  -NXT(1,IOLD),XOLD,YOLD)
      CALL PNTGET(U,V,NUV,X,Y,NXY,XYT,NWORK,
     &  -NXT(1,INEW),XNEW,YNEW)
47    IOFMID=INSYD3((XOLD+XNEW)/2.0,(YOLD+YNEW)/2.0,X,Y,NXY)
      SEG(1,NSEG)=KK+IOFMID
49    IF(MSTART.NE.INEW) GO TO 60
      IF(SUMLNK) RETURN
      IOF=INSYD2(U(OFFSET+1),V(OFFSET+1),X,Y,NXY)
      NSEG=NSEG+1
      IF(NSEG.LE.MAX2) GO TO 52
51    NSEG=-12
      GO TO 53
52    SEG(1,NSEG)=KK+IOF
      SEG(2,NSEG)=OFFSET+1
      SEG(3,NSEG)=SEG(2,NSEG)
53    RETURN
60    IOLD=INEW
      GO TO 40
      END
```

```
      INTEGER FUNCTION INSYD3(U,V,X,Y,N)
C     ***********************************************************************
C     INTEGER FUNCTION INSYD3
C     THE FUNCTION INSYD3 IS -1 IF THE POINT (U,V) IS ON THE
C     BOUNDARY OF THE X, Y POLYGON, 0 IF OUTSIDE THE POLYGON,
C     +1 IF INSIDE.
C     ***********************************************************************
      INTEGER N
      REAL X(N),Y(N),U,V
      DOUBLE PRECISION SINE
      LOGICAL BOOL
      INSYD3=0
      BOOL=.FALSE.
      DO 10 I=1,N
      IN=I+1
      IF(IN.GT.N) IN=1
      IF(Y(IN).EQ.Y(I).AND.X(IN).EQ.X(I)) GO TO 10
      SINE=(U-X(I))*(Y(IN)-Y(I))-(V-Y(I))*(X(IN)-X(I))
      IF(SINE.NE.0.0D0) GO TO 5
      IF(((U-X(I))*(X(IN)-X(I))+(V-Y(I))*(Y(IN)-Y(I)))*
     & ((U-X(IN))*(X(IN)-X(I))+(V-Y(IN))*(Y(IN)-Y(I))).GT.0.0D0)
     & GO TO 10
      INSYD3=-1
      GO TO 20
5     IF(V.GT.Y(IN).AND.V.LE.Y(I).AND.SINE.LT.0.0D0 .OR.
     & V.LE.Y(IN).AND.V.GT.Y(I).AND.SINE.GT.0.0D0)
     & BOOL=.NOT.BOOL
10    CONTINUE
      IF(BOOL) INSYD3=1
20    RETURN
      END
      INTEGER FUNCTION INSYD2(U,V,X,Y,N)
C     ***********************************************************************
C     INTEGER FUNCTION INSYD2
C     THE FUNCTION INSYD2 IS 1 IF THE POINT (U,V) IS INTERIOR TO
C     THE X, Y POLYGON, INSYD2 IS ZERO OTHERWISE.  THE POINT (U,V)
C     IS ASSUMED NOT ON THE BOUNDARY OF THE X, Y POLYGON.
C     ***********************************************************************
      INTEGER N
      REAL X(N),Y(N),U,V
      LOGICAL BOOL
      INSYD2=0
      BOOL=.FALSE.
      DO 10 I=1,N
      IN=I+1
      IF(IN.GT.N) IN=1
      IF(Y(IN).EQ.Y(I).AND.X(IN).EQ.X(I)) GO TO 10
      IF(V.LE.Y(IN).OR.V.GT.Y(I)) GO TO 5
```

```
      IF((U-X(I))*(Y(IN)-Y(I))-(V-Y(I))*(X(IN)-X(I)).LT.0.0D0)
     & BOOL=.NOT.BOOL
      GO TO 10
5     IF(V.GT.Y(IN).OR.V.LE.Y(I)) GO TO 10
      IF((U-X(I))*(Y(IN)-Y(I))-(V-Y(I))*(X(IN)-X(I)).GT.0.0D0)
     & BOOL=.NOT.BOOL
10    CONTINUE
      IF(BOOL) INSYD2=1
      RETURN
      END
      SUBROUTINE PNTGET(X,Y,NA,U,V,NB,XYT,NWORK,K,A,B)
C     ************************************************************************
C     SUBROUTINE PNTGET
C     ************************************************************************
      REAL X(NA),Y(NA),U(NB),V(NB),XYT(2,1)
      INTEGER K
      IF(K.GT.NA+NB) GO TO 20
      IF(K.GT.NA) GO TO 10
      A=X(K)
      B=Y(K)
      GO TO 30
10    A=U(K-NA)
      B=V(K-NA)
      GO TO 30
20    A=XYT(1,NWORK/2+1-K+NA+NB)
      B=XYT(2,NWORK/2+1-K+NA+NB)
30    RETURN
      END
      SUBROUTINE PNTALT(X,Y,NA,U,V,NB,XYT,NWORK,K)
C     ************************************************************************
C     SUBROUTINE PNTALT
C     ************************************************************************
      REAL X(NA),Y(NA),U(NB),V(NB),XYT(2,1)
      INTEGER K
      IF(K.GT.NA+NB) GO TO 20
      IF(K.GT.NA) GO TO 10
      A=X(K)
      B=Y(K)
      GO TO 30
10    A=U(K-NA)
      B=V(K-NA)
      GO TO 30
20    A=XYT(1,NWORK/2+1-K+NA+NB)
      B=XYT(2,NWORK/2+1-K+NA+NB)
30    WRITE(21,9999) A,B
9999  FORMAT(2G15.6)
      RETURN
      END
```

```
      SUBROUTINE PNT001(NONIU,NIUS,XIU,YIU,NIUMAX)
C     ***************************************************************************
C     SUBROUTINE PNT001
C     ***************************************************************************
      INTEGER NONIU,NIUMAX,NIUS(2,1)
      REAL XIU(1),YIU(1)
      REAL SENTNL
      DATA SENTNL/0.0E-78/
C     REWIND 21
      LIMIT=MIN0(NONIU,NIUMAX)
      DO 5 I=1,LIMIT
      ISTART=NIUS(1,I)
      ICOUNT=NIUS(2,I)
      IF(I.EQ.NONIU) ICOUNT=ICOUNT-1
      IF(ICOUNT.EQ.0) GO TO 5
      DO 4 J=1,ICOUNT
4     WRITE(21,9999) XIU(J+ISTART),YIU(J+ISTART)
      IF(I.NE.NONIU) WRITE(21,9999) SENTNL,SENTNL
9999  FORMAT(2G15.6)
5     CONTINUE
      RETURN
      END
      SUBROUTINE QINVAR
C     ***************************************************************************
C     ENTER PARAMETERS FOR SUBROUTINE ANGLE CALL
C     ***************************************************************************
      COMMON /BLOCK1/IWRITE,IREAD,IFILER,IFILEW
      WRITE(IWRITE,10)
10    FORMAT('  >> (1) OVERALL OR (2) AT CERTAIN AZMU. ANGLE? (1/2)')
      READ(IREAD,20) IANS
20    FORMAT(I1)
      WRITE(IWRITE,30)
30    FORMAT('  >> SAVE THE ANGULAR DATA? (Y/N)')
      READ(IREAD,40) ANS
40    FORMAT(A1)
      IF(ANS.EQ.'N') GO TO 70
      WRITE(IWRITE,50)
50    FORMAT('  >> ENTER FILE NUMBER TO SAVE ANGULAR DATA (I2)')
      READ(IREAD,60) IFILEW
60    FORMAT(I2)
70    IF(IANS.EQ.1) GO TO 140
80    WRITE(IWRITE,90)
90    FORMAT('  >> ENTER ANGLE OF SLICE (G15.6)')
      READ(IREAD,100) AZMU
100   FORMAT(G15.6)
      IF(AZMU.LE.90.0.AND.AZMU.GE.-90.0) GO TO 120
      IF(AZMU.GT.90.0.OR.AZMU.LT.-90.0) WRITE(IWRITE,110)
110   FORMAT(' ... INVALID ... TRY AGAIN ...')
      GO TO 80
120   WRITE(IWRITE,130)
130   FORMAT('  >> ENTER CHANNEL WIDTH OF THE SLICE (G15.6)')
```

```
      READ(IREAD,100) W2
      IF(W2.LE.0.0) W2=2.0
      CALL ANGLE(AZMU,W2,ANS)
      CALL INVARI(ZEROIN,RG,Q,VOIDFR)
      RETURN
140   WRITE(IWRITE,150)
150   FORMAT('  >> ENTER ANGLE INCREMENT (G15.6)')
      READ(IREAD,100) ANGINC
      IF(ANGINC.LE.0.0) ANGINC=10.
      NANGLE=180./ANGINC+1
      WRITE(IWRITE,130)
      READ(IREAD,100) W2
      IF(W2.LE.0.0) W2=2.0
      WRITE(23,160)
160   FORMAT(6X,'AZMU',10X,'ZEROIN',11X,'RG',11X,'Q',8X,'VOID FRAC.')
      DO 170 I=1,NANGLE
      AZMU=ANGINC*(I-1)-90.0
      CALL ANGLE(AZMU,W2,ANS)
      CALL INVARI(ZEROIN,RG,Q,VOIDFR)
      WRITE(23,180) AZMU,ZEROIN,RG,Q,VOIDFR
180   FORMAT(5G15.6)
170   CONTINUE
      RETURN
      END
      SUBROUTINE INVARI(ZEROIN,RG,Q,VOIDFR)
C     ************************************************************************
C     SUBROUTINE TO CALCULATE INVARIANT AT CERTAIN AZMUTHAL ANGLE
C     BY ASSUMING CIRCULAR SYMMETRY.
C     ************************************************************************
C         TWOTHE:  SCATTERING ANGLE
C              S:  RECIPROCAL SPACE SCATTERING VECTOR
C                  = 2.0 * SIN(THETA) / WAVELENGTH
C           SCAT:  SCATTERING INTENSITY
C         ZEROIN:  ZERO ANGLE SCATTERING INTENSITY
C             RG:  RADIUS OF GYRATION CALCULATED BY GUINIER APPROX.
C              Q:  INVARIANT
C                  = 4.0 * PI * SUM(S**2*SCAT)
C         VOIDFR:  VOID FRACTION
C     ************************************************************************
      DIMENSION TWOTHE(100),SCAT(100),S(100)
      DIMENSION SV(2),SPOW(2),SM(2),SA(2,2)
      COMMON /BLOCK1/IWRITE,IREAD,IFILER,IFILEW
      COMMON /BLOCK6/NI,NPT,TWOTHE,SCAT
      PI=4.0*ATAN(1.0)
      DO 40 I=NI,NPT
      S(I)=2.0*SIN(TWOTHE(I)/2000.0)/1.5417
40    CONTINUE
      Q=0.
```

```
C***
C***    FOR S < 0
C***
C***    DETERMINE MAXIMUM INTENSITY
C***
        XMAX=0.0
        MAX=1
        MED=0
        DO 50 I=NI,NPT
        IF(S(I).GT.0.0) GO TO 55
        MED=I
        IF(SCAT(I).LE.XMAX) GO TO 50
        XMAX=SCAT(I)
        MAX=I
50      CONTINUE
55      CONTINUE
C***
C***    FIT THE SMALL ANGLE REGION SCATTERING CURVE BY GUINIER APPROX.
C***
        DO 60 K=1,2
        SV(K)=0.
        DO 60 L=1,2
60      SA(K,L)=0.0
        DO 70 I=MAX-4,MAX-1
        SPOW(1)=1.0
        SPOW(2)=S(I)**2
        DO 70 K=1,2
        SV(K)=SV(K)+SPOW(K)*ALOG(SCAT(I))
        DO 70 L=1,2
70      SA(K,L)=SA(K,L)+SPOW(K)*SPOW(L)
        SNOEM=SA(1,2)**2-SA(1,1)*SA(2,2)
        SM(1)=(SV(2)*SA(1,2)-SV(1)*SA(2,2))/SNOEM
        SM(2)=(SV(1)*SA(1,2)-SV(2)*SA(1,1))/SNOEM
        ZEROI1=EXP(SM(1))
        RG1=SQRT(-3.0*SM(2))/2.0/PI
        DX=-S(MAX-1)/100.
        XI=0.0
        DO 75 I=1,100
        XIP1=XI+DX
        ARG1=ZEROI1*XI**2*EXP(SM(2)*XI**2)
        ARG1P1=ZEROI1*XIP1**2*EXP(SM(2)*XIP1**2)
        QS=DX*(ARG1+ARG1P1)/2.0
        XI=XIP1
75      Q=Q+QS
        DO 80 I=NI,MAX-2
        XI=-S(I)
        XIP1=-S(I+1)
        QS=(XI-XIP1)*(SCAT(I)*XI**2+SCAT(I+1)*XIP1**2)/2.0
80      Q=Q+QS
```

```
C***
C***    FOR S > 0.0
C***
C***    DETERMINE THE MAXIMUM INTENSITY
C***
        XMAX=0.0
        MAX=32
        DO 150 I=MED,NPT
        IF(SCAT(I).LE.XMAX) GO TO 150
        XMAX=SCAT(I)
        MAX=I
150     CONTINUE
C***
C***    FIT THE SMALL ANGLE REGION SCATTERING CURVE BY GUINIER APPROX.
C***
        DO 160 K=1,2
        SV(K)=0.
        DO 160 L=1,2
160     SA(K,L)=0.0
        DO 170 I=MAX+1,MAX+4
        SPOW(1)=1.0
        SPOW(2)=S(I)**2
        DO 170 K=1,2
        SV(K)=SV(K)+SPOW(K)*ALOG(SCAT(I))
        DO 170 L=1,2
170     SA(K,L)=SA(K,L)+SPOW(K)*SPOW(L)
        SNOEM=SA(1,2)**2-SA(1,1)*SA(2,2)
        SM(1)=(SV(2)*SA(1,2)-SV(1)*SA(2,2))/SNOEM
        SM(2)=(SV(1)*SA(1,2)-SV(2)*SA(1,1))/SNOEM
        ZEROI2=EXP(SM(1))
        RG2=SQRT(-3.0*SM(2))/2.0/PI
        DX=S(MAX+1)/100.
        XI=0.0
        DO 175 I=1,100
        XIP1=XI+DX
        ARG1=ZEROI2*XI**2*EXP(SM(2)*XI**2)
        ARG1P1=ZEROI2*XIP1**2*EXP(SM(2)*XIP1**2)
        QS=DX*(ARG1+ARG1P1)/2.0
        XI=XIP1
175     Q=Q+QS
        DO 180 I=MAX+1,NPT-1
        XI=S(I)
        XIP1=S(I+1)
        QS=(XIP1-XI)*(SCAT(I)*XI**2+SCAT(I+1)*XIP1**2)/2.0
180     Q=Q+QS
        DELEC=1.049*56/104*6.023E23/1.0E24
        Q=4.0*PI*Q/2.0
        AAA=Q/DELEC**2
        VOIDFR=(1.0-SQRT(1.0-4.0*AAA))/2.0
        ZEROIN=(ZEROI1+ZEROI2)/2.0
        RG=(RG1+RG2)/2.0
```

```
      WRITE(IWRITE,190) ZEROIN,RG,Q,VOIDFR
190   FORMAT(4G15.6)
      RETURN
      END
      SUBROUTINE REFLEC
C     ********************************************************************************
C     FORTRAN PROGRAM TO CALCULATE THEORETICAL TOTAL
C     REFLECTION SPECTRA
C     PHI,KAI: SPHERICAL COORDINATE OF SURFACE NORMAL NS IN X,Y,Z
C     PHIP,KAIP: SPHERICAL COORDINATE OF NS IN X',Y',Z'
C     X',Y',Z': X,Y,Z TILT ALPHA RADIAN
C     ALPHA: TILTED ANGLE IN RADIAN
C     ********************************************************************************
      REAL KAI,KAIP,INMAX
      WAVE=1.5417
      HALFPI=2.0*ATAN(1.0)
      PI=HALFPI*2.0
      TWOPI=2.0*PI
      DELTA=SQRT(7.94E-10)*WAVE**2*6.023E23*1.049*56/TWOPI/104.E24
      REFRAC=1.0-DELTA
      THETAC=SQRT(2.0*DELTA)
      WRITE(5,100)
100   FORMAT('  ENTER THICKNESS IN ANG (G15.6)')
      READ(5,150) THICK
150   FORMAT(G15.6)
      ALPHA=0.0
      WRITE(5,200)
200   FORMAT('  ENTER VALUE OF TILTED ANGLE (?  DEGREE) (G15.6)')
      READ(5,150) ALPHA
      ALPHA=ALPHA*TWOPI/360.0
      SINALP=SIN(ALPHA)
      COSALP=COS(ALPHA)
      WRITE(5,300)
300   FORMAT('  ENTER VALUE OF SIGMAPHI (? * DEGREE) (G15.6)')
      READ(5,150) SIGMAP
      SIGMAP=SIGMAP*TWOPI/360.0
C***
C***  SET MINIMUM INTENSITY VALUE TO SAVE
C***
      PHILIM=SQRT(ALOG(1.0E-8)*(-2.0)*SIGMAP**2)
C***
C***                        EXP(-(PHIP-PHIPAVE)**2/2/SIGMAP**2)
C***  RHO(PHIP,KAIP) = ------------------------------------
C***                              SQRT(TWOPI*SIGMAP**2)
C***   CYLINDRICAL SYMMETRY IS ASSUMED FOR DISTRIBUTION OF KAIP
C***  RHOKAI=1.0
C***
```

```
      SSS=TWOPI*2.0/WAVE
      INMAX=1.0/SQRT(TWOPI*SIGMAP**2)
      SSQ=SSS**2
      DSZ=0.04/40.
      DSY=0.04/40.
      DO 2000 K=1,81
      SZ=DSZ*FLOAT(K-41)
      DO 2000 J=1,81
      SY=DSY*FLOAT(J-41)
      DATA=0.0
      THESQ=SQRT(SSQ**2-4.0*SSQ*(SY**2+SZ**2))
      THESQ=(SSQ-THESQ)/2.0/SSQ
      SINTHE=SQRT(THESQ)
      IF(SINTHE.GT.1.0) GO TO 1900
      IF(SZ.GT.0.0) SINTHE=-SINTHE
      THETA=ASIN(SINTHE)
      SX=-SSS*SINTHE*SINTHE
      S=SQRT(SX**2+SY**2+SZ**2)
      IF(SINTHE.LT.0.0) S=-S
      IF(S.EQ.0.0) GO TO 1000
      TNX=SINTHE
      TNY=SY/(-S)
      TNZ=SZ/(-S)
      GO TO 1500
1000  TNX=SINTHE
      TNY=0.0
      TNZ=1.0
1500  CONTINUE
      TNXP=TNX*COSALP-TNZ*SINALP
      TNYP=TNY
      TNZP=TNZ*COSALP+TNX*SINALP
      IF(ABS(TNZP).GT.1.0) GO TO 1900
      PHIP=ACOS(TNZP)
      IF(PHIP.EQ.0.0) GO TO 1600
      IF(ABS(PHIP).GT.PHILIM) GO TO 1900
      SINKAI=TNYP/SIN(PHIP)
      IF(ABS(SINKAI).GT.1.0) GO TO 1900
1600  CONTINUE
      RHOPHI=1.0/EXP((PHIP/SIGMAP)**2/2.0)*INMAX
      CALL SREFLE(THICK,THETA,REFLE)
      DATA=RHOPHI*REFLE
1900  CONTINUE
      WRITE(1,20) SY,SZ,DATA
2000  CONTINUE
20    FORMAT(3E15.6)
      RETURN
      END
```

```
      SUBROUTINE SREFLE(THICK,THETA,REF)
C     ********************************************************************************
C     SUBROUTINE TO CALCULATE REFLECTANCE
C              WAVE: WAVELENGTH
C             THETAC: CRITICAL GLANCING ANGLE
C             REFIND: REFRACTIVE INDEX
C               REF: REFLECTANCE
C     ********************************************************************************
      SINHO(X)=(EXP(X)-EXP(-X))/2.
      WAVE=1.5417
      TWOPI=8.0*ATAN(1.0)
      DELTA=SQRT(7.94E-10)*WAVE**2*6.023E23*1.049*56/TWOPI/104.E24
      THETAC=SQRT(2.*DELTA)
      REFIND=1.0-DELTA
C***
C***  CALCULATING REFLENTANCE
C***
      THETA=ABS(THETA)
      RR=COS(THETA)**2-REFIND**2
      SINTHE=SIN(THETA)
      IF(THICK.GT.3000.0) GO TO 200
C***
C***  FOR LIMITED THICKNESS
C***
      THI=TWOPI*THICK/WAVE
      IF(RR.LE.0.0) GO TO 100
C***
C***  THETA < THETAC
C***
      U=THI*SQRT(RR)
      REF=(1.0-REFIND**2)**2*SINHO(U)**2
      REF=REF/(REF+4.*SINTHE**2*RR)
      RETURN
C***
C***  THETA > THETAC
C***
100    CONTINUE
      IF(RR.LT.0.0) GO TO 150
      REF=1.0
      RETURN
150   RR=SQRT(-RR)
      U=COS(THI*2.0*RR)
      R12=(SINTHE-RR)/(SINTHE+RR)
      REF=2.0*R12**2*(1-U)/(1.+R12**4-2.*R12**2*U)
      RETURN
C***
C***  FOR INFINITE THICKNESS
C***
200   CONTINUE
      IF(RR.LT.0.0) GO TO 300
```

```
C****
C****   THETA < THETAC
C****
        REF=1.0
        RETURN
C****
C****   THETA > THETAC
C****
300     RR=SQRT(-RR)
        R12=(SINTHE-RR)/(SINTHE+RR)
        REF=R12**2
        RETURN
        END
```

APPENDIX B

PROGRAM TOTAL.FOR

```
C     ************************************************************************
C     PROGRAM TOTAL.FOR
C     ************************************************************************
C     FORTRAN PROGRAM TO CALCULATE SURFACE SCATTERING SPECTRUM
C     ************************************************************************
C     MAIN PROGRAM
C     ************************************************************************
C     NOMENCLATURE :
C            N(I) : REFRACTIVE INDEX OF MEDIUM I (I = 1, 2)
C             N12 = N(2)/N(1)
C            N(I) = 1 - DELTA(I)
C            WAVE : WAVELENGTH IN ANGSTROM
C           GLANC : X-RAY GLANCING ANGLE
C           ALPHA : TILT ANGLE IN MILLIRADIAN
C            PHIC : CRITICAL INCIDENT ANGLE FOR TOTAL REFLECTION
C              KO : WAVE VECTOR OF INCIDENT BEAM
C                 = 2*PI/WAVE
C            PHIO : POLAR ANGLE OF INCIDENT BEAM IN RADIAN
C                 = PI/2.0 - ALPHA/1000.0
C             KOP : PROJECTION OF WAVE VECTOR KO ON PLANE Z = 0
C                 = SIN(PHIO)
C              QO : COMPONENT OF WAVE VECTOR KO NORNAL TO PLANE Z = 0
C                 = COS(PHIO)
C              VO = (2*PI/WAVE)*SQRT(SIN(PHIO)**2-N12**2)
C               K : WAVE VECTOR OF SCATTERED BEAM
C             PHI : POLAR ANGLE OF SCATTERED BEAM IN RADIAN
C             KAI : AZIMUTHAL ANGLE OF SCATTERED BEAM IN RADIAN
C            KAID : KAI IN DEGREE
C              KP : PROJECTION OF WAVE VECTOR K ON PLANE Z = 0
C                 = SIN(PHI)
C               Q : COMPONENT OF WAVE VECTOR K NORMAL TO PLANE Z = 0
C                 = COS(PHI)
C               V = (2*PI/WAVE)*SQRT(SIN(PHI)**2-N12**2)
C     SURFACE SCATTERING POWER = (OPTICAL FACTOR) * (SURFACE FACTOR)
C          OPTFAC : OPTICAL FACTOR
C     ************************************************************************
      DIMENSION DELTA(2),CHIPHI(8),CHIKAI(8)
      DIMENSION THETWO(2,100),TWOTHE(100),SCAT(2,100),SURSCA(100)
      DIMENSION ANEW(2,100),BNEW(2,100)
      REAL N(2),N12,KO,KOP,K,KP,KAI,KAID
       COMMON /BLOCK9/NI,NPT,TWOTHE,SURSCA
       OPEN (UNIT=20,FILE='SCAINT.DAT')
       OPEN (UNIT=21,FILE='SCAORI.DAT')
       OPEN (UNIT=24,FILE='SCACOR.DAT')
       OPEN (UNIT=23,FILE='FLUC.DAT')
```

```
C***
C***     SET PARAMETERS
C***
         WAVE=1.5417
         PI=4.0*ATAN(1.0)
         KO=2.0*PI/WAVE
         K=KO
         DELTA(1)=0.0E-06
         DELTA(2)=3.63E-06
         DO 300 IREAD=1,7
         N(1)=1.0-DELTA(1)
         N(2)=1.0-DELTA(2)
         N12=N(2)/N(1)
         CONST=4.0*PI**2/WAVE**4*(1.0-N12**2)**2
C***
C***     INPUT PARAMETERS
C***
         GLANC=0.0
         ALPHA=0.0
         COSALP=COS(ALPHA/1000.0)
         SINALP=SIN(ALPHA/1000.0)
         PHIO=PI/2.0-GLANC/1000.0-ALPHA/1000.0
         QO=COS(PHIO)
         KOP=SIN(PHIO)
         VO=SIN(PHIO)**2-N12**2
         IF(VO.LE.0.0) VO=-SQRT(-VO)
         IF(VO.GT.0.0) VO=SQRT(VO)
         KAID=0.0
         KAI=0.0
         SINKAI=SIN(KAI)
         COSKAI=COS(KAI)
         PPQQ=0.0
         DO 59 IJKL=1,2
         READ(1,40) PPQQ,PQPQ
40       FORMAT(2G15.6)
         MED=0
         NPTO=IFIX(PQPQ)
         DO 50 IJK=1,NPTO
         READ(1,40) THETWO(IJKL,IJK),SCAT(IJKL,IJK)
         IF(THETWO(IJKL,IJK).EQ.0.0) GO TO 50
         SCAT(IJKL,IJK)=0.0794*SCAT(IJKL,IJK)
         IF(THETWO(IJKL,IJK).GT.0.0) GO TO 50
         MED=MED+1
50       CONTINUE
         IF(MED.LT.1) GO TO 56
         MM=NPTO-MED
         IF(MM.GT.MED) NPTO=MED
         IF(MM.LE.MED) NPTO=MM
         DO 52 IJK=1,NPTO
         ANEW(IJKL,IJK)=THETWO(IJKL,MED+IJK)
         BNEW(IJKL,IJK)=(SCAT(IJKL,MED+IJK)+SCAT(IJKL,MED+1-IJK))/2.0
52       CONTINUE
```

```
      GO TO 59
56    CONTINUE
      DO 59 IJK=1,NPTO
      ANEW(IJKL,IJK)=THETWO(IJKL,IJK)
      BNEW(IJKL,IJK)=SCAT(IJKL,IJK)
59    CONTINUE
       NI=1
      PPQQ=0.0
       DO 60 IJKL=1,NPTO
      PQPQ=BNEW(1,IJKL)-BNEW(2,IJKL)
       IF(PQPQ.LE.0.0) GO TO 60
       PPQQ=PPQQ+1.0
       NPT=PPQQ
       SURSCA(NPT)=PQPQ
       TWOTHE(NPT)=ANEW(1,IJKL)
60     CONTINUE
       WRITE(20,70) PPQQ
       WRITE(21,70) PPQQ
       WRITE(22,70) PPQQ
       WRITE(23,70) PPQQ
70     FORMAT('DATA',T16,G15.6)
      DO 200 IJKL=1,NPT
      IF(SURSCA(IJKL).LE.0.0) GO TO 200
      TWOTH=TWOTHE(IJKL)
       PHI=PI/2.0-ABS(TWOTH)/1000.0
C***  SINPHI=SIN(PHI)=COS(TWOTH)
      SINPHI=COS(TWOTH/1000.0)
C***  COSPHI=COS(PHI)=SIN(TWOTH)
      COSPHI=SIN(TWOTH/1000.0)
      SQSINP=SINPHI**2
      Q=COSPHI
      KP=SINPHI
      V=SQSINP-N12**2
      IF(VO.LE.0.0) GO TO 140
C***
C***  VO > 0.0; I.E. PHIO > PHIC
C***
      CHIPHI(1)=VO
      CHIPHI(2)=QO*N12**2
      CHIPHI(5)=VO
      CHIPHI(6)=QO
      CHIKAI(1)=VO
      CHIKAI(2)=CHIPHI(2)
      CHIKAI(3)=VO*SINKAI
      CHIKAI(4)=0.0
      CHIKAI(5)=VO
      CHIKAI(6)=QO
      CHIKAI(7)=0.0
      CHIKAI(8)=COSKAI
      IF(V.LE.0.0) GO TO 130
```

```
C***
C***     V > 0.0; I.E. PHI > PHIC
C***
         V=SQRT(V)
         CHIPHI(3)=V*VO*COSPHI+KP*KOP*N12**2
         CHIPHI(4)=0.0
         CHIPHI(7)=0.0
         CHIPHI(8)=-V*SINKAI
         CALL ABSOLU(CHIPHI,SQCHIP)
         SQCHIP=SQCHIP/(V**2+Q**2*N12**4)
         CALL ABSOLU(CHIKAI,SQCHIK)
         SQCHIK=SQCHIK/(V**2+Q**2)
         GO TO 160
130      CONTINUE
C***
C***     V < 0.0; I.E. PHI < PHIC
C***
         V=-SQRT(-V)
         CHIPHI(3)=KP*KOP*N12**2
         CHIPHI(4)=V*VO*COSKAI
         CHIPHI(7)=V*SINKAI
         CHIPHI(8)=0.0
         CALL ABSOLU(CHIPHI,SQCHIP)
         SQCHIP=SQCHIP/(V-Q*N12**2)**2
         CALL ABSOLU(CHIKAI,SQCHIK)
         SQCHIK=SQCHIK/(V-Q)**2
         GO TO 160
140      CONTINUE
C***
C***     VO < 0.0; I.E. PHIO < PHIC
C***
         CHIPHI(1)=0.0
         CHIPHI(2)=QO*N12**2-VO
         CHIPHI(5)=0.0
         CHIPHI(6)=QO-VO
         CHIKAI(1)=0.0
         CHIKAI(2)=CHIPHI(2)
         CHIKAI(3)=0.0
         CHIKAI(4)=VO*SINKAI
         CHIKAI(5)=0.0
         CHIKAI(6)=QO-VO
         CHIKAI(7)=0.0
         CHIKAI(8)=COSKAI
         IF(V.LE.0.0) GO TO 150
C***
C***     V > 0.0; I.E. PHI > PHIC
C***
         V=SQRT(V)
         CHIPHI(3)=KP*KOP*N12**2
         CHIPHI(4)=V*VO*COSKAI
         CHIPHI(7)=0.0
         CHIPHI(8)=-V*SINKAI
```

```
      CALL ABSOLU(CHIPHI,SQCHIP)
      SQCHIP=SQCHIP/(V**2+Q**2*N12**4)
      CALL ABSOLU(CHIKAI,SQCHIK)
      SQCHIK=SQCHIK/(V**2+Q**2)
      GO TO 160
150   CONTINUE
C***
C***  V < 0.0; I.E. PHI < PHIC
C***
      V=-SQRT(-V)
      CHIPHI(3)=KP*KOP*N12**2-V*VO*COSKAI
      CHIPHI(4)=0.0
      CHIPHI(7)=V*SINKAI
      CHIPHI(8)=0.0
      CALL ABSOLU(CHIPHI,SQCHIP)
      SQCHIP=SQCHIP/(V-Q*N12**2)**2
      CALL ABSOLU(CHIKAI,SQCHIK)
      SQCHIK=SQCHIK/(V-Q)**2
160   CONTINUE
      OPTFAC=CONST*(SQCHIP+SQCHIK)*COSPHI**2
      WRITE(21,170) TWOTH,SURSCA(IJKL)
      SURSCA(IJKL)=SURSCA(IJKL)/OPTFAC
       SP=-2.0*PI/WAVE*(SINPHI*COSKAI*COSALP-COSPHI*SINALP-1.)
      WRITE(20,170) SP,SURSCA(IJKL)
170   FORMAT(2G15.6)
200   CONTINUE
       CALL SURCOR
300    CONTINUE
      STOP
      END
      SUBROUTINE ABSOLU(A,ABSO)
      DIMENSION A(8)
      SSSS(X,Y)=X**2+Y**2
      AA=SSSS(A(1),A(2))
      BB=SSSS(A(5),A(6))
      ARGU1=(A(1)*A(3)-A(2)*A(4))/AA+(A(5)*A(7)-A(6)*A(8))/BB
      ARGU2=(A(1)*A(4)+A(2)*A(3))/AA+(A(5)*A(8)+A(6)*A(7))/BB
      ABSO=SSSS(ARGU1,ARGU2)
      RETURN
      END
       SUBROUTINE SURCOR
C     ********************************************************************************
C     SUBROUTINE TO CALCULATE INVARIANT AT CERTAIN AZMUTHAL ANGLE
C     BY ASSUMING CIRCULAR SYMMETRY.
C     ********************************************************************************
C         TWOTHE:  SCATTERING ANGLE
C             SP:  RECIPROCAL SPACE SCATTERING VECTOR
C          SURSCA:  SURFACE SCATTERING FACTOR
C          Q:  SURFACE ROUGHNESS INVARIANT
C                  = PI * SUM(SP*SURSCA)
C     ********************************************************************************
```

```
      DIMENSION TWOTHE(100),SURSCA(100),SP(100)
      DIMENSION CORRE(101),SPX(50),SCAT(50)
      DIMENSION SV(2),SPOW(2),SM(2),SA(2,2)
      COMMON /BLOCK9/NI,NPT,TWOTHE,SURSCA
       PPQQ=101.0
       WRITE(24,1010) PPQQ
1010   FORMAT('DATA',T16,G15.6)
      PI=4.0*ATAN(1.0)
       TWOPI=2.0*PI
      CMIN=SQRT(SQRT(120.0*1.0E-6))
C***  SX=(SIN(PHI)*COS(KAI)*COS(ALPHA)-COS(PHI)*SIN(ALPHA)-1.0)/WAVE
C***  SY=(SIN(PHI)*SIN(KAI))/WAVE
C***  KAI=0,ALPHA=0:  SY=0, SX=(SIN(PHI)-1)/WAVE=(COS(TWOTHE)-1)/WAVE
C***                  SP=SQRT(SY**2+SX**2)=SX
      DO 40 I=NI,NPT
       SP(I)=(1.0-COS(TWOTHE(I)/1000.0))/1.5417
40    CONTINUE
      DO 45 I=1,101
45    CORRE(I)=0.0
C***
C***  FOR THETA < 0
C***
C***  DETERMINE THE ORIGIN
C***
      MED=0
      DO 50 I=NI,NPT
      IF(TWOTHE(I).GT.0.0) GO TO 55
      MED=I
50    CONTINUE
55    CONTINUE
      IF(MED.LT.1) GO TO 150
C***
C***  FIT THE SMALL ANGLE REGION SCATTERING CURVE BY GUINIER APPROX.
C***
      DO 60 K=1,2
      SV(K)=0.
      DO 60 L=1,2
60    SA(K,L)=0.0
      DO 70 I=MED-4,MED
      SPOW(1)=1.0
      SPOW(2)=SP(I)**2
      DO 70 K=1,2
      SV(K)=SV(K)+SPOW(K)*ALOG(SURSCA(I))
      DO 70 L=1,2
70    SA(K,L)=SA(K,L)+SPOW(K)*SPOW(L)
      SNOEM=SA(1,2)**2-SA(1,1)*SA(2,2)
      SM(1)=(SV(2)*SA(1,2)-SV(1)*SA(2,2))/SNOEM
      SM(2)=(SV(1)*SA(1,2)-SV(2)*SA(1,1))/SNOEM
      ZEROI1=EXP(SM(1))
```

```
C***
C***    THE INTENSITY CURVE IS EXTENDED TO ORIGIN BY TEN POINTS
C***
        DO 80 I=1,10
        SPX(I)=SP(MED)/10.0*I
80      SCAT(I)=ZEROI1*EXP(SM(2)*SPX(I)**2)
        MM=MED+10
        DO 90 I=11,MM
        J=MED-I+11
        SPX(I)=SP(J)
90      SCAT(I)=SURSCA(J)
        DO 110 IRP=1,101
        RP=FLOAT(IRP-1)*5000.0
        CONST=TWOPI*RP
        XI=0.0
        CI=CONST*XI
        Q=0.0
        ARG1=0.0
        DO 100 ISP=1,MM
        XIP1=SPX(ISP)
        CIP1=CONST*XIP1
        ARGIP1=XIP1*SCAT(ISP)
        IF(CIP1.LT.CMIN) ARGIP1=ARGIP1*(1.0-CIP1**2/6.0)
        IF(CIP1.GE.CMIN) ARGIP1=ARGIP1*SIN(CIP1)/CIP1
        DX=XIP1-XI
        Q=Q+DX*(ARG1+ARGIP1)/2.0
        XI=XIP1
100      ARG1=ARGIP1
        CORRE(IRP)=Q*TWOPI
110     CONTINUE
C***
C***    FOR TWOOTHE > 0.0
C***
C***    FIT THE SMALL ANGLE REGION SCATTERING CURVE BY GUINIER APPROX.
C***
150     CONTINUE
        MM=NPT-MED
        MED=MED+1
        DO 160 K=1,2
        SV(K)=0.
        DO 160 L=1,2
160     SA(K,L)=0.0
        DO 170 I=MED,MED+4
        SPOW(1)=1.0
        SPOW(2)=SP(I)**2
        DO 170 K=1,2
        SV(K)=SV(K)+SPOW(K)*ALOG(SURSCA(I))
        DO 170 L=1,2
170     SA(K,L)=SA(K,L)+SPOW(K)*SPOW(L)
```

```
      SNOEM=SA(1,2)**2-SA(1,1)*SA(2,2)
      SM(1)=(SV(2)*SA(1,2)-SV(1)*SA(2,2))/SNOEM
      SM(2)=(SV(1)*SA(1,2)-SV(2)*SA(1,1))/SNOEM
      ZEROI2=EXP(SM(1))
C***
C***  THE INTENSITY CURVE IS EXTENDED TO ORIGIN BY TEN POINTS
C***
      DO 180 I=1,10
      SPX(I)=SP(MED)/10.0*I
180   SCAT(I)=ZEROI2*EXP(SM(2)*SPX(I)**2)
      MM=MM+10
      DO 190 I=11,MM
      J=MED+I-11
      SPX(I)=SP(J)
190   SCAT(I)=SURSCA(J)
      DO 210 IRP=1,101
      RP=FLOAT(IRP-1)*5000.0
      XI=0.0
      Q=0.0
      CONST=TWOPI*RP
      ARG1=0.0
      DO 200 ISP=1,MM
      XIP1=SPX(ISP)
      CIP1=CONST*XIP1
      ARGIP1=XIP1*SCAT(ISP)
      IF(CIP1.LT.CMIN) ARGIP1=ARGIP1*(1.0-CIP1**2/6.0)
      IF(CIP1.GE.CMIN) ARGIP1=ARGIP1*SIN(CIP1)/CIP1
      DX=XIP1-XI
      Q=Q+DX*(ARG1+ARGIP1)/2.0
      XI=XIP1
200    ARG1=ARGIP1
      CORRE(IRP)=CORRE(IRP)+Q*TWOPI
210   CONTINUE
       FLUC=CORRE(1)
       WRITE(23,310) FLUC,FLUC
       DO 300 IRP=1,101
       CORRE(IRP)=CORRE(IRP)/FLUC
       RP=(IRP-1)*5000.0
300    WRITE(24,310) RP,CORRE(IRP)
310    FORMAT(2G15.6)
      RETURN
      END
```

APPENDIX C

PROGRAM GAMMA.FOR

```
C     ************************************************************************
C     PROGRAM GAMMA.FOR
C     ************************************************************************
C     FORTRA PROGRAM TO CALCULATE THE 3-D CORRELATION FUNCTION
C     FOR THE ELECTRON DENSITY FLUCTUATION OF AN ISOTROPIC
C     TWO-PHASE SYSTEM
C     ************************************************************************
C         TWOTHE:  SCATTERING ANGLE
C              S:  RECIPROCAL SPACE SCATTERING VECTOR
C                  = 2.0 * SIN(THETA) / WAVELENGTH
C           SCAT:  SCATTERING INTENSITY
C     ************************************************************************
      DIMENSION TWOTHE(100),SCAT(100),S(100)
      DIMENSION SV(2),SPOW(2),SM(2),SA(2,2)
      DIMENSION GAMMA(501)
1     WRITE(5,2)
2     FORMAT('  CALCULATE AGAIN? (Y/N)')
      READ(5,3) ANS
3     FORMAT(A1)
      IF(ANS.EQ.'N') STOP
      READ(20,10) A,B
10    FORMAT(F4.2,T16,G15.6)
      NPT=IFIX(B)
      CONST=4.0*4.0*ATAN(1.)/1.5417
      DO 40 I=1,NPT
      READ(20,30) A,B
30    FORMAT(2G15.6)
      SCAT(I)=B
40    S(I)=CONST*SIN(A/2000.)
C***
C***  FOR S < 0
C***
C***  DETERMINE MAXIMUM INTENSITY
C***
      XMAX=0.0
      MAX=1
      MED=0
      DO 50 I=1,NPT
      IF(S(I).GT.0.0) GO TO 55
      MED=I
      IF(SCAT(I).LE.XMAX) GO TO 50
      XMAX=SCAT(I)
      MAX=I
50    CONTINUE
55    CONTINUE
```

```
C***
C***    FIT THE SMALL ANGLE REGION SCATTERING CURVE BY GUINIER APPROX.
C***
        DO 60 K=1,2
        SV(K)=0.
        DO 60 L=1,2
60      SA(K,L)=0.0
        DO 70 I=MAX-4,MAX-1
        SPOW(1)=1.0
        SPOW(2)=S(I)**2
        DO 70 K=1,2
        SV(K)=SV(K)+SPOW(K)*ALOG(SCAT(I))
        DO 70 L=1,2
70      SA(K,L)=SA(K,L)+SPOW(K)*SPOW(L)
        SNOEM=SA(1,2)**2-SA(1,1)*SA(2,2)
        SM(1)=(SV(2)*SA(1,2)-SV(1)*SA(2,2))/SNOEM
        SM(2)=(SV(1)*SA(1,2)-SV(2)*SA(1,1))/SNOEM
        ZEROI1=EXP(SM(1))
        INCR=101
        DR=250./(INCR-1)
        DO 1000 IRS=1,INCR
        Q=0.
        ZZZ=DR*(IRS-1.)
        DX=-S(MAX-1)/100.
        XI=0.0
        ZSR=ZZZ*XI
        IF(ZSR.LT.0.045) ARG5=1.0-ZSR**2/6.0
        IF(ZSR.GE.0.045) ARG5=SIN(ZSR)/ZSR
        DO 75 I=1,100
        XIP1=XI+DX
        ZSRP1=ZZZ*XIP1
        IF(ZSRP1.LT.0.045) ARG5P1=1.0-ZSRP1**2/6.0
        IF(ZSRP1.GE.0.045) ARG5P1=SIN(ZSRP1)/ZSRP1
        ARG1=ARG5*ZEROI1*XI**2*EXP(SM(2)*XI**2)
        ARG1P1=ARG5P1*ZEROI1*XIP1**2*EXP(SM(2)*XIP1**2)
        QS=DX*(ARG1+ARG1P1)/2.0
        XI=XIP1
        ARG5=ARG5P1
75      Q=Q+QS
        DO 80 I=1,MAX-2
        XI=-S(I)
        ZSR=ZZZ*XI
        IF(ZSR.LT.0.045) ARG5=1.0-ZSR**2/6.0
        IF(ZSR.GE.0.045) ARG5=SIN(ZSR)/ZSR
        XIP1=-S(I+1)
        ZSR=ZZZ*XIP1
        IF(ZSR.LT.0.045) ARG5P1=1.0-ZSR**2/6.0
        IF(ZSR.GE.0.045) ARG5P1=SIN(ZSR)/ZSR
        QS=(XI-XIP1)*(SCAT(I)*XI**2*ARG5+SCAT(I+1)*XIP1**2*ARG5P1)/2.0
80      Q=Q+QS
1000    GAMMA(IRS)=Q
```

```
C***
C***    FOR S > 0.0
C***
C***    DETERMINE THE MAXIMUM INTENSITY
C***
        XMAX=0.0
        MAX=32
        DO 150 I=MED,NPT
        IF(SCAT(I).LE.XMAX) GO TO 150
        XMAX=SCAT(I)
        MAX=I
150     CONTINUE
C***
C***    FIT THE SMALL ANGLE REGION SCATTERING CURVE BY GUINIER APPROX.
C***
        DO 160 K=1,2
        SV(K)=0.
        DO 160 L=1,2
160     SA(K,L)=0.0
        DO 170 I=MAX+1,MAX+4
        SPOW(1)=1.0
        SPOW(2)=S(I)**2
        DO 170 K=1,2
        SV(K)=SV(K)+SPOW(K)*ALOG(SCAT(I))
        DO 170 L=1,2
170     SA(K,L)=SA(K,L)+SPOW(K)*SPOW(L)
        SNOEM=SA(1,2)**2-SA(1,1)*SA(2,2)
        SM(1)=(SV(2)*SA(1,2)-SV(1)*SA(2,2))/SNOEM
        SM(2)=(SV(1)*SA(1,2)-SV(2)*SA(1,1))/SNOEM
        ZEROI2=EXP(SM(1))
        RG2=SQRT(-3.0*SM(2))/2.0/PI
        DO 2000 IRS=1,INCR
        Q=0.
        ZZZ=DR*(IRS-1.)
        DX=S(MAX+1)/100.
        XI=0.0
        ZSR=ZZZ*XI
        IF(ZSR.LT.0.045) ARG5=1.0-ZSR**2/6.0
        IF(ZSR.GE.0.045) ARG5=SIN(ZSR)/ZSR
        DO 175 I=1,100
        XIP1=XI+DX
        ZSRP1=ZZZ*XIP1
        IF(ZSRP1.LT.0.045) ARG5P1=1.0-ZSRP1**2/6.0
        IF(ZSRP1.GE.0.045) ARG5P1=SIN(ZSRP1)/ZSRP1
        ARG1=ARG5*ZEROI2*XI**2*EXP(SM(2)*XI**2)
        ARG1P1=ARG5P1*ZEROI2*XIP1**2*EXP(SM(2)*XIP1**2)
        QS=DX*(ARG1+ARG1P1)/2.0
        XI=XIP1
        ARG5=ARG5P1
175     Q=Q+QS
```

```
      DO 180 I=MAX+1,NPT-1
      XI=S(I)
      ZSR=ZZZ*XI
      IF(ZSR.LT.0.045) ARG5=1.0-ZSR**2/6.0
      IF(ZSR.GE.0.045) ARG5=SIN(ZSR)/ZSR
      XIP1=S(I+1)
      ZSR=ZZZ*XIP1
      IF(ZSR.LT.0.045) ARG5P1=1.0-ZSR**2/6.0
      IF(ZSR.GE.0.045) ARG5P1=SIN(ZSR)/ZSR
      QS=(XIP1-XI)*(SCAT(I)*XI**2*ARG5+SCAT(I+1)*XIP1**2*ARG5P1)/2.0
180   Q=Q+QS
2000  GAMMA(IRS)=GAMMA(IRS)+Q
      GMAX=GAMMA(1)
      WRITE(5,30) GMAX
      A=FLOAT(INCR)
      WRITE(24,2090) A
2090  FORMAT('DATA',T16,G15.6)
      DO 3000 IRS=1,INCR
      GAMMA(IRS)=GAMMA(IRS)/GMAX
      ZZZ=DR*(IRS-1.)
3000  WRITE(24,30) ZZZ,GAMMA(IRS)
      GO TO 1
      STOP
      END
```

VITA

Ming-Ya Tang (湯 茗 雅) was born in Taiwan, Republic of China on December 16, 1955. Her parents moved to Taiwan with Nationalist government when Communist took over mainland China in 1949. She lived in Pingtung located in the south part of Taiwan from her birth till graduation from Taiwan Provincial Pingtung Girl's High School in 1973. She then entered National Taiwan University at Taipei. After graduating in June, 1977 with a Bachelor of Science degree in Chemical Engineering, she was awarded a research assistantship in the Chemical Engineering Program at The University of Idaho, Moscow. After receiving a master degree in May, 1979, she entered The University of Tennessee, Knoxville in September, 1979 to study toward a doctoral degree in Polymer Engineering. This degree was awarded in March, 1984.

She is a member of the Society of Plastics Engineers, American Chemical Society, and American Physical Society.